Microcomputed Tomography Dosimetry and Image Quality in Preclinical Image-Guided Radiation Therapy

by

Christopher Daniel Johnstone
A.A., Fullerton College, 2009
B.S., California State Unversity, Fullerton, 2011
M.S., San Diego State University, 2013

A Dissertation Submitted in Partial Fulfillment of the
Requirements for the Degree of

DOCTOR OF PHILOSOPHY

in the Department of Physics and Astronomy

Microcomputed Tomography Dosimetry and Image Quality in Preclinical Image-Guided Radiation Therapy

by

Christopher Daniel Johnstone
A.A., Fullerton College, 2009
B.S., California State Unversity, Fullerton, 2011
M.S., San Diego State University, 2013

Supervisory Committee

Dr. M. Bazalova-Carter, Supervisor
(Department of Physics and Astronomy)

Dr. D. Wells, Department Member
(Department of Physics and Astronomy)

Dr. J. J. Lum, Outside Member
(Department of Biochemistry and Microbiology)

ABSTRACT

Motivated by the need to standardize preclinical imaging for image-guided radiation therapy (IGRT), we examine the parameters that influence microcomputed tomography (microCT) scans in the realm of image quality and absorbed dose to tissue, including therapy beam measurements of small fields.

Preclinical radiation research aims to understand radiation-induced effects in living tissues to improve quality of life. Small targets and low kilovoltage x-rays create challenges that do not arise in clinical radiation therapy.

Evidence based on our multi-institutional study reveals a considerable aberration in microCT image quality from one institution to the next. We propose the adoption of recommended tolerance levels to provide a baseline for producing satisfactory and reproducible microCT image quality scans for accurate dose delivery in preclinical IGRT.

Absorbed dose imparted by these microCT images may produce deterministic effects that can negatively influence a radiobiological study. Through Monte Carlo (MC) methods we establish absorbed microCT imaging dose to a variety of tissues and murine sizes for a comprehensive combination of imaging parameters. Radiation beam quality in the small confines of a preclinical irradiator is also established to quantify the effects of beam scatter on half-value layer measurements.

MicroCT scans of varying imaging protocols are also compared for murine subjects. Absorbed imaging dose to tissues are established and presented alongside their respective microCT images, providing a visual bridge to systematically link image quality and imaging dose.

We then characterize a novel small plastic scintillating dosimeter to experimentally measure microCT imaging and therapy beams in real-time. The presented scintillating dosimeter is specifically characterized for the low energies and small fields found in preclinical research. Beam output is measured for small fields previously only achievable using film. Finally, quality assurance tests are recommended for a preclinical IGRT unit.

Within this dissertation, a narrative is presented for guiding preclinical radiotherapy towards producing high quality microCT images with an understanding of the absorbed imaging dose deposited to tissues, including providing a tool to measure small radiation fields.

Contents

Publications

PEER-REVIEWED PAPERS

1. **CD Johnstone**, F Therriault-Proulx, L Beaulieu, and M Bazalova-Carter. Characterization of a Plastic Scintillating Detector for the Small Animal Radiation Research Platform (SARRP). *Medical Physics*, 46(1) 2019.

2. DY Breitkreutz, S Bialek, B Vojnovic, A Kavanagh, **CD Johnstone**, Z Rovner, P Tsouchlos, T Kanesalingan, and M Bazalova-Carter. A 3D-Printed Modular Phantom for Quality Assurance of Image-Guided Small Animal Irradiators: Design, Imaging Experiments and Monte Carlo Simulations. *Medical Physics*, 46(5) 2019.

3. Y Poirier, **CD Johnstone**, C Kirby. The Potential Impact of Ultrathin Filter Design on Dosimetry and Relative Biological Effectiveness in Modern Image-Guided Small Animal Irradiators. *The British Journal of Radiology*, 92(1095) 2019.

4. NM Esplen, L Chergui, **CD Johnstone**, and M. Bazalova-Carter. Monte Carlo Optimization of a Microbeam Collimator Design for the use on the Small Animal Radiation Research Platform (SARRP). *Physics in Medicine & Biology*, 63(17) 2018.

5. **CD Johnstone** and M Bazalova-Carter. MicroCT Imaging Dose to Mouse Organs Using a Validated Monte Carlo Model of the Small Animal Radiation Research Platform (SARRP). *Physics in Medicine & Biology*, 11(63) 2018.

6. **CD Johnstone**, P Lindsay, EE Graves, E Wong, JR Perez, Y Poirier, Y Ben-Bouchta, T Kanesalingam, H Chen, AE Rubinstein, K Sheng, and M Bazalova-Carter. Multi-institutional MicroCT Image Comparison of Image-Guided Small Animal Irradiators. *Physics in Medicine & Biology*, 14(62) 2017.

7. **CD Johnstone**, R LaFontaine, Y Poirier, and M Tambasco. Modeling a Superficial Radiotherapy X-ray Source for Relative Dose Calculations. *Journal of Applied Clinical Medical Physics*, 16(3) 2015.

PEER-REVIEWED ABSTRACTS

1. **CD Johnstone** and M Bazalova-Carter. MicroCT Imaging Dose for a Commercial Image-Guided Small Animal Irradiator. *Radiotherapy and Oncology*, Vol. 129, Suppl. 1, S33, 2018.

2. C Kirby, **CD Johnstone**, and Y Poirier. Effect of Thin X-Ray Filter Design in Modern Image-Guided Small Animal Irradiators on X-Ray Dosimetry and Radiation Biological Effectiveness. *Radiotherapy and Oncology*, Suppl. 1, 129, S45, 2018.

3. DY Breitkreutz, **CD Johnstone**, and M. Bazalova-Carter. MC Simulations of microCT Imaging on the Small Animal Radiation Research Platform (SARRP). *Radiotherapy and Oncology*, Suppl. 1, 129, S39, 2018.

4. NM Esplen, **CD Johnstone**, L Chergui, and M Bazalova-Carter. Optimization of a Microbeam Collimator for use on the Small Animal Radiation Research Platform: TU-GH-KDBRA1-04. *Medical Physics*, 45(6) E533, 2018.

5. S Bialek, B Vojanovic, A Kavanagh, **CD Johnstone**, T Kanesalingam, and M Bazalova-Carter. 3D Printed Phantom for MicroCT Imaging QA: MO-E115-GePD-F9-01. *Medical Physics*, 45(6) E421, 2018.

6. **CD Johnstone**, L Beaulieu, F Therriault-Proulx, and M Bazalova-Carter. Development and Characterization of a Plastic Scintillating Detector for Small Animal Irradiators Sci-Thur AM: YIS 01. *Medical Physics*, 44(8) 4369, 2017.

7. **CD Johnstone** and M Bazalova-Carter. Establishing MicroCT Imaging Dose to Mouse Organs Using a Validated Monte Carlo Model of the Small Animal Radiation Research Platform: su-e-fs1-04. *Medical Physics*, 44(6) 2729, 2017.

8. Y Poirier, M Bazalova-Carter, **CD Johnstone**, A Anvari, and A Sawant. FMEA Quality Management Framework for Small Animal Image-Guided Radiotherapy Based on TG-100 Methodology: mo-de-605-03. *Medical Physics*, 44(6) 3063, 2017.

9. **CD Johnstone** and M Bazalova-Carter. Automated Imaging Quality Assurance for Image-Guided Small Animal Irradiators: Sci-Thur AM: YIS-08. *Medical Physics*, 43(8) 4930, 2016.

10. Y Poirier, M Sommerville, **CD Johnstone**, J Grafe, I Nygren, R Khan, JE Villareal-Barajas, F Jasco, and M. Tambasco. Validation of a General Empirically-Based Beam Model for kV X-ray Sources: Sci-Thur AM: YIS-09. *Medical Physics*, 41(8) 2014.

11. **CD Johnstone**, R LaFontaine, Y Poirier, and M Tambasco. Validation of In-House Dose Calculation Software for Superficial Therapy. *Radiotherapy and Oncology*, Vol. 108, Suppl. 1, 114, 2013.

List of Tables

List of Figures

List of Abbreviations

AAPM	American Association of Physicists in Medicine
ADCL	Accredited Dosimetry Calibration Laboratory
COMP	Canadian Organization of Medical Physicists
CBCT	Cone Beam Computed Tomography
CT	Computed Tomography
DNA	Deoxyribonucleic Acid
DICOM	Digital Imaging and Communications in Medicine
ESF	Edge-Spread Function
EPID	Electronic Portal Imaging Devices
fps	Frames per Second
FWHM	Full-Width Half-Max
GUI	Graphical User Interface
HVL	Half-Value Layer
HU	Hounsfield Unit
IGRT	Image-Guided Radiation Therapy

LET	Linear Energy Transfer
LINAC	Linear Accelerator
kVp	Peak Kilovoltage
LSF	Line Spread Function
MeV	Megaelectron Volt
microCT	Microcomputed Tomography
MRI	Magnetic Resonance Imaging
MTF	Modulation Transfer Function
NIST	National Institute of Standards and Technology
NRCC	National Research Council Canada
OSLD	Optically Stimulated Luminescent Dosimeter
PET	Positron Emission Tomography
PMMA	Polymethyl Methacrylate
PSD	Plastic Scintillation Detector
RBE	Relative Biological Effectiveness
ROI	Region of Interest
SNR	Signal-to-Noise Ratio

SARRP	Small Animal Radiation Research Platform
SAPA	Small Animal Phantom Analyzer
SDD	Source-to-Detector Distance
SID	Source-to-Isocenter Distance
SI	International System of Units
SID	Source-to-Isocenter Distance
TG	Task Group
TIFF	Tagged Image File Format
TLD	Thermoluminescent Dosimeter
UVIC	University of Victoria
QA	Quality Assurance
VOI	Volume of Interest

ACKNOWLEDGEMENTS

Have you heard of **Dr. Magdalena Bazalova-Carter**? If not, go online right now and look her up. Not only is she prolific in the field, but I've never met a supervisor who genuinely cares more about her students than she does. Anytime I had a question, no matter how busy she was, she dedicated all of her time until I had the necessary tools to turn my fumbling steps into a forwards sprint. All of the time she spent over the years making me a better scientist really means a lot to me. I would have her as a supervisor all over again in a heartbeat, and as her first PhD student, I want to make her proud! Email her (bazalva@uvic.ca) and tell her that you've read my dissertation, I know that she would appreciate it!

The many years of research and the compiling of this document was one of the most challenging experiences that I've ever encountered, and I would not wish such a journey onto my worst enemy! However, the rewarding personal growth, adventures with friends in nature, and the ultimate conquering of such a beast made it well worth it. This would not have been possible without those who've put up with me along the way. Things can be difficult at times, like the difficulty you're experiencing right now trying to read this, but with the help of friends (or a mirror), it gets a lot easier.

Dr. Samantha Van Nest for being the person who got me to adventure around the island, into running, and was the reason why I was able to graduate. She was always there to help me out and to push me forward when I didn't believe in myself, and I will be forever grateful. You should look her up, she's going places.

Alex Beckmann for being one of my first friends and outdoor adventure friend in Victoria. **Nolan Esplen** for always organizing the fun (2016!), **Chelsea Dunning**, "Voice." for always being awesome (I finally bought a houseplant!). **Leah Nicholson** for inviting me to my first Thanksgiving in Canada, "Are you kidding me!??" **John Trafford** for being the best neighbor and great friend (see you in Ontario!). **Dr. Tom Banks** for daring me to run my first marathon. The greatest **Zoe MacDonald** for always giving me a wonderful place to say in Victoria, especially when I first moved here. **Ben Hendricks** and **Katrin** for creating the extraordinary experience of writing our dissertations\papers in nature with "Writing in the Woods" and "Thesis Island." **Mark Pe** and **Chris Hollon** for being my best friends back in the states. **Dr. Derek Wells** and **Dr. Julian Lum** for being on my committee. **Angie Johnstone** is still the best editor (and Mom) I know.

And Vancouver Island, its beauty, nature, and adventure will always be the standard to which I hold all other places.

DEDICATION

For my parents, Dan and Angie, who have always believed in me.
For my sister, Tiffany, who always exudes inspiration.
For my brother, Kevin, who demonstrates what hard work can accomplish.
And for the Trees. People who cut them down are assholes.

EPIGRAPH

WARNING: If you are reading this then this warning is for you. Every word you read of this useless fine print is another second off your life. Don't you have other things to do? Is your life so empty that you honestly can't think of a better way to spend these moments? Or are you so impressed with authority that you give respect and credence to all who claim it? Do you read everything you're supposed to read? Do you think everything you're supposed to think? Buy what you're told you should want? Get out of your apartment. Quit your job. Start a fight. Prove you're alive. If you don't claim your humanity you will become a statistic. You have been warned .....

Chuck Palahniuk
Fight Club

FRONTISPIECE

Weekdays - In The New Office

Weekends - In The Old Forest

Chapter 1

Introduction

"I can't remember, were you into Canada Geese?"

–Mount Eerie

Preclinical radiation research is a field that applies scientific experimentation to non-human models, ultimately for the benefit of human health with respect to radiation interactions with tissues. This avenue in research aims to understand both the benefits and consequences of radiation-induced effects in living tissues without the potential repercussions of harming human life. With the fundamental biological processes much like our own, this field of study often extends towards the use of murine models. The knowledge obtained through this form of research may then be translated towards understanding radiation interactions in people to improve human life.

One of the major goals in this type of research is understanding how radiation can be better used for the treatments of human cancers. Human tumors are often implanted into murine hosts and irradiated to test different fractionation schemes, treatment techniques, and radiation responses. These types of studies have been conducted for decades [28]. Interactions between the immune system of the host and the implanted malignant cells together play a key role in immunotherapy experimentation, as an immune system is required to model the tumor response to preclinical immunotherapy research [95]. Radiation treatments induce apoptosis and mitotic cell death in tumors by creating single and double strand breaks in the deoxyribonucleic acid (DNA), thus many preclinical studies monitor and quantify DNA damage and chromosomal

aberrations [77,97]. Studies are also interested not only in cellular damage, but also in cellular repair and resistance to apoptosis [55,86], including finding predictive markers to determine the survival response to specific therapies [8].

Modern research in the field includes using gold nanoparticles as a radiosensitizer agent to make tumor cells more sensitive to radiation therapy [38,44,56,57,163]. It has been found that irradiating gold nanoparticles implanted inside tumor cells increases the amount of double strand DNA breaks within the tumor. Another area of up-and-coming research is the use of radiation therapy in conjunction with immunotherapy, where radiation therapy is supplemented by boosting the body's natural defenses, improving the immune system to better fight cancer cells [52, 164, 179, 180]. More recently, it has been found that there may be an abscopal effect caused by radiation therapy, an amazing phenomenon in metastatic cancers where the localized treatment of a primary tumor also shrinks migrated tumors located outside of the treatment area [34, 92, 96, 138, 148]. Among radiation therapy treatments, imaging also plays a role in preclinical radiation research. The use of imaging modalities are used to visualize the internal anatomy of a subject to study and monitor disease, and to precisely target tumors for radiation therapy treatments.

1.1 Imaging in Preclinical Radiation Research

A number of imaging modalities exist that offer a non-invasive mechanism for tracking tumor response, finding new biomarkers, and are used as indispensable tools to allow for treatment planning and image-guided radiation therapy (IGRT). *In-vivo* imaging can allow for opportunities to visualize, characterize, and quantitatively study disease at the molecular level in a living subject. During treatment planning, obtained images are also used to position the subject and identify the location of the tumor. Treatment planning software commonly uses obtained microcomputed tomography (microCT) images to calculate complex dose distributions to irradiate the tumor with extreme precision while avoiding surrounding critical structures and normal tissues. Preclinical radiation research would not be possible without imaging, and thus is an incredible driving force at the heart of cancer research. Imaging modalities used include micro-single-photon emission computed tomography (SPECT), micro-positron emission tomography (PET), mirco-magnetic resonance imaging (MRI), micro-ultrasound, and

microCT. The term *micro* projects the micrometer (μm) degree of imaging resolution achievable by such modalities.

A brief survey of the many preclinical imaging modalities and their uses will be outlined. Micro-SPECT has strengths in imaging small lesions in organs by injecting small amounts of radioactive tracers for radio-labeling of biomolecules such as peptides, antibodies, and hormones, and the tracers are detected by crystal detectors. This is also useful for analyzing how internal organs are functioning, where traditional imaging only gives visual representations of the structure of the internal organs [43, 69, 157]. Micro-PET applies positron-emitting radioisotopes to image and measure different biochemical and physiological processes, and these are detected by inorganic scintillators which are used to detect accumulated radioactive uptake in tumor locations. These images can be overlaid to microCT scans to visualize small tumors that could not be seen by microCT alone [105, 130, 207]. Optical imaging uses light sources to capture photon distributions, including optical bioluminescence that uses light emitted by enzyme-catalyzed reactions that can be used to track tumor growth and metastases. This modality can also detect specific protein interactions in live specimens, as proteins are very important in studying DNA damage and radiation responses [190, 200]. Micro-ultrasound is a special modality as it uses sound to produce images by determining the shift in sound-wave frequencies through different tissues, and can be used for real-time tumor tracking and *in-vivo* instrument positioning [3, 68, 145]. Micro-MRI is a modality that uses non-ionizing radiation by using a combination of the magnetic properties of tissues and an external magnetic field with a strength in imaging soft tissues [12, 103]. Lastly, microCT uses x-ray attenuation through matter to measure the differences in tissue densities within the subject for imaging, and is one of the most widely used imaging modalities in preclinical research [9, 41, 168].

The microCT imaging modality will exclusively be the focus of this dissertation. There are currently two commercial image-guided irradiators available that are specifically made for state-of-the-art preclinical radiation research with murine models, and both irradiators use microCT as the primary built-in imaging modality [46, 193]. These irradiators rely solely on obtaining high quality microCT images to perform highly accurate radiotherapy treatments to tumor volumes with unprecedented micron-precision. Since these treatments rely so heavily on acquiring high quality, high resolution microCT images, it is of utmost importance to acquire the best images

possible while simultaneously not giving unnecessarily high dose to the subject.

1.2 The Problem to be Solved

The focus of this work first delves into the microCT images acquired using the two commercially available image-guided small animal irradiators– the PXi X-RAD SmART (Precision X-ray Incorporated, North Brandford, CT) and the Xstrahl SARRP (Xstrahl, Suwanee, GA). The work then concludes with a novel method to measure radiation dose within the Xstrahl SARRP irradiator. A detailed analysis of problems in the field regarding image quality, the resulting imaging dose, and accurate experimental dosimetry of imaging dose will be explained.

1.2.1 Image Quality Standards

Currently, the community has no set standards for microCT image quality to ensure that proper image quality is being produced and maintained for the two commercial small animal irradiators, including a wide variation in image quality between institutions using the same commercial irradiator. [111]. It will be shown that many users of the commercial small animal irradiators follow a myriad of imaging protocols that vastly influence the resulting image quality, both for better and for worse. There has been previously no body of work to serve as a frame of reference to compare a given institution's image quality to a gold-standard baseline value. Institutions have mostly been relying either on individual in-house data, or have completely forgone imaging quality assurance (QA) altogether. Complementary to image quality is the corresponding imaging dose which must also be taken into consideration.

1.2.2 Imaging Dose Quantification

Absorbed x-ray dose acquired from microCT imaging in small animal irradiators has, for the most part, been largely overlooked. Imaging dose has been previously approximated using Monte Carlo (MC) methods by simplifying the murine model as either a solid cylinder of water or tissue-equivalent material [30], or a composition of

crude heterogeneous materials [32]. Experimentally, imaging dose has been estimated by implanting TLDs within the murine host, effectively obtaining dose to the different organs [109]. The problem that arises in these techniques is the lack of accuracy in these estimates. The many intricacies of the murine model have been over simplified in MC models, and dose to the thermoluminescent dosimeters (TLDs) are not necessarily the dose to the respective adjacent organ. Accurate imaging dose quantification to the body, tumor, and individual organs in murine hosts has thus far been imprecise, and improvements in the techniques used to obtain imaging dose need to be made.

1.2.3 Dosimetry

Dosimetry in image-guided small animal irradiators demands the ability of a dosimeter to appropriately measure the small radiation fields ($\leq$ 1 cm diameter) employed in small animal radiotherapy. The ideal dosimeter would allow for fast and efficient acquisition of absorbed dose, would be cost-effective and small in size, and would have high enough spatial resolution to measure profiles in small fields. This is important in order to be a useful tool for real-time measurements for QA and treatment and imaging dose verification [112]. Currently, Gafchromic film (Ashland Advanced Materials, Bridgewater, NJ) is the only commercial dosimeter that has high enough resolution capabilities to accurately measure sub-millimeter fields. However, the drawbacks to Gafchromic film are abundant– a box of Gafchromic film can cost upwards of $600, it is time-consuming to calibrate, and it often requires 24 hours to obtain absorbed dose measurements. Pinpoint ionization chambers are capable of measuring absolute dose in real-time, however, the 0.015 cm^3 sensitive volume is too large to measure small fields. Recently, a microDiamond detector was created for small field dosimetry with a very small 0.004 mm^3 sensitive volume [2], but has not been validated for the low radiation energies used in preclinical radiation studies. Thus, a need for an improved dosimeter is essential to measure absorbed radiation dose in image-guided small animal irradiators.

1.3 Importance and Impact

Standardization of microCT image quality is absolutely vital for the emerging preclinical irradiators in the field, as imaging the tiny structures of murine hosts requires extremely high resolution and high image quality for the required accuracy of treatment planning of radiotherapy treatments. MicroCT imaging requires higher resolution than what is currently capable in diagnostic medical imaging of humans (0.1 mm compared to 1 mm, respectively). A lack of microCT imaging QA can produce potentially detrimental outcomes to the field of preclinical radiation therapy, such as producing improper treatment plans due to using suboptimal images. As discussed, a high degree of resolution and imaging quality are not being verified, thus a standardization of image quality is greatly needed. This work begins by obtaining QA tolerance levels from a multi-institutional study to establish a standard to which microCT imaging should be met and maintained over time, and followed by all users of the commercially available small animal irradiators. This study was lead by the American Association of Physicists in Medicine (AAPM) Working Group on Conformal Small Animal Irradiation Devices (WGCSAI). The resulting imaging dose imparted by an IGRT study must be taken into consideration.

Imaging dose is absorbed within the subject to produce microCT images, but this dose must not be high enough to interfere with the biological pathways (i.e. the DNA damage response [DDR] or cellular metabolism) of the murine model. The amount of time, preparation, and funding that goes into conducting preclinical radiation research in murine models can be vast. It is imperative that studies are not unnecessarily repeated, especially from an ethical standpoint. A complete knowled***g***e of the imaging dose (not just dose to the tumor and body, but to the individual organs as well) must be attained to prevent experiments from being compromised from potentially damaging doses. For the first time in a commercial image-guided small animal irradiator, a comprehensive report is presented on the microCT imaging dose to murine organs for a large variation of imaging protocols and parameter combinations. This is achieved by using a highly accurate in-house MC model that establishes imaging dose to the tumor, whole-body, and to a number of major organs, and obtained for a large range of murine sizes. This data will assist the community in making informed decisions on the amount of imaging dose they are administering. Lastly, experimental dosimetry of this absorbed dose will be examined.

Starting a decade ago, the relatively new field of preclinical radiation research using dedicated image-guided small animal irradiators has been slow at developing dosimeters for measuring its scaled-down field sizes, relative to the larger field sizes of its linear accelerator (LINAC) analogue. The dosimeters used with LINACs, namely ionization chambers, are adequate for the range of field sizes used for most LINAC irradiations and QA purposes (3 x 3 cm^2 to 40 x 40 cm^2) [131]. When the sensitive volume of a detector is large enough compared to a measured field size, the dose value changes over the dosimeter's active volume and results in an averaged dose. The averaging of dose across the active volume of a detector is called volume averaging, where the result is a lower dose readings compared to its true value [39, 108]. The 0.6 cm^3 active volumes of the common PTW farmer-type ionization chamber is small enough to measure field sizes down to a 5 cm diameter (as reported by the manufacturer). The smaller PTW pinpoint ionization chambers with an active volume of 0.015 cm^3 can measure down to a 2 cm diameter field size (as reported by the manufacturer). This helps make dosimetry using ionization chambers the gold-standard within LINACs. However, these same ionization chambers are currently being used for dosimetry within small animal irradiators, but they are too large to accurately measure absorbed dose for the small field sizes used in image-guided small animal radiotherapy [112].

In collaboration with François Therriault-Proulx and Luc Beaulieu at the University of Laval, QC, Canada, a small prototype scintillator dosimeter has been developed and characterized, with the ability to measure small fields down to 3 mm in diameter with minimal volume averaging [112]. This is currently the only real-time dosimeter capable of measuring the small fields that are demanded in image-guided small animal irradiators. This dosimeter will allow for real-time small field QA and *in-vivo* imaging and treatment dose verification, previously impossible to perform. This will allow a higher degree of accuracy in dose monitoring that is a much needed addition to the field, ensuring that the dose being administered is the dose that was intended.

1.4 Dissertation Scope

This dissertation aims to solve the problems presented in Section 1.2 by way of the research conducted in Chapters 5, 6, 7, and 8. This is first achieved through a four-

part introduction represented by Chapters 1, 2, 3, and 4, where the reader will acquire the necessary background and tools needed to secure a firm footing in the fundamental foundations that make up the core research material presented in the later chapters.

A brief overview and structure of what this dissertation covers, including the problems to be solved and the importance of finding a solution, are presented here in Chapter 1. More often than not, a work is elegantly presented, however the reader is left with thoughts of, *"This work sounds great, but why is it being done in the first place? Why does it matter? What's the point?"* The structure of Chapter 1 was conceived to give the reader a frame of reference to what this dissertation actually covers, and to give a sense of *why*, before getting an onslaught of background information that may prove to feel drab, mundane, and meaningless without first having a framework to what the background information is being applied to.

The next three chapters are this onslaught of background information. First, a history of microCT imaging is presented, including necessary information regarding x-ray generation, image acquisition, and image quality regarding microCT scans. Second, is information needed to understand the quantification of radiation dose produced by the aforementioned microCT images. Third, is an account of the equipment used throughout this dissertation with their detailed workings dissected and explained, including a detailed description of the MC methods used.

This then leads into the meat of the dissertation, embodied by Chapters 5, 6, 7, and 8, where the research tells a story investigating the importance of microCT image quality, quantification of microCT imaging dose in one of the two commercially available image-guided preclinical irradiators, what the absorbed imaging dose is relative to the image quality of murine subjects and, finally, how to experimentally obtain these absorbed doses for the energies and small fields used in small animal irradiators. These chapters (save for Chapter 7) contain my three published PhD papers, presented in full and unedited from the original published bodies of work, but bookended by added chapter introductions and summaries [109, 111, 112].

The dissertation concludes with Chapters 9 and 10. In Chapter 9, a description of quality assurance procedures are recounted to verify that the proper image quality and dose are being produced by the irradiator over time. Chapter 10 presents an overall conclusion of the entire dissertation.

All figures, figure constituents, images, and tables within this dissertation were created by Chris Johnstone (except images from Figures 4.5, 4.6, and 4.9 were taken by office mates).

1.5 Dissertation Summary

- **Chapter 1:** Presents the purpose of the dissertation, mapping out the problems to be solved, including the importance and impact on the field.
- **Chapter 2:** A history of microCT imaging, including x-ray generation, image acquisition, and characterization of parameters affecting image quality.
- **Chapter 3:** Information regarding ionizing radiation interactions in matter, specifically on x-ray energy absorption through photon interactions with atomic electrons.
- **Chapter 4:** A detailed description and analysis of the materials, equipment, and software used throughout this work.
- **Chapter 5:** Standardization of microCT image quality for quality assurance in commercial image-guided small animal irradiators, obtained through tolerance levels from a multi-institutional study.
- **Chapter 6:** Establishing microCT imaging dose to mouse organs through Monte Carlo methods, including quantifying backscatter contributions to half-value-layer measurements for absorbed dose calculations within the Small Animal Radiation Research Platform.
- **Chapter 7:** An extension of microCT imaging dose from Chapter 6, now with respect to varying imaging quality that includes microCT mouse images for visual comparison.
- **Chapter 8:** A characterization of a plastic scintillator detector for the Small Animal Radiation Research Platform used for empirical small field dosimetry.
- **Chapter 9:** Quality assurance performed on the Small Animal Radiation Research Platform at the University of Victoria, BC, Canada, for verifying image quality and dose output over time.

- **Chapter 10:** Overall conclusions drawn from this work and final remarks, including a summary of future directions.
- **Appendix A:** Important biological considerations for Medical Physics.
- **Appendix B:** An appendix providing experimental validation of the in-house Monte Carlo model of the Small Animal Radiation Research Platform used throughout this dissertation.
- **Appendix C:** An appendix providing a dedicated space to the reader for notes.

Chapter 2

MicroCT Imaging

"I See Everything"

–La Dispute

This chapter introduces microcomputed tomography (microCT) which is the fundamental backbone and major research area of this body of work. MicroCT is a non-invasive x-ray imaging modality that produces high-resolution 3D images made up of hundreds of 2D trans-axial projections. These axial reconstructions are commonly refered to as computed tomography, or CT. MicroCT is mainly a smaller micrometer-resolution version of the larger millimeter-resolution CT modality that most people are familiar with. Here, we will delve into a brief history of microCT, x-ray generation, and the different types of imaging parameters that affect microCT image quality.

2.1 MicroCT History

Within the first year of Dr. Wilhelm Röntgen's discovery of x-rays (originally named the Röntgen ray) in 1895 from research involving a cathode ray tube, over one thousand journal articles regarding x-rays were published [73], illustrating the immediate impact and recognition of x-rays. Within the first five years of discovery, x-rays began to become widely recognized as essential for clinical care through diagnostic imaging [88]. For much of the 20th century, a lack of fundamental understanding regarding x-ray interactions combined with primitive technology alluded researches into standardizing diagnostic imaging in the medical field, until Dr. Allan Cormack and Sir Godfrey Hounsfield invented the computerized transverse axial scanning (tomography) system in the early 1970s, which exploits x-rays to obtain axial images within a person. The first patient was scanned in 1971 in the basement of Morely Hospital in Wimbledon, England, with the first paper in tomography published in 1973 [87]. Then in 1979, Dr. Cormack and Sir Hounsfield won the Nobel Prize in Physiology or Medicine for their invention of their imaging modality, which ultimately promoted the widespread use of CT imaging.

CT images were limited to only millimeter resolution, so in the early 1980s a Ford Motor Company physicist, Dr. Lee Feldkamp, developed a system to evaluate structural defects of automotive materials using micrometer resolution. Inspired by the possibility to expand his automotive high-resolution imaging technology to the medical field, Dr. Feldkamp developed the cone-beam algorithm to create 3D reconstructed images [64]. Then, with a collaboration between Dr. Feldkamp and Dr. Michael Kleerekoper of Henry Ford Hospital, micron-resolution CT was first described in a 1983 abstract [65]. Around the same time, researcher Jim Elliott created the first 2D micro-tomography system, and with it published the first micro-tomography x-ray image– a scan of a Biomphalaria glabrata (a species of air-breathing freshwater snail) with 12 x 12 μm^2 pixel resolution. Shortly after this, in collaboration between Dr. Feldkamp and Dr. Steven Goldstein from the University of Michigan, Dr. Goldstein would coin the term "microcomputed tomography" and built the Feldkamp microCT scanner at the University of Michigan in 1984. This scanner became the first microCT system on a university campus. This would ultimately lead to the first publication of *in-vitro* 3D microCT which involved the analysis of subchondral bone architecture in 1989 [66]. MicroCT would become commercially available in 1994 for bone scanning,

and would serve as a catalyst in paving the way for micron-resolution x-ray imaging to change the field of CT imaging [147, 173].

Today there are about two dozen companies that commercially manufacture microCT imaging systems, with different strengths and focuses, ranging from dedicated imaging systems to multi-modality units. Some units are dedicated to imaging small animals with sub 100 μm voxel sizes (i.e., NanoFocus Ray Polaris-G90, Jeollabuk-do, Republic of Korea) and some units are also non-tissue related and made to scan micro-structural core samples and oil for geologists and petrophysicists (Thermo Fisher Scientific Heliscan microCT, Waltham, MA). This dissertation is focused on microCT imaging of small animals, specifically for the two commercial image-guided small animal irradiators currently on the market– the Precision X-ray X-RAD SmART (PXi,North Brandford, CT) and the Xstrahl SARRP (Suwanee, GA). We will now describe the microCT imaging technology of an image-guided small animal irradiator.

2.2 MicroCT X-ray Generation

MicroCT imaging units generate x-rays through a dedicated x-ray tube. These tubes can be thought of as an energy converter where electrical energy is converted into ionizing radiation. An x-ray tube (**Figure 2.1**) generates x-rays by first producing electrons using a cathode filament located within a vacuum. The cathode filament is made up of tungsten and is heated through electrical resistance to produce electrons, where these electrons leave the surface of the filament through thermionic emissions at a rate based on the tube current applied. Electrons are then accelerated towards an anode by applying a potential difference created by a tube voltage across the cathode and anode. This produces a stream of electrons that transverse through the vacuum tube and are directed towards a tungsten target connected to a stationary anode. The diameter of this electron beam for microCT imaging (˜0.4 - 3.0 mm) that hits a very small area on the tungsten target is known as the focal spot. The size of the focal spot determines the size of the x-ray beam; smaller focal spots are more suited for producing sharp microCT images, and larger focal spots (i.e. 3 mm) create a wider beam that is more useful for radiation therapy treatments. Some microCT x-ray tubes have small and large focal spot sizes to produce imaging and therapy x-ray beams, respectively.

The electrons bombard the tungsten target and produce x-rays through Bremsstrahlung (German for *braking radiation*) interactions as illustrated in **Figure 2.1**. When the electrons approach the nucleus of the tungsten atoms, the Coulomb force of the nucleus applies a force that causes a deceleration of the electrons and bends its incident path. This deceleration of the electrons allows for the release of energy perpendicular to the path of the electrons. Less than 2% of the energy generated is in the form of Bremsstrahlung radiation, where the rest is dissipated as heat [119]. Tungsten is an optimal material for an x-ray generating target as its very high heat capacity allows for the large heat absorption without melting. The x-rays produced are comprised of a spectrum of energies based on the kVp of the applied tube voltage. For example, if 220 kVp is generated within an x-ray tube, the x-rays will contain all energies between 0 keV through 220 keV. This is because the closer the Bremsstrahlung interactions occur to the nucleus of the tungsten atoms, the higher the x-ray energy produced. A larger percentage of the interactions happen at distances away from the center of tungsten nuclei, thus many lower-energy x-rays are produced below the nominal peak tube voltage applied.

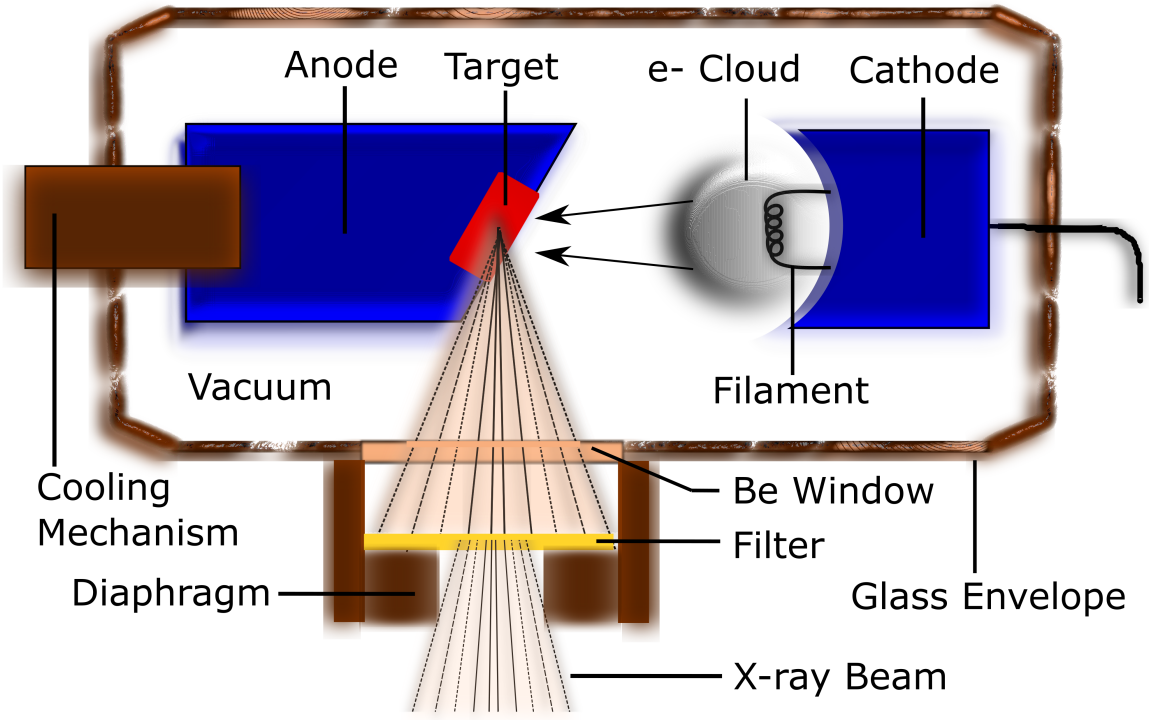

Figure 2.1: An illustration of a microCT x-ray tube used to generate x-rays using a cathode and anode within a vacuum.

Another form of x-rays that can be generated are called characteristic x-rays. This happens when an incident electron collides with an inner shell atomic electron, where the inner electron is ejected, making an outer shell electron fill the vacancy. This process produces the emission of x-rays that are said to be "characteristic," in that different types of bombarded materials produce an x-ray emission signal distinct to that specific material. The produced characteristic x-ray spectra compared to that of Bremsstrahlung is illustrated in **Figure 2.2**. Characteristic x-rays are usually generated only at 80 kVp tube potentials and greater for microCT x-ray beams.

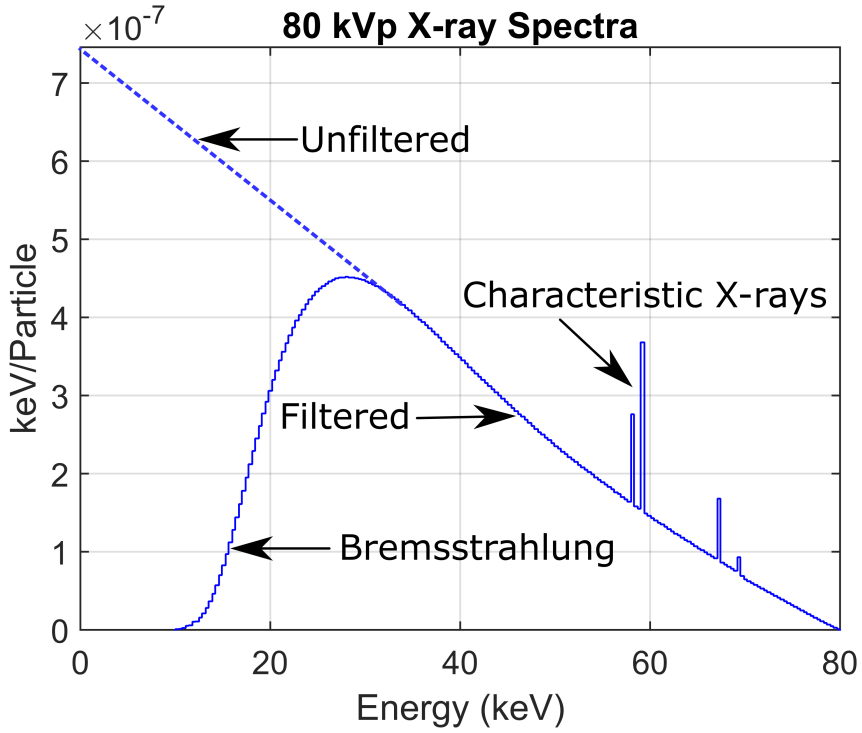

Figure 2.2: Spectra of an unfiltered and filtered x-ray beam produced in a microCT irradiator using a tungsten target, illustrating Bremstrahlung and characteristic x-rays at a tube potential of 80 kVp.

The resulting x-rays are then directed through a beryllium window, set as the vacuum/air interface, and attenuate through a filter (made of copper and aluminum for therapy and imaging beams, respectively). This filter is used to absorb the lower energies in the x-ray spectra in order to allow the more useful higher-energies to pass. The x-rays are then internally collimated and leave the diaphragm at the head of the irradiator. A cooling mechanism uses water to cool the anode and target to prevent overheating.

2.3 MicroCT X-ray Detection

The x-rays that are generated are recorded by a flat-panel detector located directly opposite that of the x-ray source. Many detectors in microCT imaging are based on a combination of scintillators (such as CsI or Gd_2O_2S:Tb) and amorphous silicon photodiode technology. These detectors are composed of a matrix of pixel electrodes that read the signal generated by the photodiodes. As illustrated in (**Figure 2.3**), the incident x-rays that reach the detector are absorbed by a scintillator, which converts the incident x-rays into light. The light is then read by photodiodes that converts the light into electrons that are sent into an electric circuit and out through a thin film transistor. This electric circuit keeps track of which pixels contain x-ray interactions.

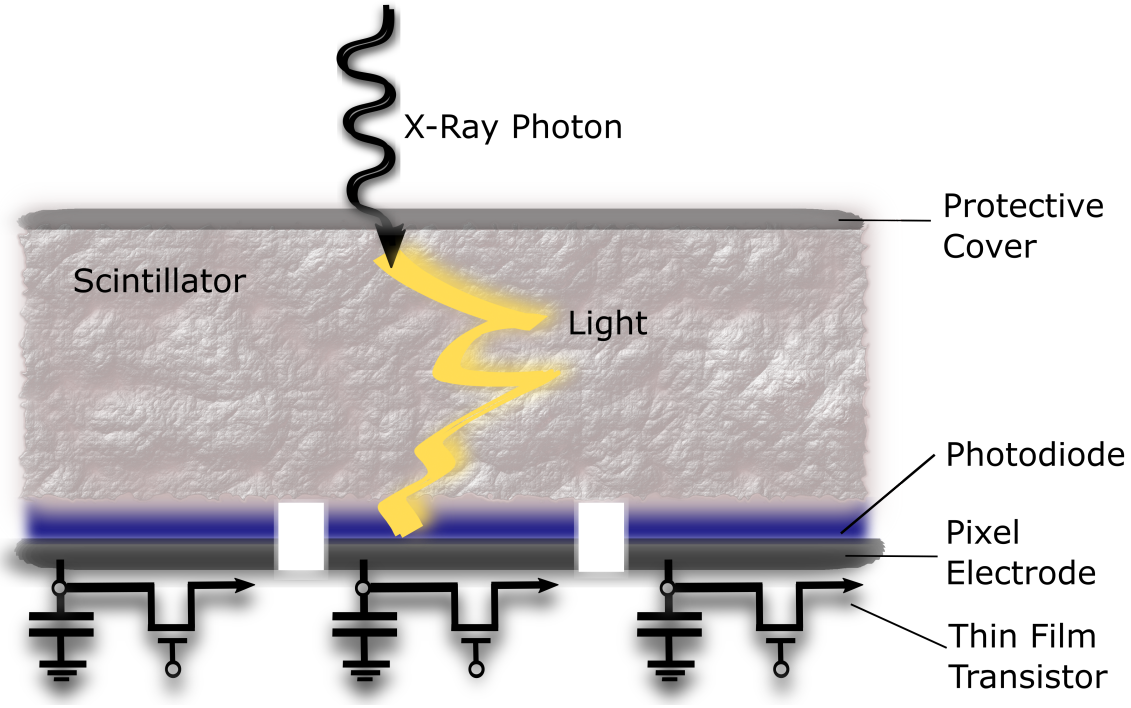

Figure 2.3: A zoomed-in cross-section of a microCT flat panel detector to illustrate the conversion of an x-ray photon into an electric signal within a specific pixel of the detector. The main detector components are the scintillator, photodiodes, pixel electrodes, and thin film transistors.

What makes these microCT detectors specifically unique compared to their larger CT detector counterpart is the number of pixels and their pixel pitch. Pixel pitch is defined as the distance from the center of a pixel to the center of an adjacent pixel.

Typically, microCT detectors contain an array of 1,000 x 1,000 pixels with a pixel pitch of 0.200 mm. This translates to an active detector field of 20 x 20 cm^2. A very small pixel pitch allows for the micron-resolution that is needed to image the tiny anatomy of small animals.

2.4 MicroCT Image Reconstruction

So how do these x-rays absorbed by the detector produce images? As x-rays travel through matter, some of the x-rays get absorbed while the rest penetrate all the way through an object to the detector. The brightness of the individual pixels in a microCT image is related to the x-ray intensity that reaches the detector after traveling through the imaged object. This intensity can be described by the linear attenuation coefficient (μ),

$$\mu = -\frac{1}{x}\ln\left(\frac{I}{I_0}\right), \tag{2.1}$$

where I_0 is the initial intensity of the x-ray beam leaving the source, I is the intensity of the x-ray beam that reaches the detector for a given pixel, and x is the distance the x-rays traverse throughs material. The closer I is to I_0, the darker the pixel is on the microCT image.

In general, images are acquired through hundreds of 2D projections where x-rays are projected through an object towards the 2D flat-panel detector of **Figure 2.3**. As illustrated in **Figure 2.4**, both the x-ray source and the detector rotate relative to the object being imaged in a 360° arc. The source emits a continuous beam of x-rays while the detector acquires a 2D map of attenuated x-ray intensities at every projection around the object. These 2D images are reconstructed to form a 3D volume representation of the inner anatomy of the object being scanned. This form of geometry for image-guided radiation therapy is known as cone beam CT [100].

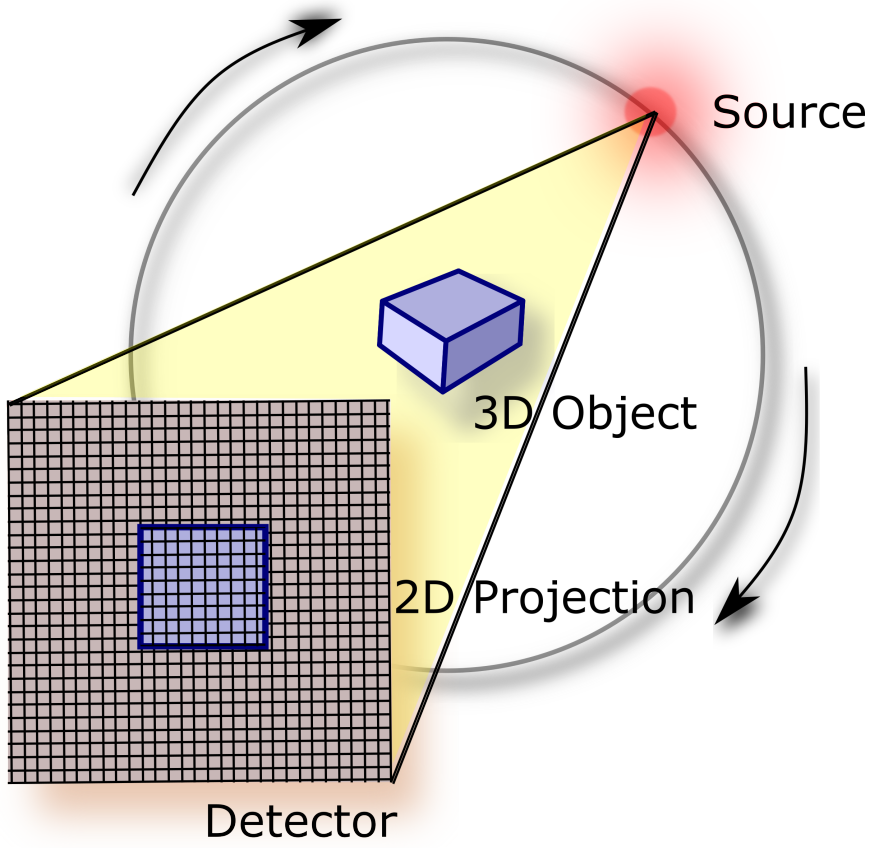

Figure 2.4: An illustration of a flat panel detector with pixel matrix and source rotating around relative to a 3D object, as hundreds of 2D projections are obtained at the detector to obtain a 3D image after reconstruction.

One of the most popular forms of cone beam reconstruction is using filtered back projection. This process is solved by using Fourier transforms. A Fourier transform, *F(ω)*, is given by

$$F(\omega) = \int_{-\infty}^{\infty} g(x) e^{-i\omega x} dx, \tag{2.2}$$

where $g(x)$ is a function to be transformed from the spatial domain (x) into the frequency domains (ω). Filtered back projection mathematically simulates an image acquisition by taking each projection data in the spatial domain, filters the data in the frequency domain, then backprojects the data back into the spatial domain onto an image matrix. The filtration process must be applied to correct for blurring that occurs during unfiltered backprojection. The filtered projection $p'(x)$ is calculated by

$$p'(x) = p(x) \circledast k(x), \tag{2.3}$$

where the original projection data $p(x)$ is convolved with a reconstruction kernel $k(x)$. This convolution mathematically combines two functions to create a third function, and computationally intensive, so it is faster to perform the filtration in the frequency domain using multiplication. Once this is completed, the data must then be transformed back into the spatial domain using an inverse Fourier transform to ultimately produce a microCT image. The final filtered projection can thus be calculated using

$$p'(x) = F^{-1}(F[p(x) \text{ x } k(x)]). \tag{2.4}$$

After all of the projections have been transformed, the entire dataset is then reconstructed and presented as the resulting corrected microCT image. Ultimately, each pixel of a microCT image represents the attenuation properties of the specific imaged object. MicroCT imaging commonly use the Feldkamp, Davis, and Kress (FDK) algorithm [64], which is a form of filtered back projection using an approximation that solves cone beam geometry using fan beam reconstructions. Fan beam reconstruction reconstructs the data using a set of line integrals spreading out from a single point rotated about the object being imaged. The FDK algorithm can be combined with various weighting functions to optimize its performance for different imaging parameters.

2.4.1 Reconstruction Kernels

Reconstruction kernels are part of the reconstruction algorithm for a detector that filters the image data during filtered backprojections. Some of the standard kernels are designed to improve the image quality when viewing different structures such as bone and soft tissue. For example, soft tissue kernels intentionally blur the image noise to better view soft tissue, while bone kernels intentionally reduce blurring to better view the sharp edges found in bone, however, this also increases the image noise [37, 74]. This is controlled by low and high pass filters. Low pass filters only allow low frequency information to pass, effectively averaging out rapid changes in

intensity to reduce image noise but at the cost of blurring the image. High pass filters only allow high frequency information to pass, making images look sharper by enhancing contrast in low contrast areas of an image, but results in amplifying the noise. Commercial image-guided small animal irradiators are factory set to use soft tissue kernels.

Common filters for image-guided small animal irradiators are the *Hann*, *Hamming*, *Bartlett*, *Welch*, *Shepplogan*, and *Square* filters. These filters are mathematical functions that are applied to filtered backprojection within the frequency domain and used to enhance the attributes of an image. Briefly, a Hann filter is a low pass filter used to reduce aliasing but at the cost of decreasing resolution. The Hamming filter is also a low pass filter that smooths the image. A Bartlett filter and Welch filter are similar band pass filters that reduce the noise of an image. The Shepplogan filter is a high pass filter that increases image noise but also increases resolution. Finally, the square filter is the equivalent reconstruction to using no filter.

2.5 Image Normalization

Once a microCT image has been obtained, the intensities within each pixel of the microCT image should be normalized. This normalization produces a standardized unit, known as a Hounsfield Unit (HU), which describes all pixel intensities relative to water. This method in normalization was chosen because the density and x-ray absorption characteristics of water can be approximated to that of human soft tissue. HUs are defined as,

$$HU = 1000\frac{\mu - \mu_{water}}{\mu_{water}} \tag{2.5}$$

where μ is the linear attenuation coefficient (discussed in Chapter 3) of a pixel located at position (x,y) in the image matrix, and μ_{water} is the linear attenuation coefficient of water. We can see that the equation was tailored to set water equal to 0 HU. HUs of common tissues are shown in **Table 2.1**, where higher HU numbers translate to brighter pixels. These HU values were calculated based on the mean energy of a 60 kVp imaging beam from a commercial small animal irradiator (Xstrahl SARRP), and from the x-ray mass attenuation coefficients of the National Institute of Standards

in Technology (NIST) tables [94] and tissue from the International Commission on Radiation Units and Measurement (ICRU) Report 44 [76].

Table 2.1: HU numbers of common tissues found in the body, calculated using the mean 60 kVp imaging beam (32 keV) of a commercial small animal irradiator (Xstrahl SARRP) using NIST x-ray mass attenuation coefficients and tissues from the ICRP Report 44. Scintillator dosimeter materials of Chapter 8 are also included.

Tissues and Materials	HU
Air	-999
Lung	-746
Polyethylene	-304
Polystyrene	-237
Adipose Tissue	-236
Water	0
Testis	2
Soft Tissue	8
Brain	44
Muscle	46
Cortical Bone	5,284

HU standardization is important as it simplifies the process of image analysis by segregating different tissue types within an image based solely on HU number. This process is also very important in producing accurate dose calculation algorithms [16]. MicroCT images are thus comprised of a spectra of pixel intensities/brightnesses that can be described using HUs, and these images are susceptible to different types of image qualities.

2.6 Imaging Acquisition Parameters

The quality of an image is directly related to the imaging parameters used that control the beam output in the x-ray tube. These parameters include tube voltage, tube current, and scan time. Reconstruction parameters that influence image quality such as voxel size and frame rate are also discussed.

2.6.1 Tube Voltage

As mentioned, the energy spectrum of an x-ray beam is determined by the peak tube voltage applied to the x-ray tube. The tube voltage influences the electron velocity as

it accelerates towards the anode from the cathode. The higher the peak tube voltage, the higher the mean energy of the x-rays that are generated. These higher energies results in a greater number of x-rays that penetrate through tissue compared to the lower energy x-rays that are more likely to become absorbed in tissue. Increasing the tube voltage is useful when imaging larger objects or when imaging high-density objects such as bone, as more x-rays will reach the detector which can help decrease image noise [106, 119]. However, this can also lead to reducing the contrast in an image if the tube voltage is too high when imaging smaller objects, as not enough x-rays will be abs***o***rbed in the object when producing an image [106]. Contrast can be defined as the difference in pixel intensities that makes two objects distinguishable. The tube voltage commonly used in image-guided small animal irradiators is 60 kVp for imaging beams. Increasing the tube voltage also indirectly increases the intensity of the beam (the amount of x-rays passing through a given area per unit time) because a higher number of Bremsstrahlung x-rays are produced when a higher tube voltage is used [7]. Changing the intensity of the beam is also the main function of tube current.

2.6.2 Tube Current

The density of the accelerated electrons in the x-ray tube is dependent on the applied tube current. The number of electrons that are produced at the cathode filament is linearly increased with an increase in tube current [91]. Increasing the amount of electrons that bombard the tungsten target does not increase the mean energy of the x-rays produced, but increases the number of Bremsstrahlung interactions that occur. What this means is that increasing tube current also linearly increases the amount of x-rays produced. Increasing tube current is useful for imaging larger objects which require more x-rays to produce satisfactory images, but this also gives a higher dose to the object [37, 119]. The range in tube current usually used in commercial image-guided small animal irradiators is between 0.6 to 1.5 mA.

2.6.3 Exposure Time

Like tube current, the amount of noise in an image is directly related to the exposure time. Exposure time is the amount of time the x-ray beam is on during image

acquisition. Increasing exposure time reduces the amount of noise in an object while also linearly increasing the amount of dose absorbed in an object. This is because the object being imaged is exposed to x-rays for a longer duration of time. The usual exposure time used in image-guided small animal irradiators is 60 seconds, but can be as high as 240 seconds for larger animals.

2.6.4 Voxel Size

The amount of resolution that is produced in a microCT image is directly dependent on the voxel size used in the image reconstruction. A smaller voxel size means less photons available per voxel to create an image, and thus increases the noise in an image. However, a smaller voxel size results in higher resolution, so a trade-off must be made. A voxel represents the smallest sampled 3D element in an image and smaller voxels help resolve smaller structures. Spatial resolution is quantified by how close two objects can be to each other and still be visually resolved. On the other hand, blurring happens when two objects are contained within the same voxel and thus cannot be resolved. Resolution in imaging is commonly defined by how many line pairs (a dark line and an adjacent light line) per mm can be resolved, where the higher amount of line pairs seen per mm in a given image constitutes higher image resolution. A voxel is comprised of a square pixel in the x and y plane of an image that has a slice thickness in the z-direction. While the slice thickness can be different from the pixel width, a voxel is commonly a cube of all equal sides in microCT imaging. A common voxel size used in image-guided small animal irradiators is 0.200 x 0.200 x 0.200 mm^3.

2.6.5 Frame Rate

Frame rate is a characteristic of the detector, where a single frame acquires a pixel intensity matrix of x-rays to be reconstructed. Frame rate is how many image acquisitions the detector makes per second, or the frequency of information that the detector takes in about the irradiated object. This is measured in frames per second (fps). There is a trade-off with the frequency of images acquired. Images acquired over a longer period of time (lower frequency) lowers the noise per frame, but are more susceptible to blurring from the relative movement of the source-detector with

the object. Likewise, images acquired over a shorter period of time (higher frequency) will not suffer from blurring, but will contain a higher amount of noise per frame. The frame rates commonly used in commercial image-guided small animal irradiators are 5 and 6 fps.

2.7 Degradation in Image Quality

We have discussed the major image acquisition and reconstruction parameters that affect microCT image quality. Here, we focus on factors that mainly degrade image quality in microCT imaging, such as unwanted image noise and artifacts. We will discuss artifacts which appear as features in a microCT scan but do not exist in reality. These artifacts can appear as a false structure or corruption in the microCT data as displayed in **Figure 2.5**. Some of the major artifacts in microCT imaging are beam hardening, streaking and ring artifacts, motion artifacts, and partial volume artifacts.

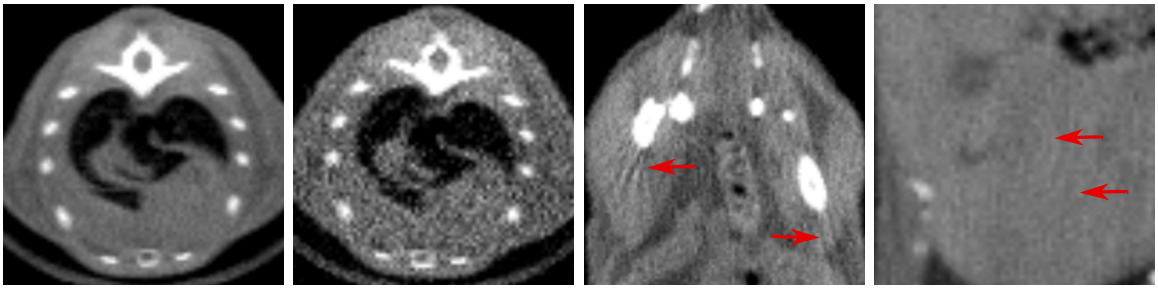

(a) Low Noise **(b)** High Noise **(c)** Streaking **(d)** Ring

Figure 2.5: MicroCT scans of a 32 g mouse for various scans and artifacts, illustrating a a) low noise scan, b) high noise scan, c) streaking artifacts next to bone, and d) ring artifacts.

2.7.1 Noise

Noise in microCT images can be thought of as unwanted change in pixel values in a region that contains a homogeneous material. It creates a grainy appearance in an image and, in the worst cases, can even look like static from an old analogue TV

stuck on channel 3. This can have a negative impact on image quality, and efforts are taken to reduce image noise as much as possible without giving too much dose to an object. Noise can be calculated as the standard deviation of pixel intensity within a given region of interest (ROI).

Noise is mainly caused by the statistical nature of interactions of ionizing radiation with matter [37]. Noise can be mitigated by increasing the amount of x-rays used during imaging, and is achieved by increasing the tube current or exposure time. However, there must be a balance between the amount of x-rays used and dose delivered. Another factor that increases noise includes scattered radiation from external objects, where the primary radiation beam diverges due to interactions within external objects, including within the scanned object itself. This allows for x-rays to find their way into the wrong pixel in the detector, producing a pixel intensity in the wrong location in a reconstructed image.

2.7.2 Beam Hardening

Beam hardening can be defined as an increase in the average energy of an x-ray beam due to the filtration of lower energy x-ray beams as they pass through matter. This increase in average energy of a radiation beam has been described as "hardening" the beam, where the higher the average energy, the "harder" the beam. Usually this is a sought-after effect, commonly obtained through external filtration to filter out the lower energies that do not contribute to the image. However, when beam hardening happens within the scanned object (more pronounced when the beam has to transverse through the longer axis of an object), this artificially lowers the pixel intensity at the center of the object as the lower energy x-rays get absorbed, leaving only the very highest energy x-rays to transverse the entire length of the object to the detector [37]. This can cause an artificial decrease in pixel intensity readout within the center of an otherwise homogeneous medium, with a higher pixel intensity near the edges of the phantom, which has been described as a cupping artifact [142, 189, 191], and this artifact can also be caused by scatter.

2.7.3 Streaking and Ring artifacts

Streaking artifacts are bright or dark lines within an image that can be caused by high density materials such a bone or metal present within an image. This is because the backprojection algorithm cannot accurately reconstruct an image when insufficient photons reach the detector due to highly dense objects obstructing the path of the beam. On the other hand, ring artifacts are bright or dark rings in an image that are caused by either a miscalibration or defective element within a detector. These streaking and ring artifacts can be located anywhere in an image, and may make it difficult to correctly assess a microCT image if these artificial additions in the image are obstructing anatomy of interest [37, 75].

2.7.4 Motion artifacts

Motion artifacts in an image can be caused by any voluntary or involuntary movement of the subject being imaged. This is more likely to occur during longer microCT scans, as movement across longer exposure times can be enough to blur the image and cause double images. This can be problematic as blurring can reduce the visibility of small objects and image detail. Shorter scan times can reduce motion artifacts, but this also runs the risk of producing lower quality images due to higher noise.

2.7.5 Partial Volume Effect

Lastly, the partial volume effect occurs when two different tissue types containing different densities are found in the same voxel. The pixel intensities of the different tissues are averaged together within the same voxel, and the resulting image produces a single structure intensity that is not representative of the two separate structures [37]. This is most apparent in structure boundaries within the anatomy of an animal, where sharp changes in structure boundaries become blurred. This may be resolved by increasing the resolution of an image through a reduction in voxel size but, as explained earlier, this can causes increased noise in the microCT image.

2.8 Summary

MicroCT imaging has been introduced, including the history, x-ray generation, x-ray detection, image reconstruction, and reconstruction parameters used in microCT imaging. The x-rays absorbed within an object that produce microCT images also absorb ionizing radiation dose within that object. This delivered dose occurs through interactions of radiation with matter, as this must be measured and quantified in order to fully understand the physics involved in microCT imaging, as well as to deliver an ethical amount of radiation dose to an animal. These interactions will now be analyzed in detail in Chapter 3.

Chapter 3

Interactions of Radiation with Matter

"Look here brother, who you jivin' with that Cosmik Debris?"

–Frank Zappa

Exposure to ionizing radiation, such as x-rays, electrons, and γ-rays, allows for interactions on the atomic scale that produces energy absorption in matter. This chapter will focus on the interactions produced by the x-ray interactions found in image-guided preclinical irradiators. The basic principles of ionizing radiation interactions will be described, including the photoelectric effect, Compton scattering, and pair-production. Mass energy-absorption and radiation dosimetry annotation will also be discussed, including the methods for absorbed dose measurements for the low x-ray energies found in preclinical irradiations.

3.1 Ionizing Radiation

Electromagnetic radiation refers to waves of synchronized oscillations of electric and magnetic fields that can be emitted by electrically charged particles undergoing acceleration. These waves carry energy ($E = hc/\lambda = h\nu$, units of J) and can interact with charged particles by exerting force onto them [47]. Electromagnetic radiation can be categorized as two types of radiation: non-ionizing and ionizing radiation. Non-ionizing radiation refers to electromagnetic waves that carry insufficient energy to knock-off electrons from the atoms within the matter that which it interacts. Likewise, ionizing radiation does contain enough energy, and thus is the focus of this chapter. The removal of electrons from atoms by the applied force of ionizing radiation causes unstable energy withing the atom (effectively ionizing the atom) and is of particular importance when these interactions happen within living tissues [119]. Ejected atomic electrons can either contain enough energy to ionize further atoms, or cause excitation by raising an electron to a higher energy shell in a interacting atom. Ionization of atoms break chemical bonds in molecules and change the basic makeup of the atoms in the interacting tissues, ultimately creating single and double strand breaks in DNA within tissue. These breaks in the DNA can either be naturally repaired over time or, if not, create apoptosis or develop cancerous cells [72].

Ionizing and non-ionizing radiation come in a vast spectrum of different photon energies that make up the entire electromagnetic spectrum, illustrated in **Figure 3.1**. A photon can be described as either an elementary particle or wave, where the former is defined as discrete quantum packets that have zero rest mass and travel at the speed of light. The amount of energy a photon contains defines what type of ionizing or non-ionizing radiation it is, and when considered as a wave, can be described by its frequency and wavelength where $\nu = \frac{c}{\lambda}$. Depending on the wavelength (or frequency) of the photon, the types of electromagnetic radiation a photon embodies can be broadly defined as (in order of decreasing wavelength) radio wave, microwave, infrared, visible light, ultraviolet, x-ray, and gamma (γ)-radiation [106,119,175]. The lower wavelength photons contain the highest energy, and are the most harmful to human tissues, and include ultraviolet, x-ray, and γ-radiation. Out of all the different types of electromagnetic radiation, x-ray and γ-radiation are the only types that contain enough energy to ionize an atom, thus are defined as types of ionizing radiation. The amount of energy imparted to tissues can be described by absorbed radiation

dose, and will be discussed now.

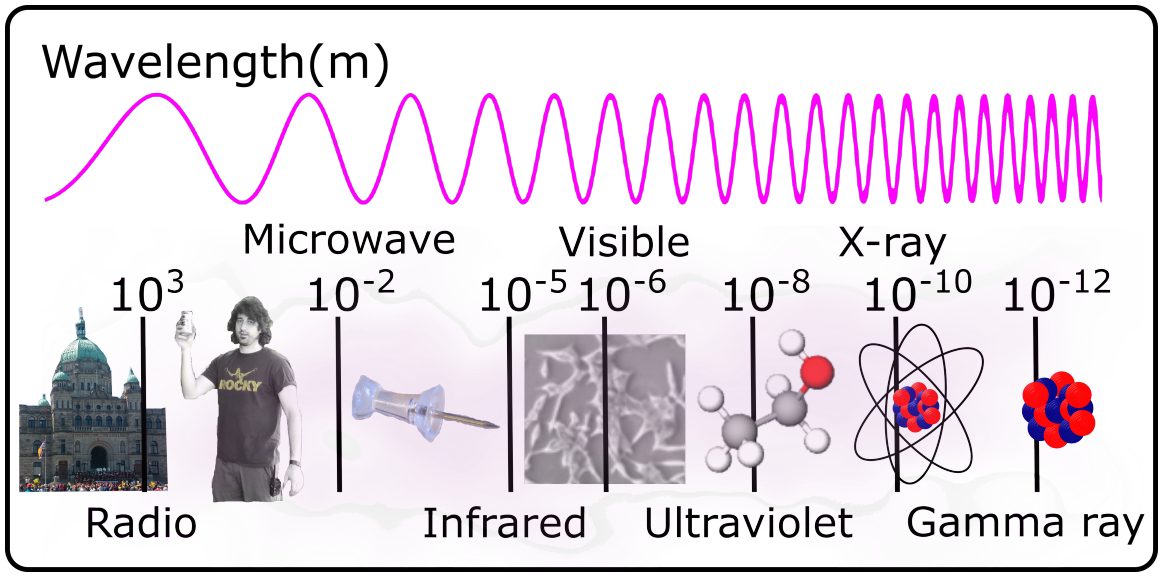

Figure 3.1: The electromagnetic spectrum illustrating the wavelengths of different types of radiation. For comparison, objects of approximately the same size as the wavelengths of each respective radiation type are illustrated. Objects from left to right: building, person, thumb tack, cells, molecule, atom, nucleus of atom.

3.2 Interaction of Photons with Matter

X-ray photons are electrically neutral particles of electromagnetic radiation that can penetrate relatively deep distances in tissue before interacting with atomic electrons, with higher energy photons generally having a higher penetrating capacity. At a given energy and medium, x-ray photons found, specifically in imaging and radiotherapy procedures, interact with atomic electrons based on statistical and probabilistic interactions that either result in photon scatter without loss of energy, photon absorption, or photon scatter with loss of energy [106, 119]. The main processes of photon interactions with atoms include Raleigh scattering, the photoelectric effect, Compton scattering, and pair production.

3.2.1 Raleigh (Coherent) Scattering

Rayleigh scattering (or coherent scattering) consists of a photon interacting with an atom by elastically scattering from bound electrons, resulting in the deflection of the photon and leaving the atom unchanged. This process does not result in energy deposition from ionizing the atom, but changes the direction of the photon with no net transfer of energy. This interaction ultimately attributes to the statistical probability of the final location of photon interaction and energy deposition within a medium [119]. Coherent scattering cross-section curves for cortical bone, water, and lung are shown in **Figure 3.2**. Cross-sections are important as they describe photon attenuation which is dependent on the photon energy and the materials it interacts with.

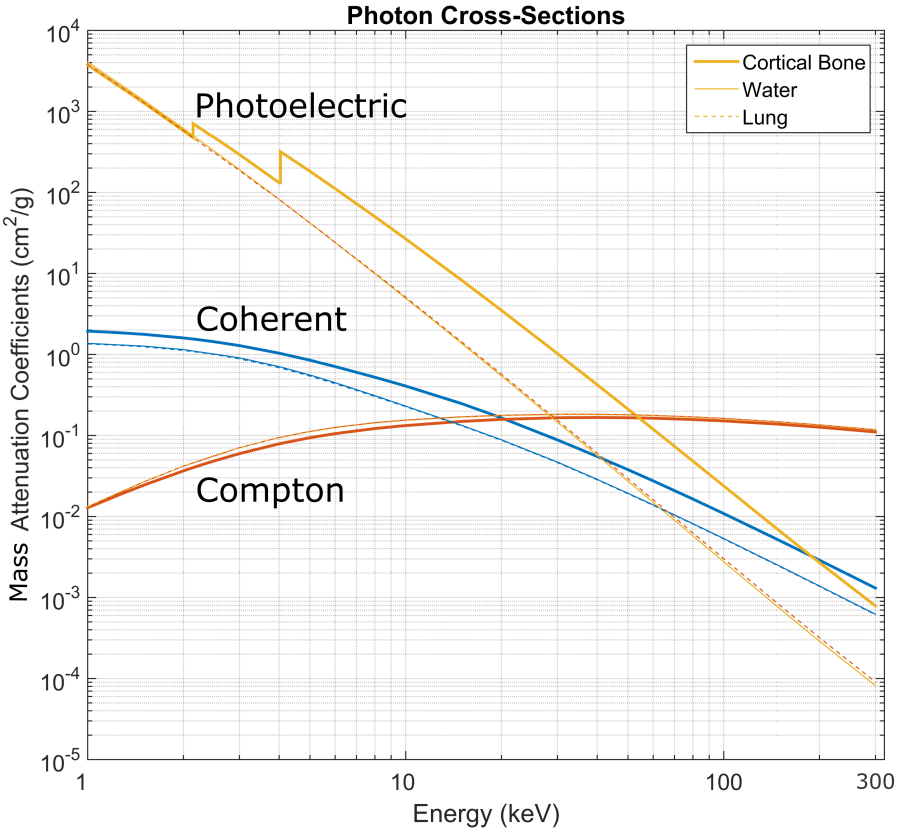

Figure 3.2: Coherent, photoelectric, and Compton photon attenuation cross-sections for cortical bone (thick lines), water (thin lines), and lung (dashed-lines) for the 1 to 300 keV energies found in preclinical irradiators. Note that pair production starts at approximately 1 MeV and is not illustrated. Data compiled from the NIST XCOM Photon Cross Sections Database [23].

3.2.2 The Photoelectric Effect

The photoelectric effect (**Figure 3.3**) takes place when an electron is ejected after a photon is completely absorbed in an atom. This ejected electron is known as a photoelectron. The probability of this photoelectron being produced is dependent on the atomic number (Z) of an element and the energy of the incident photon. This probability, P, is proportional to

$$P \propto \frac{Z^4}{E^3}, \tag{3.1}$$

illustrating that the higher the atomic number of an element and lower the photon energy, the greater the probability of the photoelectric effect occurring.

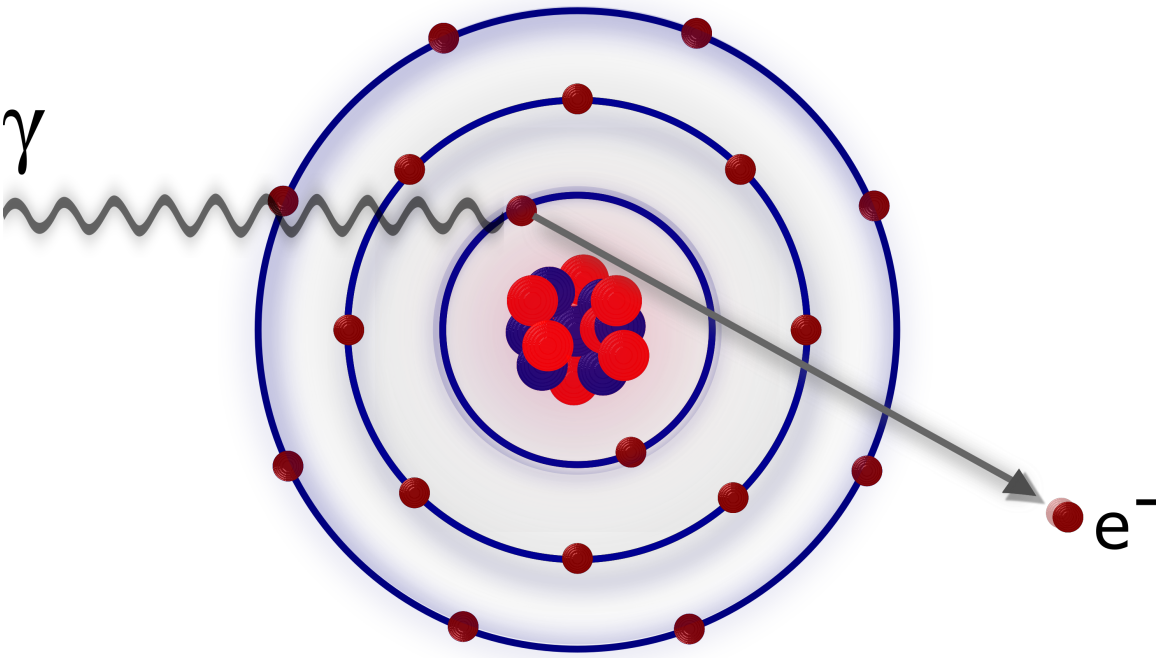

Figure 3.3: The photoelectric effect, where an incident photon (γ) is absorbed by an inner-shell atomic electron, producing the ejection of a photoelectron e^-.

The ejection of the photoelectron creates a vacant electron in one of the inner electron shells. This vacancy is filled by an electron located from a higher energy shell, and in the process releases energy in the form of characteristic x-rays. Auger electrons may

be produced when characteristic x-rays are transfered to another electron within the same atom, with this second electron (Auger electron) ejected from the atom. These releases of energy help return the atom back to its relaxed ground state. Ejected electrons have the potential to further deposit energy in the form of secondary tracks through ionization of other atoms, and defined as a δ-ray [106,119]. The photoelectric scattering cross-section curves for cortical bone, water, and lung are shown in **Figure 3.2**.

3.2.3 Compton Scattering

Compton scattering (**Figure 3.4**) takes place when a photon collides with an outer-shell electron of an atom, with the incident photon transferring part of its energy and scattering at an angle θ. The energy deposited ejects the electron at an angle ϕ, as the binding energy of the electron is less than the energy deposited into it from the photon. Compton scattering is mostly independent on atomic number, unlike the photoelectric effect, and is almost exclusively dependent on photon energy.

During Compton scattering interactions, the incident photon of energy $h\nu$ transfers some of its energy to an atomic electron, with the photon recoiling at an angle θ and continuing at a reduced energy $h\nu'$. The electron scatters at an angle ϕ after the collision. This is described by

$$h\nu' = \frac{h\nu}{1 + (h\nu/m_0c^2)(1 - \cos\phi)}, \tag{3.2}$$

where $m_0c^2 = 0.511$ MeV and is the rest mass energy of an electron. The angle of the scattered photon can be found using

$$\cot\theta = \left(1 + \frac{h\nu}{m_0c^2}\right) \tan\left(\frac{\phi}{2}\right). \tag{3.3}$$

An important parameter is the differential cross-section which describes the angular distribution of the electromagnetic energy scattered by particles. The differential cross-section for Compton scattering is given by the Klein-Nishina equation,

$$\frac{d_e\sigma}{d\Omega} = \frac{r_0^2}{2}\frac{(1+\cos^2\theta)}{[1+\alpha(1-\cos\theta)]^2}\left\{1+\frac{\alpha^2(1-\cos\theta)^2}{[1+\alpha(1-\cos\theta)](1+\cos^2\theta)}\right\}, \tag{3.4}$$

where $\alpha = h\nu/m_0c^2$ and $r_0 = 2.818 \times 10^{-13}$ cm is the classical electron radius [178]. The probability of Compton scattering in tissue increases at higher photon energies until the energy approaches 10 MeV. The majority of Compton interactions in tissue are produced from 100 keV to 10 MeV photon energies, and is the leading interaction between approximately 200 keV and 5 MeV in tissue [106, 119]. Compton scattering attenuation cross-section curves for cortical bone, water, and lung are shown in **Figure 3.2**.

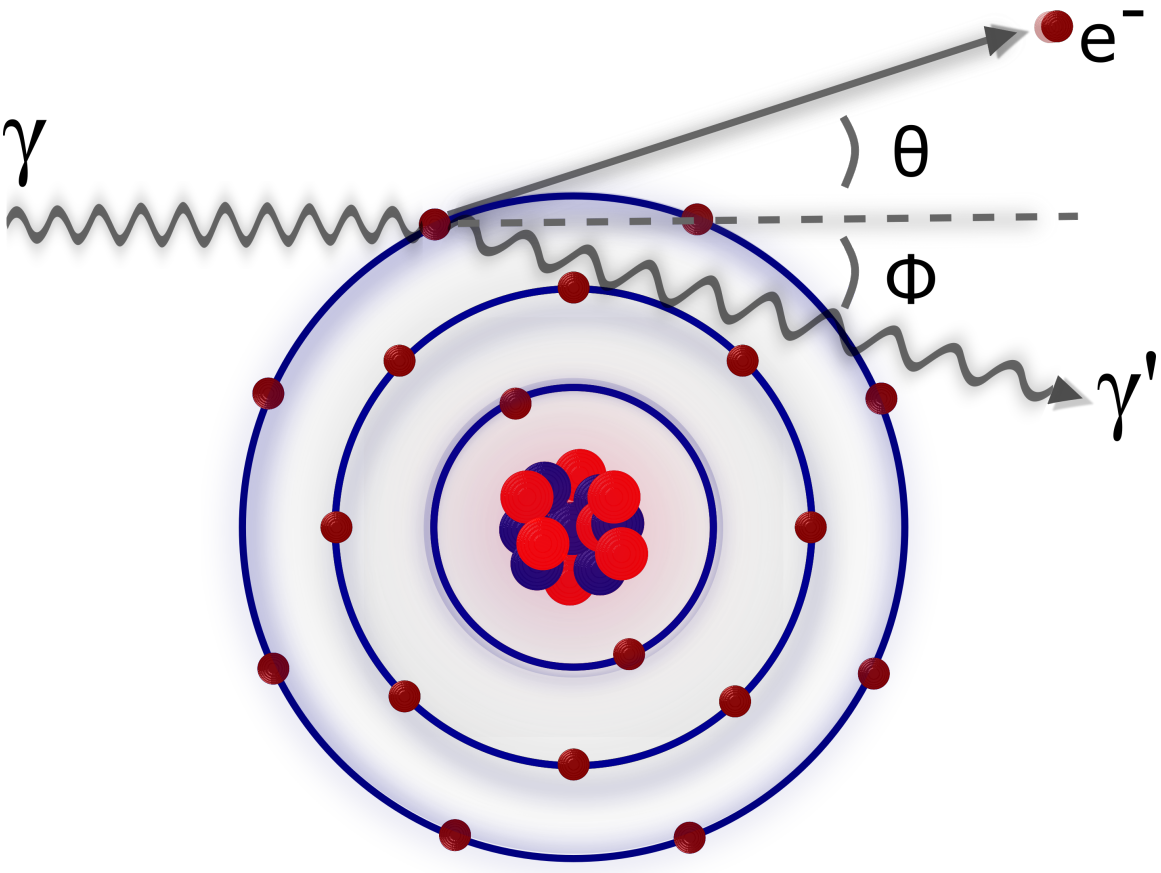

Figure 3.4: Compton scattering, where an incident photon (γ) collides with an outer-shell atomic electron and scatters away (γ') at angle θ. This results in the ejection of the electron (e^-) at angle ϕ.

3.2.4 Pair Production

When a photon is incident on the nucleus of an atom and contains twice the electron rest mass energy or greater ($\geq$ 1.02 MeV), an electron-positron pair can be produced. This production of an electron-positron pair is called pair production and illustrated in **Figure 3.5**. The photon's energy is converted to mass in accordance with the mass-energy equivalence from Einstein's equation $E = mc^2$, where m is the mass of the electron and c is the speed of light. Pair production can also be generated when photons are incident on atomic electrons, but it is less probable as the photon requires at least four times the electron rest mass energy ($\geq$ 2.04 MeV), in addition to interacting with a much smaller target. This interaction is referred to as triplet production, as the resulting recoiling electron contributes to a third body in the system. With respect to pair production within the nuclear field of the atom, the relatively massive nucleus responds with a small recoil of negligible energy. After creation, when the positron reaches its rest energy, it will then annihilate with a free electron to produce two 0.511 MeV photons, further attributing to possible ionization events.

The average energy of an electron positron pair, $\bar{E}$, is given by

$$\bar{E} = \frac{h\nu - 1.022\text{MeV}}{2}, \tag{3.5}$$

where 1.022 MeV is twice the rest energy of an electron. The average ejection angle of the electron and positron pair relative to the incident photon's trajectory is

$$\bar{\theta} \cong \frac{m_0 c^2}{\bar{E}}, \tag{3.6}$$

where the greater the average energy of the pair, the smaller the ejection angle relative to the incident photon. The probability of pair production increases with photon energy, as well as increasing with atomic number by Z^2. This process dominates at energies above approximately 10 MeV in tissue [106, 119]. The cross-sections for pair production do not occur within human tissues until approximately 1 MeV, thus these interactions do not take place during preclinical irradiations that commonly use a maximum energy of 220 kVp.

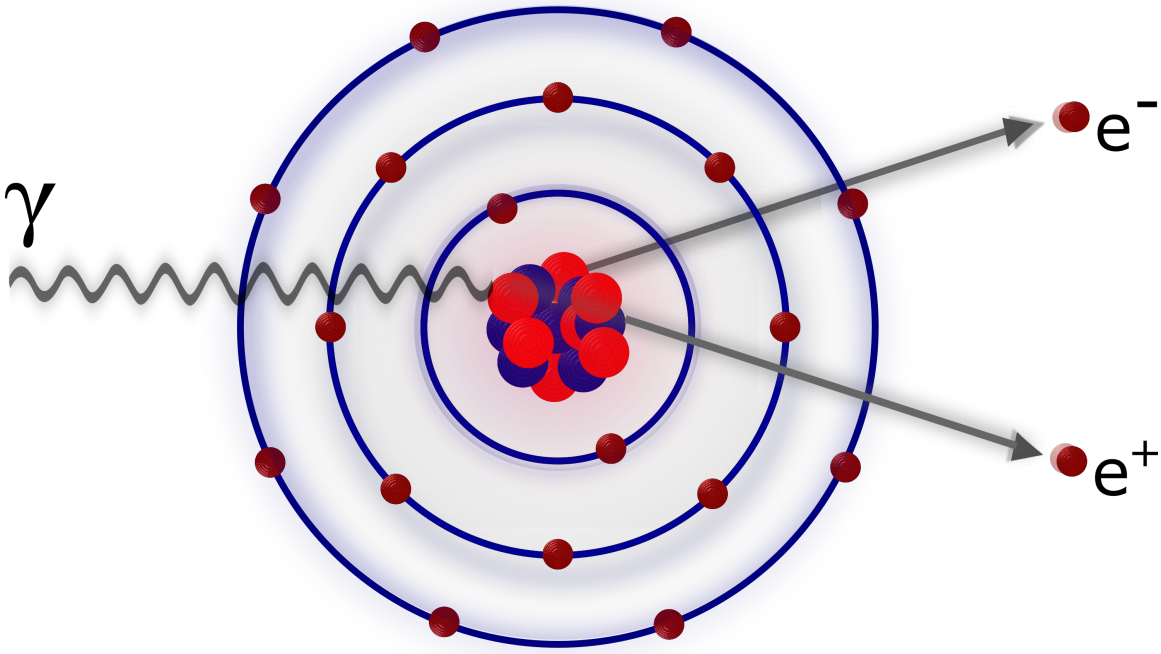

Figure 3.5: Pair production, where an incident photon (γ) is absorbed by the nucleus of an atom, resulting in the production of an electron-positron pair (e^- and e^+).

3.3 Electron Interactions

Electrons liberated from atoms during preclinical irradiations arise from the photoelectric effect, compton scattering, and Auger electron interactions. These free electrons can then go through many elastic and inelastic scattering events with atomic electric fields, depositing energy in tissues all along the way. The charge of an electron makes it likely to interact with almost every atom they encounter during their scattering path [7]. During elastic collisions the electron's kinetic energy is not lost, but redistributed to other particles as the electron's incident direction becomes diverted [119]. For inelastic collisions, the electron's kinetic energy can be converted into collisional energy. When an incident electron interacts with an atomic electric field, energy distributed from the electron to the atom may ionize the atom by the ejection of an atomic valence electron. These electronic interactions are most likely to occur for very low eV interaction energies. For example, an energy of 13.6 eV

is required to eject an electron from a hydrogen atom, as this is its ground state energy. These ejected electrons from ionization events may cause further secondary electrons to undergo additional ionization events (delta rays), depositing additional energy to tissues from these additional electron trajectories. The maximum possible kinetic energy an incident electron can transfer by collisions is half of its initial kinetic energy [106]. Electron energy loss from collisional interactions are more likely with lower Z materials [119]. It is these electron interactions that produce the absorbed dose to tissues during irradiation procedures.

Aside from the collisional interactions that an electron may go through, an electron may also go through radiative interactions. Radiative interactions occur when incident electrons undergo inelastic interactions with the nucleus of atom. These nuclear interactions can significantly slow down the acceleration of an electron which causes a large portion of the electron's kinetic energy to become released. This relatively large release of an electron's kinetic energy from a change in acceleration is what produces Bremsstrahlung x-rays [7]. As discussed in Chapter 2, this form of energy release is the process that is exploited for the production of x-rays within an x-ray tube used for both imaging and therapy procedures during irradiations. Electron energy loss from radiative interactions is proportional to Z^2 and increases with increasing energies [119].

3.4 Mass Energy-Absorption Coefficient

Photon penetration through matter is governed statistically by the probability per unit distance traveled that a photon interacts by one of the atomic interactions discussed. The probability is defined by the linear attenuation coefficient, μ, which has units of inverse length (cm^{-1}), and is dependent on both the photon energy and the medium it transverses [7, 119]. We can describe the number of particles that are attenuated exponentially in a uniform target, described by

$$N(x) = N_0 e^{-\mu x}, \tag{3.7}$$

where $N(x)$ is the number of photons that reach a depth x without interacting in the medium, with N_0 representing the initial photons incident on the medium. **Figure**

3.6 illustrates the measurement of the linear attenuation coefficient under narrow-beam geometry, as the initial beam N_0 is incident on a material of known thickness x (usually Cu and Al for preclinical therapy and imaging beams, respectively). This is also the experimental setup to measure HVL for a given beam quality, defined as the thickness of a material to attenuate the beam such that the air kerma is reduced to one-half its original unattenuated value. The photons that reach the detector are the ones that bypass these atomic interactions unscathed without being scattered or absorbed. The lower energy photons of the beam spectra tend to be the ones absorbed in the material, with most of the higher photon energies of the beam spectra penetrating the material and ultimately making it to the detector.

The mass attenuation coefficient is given by $\frac{\mu}{\rho}$, which is the linear attenuation coefficient normalized by the density ρ of the material, with units of cm^2g^{-1}. Using **Equation 3.7**, we can derive the mass attenuation coefficient and define it as $\frac{\mu}{\rho} = (x\rho)^{-1} ln(N_0/N(x))$. This mass attenuation coefficient is the probability of interactions between incident photons and the medium every cm^2g^{-1} of the medium transversed [7].

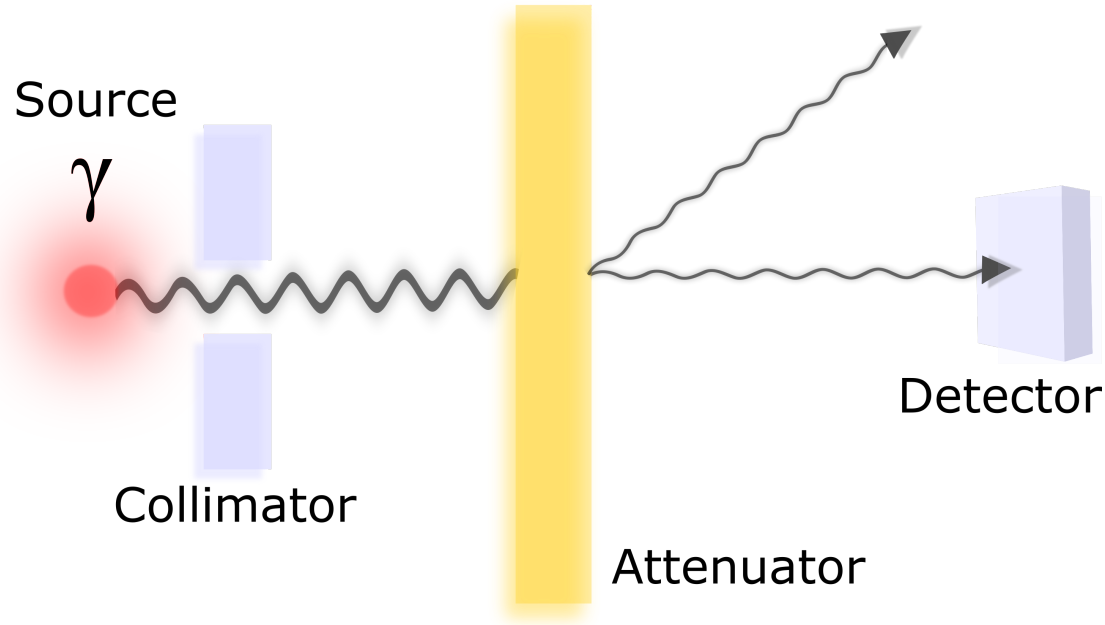

Figure 3.6: Linear attenuation coefficient measurement, where a photon source is collimated with shielding blocks to produce narrow beam geometry, with photons attenuated through a slab of material. Photons that are not either absorbed or scattered reach the detector as the primary beam.

On the other hand, the mass energy-absorption coefficient, $\frac{\mu_{\text{en}}}{\rho}$, describes the average fractional amount of incident photon energy transfered to kinetic energy of secondary charged particles within the medium from the ionization interactions illustrated by the mass attenuation coefficient [93]. This imparted kinetic energy is of particular importance from the ionization interactions attributed to the photoelectric effect, Compton scattering, and pair production, as these interactions determine the amount of energy that is absorbed in matter. This is used as an approximation to the amount of energy imparted to produce chemical and biological effects associated with ionizing radiation exposure. This translates to using the mass energy-absorption coefficient to estimate absorbed dose to matter.

To obtain the mass energy-absorption within the material, we must calculate all of the energy absorbed within the material from the ionization reactions described by the mass attenuation coefficient, however, not all of the ionization events that take place in the material are absorbed in the material. This is due to photon and electron ionization interactions that begin within the material, but contain enough energy to travel and impart energy outside of the volume of interest. This difference in ionization energy absorbed in the material compared to the energy absorbed outside of the material must be quantified, with the probability of absorbed energy within the material to be less than the total amount of ionization energy. We must now consider this decrease in absorbed dose for each of the major ionization interactions before we can ultimately obtain $\frac{\mu_{\text{en}}}{\rho}$, and this can be explained by the energy-transfer coefficient [187] (describes the energy transfered outside of the material).

The mass energy-transfer coefficient $\frac{\mu_{\text{tr}}}{\rho}$ can be defined as

$$\frac{\mu_{\text{tr}}}{\rho} = \frac{\tau_{\text{tr}}}{\rho} + \frac{\sigma_{\text{tr}}}{\rho} + \frac{\kappa_{\text{tr}}}{\rho}, \tag{3.8}$$

where ρ is the material density, and τ_{tr}, σ_{tr}, and κ_{tr} are the energy-transfer coefficients for the photoelectric effect, Compton scattering, and pair production, respectively.

For the photoelectric effect, the fraction of photons incident to electrons can be expressed as $1 - \delta/h\nu$, where δ is the average energy emitted as fluorescence radiation, τ/ρ is the mass attenuation coefficient for the photoelectric effect which describes all photoelectric energy absorption in its entirety per g cm^{-2} traveled, and $h\nu$ is the incident photon energy [187]. This gives rise to the mass energy-transfer coefficient,

which describes the fraction of transmitted energy from the photoelectric effect,

$$\frac{\tau_{\text{tr}}}{\rho} = \frac{\tau}{\rho}(1 - \frac{\delta}{h\nu}). \tag{3.9}$$

Likewise, we can find the fraction of transmitted energy from Compton scattering, given by

$$\frac{\sigma_{\text{tr}}}{\rho} = \frac{\sigma}{\rho}\frac{T_{\text{avg}}}{h\nu}, \tag{3.10}$$

where $\frac{T_{\text{avg}}}{h\nu}$ is the average fraction of incident photon energy that is converted into the initial kinetic energy of the Compton electrons. Finally, the fraction of transmitted energy from pair production is given by

$$\frac{\kappa_{\text{tr}}}{\rho} = \frac{\kappa}{\rho}(1 - \frac{2mc^2}{h\nu}), \tag{3.11}$$

where photons produce electron-positron pairs with total initial kinetic energy of $h\nu - 2mc^2$, with $2mc^2$ being the rest energy of the pair [187]. With these equations together, we can then describe the total mass-energy transfer coefficient of the entire system by inserting them into **Equation 3.8**, and is given by

$$\frac{\mu_{\text{tr}}}{\rho} = \frac{\tau}{\rho}(1 - \frac{\delta}{h\nu}) + \frac{\sigma}{\rho}\frac{T_{\text{avg}}}{h\nu} + \frac{\kappa}{\rho}(1 - \frac{2mc^2}{h\nu}). \tag{3.12}$$

Barring subsequent Bremsstrahlung (discussed in section 2.2) generated by interactions created from liberated electrons in the surrounding material, the energy absorbed in the immediate region of the ionization interactions will be the same as the energy transfered at that same region [187]. Thus, the mass energy-absorption coefficient is compromised of the total mass-energy transfer coefficient with the contributions of Bremsstrahlung taken into account. We will define g as the average fraction of the initial kinetic energy transfered to electrons that result in Bremsstrahlung, and the mass energy-absorption coefficient $\frac{\mu_{\text{en}}}{\rho}$ can be finally described as

$$\frac{\mu_{\text{en}}}{\rho} = \frac{\mu_{\text{tr}}}{\rho}(1 - g). \tag{3.13}$$

The g factor is mostly larger for higher energy photons and higher Z materials due to the higher probability of Bremsstrahlung interactions under these conditions. This factor increases its effect for photon energies larger than approximately 10 MeV, and $\frac{\mu_{\text{en}}}{\rho}$ is approximately equivalent to $\frac{\mu_{\text{tr}}}{\rho}$ for lower photon energies. The mass energy-absorption coefficient will show to play an important role in Chapter 8.

3.5 Radiation Quantification

Radiation dosimetry attempts to acquire measurements within a radiation field (**Figure 3.7**) to quantify physical changes that the radiation would produce in matter. Radiation propagates in a way such that the total amount of radiation never changes with distance away from the source, but spreads out over a larger area while the concentration of radiation decreases. Dosimetry is helpful for quantifying biological changes with respect to the amount of radiation absorbed, monitoring radiation exposure in people, and verifying if radiation treatment equipment is properly giving the radiation dose prescribed.

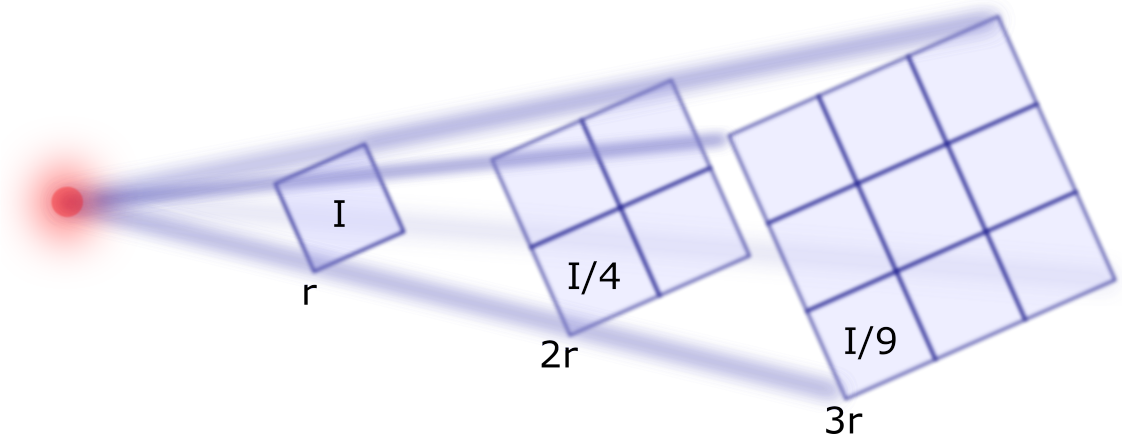

Figure 3.7: Illustration of radiation field propagation, with radiation emanating outward from a point source with decreasing intensity with distance r from the source. The intensity (I) 3r away from the point source is spread over nine times the area.

3.5.1 Exposure

There exists a number of different annotations and definitions that are given to quantify radiation. One quantity for radiation measurement is called exposure (X), and is defined as the amount of ionization produced in-air per kg [7]. The unit of exposure is the roentgen (R), where

$$1\,\mathrm{R} = 2.58\,\mathrm{x}\,10^{-4}\,\mathrm{C/kg}, \tag{3.14}$$

and is measured by taking a small volume of air and obtaining the electric charge created by the ionization produced in that volume divided by the mass of the volume of air. The electric charge is described by the coulomb (C), and is defined as the quantity of electricity conveyed in one second by a current of one ampere (A). This can be measured with an ionization chamber (described in section 4.3.1). Exposure is helpful for quantifying the amount of radiation imparted to a given volume of air.

Exposure is calibrated for different qualities of radiation traceable to national standards from organizations such as NIST, ADCL, or NRCC, to obtained calibration factors for ionization chambers. The readings obtained from ionization chamber measurements can be converted to to exposure by,

$$X = MN_k P_{T,P} P_{ST} P_{\mathrm{ion}}, \tag{3.15}$$

where M is the chamber reading (C) measured under equilibrium conditions and corrected for any polarity effect, N_k is the chamber exposure calibration factor (R/C) for a given beam quality, $P_{T,P}$ is the temperature and pressure correction, P_{ST} is the stem leakage correction, and P_{ion} is the ion recombination correction. The result is the exposure X that would be expected in-air at the location of measurement in the absence of the chamber. Any correction of perturbation produced in the beam by the ionization chamber is inherent in the chamber-specific calibration factor N_k [119].

Ionization chambers free in-air are the standard for measuring exposure for the relatively low energy beams found in preclinical irradiators in which electronic equilibrium can be achieved in-air. This measurement of exposure can be extended to measure air kerma and absorbed dose.

3.5.2 Air Kerma

Air kerma is a radiation quantity used to quantify the amount of radiation delivered in-air. One of the differences between exposure and air kerma is that air kerma is measured in units of gray (Gy), which is defined as energy (J) deposited per unit mass of air, given by

$$1\,\mathrm{Gy} = \frac{1\,\mathrm{J}}{\mathrm{kg}}, \tag{3.16}$$

where joules (J) is the unit of energy, and the mass is in kg. Kerma originated from the acronym KERMA, meaning Kinetic Energy Released per unit MAss [7]. Air kerma has replaced the quantity of exposure due to its practical nature as a standardized SI unit for measuring radiation dose. Air kerma can be used as a relatively easy means towards calibrating machines, obtaining a radiation beam quality, and quickly verifying output in-air.

Air kerma, K_{air}, relates to exposure by

$$K_{\mathrm{air}} = X\left(\frac{\bar{W}}{e}\right)\frac{\mu_{\mathrm{tr}}/\rho}{\mu_{\mathrm{en}}/\rho}, \tag{3.17}$$

where $\bar{W}/e$ is the average energy absorbed per unit charge needed to create an ion pair in-air, having a value of 33.97 J/C, with the mass-energy transfer coefficient μ_{tr}/ρ and mass energy-absorption coefficient μ_{en}/ρ defined in section 3.4. Using the aforementioned national standards calibration factor N_{k} for x-ray beams incident on an ionization chambers, equation 3.17 can be simplified to

$$K_{\mathrm{air}} = MN_k, \tag{3.18}$$

with M being the chamber reading in coulombs corrected for temperature, pressure, recombination, polarity effect, and electrometer accuracy [136]. The reference point for this air kerma measurement must be measured with a field size large enough to cover the entire sensitive volume of the ionization chamber with a uniform exposure across the sensitive volume.

Air kerma measures the amount of energy released in Gy to a volume of air. This can be expanded to measuring the energy deposited and absorbed to tissues, also measured in the unit of Gy. Absorbed dose is the most useful description of radiation quantification between exposure, air kerma, and absorbed dose, as it can be used to quantify the amount of radiation deposited in tissue.

3.5.3 Absorbed Dose

Air kerma provides practical standards of radiation measurement, but an additional measurement technique is needed to allow for the measurement of radiation deposition in materials, such as tissue. The main physical quantity used in radiation dosimetry is absorbed dose [7]. Absorbed dose is the energy absorbed per unit mass from any kind of ionizing radiation in any medium. Much like air kerma, the unit of absorbed dose is also Gy but includes an older unit, the rad (defined by the antiquated erg),

$$1\,\mathrm{Gy} \equiv \frac{1\,\mathrm{J}}{\mathrm{kg}} = 10^4 \frac{\mathrm{erg}}{\mathrm{g}} = 100\,\mathrm{rad}, \tag{3.19}$$

with absorbed dose (just commonly referred to as dose), measured in an irradiated object [7]. Photons can produce secondary electrons in-air, and using the average energy needed to make an ion pair, 33.97 J/C, we can calculate

$$1\,\mathrm{R} = \frac{2.58\,\mathrm{x}\,10^{-4}\,\mathrm{C}}{\mathrm{kg}} \times \frac{33.97\,\mathrm{J}}{\mathrm{C}} = 8.76\,\mathrm{x}\,10^{-3}\,\mathrm{Gy}. \tag{3.20}$$

This illustrates that 1 R can be converted to dose in-air of 8.76x10^{-3} Gy. X-ray beams attenuate differently within the body depending on the tissue type and incident radiation energy, resulting in different tissues absorbing different amounts of dose. Absorbed dose is one of the most important units of radiation measurement, as it is used to quantify the amount of radiation absorbed in human tissues for both radiation therapy and imaging procedures, with imaging dose being a hotly debated subject among the community.

In-Air Method

For x-ray energies of 300 kV and lower, the AAPM TG-61 protocol is the gold standard for measuring dose in preclinical irradiators. Within the AAPM TG-61 protocol, dose is measured by two different methods, the "in-air" method and the "in-phantom" method [136]. The in-air method determines dose deposited to the surface of a water phantom while using an ionization chamber placed in-air without the presence of a water phantom. This method is recommended for x-ray energies between 40 and 300 kV inclusive. In order to determine the dose at a phantom's surface without the presence of a phantom, a backscatter factor, B_w from the AAPM TG-61 protocol must be applied to account for the effect of phantom scatter. This method is given by the equation

$$D_{w,z=0} = MN_kB_wP_{\text{stem,air}}\left[\left(\frac{\bar{\mu}_{en}}{\rho}\right)^{w}_{air}\right]_{air}, \tag{3.21}$$

where M is the free in-air ionization chamber reading (C) corrected for temperature, pressure, ion recombination, polarity effect, and electrometer accuracy, with the center of the sensitive volume of the ionization chamber placed at the measurement point $z = 0$ cm. The air kerma calibration factor N_k is calibrated to a specific beam quality, B_w is the backscatter factor that accounts for scatter that would be created by the presen***c***e of a phantom, $P_{\text{stem,air}}$ is the chamber stem correction factor accounting for the change in photon scatter from the ionization chamber stem (mainly due to change in field size from calibration conditions), and $[(\bar{\mu}_{en}/\rho)^{w}_{air}]_{air}$ is the ratio for water-to-air of the mean mass energy-absorption coefficients averaged over the incident photon spectrum [136].

The N_k factor is determined from a national standards calibration report obtained from an organization such as the NIST, ADCL, or NRCC. The B_w values are obtained from tables of the AAPM TG-61 and are dependent on SSD, field size, and HVL. The in-air mass energy absorption coefficient $[(\bar{\mu}_{en}/\rho)^{w}_{air}]_{air}$ is also obtained from tables in the AAPM TG-61 and are dependent on HVL. All other correction factors in equation 3.21 are calculated with the equations found in the appendix of the AAPM TG-61.

In-Phantom Method

The in-phantom method determines dose deposited at a depth within water. Unlike the in-air method, the in-phantom method measures dose with the ionization chamber placed inside a water phantom. This method is recommended for x-ray energies between 100 and 300 kV. A 2 cm reference depth for calibration measurements are recommended, as shallower depths may not contain enough buildup material in the upstream direction to cover the entire sensitive volume of the ionization chamber. If the depth is much larger than 2 cm, the signal from the ionization chamber may be too small to produce a low measurement uncertainty. The absorbed dose to water at a reference depth of 2 cm ($z = 2$ cm) in water defined for a 10 x 10 cm^2 field size and 100 cm SSD is determined by

$$D_{w,z=2} = MN_k P_{Q,\text{cham}} P_{\text{sheath}} \left[\left(\frac{\bar{\mu}_{en}}{\rho} \right)^{w}_{air} \right]_{water}, \tag{3.22}$$

where M is the ionization chamber reading (C) corrected for temperature, pressure, ion recombination, polarity effect, and electrometer accuracy, N_k is the air kerma calibration factor for a given beam quality, $P_{Q,\text{cham}}$ is the overall ionization chamber correction factor that accounts for the change in response due to the displacement of water by the ionization chamber, the presence of the ionization chamber stem, the change in energy, and the angular distribution of the photon beam in the phantom compared to that used in the in-air calibration geometry. The correction factor P_{sheath} corrects the photon absorption and scattering in the waterproof sleeve (if present), and $[(\bar{\mu}_{en}/\rho)^{w}_{air}]_{water}$ is the ratio for water-to-air of the mean mass energy-absorption coefficients, averaged over the photon spectrum at the reference point in water in the absence of the chamber [136].

The correction factor $P_{Q,\text{cham}}$ is obtained from tables in the AAPM TG-61 and varies as a function of ionization chamber type and HVL. The correction factor P_{sheath} varies as a function of sheath thickness and HVL, and $[(\bar{\mu}_{en}/\rho)^{w}_{air}]_{water}$ is the ratio of the average mass energy-absorption coefficients of water-to-air at a depth in water, and changes as a function of HVL, with correction factors found in tables presented in the AAPM TG-61 protocol. All other correction factors in equation 3.22 are calculated with the equations found in the appendix of the AAPM TG-61.

Future Considerations for Dose Measurements

While these measurements are currently the gold standard for dose measurements within preclinical irradiators, a number of shortcomings are encountered with no set standard in measurements established as of yet for kilovoltage radiation beams. The issues that need to be addressed (as stated in the AAPM TG-61 [136]) are- the determination of dose to biological tissues at a depth, dose to water using solid phantoms, dosimetry specifically for kilovoltage cabinet irradiators (potential problems with short SDDs and backscatter from the small confines of cabinet irradiators), biological effects of low energy electron contamination, biological effects of photon and electron backscattering at high Z interfaces, and the relative biological effectiveness (RBE) of kilovoltage x-ray beams. While physicists are mostly concerned with the physics behind radiation interactions, there are biological considerations that must be addressed that impact the measurement of dose to biological tissues as outlined in the AAPM TG-61 report. A discussion of biological considerations for Medical Physics is presented in **Appendix A**.

3.6 Summary

Interactions of radiation with matter were presented in this chapter, specifically for the interactions found in preclinical irradiators. The basic principles of atomic interactions that attribute to absorbed dose calculations were discussed, including methods for measuring absorbed dose for x-ray beam energies of 300 kV and below. The aim of this chapter was to help give the reader a grounding on the foundations behind the radiation interactions found in preclinical irradiators. The next chapter will now discuss all of the materials used that generate, measure, and analyze the radiation encountered throughout the experiments of this dissertation.

Chapter 4

Materials

"I Will Make Lasagna For You"

–BA Johnston

Performing experiments that implement a research hypothesis requires a number of materials. These materials are assembled together to execute the task at hand, and each constituent must be firmly known and understood in order to effectively and efficiently perform a successful experiment. Here, the materials used for the experiments throughout this dissertation are examined, namely, the irradiators and dosimetry equipment. The different types of software used to carry out the research objectives are also described.

4.1 Irradiators

Mice are one of the most used animals in preclinical research, used for decades as models for studying biological effects in living tissues [48]. Preclinical research has improved our understanding of tumor detection, development, and treatment, helping us better understand human cancers. Since the 1970s, small cabinet irradiators have been used to irradiate small animals for translational research [89]. These types of small animal irradiators are ideal as a cost-effective means to carry out translational research on a smaller scale, as compared to using larger multi-million dollar LINACs designed to treat humans. However, these cabinet irradiators lack the ability to reduce the uncertainty in radiation dose delivery, as they are not equipped with on-board imaging technology to accurately plan and deliver radiation therapy treatments. It wasn't until the mid 2000s that image guidance was incorporated into commercial small animal irradiators [99], and it was at this time that image-guided small animal irradiators began to move into the forefront of translational research.

Currently, there are two commercial image-guided small animal irradiators on the market, the Xstrahl Small Animal Radiation Research Platform (SARRP, Xstrahl Inc., Suwanee, GA) and the PXi X-RAD SmART (Precision X-ray Inc., North Branford, CT). These irradiators have the dual ability to both image and treat small animals for accurate treatment planning and delivery. These types of irradiators are commonly self-shielded with lead and are small enough to be used in relatively small spaces without shielding requirements in the room. These image-guided irradiators are designed to deliver targeted radiation with better accuracy than clinical radiotherapy (i.e., 0.2 mm delivery accuracy [140] compared to 0.5 mm from traditional LINACs). These irradiators will now be discussed in detail, with a specific emphasis on the Xstrahl SARRP, as this is the main irradiator used throughout this dissertation. The PXi X-RAD SmART and in-house image-guided small animal irradiators are briefly discussed.

4.1.1 Xstrahl SARRP

The Xstrahl SARRP is one of two commercial image-guided small animal irradiators [201] currently in production, operating within a 20-225 kVp tube voltage range, 0.1-25 mA tube current, and maximum power output of 3 kW. The external shielding

dimensions are 148 x 104 x 205 cm^3 with a total weight of 2,540 kg (the unit is also available unshielded, with a weight of 454 kg). Treatment and imaging distances range from 30 to 38 cm with a 35 cm source-to-isocenter distance (SID). The maximum field size at the isocenter is approximately 15 cm in diameter. Dual focal spots of 3.0 mm (large) and 0.4 mm (small) are used for the therapy and imaging beams, respectively. A 220 kVp tube voltage, 13 mA tube current, and 0.15 mm Cu external filtration are commonly used for therapy beam delivery. The dose rate in 2 cm of water at isocenter is approximately 3.6 Gy/min for the therapy beam, and varies between different Xstrahl SARRP units by approximately ± 0.2 Gy. Possible imaging parameters range from 40-80 kVp tube voltages, 0.1-16 mA tube current, 20 seconds to 4 minute scan times (unpractical to scan mice for longer), up to a 15 fps frame rate, and a nominal 1.0 mm Al external filtration. The imaging dose rate in 2 cm of water at isocenter for a standard imaging protocol of 60 kVp, 0.8 mA, 60 second scan time, and 6 fps is approximately 2.7 cGy/min for the imaging beam. The irradiator operates using an x-ray tube containing a 20° tungsten target and a 0.8 mm beryllium internal filtration.

The Xstrahl SARRP obtains CBCT images using a stationary source and detector with a 360° rotating couch (sections 5.2.3 and 6.2.3). The imaging/treatment couch can move in the x-, y-, and z-directions by ± 50 mm, ± 50 mm, and ± 25 mm, respectively, relative to the isocenter. The couch is made of 1 mm thick carbon fiber, comes in a number of different shapes such as flat and u-shaped (to hold mice in place), with a translational speed of 5 mm per second and rotational speeds ranging from $<$ 3° per second to a maximum speed of 18° per second.

X-Ray Tube

The Xstrahl SARRP uses a Varian NDI-225-22 stationary anode x-ray tube (Varian Medical Systems Inc., Salt Lake City, UT) for x-ray production. It utilizes the aforementioned tungsten target, large and small focal spot sizes, and Beryllium window. The large and small focal spot irradiations operate at 3,000 W and 640 W power, respectively, with a 4 liter/min cooling flow. The cooling medium is water, with a maximum cooling temperature of 35°C. The radiation coverage is 40° and the x-ray system weights approximately 10.5 kg. The high voltage and filament current are supplied through type R24 high voltage cables.

Figure 4.1: Xstrahl SARRP small animal irradiator, with cabinet door open.

Flat Panel Detectors

There are two different types of flat panel detectors that can come equipped in the Xstrahl SARRP, the PaxScan 2520DX flat panel detector (Varex Imaging, Salt Lake City, UT, USA) and the PerkinElmer XRD 0822 xO Digital X-Ray Flat Panel Detector (PerkinElmer Inc, Santa Clara, CA). The two different types of detectors will now be discussed.

The flat panel detector used to acquire CBCT images within the Xstrahl SARRP in this dissertation is the PaxScan 2520DX flat panel detector. The PaxScan 2520DX was designed for panoramic imaging for dental applications, with their imaging technology self-proclaimed as the gold standard for CBCT in medical, dental, and industrial applications. The flat panel detector consists of thin film technology based on amorphous silicon photodiodes. Sensors work like conventional photodiode arrays, with each pixel in the array consisting of a light-sensing photodiode and switching Thin Film Transistor within the electronic circuit. Scintillators are made of CsI that

produce light when excited by x-rays, with the electric circuit producing a linear light-to-charge response. Section 2.3 discusses and illustrates these interactions. The power supply uses 12 Watts of nominal power consumption supporting a 100 to 240 V input range operating with a 47 to 63 Hz frequency range. The detector weighs 2.51 kg with the imaging surface protected by a 2.5 mm thick carbon fiber plate, with the detector covered by radiation shielding to protect electronics.

The flat panel detector's total pixel area is 19.5 x 24.4 cm^2 that includes a total pixel matrix of 1,536 x 1,920 pixels when used with 1 x 1 binning (the default setting). When 2 x 2 binning is used, the total pixel matrix is 768 x 960 pixels. Pixel pitch is 127 μm, contains a limiting resolution of 3.94 lp/mm, and has a 48% MTF at 1 lp/mm as reported by the manufacturer. The maximum frame rates that are supported are 12.5 fps (1 x 1 binning) and 30 fps (2 x 2 binning). The nominal x-ray energy range that the detector can handle is 40 to 160 kVp, while the detector sends image data through a Gigabit Ethernet cable to the computer. A new flood field image must be acquired before changing the tube voltage for acquiring new images. The detector can operate between 10° to 35° C temperatures, humidity between 10% to 90%, and an atmospheric pressure between 525 to 795 mmHg.

Software released with the detector includes VIVA software (Varian Medical Systems, Palo Alto, CA, USA), which is a basic application for image acquisition and image viewing. The software package comes with a "Virtual Command Processor" software interface that performs detector calibration, detector setup, frame rate changes, image acquisition, and image corrections. CBCT images can be converted to .viv, .raw, .jpg, and .bmp file formats in the VIVA software. Images can be obtained in *Fluoroscopy Normal Mode* or *Fluoroscopy Full Resolution Mode* to actively acquire near real-time images with varying image quality, and *Radiography Mode* to allow high resolution CBCT images.

The PerkinElmer XRD 0822 xO Digital X-Ray flat panel detector also consists of thin film technology based on amorphous silicon photodiodes. Scintillators are made of Gd_2O_2:Tb and are used to produce light when excited by x-rays, with the electric circuit producing a linear light-to-charge response. Charge amplifiers are located on chip-on-board modules to amplify the signal within the electronic circuit. The power supply used is the XRD-EPS power supply which utilizes OEM cables and connectors supporting 100 to 240 V at 50 Hz.

The size of the PerkinElmer flat panel detector is 39.5 x 36 x 2.2 cm^3, weighs 3.7 kg, and is covered by radiation shielding to protect electronics. The maximum active area of the detector is 20.48 x 20.48 cm^2 containing 1,024 x 1,024 pixels. The detector pitch is 200 μm with a minimum integration time of 66.6 ms at a 200 μm pixel resolution using a 48 dB dynamic range, and a maximum frame rate of 15 fps. This detector is designed to be used for x-ray energies between 40 keV to 15 MeV. Detector gain settings can be changed to either a 1 or 4 pF capacity. A new flood field image must be acquired before changing the tube voltage for acquiring new images. The amount of binning the detector can produce can also be changed from 0 (1 x 1) to 2 x 2, where a binning of 0 is the default. The detector communicates to computer software by a standard Gigabit Ethernet Network Interface and a RJ45 interface port.

The detector acquires images in *Free Running mode*, or in *Trigger* mode containing *Extra Trigger*, *Software Trigger*, and *Internal Trigger* settings. Free Running mode allows for acquiring frames continuously and is the default mode, including the option for eight different frame times (default uses the fastest frame time). External Trigger synchronizes with an external trigger pulse source, Software Trigger synchronizes by a manually set trigger pulse initiated by the imaging application software, and Internal Trigger combines the Free Running and External Trigger modes.

Electronic Portal Image Device

The Xstrahl SARRP includes a built-in electronic portal imaging device (EPID) camera that provides fluoroscopic x-ray images in real-time that can be used in conjunction with the therapy beam. This may be used to guide the radiation beam to a desired location relative to the obtained 2D EPID image, and can be used to obtain portal images to verify the target position. The portal imager uses a DRZ-Plus phosphor panel containing an MTF of 0.72 at 1 lp/mm (MCI Optonix, Sedona, AZ), compared to approximately a 0.6 MTF at 1 lp/mm for the flat panel detector of the Xstrahl SARRP when using 0.200 mm pixels. This is coupled to a 16-bit, 1,280 x 960 pixels, and 1.3 MP charge-coupled Flea2G device camera (FLIR Systems, Wilsonville, OR). The panel has an area of approximately 5 x 5 cm^2 and is protected by a 0.08 mm thick carbon fiber plate. The source-to-panel distance is 45 cm. The pixel pitch is 69 μm at the detector plane, and images are acquired with the built-in DcamViewer software (A&B Software New London, CT). Both the flat panel detector and the EPID

are oriented 180 degrees opposite from the source, and the EPID must be manually extended into the beams path and retracted when not in use.

MicroCT Imaging Software

The Xstrahl SARRP uses a CBCT imaging software called Murislice created by Digisens (Digisens Company, Le Bourget-du-Lac, France). Imaging is accomplished using a rotating couch and stationary x-ray source and flat panel detector, where hundreds of sequential planar projections are mapped into a three-dimensional space through images reconstructed in the Murislice software by using the Feldkamp analytical algorithm (discussed in Chapter 2). The software imports the reconstructed images in the DICOM format and allows the user to view in the axial, sagittal, and coronal planes, including a 3D reconstructed volume. The user is free to navigate the microCT images by zooming in and out of the images and clicking through each image slice. Basic tools are available to perform distance measurements, angle measurements, profile measurements, point ROIs, and changing the window and level.

There is a password-protected area in the software where the user can change the voxel size, apply artifact removal algorithms for ring artifacts and dead pixels through post-processing, and change the reconstruction filters. The filters can be changed to *Hann*, *Hamming*, *Bartlett*, *Welch*, *Shepplogan*, and *Square* filters as discussed Chapter 2.

Geometrical calibration of the flat panel imager is completed by obtaining a CBCT image of a stick the length of the flat panel containing small metal ball bearings of known sizes and known distances apart. Calibration of the CBCT and flat panel imagers have been previously established in previous works [45, 204, 206]. The built-in software used for CBCT reconstruction in conjunction with a calibration plug-in, using the methods found in the aforementioned calibration works, identifies the ball bearings and corrects for couch tilt, and measures the distances between the ball bearings to validate the geometric accuracy and rotational isocenter. In addition, a flood field correction is made, and must be repeated every time the tube voltage or tube current is changed to correct for changes in signal gain.

Treatment Planning Software

The treatment planning software used by the Xstrahl SARRP is called Muriplan. It uses a FDK algorithm using a Tesla GPU for fast dose calculations that are completed in seconds. Much like clinical treatment planning software, Muriplan allows the user to view 3D reconstructed CBCT images, register and fuse images, and allow for the contouring and segmentation of tumors, organs, and other tissues. Treatment plans can be saved and used for future irradiations, and are important when fractionated treatments are used. Dose volume histograms and isodose lines can be obtained to assist in treatment planning, and the software can plan treatments with a 0.2 mm dose delivery accuracy [140] while delivering coplanar radiation treatments. Treatment plans can be as simple as point-and-shoot static beam treatments or as complex as continuous arc therapy treatments with multiple isocenters. However, one drawback is that the voxel values are not standardized to HU numbers, needing the user to always manually assign non-standard pixel values to tissues for contouring and dose calculations. This is one of the biggest weaknesses in the treatment planning software, as it makes it difficult to directly compare multiple microCT scans, and the treatment planning software does not assign dose to reproducible and standardized pixel values like the tried-and-true clinical treatment planning systems use.

The manual for Muriplan quotes a 5% dose measurement compared to dose calculation accuracy, and also stats that dose calculations overestimate the beam penumbra by 1 mm for a 10 x 10 mm^2 field size, producing relatively inaccurate dose delivery. The relatively high dose calculation inaccuracies are most likely due to the dose calculation method used, where a fluence-based superposition convolution dose calculation algorithm [98] is used and not MC methods (section 4.5 will discus MC methods as the most accurate means of dose calculation). The treatment planning software takes solid water PDD and profile measurements at field sizes and SSDs measured during commissioning, and turns the information into a beam fluence map for dose calculations by superimposing dose deposition kernels and summing dose contributions in surrounding voxels.

Add-On Equipment

An *In-vivo* optical imaging system using bioluminescence (BLI) can be purchased as an add-on item to be used with the Xstrahl SARRP. BLI uses photon emission data from three rotating mirrors to reflect bioluminescence emitted from the imaged object to a stationary charge-coupled device, which are processed by a 3D reconstruction engine that fuses the optically obtained data together with CBCT data [210]. An advantage in using BLI is to more accurately target lesions that may not be identifiable by CBCT alone.

Also, a motorized variable collimator can be purchased from Xstrahl that replaces the single-field collimators that come standard with the Xstrahl SARRP. Unlike the standard single-field collimators, the variable collimator has the ability to change field sizes between 1 x 1 mm^2 up to 40 x 80 mm^2. Improving further on the single-field collimators, the variable collimator comes equipped with a light field to help verify the irradiation field size and location, and is comprised of two symmetric jaws with divergent edges designed to minimize beam penumbra.

4.1.2 PXi X-RAD SmART

The PXi X-RAD SmART is one of the two commercial image-guided small animal irradiators [46], operating within a 10-225 kVp tube voltage, 30 mA maximum tube current, and maximum power output of 3 kW. The external shielding dimensions are 196 x 154 x 103 cm^3 with a total weight of 1,950 kg. Treatment and imaging distances have a 30 cm nominal SID. Dual focal spots of 3.0 mm (large) and 0.4 mm (small) are used for the therapy and imaging beams, respectively. A 220 kVp tube voltage, 13 mA tube current, and 0.30 mm Cu external filtration are commonly used for therapy beam delivery. Maximum dose rate in 2 cm of water at isocenter is approximately 4 Gy/min for the therapy beam.

Imaging protocols have a range from 40-100 kVp tube voltage, 0.1-30 mA tube current, 20 second to 4 minute scan times (unpractical to scan mice for longer), 15 fps maximum frame rate (5 fps standard), and a nominal 2.0 mm Al external filtration. The PXi X-RAD SmART operates using an x-ray tube containing a 20° tungsten target and a 0.8 mm Beryllium internal filtration. Standard treatment collimators

consist of 1 to 25 mm diameter circular and 5 x 5 to 40 x 40 mm^2 square field sizes at isocenter. The PXi X-RAD SmART obtains CBCT images using a stationary couch and 360° rotating source and detector (section 5.2.3). The treatment/imaging couch can be moved ± 10 cm in the x- and y-directions, and by ± 15 cm in the z-direction.

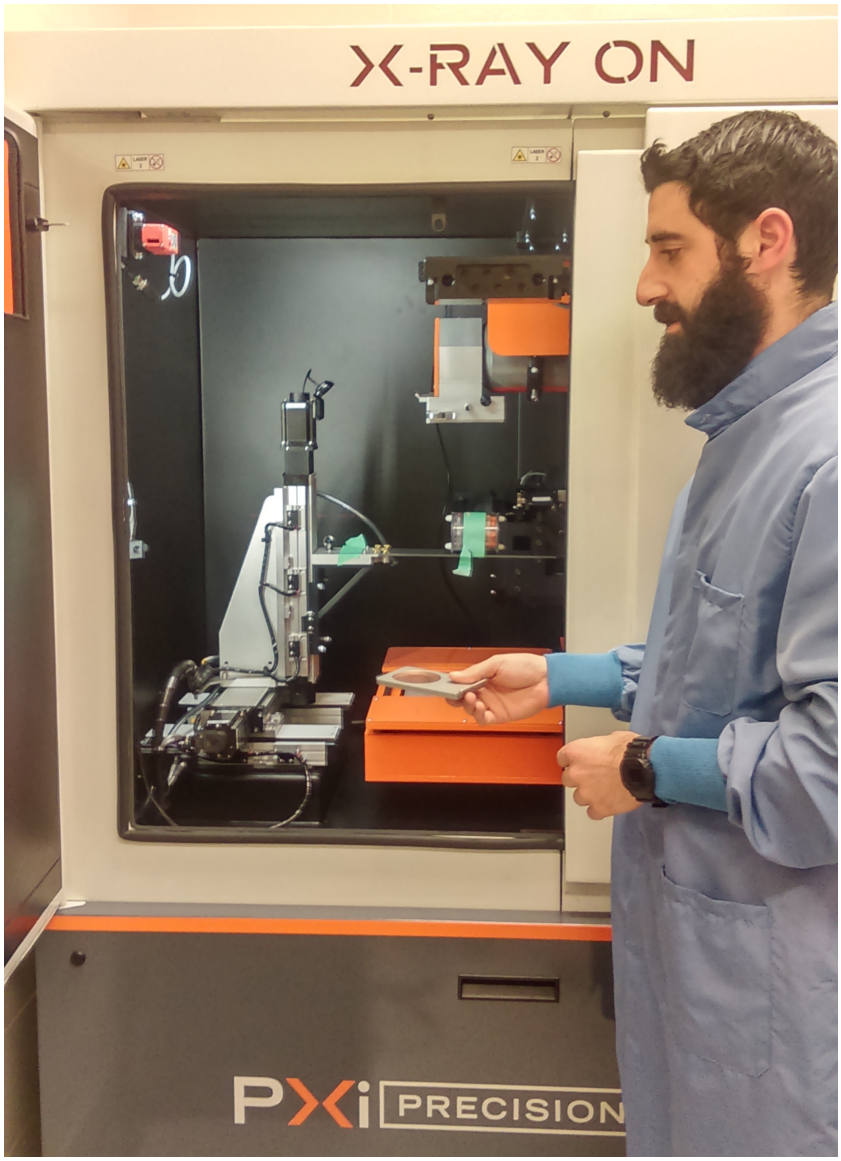

Figure 4.2: PXi X-RAD SmART small animal irradiator, with cabinet door open.

Equipment and Software

The x-ray tube used in the PXi X-RAD SmART is a COMET MXR-225 (COMET Technologies USA Inc., Shelton, CT) operating at a maximum 225 kV tube voltage. It utilizes the aforementioned tungsten target, large and small focal spot sizes, and Beryllium window. The large and small focal spot sizes operate at 3,000 W and 640 W power, respectively, using water at a 35°C maximum temperature as a cooling medium, flowing at a rate of 4 liter/min. Maximum radiation leakage is 10 mSv/h (at 225 kV and 7 mA) and weighs a total of 11 kg. The x-ray tube produces a maximum 40° radiation coverage. The high voltage and filament current are supplied through type R24 high voltage cables.

The flat panel detector used by the PXi X-RAD SmART is the same Perkin Elmer XRD 0820 that can be used in the Xstrahl SARRP discussed in section 4.1.1. Pilot image acquisition and reconstruction software (Princess Margaret Cancer Centre, Toronto, ON) is used with Co-Pilot registration and therapy treatment planning software. Much like the Xstrahl SARRP, the Co-Pilot treatment planning software can segment tissues and delineate structures based on tissue type and densities, and the Pilot imaging software can navigate through and analyze reconstructed CBCT images in a similar fashion and ability as Muriplan and Murislice, respectively. Unlike the Xstrahl SARRP, the dose calculations obtained in the Co-Pilot treatment planning software use MC dose calculations methods.

4.1.3 In-House Irradiators

Non-commercial in-house image-guided small animal irradiators have also been developed, mostly before and during the emergence of the two commercial image-guided small animal irradiators. This includes systems such as the GE eXplore RS 120 (Stanford University, Stanford, CA, USA) and GE eXplore CT/RT 140 (University of Western Ontario, London, ON, Canada) that both use a 0.3 mm imaging focal spot with an amorphous silicon flat panel detector, with pixel sizes of 49 μm and SID of 35.4 cm [169, 213]. Imaging beams for the GE eXplore RS 120 range between 70 to 120 kVp with a 40 mA tube current (10 % pulsed duty cycle), 0.49 μm minimum voxel size, 1 to 4 minute scan times, and have a 4.5 mm Al external filtration. The GE eXplore RS 120 can perform therapy irradiations using 120 kVp tube voltage, maximum

50 mA tube current, and 4.5 mm Al external filtration. The GE eXplore CT/RT 140 uses the same flat panel detector and imaging panels as the aforementioned GE eXplore RS 120. The therapy beam for the GE eXplore CT/RT 140 uses a 140 kVp tube voltage, a maximum tube current of 63 mA (10 % pulsed duty cycle), and 4.5 mm Al + 0.38 mm Cu external filtration. These parameters illustrate the differences that exist between non-commercial and commercial image-guided irradiators.

Other in-house small animal irradiators include a unit from Washington University (Washington University School of Medicine, Saint Louis, MO, USA) [182], where an ^{192}Ir radiation source for small animal irradiations was used. The CT scans were acquired on a traditional CT scanner for image-guided treatment plans [120]. Another in-house irradiator includes a unit from the University of Texas (UT Southwestern Medical Center at Dallas, Dallas, TX, USA) [181], and consists of a stereotactic small animal irradiator platform using a 320 kVp commercial x-ray tube for therapy irradiations, 1-10 mm cylindrical collimation, and a fixed imaging panel for image-guidance.

4.2 Phantoms

There are two different types of phantoms that can be used specifically for image quality quantification and dosimetry, respectively. An imaging phantom is a specially designed QA device that can be scanned to analyze and evaluate the performance of an imaging system. In terms of dosimetry, a phantom can also be a solid piece of tissue-equivalent material that can house different types of dosimeters to determine the amount of ionizing radiation absorbed within the phantom when irradiated. Phantoms can come in almost any shape, size, or material, and can even be "virtual" as discussed below in section 4.5. For imaging phantoms, different imaging characteristics that can be assessed may include the spatial resolution, noise, contrast, HU number consistency, geometric accuracy, and overall performance of an imaging system. Dosimetry phantoms are composed of solid water or tissue-equivalent slabs that can have inserts for ionization chambers, film, OSLDs, or TLDs to measure radiation dose inside the phantom. This is important as these phantoms can be used to calibrate the output of an irradiator, or used to approximate the dose to an animal as the dose absorption characteristics of phantoms are made to be similar to soft tissue.

The types phantoms used throughout this dissertation will now be described.

4.2.1 Shelley Phantom

The Micro-CT MCTP 610 phantom (Shelley Medical Imaging Technologies, London, On), herein referred to as the Shelley phantom, was the imaging QA phantom used in Chapter 5, and displayed in **Figure 4.3**. The Shelley phantom was designed to assess the image quality of microCT scanners, and used specifically in this dissertation's experiments to assess the image quality of the microCT imaging capabilities within the Xstrahl SARRP, PXi X-RAD SmART, GE eXplore 120, and GE eXplore 140 CT/RT irradiators. The Shelley phantom can perform CT number linearity, uniformity and noise, geometric accuracy, spatial resolution, and contrast QA measurements. The cylindrical phantom has a length of 9 cm and a diameter of 7 cm, and is made up of six cylindrical polycarbonate QA plates. Further details on each QA plate can be found in section 5.2.2.

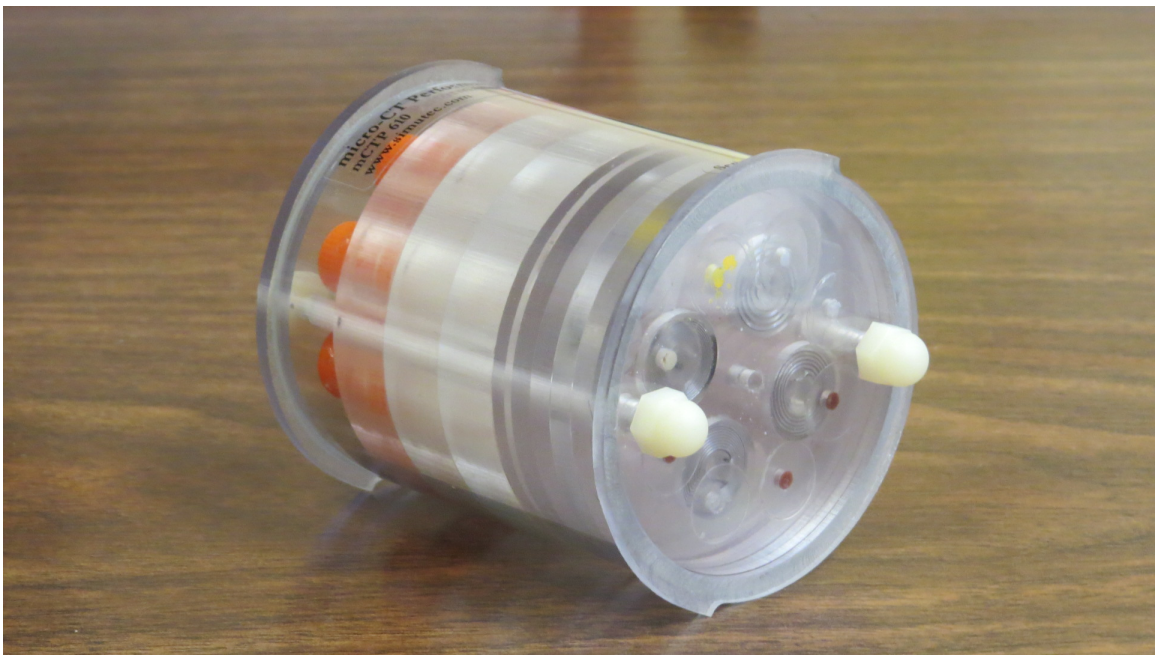

Figure 4.3: Shelley microCT 610 phantom, with a side-view of imaging QA plates displayed.

The Shelley phantom can be utilized to test a microCT system's image quality over time, with multiple image quality tests performed within a single scan. An automated

in-house QA software was created to analyze the Shelley phantom, and is described in section 4.4.1 of this chapter. **Figure 4.4** illustrates the scanning position of the phantom within the Xstrahl SARRP, where the center of the phantom is placed at a 35 cm SID to simulate the imaging geometry during a routine microCT scan. Pictured on the right hand side is the stationary source, on the left hand side is the stationary flat panel imager, and the Shelley phantom is positioned on the 360° rotating couch.

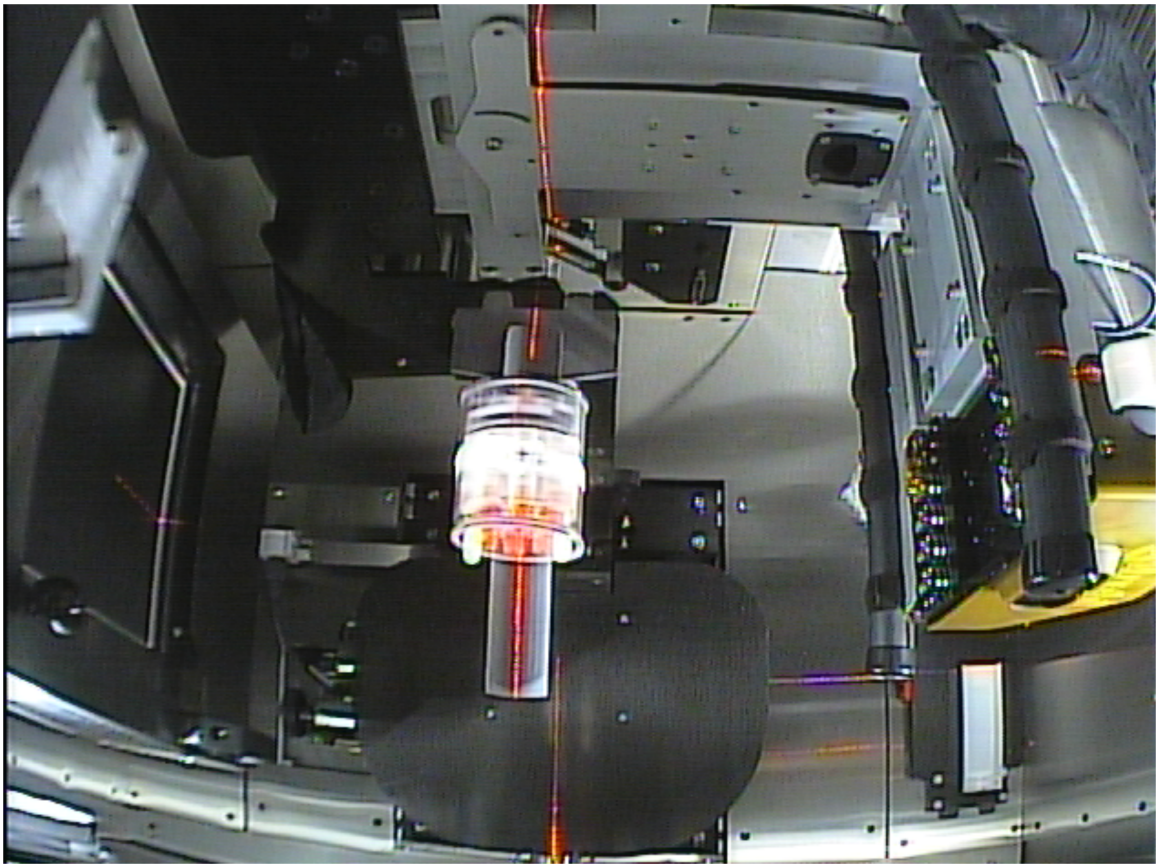

Figure 4.4: Shelley microCT 610 phantom being microCT scanned within the Xstrahl SARRP at a 35 cm SID.

4.2.2 Homogeneous and Heterogeneous Phantoms

Homogeneous solid water phantoms (Gammex Inc., Middleton, WI) were used for dosimetry measurements in this dissertation's experiments, with these tissue-equivalent solid water phantoms being the gold standard in solid water dosimetry. These phantoms consist of epoxy resin-based water-equivalent plastic, specifically designed for

radiation dosimetry applications. These solid water phantoms are used in place of actual water for setup convenience and relative ease of use. The size of solid water phantoms used ranged from 6 x 6 x 3 cm^3 slabs (CIRS, Norfolk, VA) to 30 x 30 x 1 cm^3 slabs (Gammex Model 457). A 30 x 30 x 2 cm^3 slab was specially machined to house an ionization chamber at a 1.0 cm depth within the solid water slab.

A Gammex heterogeneous phantom was also built, composed of tissue-equivalent cortical bone (Gammex Model 450), lung (Gammex Model 455), and water slabs (Gammex Model 457). Heterogeneous slab dimensions were 30 x 30 x 1 cm^2 and varied in thickness from 0.5 to 2 cm. Both solid water and heterogeneous phantoms contain absorption and scattering properties made to mimic the attenuation of different types of tissues (i.e., soft tissues, bone, and lung). These phantoms were designed for photon energies ranging between 10 kV and 100 MeV. Further information can be found in **Appendix B**.

4.3 Dosimeters

A number of different dosimeters were used throughout this dissertation's experiments to measure ionizing radiation, each offering advantages and disadvantages over the other, such as ease of use and spatial resolution capabilities. These different types of dosimeters will now be described in detail.

4.3.1 Ionization Chambers

Ionization chambers are the most commonly used dosimeters for the measurement of absorbed dose due to their accuracy, availability, and ease of use. Ionization chambers operate by applying an electric field across a small cavity of gas within the active volume of the ionization chamber. Incident ionizing radiation creates ions within the gas as the applied electric field moves these ions to electrodes. This process generates an electric current that is measured by an electrometer in real-time, as the total measured electric charge can be converted into absorbed dose by using the AAPM TG-61 protocol for kV dosimetry for x-ray energies less than 300 kV [136]. The electric charge is calibrated to convert an ion pair to be directly proportional to the amount of absorbed radiation dose imparted within an ionization chamber. The average energy

to create an ion pair in air is 33.97 eV. The two types of ionization chambers used were a Farmer-type ionization chamber and a PinPoint ionization chamber.

Farmer-Type Ionization Chamber

Farmer-type ionization chambers are the most commonly used ionization chamber, where the active volume is housed within a thimble-shaped cavity. They are specially designed for dosimetry of photon and high energy electron beams with an advantage of having a nominal useful photon energy range of 30 kV to 50 MV for photons, with a nominal useful electron energy range from 10 MeV to 45 MeV. The farmer-type ionization chamber used was the PTW 31013 (PTW, Freiburg, Germany) displayed in **Figure 4.5**. This chamber has a 0.6 cm^3 sensitive volume (0.6 cm diameter, 2.3 cm length) containing aluminum electrodes with wall material made of graphite, containing a nominal 20 nC/Gy response (as specified by the manufacturer). The diameter of the sensitive volume is 6 mm, and is suitable to measure field sizes down to 5 x 5 cm^2. The PTW ionization chamber was calibrated to national standards for dose measurements from the NRCC standards lab.

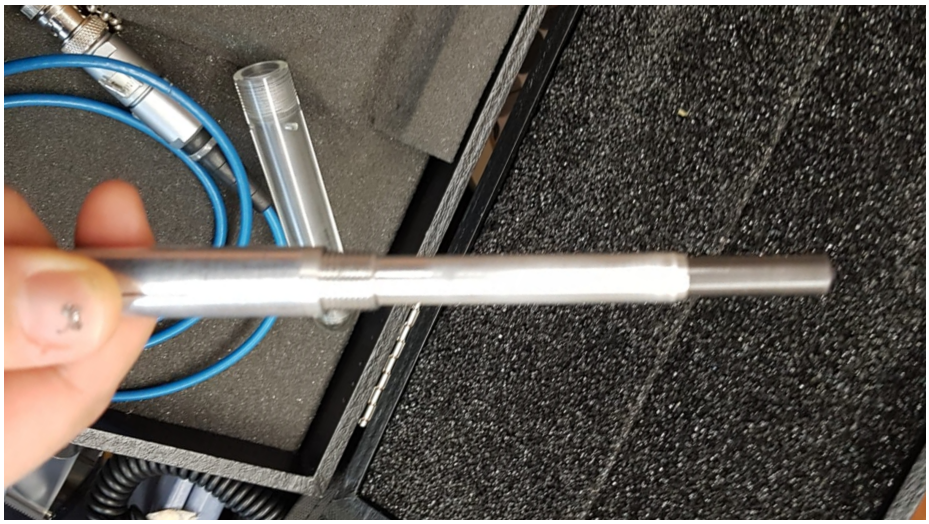

Figure 4.5: Picture of the PTW 31013 farmer-type ionization chamber.
Photo credit: Chelsea Dunning.

PinPoint Ionization Chamber

PinPoint Ionization chambers are much like farmer-type ionization chambers but with a much smaller sensitive volume **Figure 4.7**. A smaller sensitive volume correlates to the ability to measure smaller field sizes due to less volume averaging effects within the high-dose gradient regions of small radiation fields, including the ability for lateral scattering equilibrium. The PinPoint chamber used was the PTW 31014 ionization chamber which has a small 0.015 cm^3 sensitive volume (0.2 cm diameter and 0.5 cm length) and nominal 400 pC/Gy response. This allows for higher spatial resolution measurements suitable for field sizes down to approximately 2 x 2 cm.[2] The PTW PinPoint ionization chamber is suited for 60 kV to 50 MV photons for absorbed dose to solid water and air kerma measurements (as specified by the manufacturer).

Figure 4.6: Picture of the PTW 31014 PinPoint ionization chamber next to buildup cap.
Photo credit: Nolan Esplen.

4.3.2 Scintillator Dosimeter

A scintillator is a special type of material that produces luminescence when excited by ionizing radiation, with organic, plastic, and inorganic scintillators being the most common types. When x-rays are incident on organic or plastic scintillating materials, the x-ray's energy becomes absorbed and cause a transition in energy levels of

the electrons within the atoms of the scintillating material. When these electrons transition from a ground state into a higher excited state, they release energy in the form of visible light [18]. The intensity of the light is dependent on the type of scintillating material. Some common organic scintillators are anthracene ($C_{14}H_8$, organic solid), and BC531 (organic liquid). Common types of plastic scintillators are polyvinyltoluene and polystyrene (used in the experiments of Chapter 8).

For inorganic scintillators, luminescence is triggered based on the structure of the crystal lattice within the scintillating material. When x-rays are incident on inorganic scintillators, electrons become elevated from the valence band to the conduction band within the crystal lattice resulting in an electron hole, emitting photons of light in the process [127]. This process can be inefficient, so inorganic scintillators are commonly doped with impurities to improve photon efficiency by creating electronic levels in the bandgap region. Common inorganic scintillators are CsI (found in flat panel detectors), NaI:Tl, and Gd_2O_2S:Tb.

A novel plastic scintillator dosimeter system was developed by Francois Therriault-Proulx (CRCHU of Quebec, QC) and Luc Beaulieu (University of Laval, QC) [112]. The plastic polystyrene scintillating dosimeter has a 1 mm diameter, 1 mm long sensitive volume with applications suited for small field dosimetry down to approximately a 5 x 5 mm^2 field size. The scintillator is protected by a 0.6 mm thick polyethylene jacket, with the scintillator coupled to a 1 mm diameter, 15 m long Polymethyl methacrylate (PMMA) optical fiber that is then connected to a photosensor module by a silver input connector. The scintillator and protective cord are displayed in **Figure 4.7**.

Light from the scintillator is emitted into an optical PMMA fiber made light-tight by the the polyethylene jacket, and sent into the photosensor module. The photosensor module (**Figure 4.8**) contains a high voltage circuit, H10721 photomultiplier tube (PMT, Hamamatsu Photonics, Hamamatsu, Japan), and connects to a PTW UNIDOS E electrometer (PTW, Freiburg, Germany).

The potentiometer on the PMT sets the sensitivity of the PMT output; 0.7 V was chosen based on the precision and reliability of the voltage setting reported by the manufacturer. The PMT receives the light coming through the optical fiber and converts the light into electrons through the photoelectric effect when photons are absorbed in a photocathode within the PMT. The electrons are then focused into

Figure 4.7: Picture of the 15 m long polyethylene cord that protects the polystyrene scintillator and optical fiber, displaying the silver input connector (connects to photosensor module) with the scintillator housed within a 2 mm depth located at the opposite end of the cord.

dynodes that effectively multiply the electrons through secondary emissions. The enlarged signal is then sent into an electrometer to display the measured charge.

The scintillator dosimeter system ultimately converts x-rays into visible light and then reads the signal out as a charge with μC sensitivity. The signal is then calibrated to output charge to dose through methods described in Chapter 8. Polystyrene was chosen as the most suitable material for the scintillator detector based on its high light output, near instantaneous response time, radiation resistance, and durability.

Electrometers are instruments that measure electric charge in real-time. Modern electrometers use a highly sensitive digital voltmeter to measure the obtained electric potential difference using an input impedance high enough so that the dark current

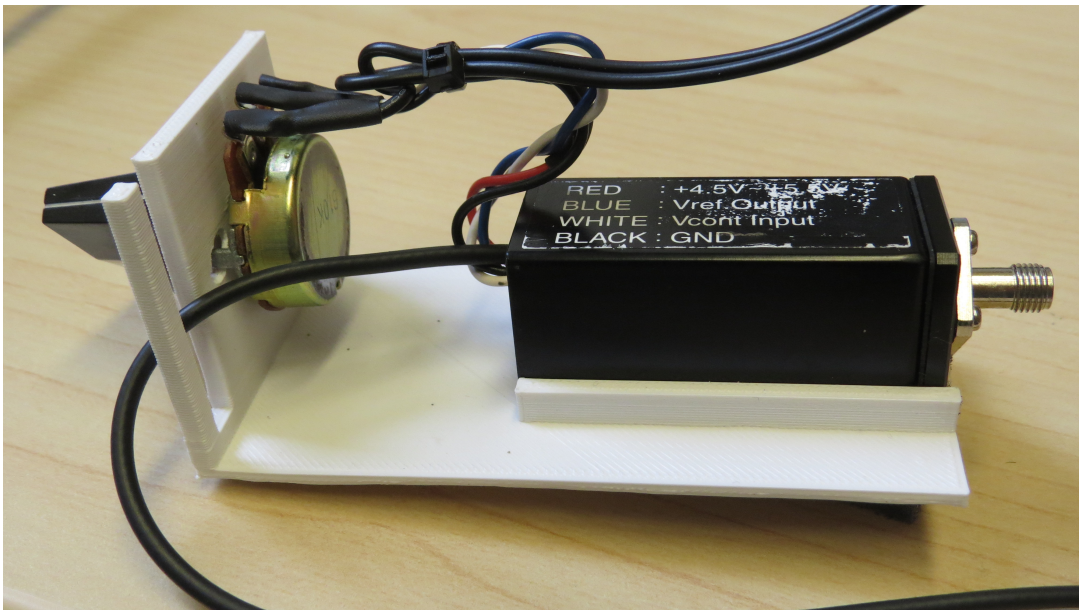

(a)

(b)

Figure 4.8: Picture of the photosensor module displaying a a) side view showing the power supply and PMT tube and b) front view displaying the potentiometer dialed to 0.7 V.

of the electrometer does not interfere with the reading. The electrometer used was the PTW UNIDOS E, displayed in **Figure 4.9**. The PTW farmer-type ionization chamber, the PinPoint ionization chamber, and the scintillator dosimeter system all

used the PTW UNIDOS E electrometer to read the measured charge.

4.3.3 Radiochromic Film

Radiochromic film is a type of self-developing film that can be used as a dosimeter for measuring absorbed radiation dose. Radiochromic film undergoes polymerization when exposed to ionizing radiation with a near real-time dose response. The greatest advantage in using radiochromic film is its very high spatial resolution, as measurement points can be resolved down to a 25 μm resolution. An example of exposed radiochromic film is displayed in **Figure 4.10**. Irradiated spots on the film become darker when exposed to ionizing radiation. The darker the shade, the higher amount of radiation dose absorbed. Radiochromic film must be handled carefully to avoid physical strains, creasing, and finger and pen marks that will influence the absorbed dose readings. The film is read on a flatbed scanner to obtain the quantitative dose response.

Figure 4.9: Picture of the PTW UNIDOS E electrometer.
Photo credit: *Dr. Samantha Van Nest.*

Before using the film as a dosimeter, it must be calibrated for a specific energy by irradiating the film using known doses of ionizing radiation. The film is then verified by irradiating the calibrated film to a known dose of radiation and seeing the reading being approximately the same as what was delivered. The dose response of the irradiated film is then mapped to the known delivered doses (i.e., 0 to 8 Gy)

to create the calibration curve. A new calibration curve must be made for different tube voltages and for different batches of film, as differences in beam quality and film batches produce different radiation responses. After ionizing radiation exposure, the film is scanned (usually 24 hours after irradiation) with a high-quality professional scanner. The RGB channels obtained from the film scan are used to determine the response of the film. Radiochromic film is approximately water equivalent, so it is well suited for absorbed dose measurements when placed against solid water slabs.

Figure 4.10: Picture of EBT3 film exposed to a 10 x 10 mm^2 radiation field with irradiation notes written on film with Sharpie pen.

The radiochromic film used was GAFCHROMIC EBT3 film (Ashland Advanced Materials, Bridgewater, NJ). EBT3 film is an improvement over the previous EBT and EBT2 films. EBT3 film contains symmetric sides that eliminate side orientation dependencies and reduces Newtons ring artifacts using a new matte film surface that EBT and EBT2 film do not have [58]. The EBT3 film has a nominal 28 μm thick active layer sandwiched between 125 μm thick matte layers (polyester-substrate), with an optimal dose range between 0.20 and 10 Gy as reported by the manufacturer. EBT3 film was used to commission the PDDs and profiles of our SARRP irradiator (**Appendix B**) and was used for the high-spatial resolution small field measurements for the scintillator profile validation in Chapter 8. The scanner used was the Epson 10000XL (Epson, Long Beach, CA), with scans saved as TIFF files with 600 dpi resolution.

4.4 Analysis Software

All data analyzed was completed using three different analysis software: SAPA, Matlab, and Fiji. All three have different strengths for certain analysis tasks, and will be described here.

4.4.1 SAPA

The Small Animal Phantom Analyzer (SAPA) is an in-house image analysis software created in Matlab (The Mathworks, Nattick, MA) and designed to extract image quality information obtained from microCT scans acquires with the Shelley phantom [111]. SAPA is a fully automated software that only requires the user to upload a microCT dataset, with all QA tests automatically performed independent of the user in seconds. QA data can be exported into an Excel (Microsoft, Redmond, WA) file, and used to compare multiple datasets to assess image quality changes over time. This software was used for comparing microCT image quality of the Xstrahl SARRP, PXi X-RAD SmART, GE eXplore 120, and GE eXplore CT/RT 140 across eleven different institutions, with further information found in Chapter 5.

4.4.2 Matlab

Matlab was the software of choice used for programing and data analysis throughout the vast majority of the experiments performed. The name Matlab stands for *matrix laboratory* as it is fundamentally a structured matrix-based numerical computing environment and programming language. Matlab allows for numerical computing, matrix manipulations, figure plotting, algorithm implementation, GUI creation, and a plethora of other abilities. Matlab is built as a scripting language where the user defines variables that can store constants, computations involving other variables, and functions. Object oriented programming is also supported in Matlab. "Quick and dirty" computations can be written quickly and immediately discarded, or scripts can be used to save code to produce complex programming, computing, data analysis, and can be used to solve virtually any mathematical expression. Together with its efficiency, powerful computation ability, and relative ease of use compared to other programming languages, Matlab has become a tool of choice for many researchers.

4.4.3 Fiji

Fiji (Fiji is Just ImageJ, National Institute of Health, Bethesda, Maryland, USA) [176] is a distribution of the popular open-source image analysis software ImageJ [177]. Building off of ImageJ's 30 year history, the most popular biologically focused plug-ins and analysis functions of ImageJ now come standard in Fiji, making it one of the most powerful and free image analysis software available. It has the ability to edit, analyze, process, and save 8-bit, 16-bit, and 32-bit images, including TIFF, GIF, JPEG, BMP, and DICOM formatted images. It can calculate and analyze pixel values from different shaped ROIs, measure distances and angles, create profiles and density histograms, and change the window and level. It can also support functions such as contrast manipulations, sharpening, smoothing, edge detection, and filter uploaded images. It can transform an image by scaling, rotating, flipping, and zooming, and it can switch between axial, coronal, and sagittal planes in 3D DICOM datasets. The software can also calibrate an image to represent physical mm distances. Fiji has recently been upgraded to incorporate cutting-edge image analysis techniques with a focus on multi-dimensional scientific imaging [172].

4.5 Monte Carlo Methods

The amount of ionizing radiation that living tissues absorb at every point in the body cannot be directly measured. Some dosimeters, such as TLDs (thermoluminescent dosimeters) or OSLDs (optically stimulated luminescent dosimeters), can be surgically implanted in tissue, however, not only is this impractical, it only reports a point-dose measurement at a single location. Furthermore, these measurements measure absorbed radiation dose deposited in the dosimeter and not the dose deposited in the actual tissue. In order to obtain the absorbed dose throughout the entire body of an object at every single location, a simulation of radiation transport and particle interactions within tissue can be made through Monte Carlo (MC) dose calculation methods. Throughout the field of medical physics, MC dose calculations are the gold standard and primary method for calculating radiation dose absorbed in living tissues. This is true for both clinical and preclinical dose calculations. Dose calculations through MC methods stochastically model particle interactions to ultimately simulate the transport and deposition of energy in matter. This is in part accomplished

by accurately simulating the path and interactions that primary particles and their secondary particles take through matter.

First, MC dose calculations are accomplished through modeling the radiation source, irradiator head, and the object to be irradiated (materials and geometry defined by the user), and secondly, the transport of photon and electron particle interactions are computed (MC algorithm-dependent). This ultimately simulates absorbed dose to tissue at any desired location in matter. The user first uses MC code to generate a computer model of the radiation source and irradiator head. For x-ray irradiators, this includes first modeling the x-ray tube that generates x-rays as discussed in Chapter 2. Primary collimation within the irradiator head and any secondary collimation outside of the irradiator head are then modeled in the MC code by assigning material types and densities to the irradiator components, and assuring that the approximate physical geometry of all pertinent components of the irradiator are used. The user also sets the physics involved in the simulation, such as the different interaction types (i.e., Rayleigh scattering, photoelectric effect, Compton scattering, etc.), the particle type and number of particles to simulate, cut off energies, Bremsstrahlung splitting, random number seeds, and many other parameters.

The rest of the process is out of the hands of the user and is handled by the MC radiation transport algorithm, with such algorithms being the major difference between different MC codes. These algorithms are governed by the attenuation coefficients and photon interactions discussed in Chapter 3, and are also governed by interaction probabilities that model the statistical n***a***ture of radiation transport through matter. Hence, the term *Monte Carlo* in the context of radiation transport was named based on the stochastic nature of photon and electron interactions with atoms.

4.5.1 Modeling

One of the most crucial parts of MC simulations is producing an accurate user-generated model of the irradiator source, irradiator head, and the object to be irradiated. This includes any component that encounters and interacts with the path of the electron beam before and during x-ray generation at the target, as well as any component in the path of the generated x-ray beam. Since most, if not all, commercial irradiators are produced from proprietary information, it is up to the

researcher to approximate the components, materials, and geometry of the irradiator head when creating a virtual model. This can result in a number of assumptions, such as focal spot size and internal filtration thickness, where the nominal values are generally used. The user must take measurements, such as the distance from the focal spot to bottom of the irradiator head, dimensions of internal collimation between the beryllium window and external filter, and determine the material composition of all components. These components can be broken down into different structures, such as the x-ray tube, target, internal filtration, primary collimation, external filtration, and secondary collimation.

After the x-rays leave the irradiator head, the photons are immediately scored into a *phase space* file within a plane perpendicular to the beam. A phase space is a file that contains all particle information at a given location, such as particle type, energy, location, weight, and direction. The information contained in the phase space file can also describe the photon fluence, mean beam energy, and the energy spectra of the beam. Phase spaces are very useful since the components in the irradiator head do not change (unless a modification is made), as repeated simulations can be avoided by storing the already generated particles in a phase space file. Generating a phase space for the Xstrahl SARRP generally takes between a couple of days to a week to run depending on the number of particles used. Once a phase space has been obtained, future dose calculations of the modeled irradiator are produced using the saved phase space file, where absorbed dose calculations of a small animal can be obtained within minutes, with speeds depending on the number of voxels in the geometry, how many CPU's are used and if used in parallel, or if a GPU is used.

4.5.2 Radiation Transport

Simulating radiation transport of particles interactions of energies at and below 220 kVp consists of Rayleigh scattering, photoelectric interactions, and Compton scattering, as discussed in Chapter 3. These processes, aside from Rayleigh scattering, transfer energy to atomic electrons in matter, where each type of interaction is dependent on the photon energy and the matter they transverse. Photon transport algorithms must determine the path length between a given interaction to the next interaction using a probability density function. The interaction is then simulated and the photon is either fully absorbed through photoelectric interactions or it changes

direction through Rayleigh or Compton scattering. These interactions can produce ejected electrons from ionization events, and ejected electrons can further interact in surrounding matter by transferring and depositing their energy through the electrostatic force and possibly cause secondary electrons. These electrons can scatter elastically with atomic nuclei a large number of times before depositing their energy inelastically through collisions with atomic electrons. The large number of interactions that electrons go through can be computationally intensive, so many MC simulations "condense" multiple electron scattering interactions into fewer interactions within a given path length by using condensed histories to reduce computation time.

MC simulations are generated through pseudo random numbers, with the interactions of the generated particles dependent on the probability density function for a given interaction. This can be used to sample the distance a photon will travel to the next interaction, and is dependent on the linear attenuation coefficient of the medium that the photon is transversing for a given photon energy. After generating a random number r, the distance x a photon will travel between interactions is given by $x = -\frac{1}{\mu}\ln(1-r)$. The interaction type is then chosen based on the cross-sections of the different types of possible interactions, and is then simulated using the energy and direction of the particle combined with the chosen cross-section. It is through these interactions that energy, or radiation dose, is deposited in tissue, where the MC code simulates these interactions to ultimately report the radiation dose deposited in tissue. The track that a primary photon takes and the corresponding secondary particles it may produce is known as a history (illustrated in **Figure 4.11**).

The dose calculation engine then calculates the dose deposited in a simulated phantom. Dose can be calculated in objects whose geometry, materials, and mass-density is defined. The size of the voxels used for the phantom will influence the resolution, computation time, and accuracy of a simulation. For example, smaller voxels will produce higher resolution data points but at the cost of increasing the uncertainty of the dose calculated in a given voxel. This is because for a fixed number of histories, less interactions will be happening in a small voxel size compared to a larger voxel size. A greater number of histories would be required to reduce this uncertainty. Smaller voxels will also increase computation time as particles that cross more voxel boundaries require additional computations for simulations. On the other hand, increasing voxel size can improve MC simulation efficiency, however, this may cause

partial volume effects in high dose gradient regions. The statistical uncertainty diminishes by $1/\sqrt{N}$, where N is the number of histories used in a simulation. To keep the statistical uncertainty less than 3%, this dissertation uses between 1 x 10^9 and 1 x 10^{10} histories depending on the experiment.

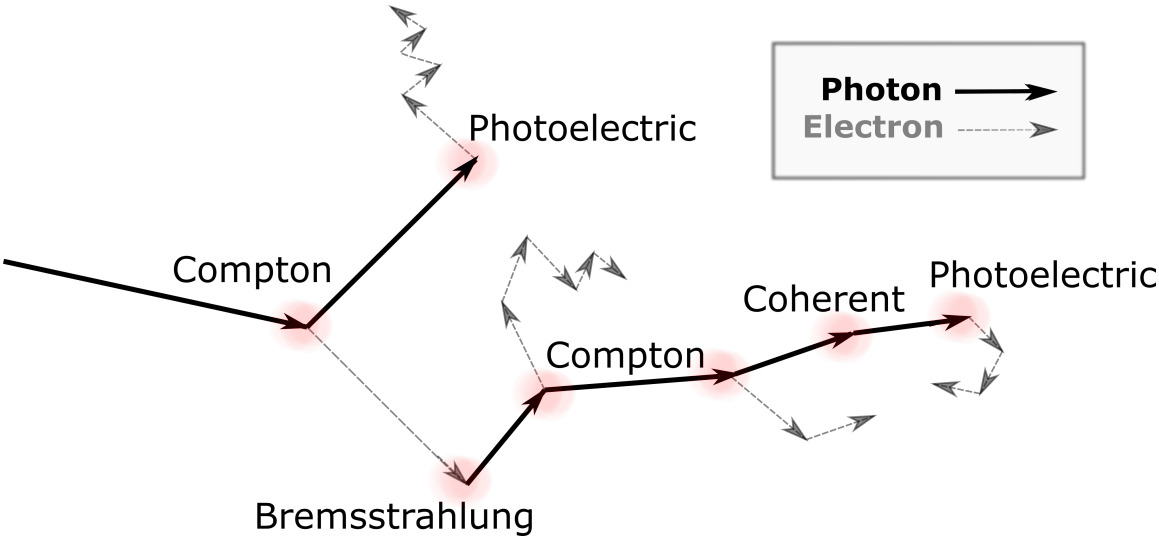

Figure 4.11: An illustration of a simplified Monte Carlo particle history, beginning with a primary photon incident from the left resulting in coherent scattering, Compton scattering, the photoelectric effect, electron scattering, and Bremsstrahlung interactions.

During dose calculations, the incident distribution of photons saved within the phase space file is projected from the phase space, through the air, and into the virtual phantom. Photon transport is simulated and particles deposit their energy into the voxels of the phantom. Dose is commonly reported as Gy per particle, and can be converted to Gy per minute by multiplying the MC output by the desired tube current, irradiation time, and divided by the electric charge of an electron (section 6.2.3). Cutoff energies can also be used to increase the speed and efficiency of locally deposited particle interactions. Since low energy particles are deposited locally because of their short range in matter, a user can set a minimum threshold energy to result in a particle's energy being locally deposited without performing computationally intense scattering interactions. The end result is an MC-derived voxelized 3D dose distribution within a virtual phantom.

There exists a number of commercial MC dose calculation engines available, namely, EGSnrc [117], Geant4 [1], MCNP [33], and Penelope [174]. Due to its widespread use

in research and its extensive validation and acceptance in the field, EGSnrc was used as the MC code of choice for the studies completed in this dissertation. A description of EGSnrc and its MC packages will now be discussed.

4.5.3 EGSnrc

The National Research Council of Canada (NRC, Ottawa, ON) created the Electron-Gamma-Shower (EGSnrc) code [118] which is an improved version of the EGS4 code [117] developed jointly by NRC and the Stanford Liner Accelerator Center (SLAC, Stanford,CA) in the 1980s. EGSnrc is one of the most widely used MC codes to determine the propagation of radiation through matter and it is specifically well suited for medical physics research purposes. The code works for photon and electron energies ranging from 1 keV to 10 GeV and contains a number of packages to further analyze radiation dose and beam characteristics.

BEAMnrc

The BEAMnrc software is an improved version of the original BEAM package developed by NRC in collaboration with Wisconsin-Madison in the 1990s [171]. The main purpose of BEAMnrc is for the MC modeling of the radiation source, irradiator head, and collimation to ultimately generate phase space files for a modeled irradiator. Phase space files can be stored in two formats, the standard EGS format, and the newer International Atomic Energy Agency (IAEA) format. The EGS phase space format scores particles in a plane, while the IAEA format allows the scoring of particles to be in a three-dimensional space allowing a greater flexibility in the geometry of the phase space file.

To model the components of the irradiator head, a user must create a number of component modules (CM). Each CM is a specific part of the irradiator head that gets assigned material, density, and geometry information, as illustrated in the BEAMnrc GUI of **Figure 4.12**. The CMs consist of predefined geometries to build components of an irradiator head. The CMs used in this dissertation to build the SARRP head were the XTUBE, SLABS, PYRAMIDS, and JAWS, which were used to build the x-ray tube, internal beryllium filtration, internal geometry and collimation, external

Al/Cu filtration, and the plastic bottom of the SARRP irradiator head. Briefly, the user can input the tube voltage, number of histories, random number seeds, phase space scoring planes, source type, Bremsstrahlung splitting, and a number of other parameters to generate a phase space.

The EGSnrc MC code is one of the most accurate methods for calculating absorbed dose within tissues, however, calculations can be computationally intensive. Excessively long computations can be simplified without compromising the accuracy of a simulation. This can be mitigated by changing the electron cutoff energy, ECUT, and the photon cutoff energy, PCUT, and is a method used in this dissertation. These parameters terminate an electron's or photon's history when a minimum threshold energy is reached. This saves unnecessary computation time by not modeling computationally intensive interactions before a particle's energy is locally deposited. The ECUT and PCUT energies used in this dissertation were 512 keV (includes the rest mass of the electron) and 10 kV, respectively, as the particles at these energies do not have enough energy to penetrate the external filtrations of the irradiator head. In terms of dosimetry in phantoms, the distance these low energy particles travel in materials, such as in water, is less than the size of the voxels used in this dissertation.

A variance reduction technique was also used to increase the efficiency and lower the computation time of simulations. Computation time can be reduced without compromising the accuracy of a dose calculation by using the Bremsstrahlung splitting parameter. This parameter effectively speeds up x-ray generation in an x-ray tube by increasing the number of Bremsstrahlung interactions that occur. In this dissertation, a Bremsstrahlung splitting number of 2,000 was used, where each single Bremsstrahlung interaction produced 2,000 photons with a weight of 1/2,000 per photon. This can be compared to only producing a single photon for each Bremsstrahlung interaction.

The MC model of the Xstrahl SARRP was created in Chapter 6, with additional MC model validation found in **Appendix B** of this dissertation. After creating the Xstrahl SARRP phase space files, dose calculations were then performed in DOSXYZnrc.

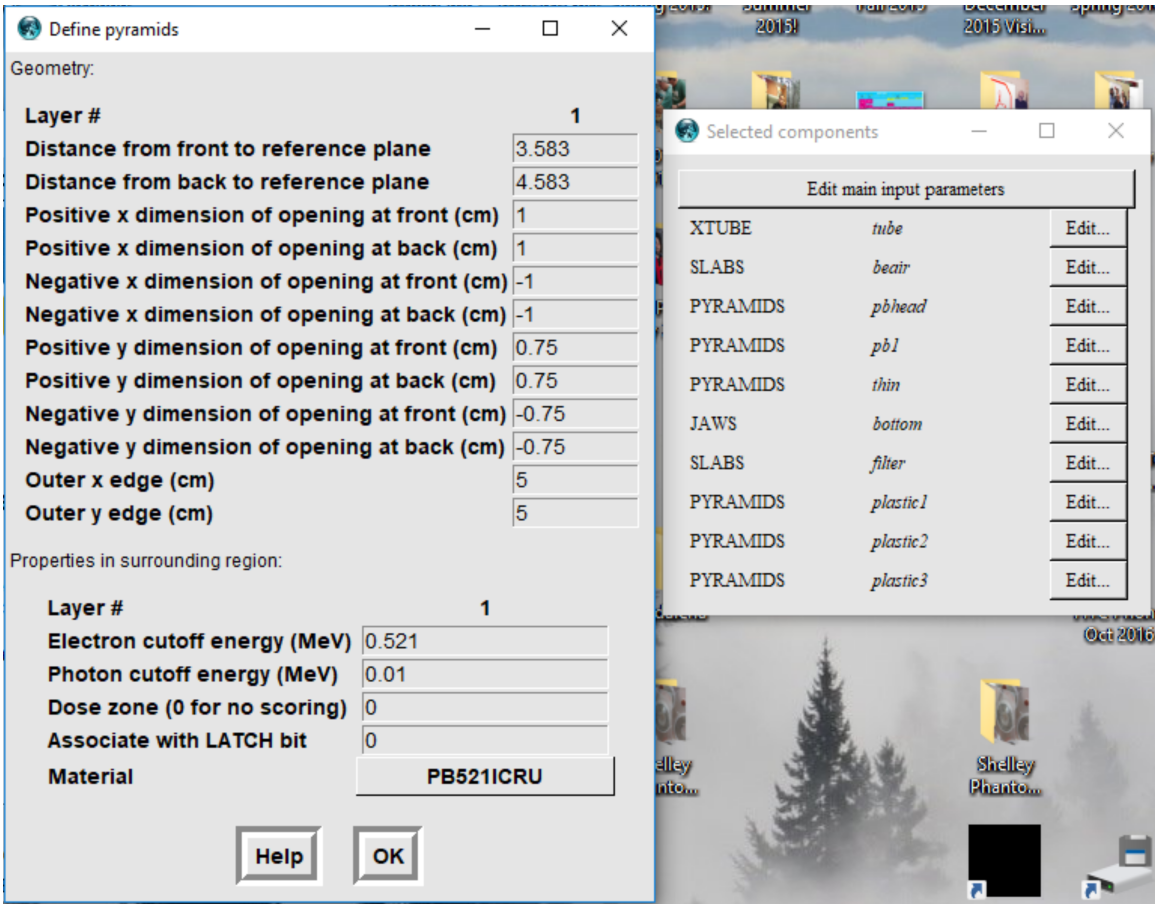

Figure 4.12: BEAMnrc GUI illustrating the building of a CM for modeling the irradiator head of the SARRP.

DOSXYZnrc

The stand-alone dose scoring software DOSXYZnrc was used to calculate absorbed radiation dose in a 3D voxelized geometry [194] using phase space files generated in BEAMnrc. Dose can be scored in either a microCT uploaded phantom or in a user-created phantom. Each dose calculation outputs the absorbed dose per particle as well as the statistical uncertainty within every voxel of the phantom. A GUI can be used to input dose calculation parameters and to create the phantoms, with GUI design and execution similar to the BEAMnrc GUI displayed in **Figure 4.12**. Dose information was extracted from the phantom voxels using in-house code written in Matlab.

The solid water slabs and heterogeneous slabs used in Chapter 6 were manually cre-

ated to obtain solid water and heterogeneous phantoms in DOSXYZnrc. The mouse phantom of Chapter 6 was created from a mouse microCT scan obtained in the SARRP with material density information mapped to each voxel of the microCT scan. The scintillator dosimeter of Chapter 8 was modeled to obtain simulated air kerma measurements. The cross-section data for all phantom materials modeled in DOSXYZnrc was obtained from the ICRU cross-section database [76], and implemented in DOSXYZnrc using PEGS4 data files [194]. Pre-installed ICRU [76] materials and tissues are also used, with elemental composition and material densities predefined for the user. After establishing the elemental compositions, material densities, material geometries, the spectra to be used, photon and electron cutoff energies, the number of histories, and many other parameters, dose was then ultimately calculated in DOSXYZnrc.

BEAMDP

Developed for the Ottawa Madison Electron Gamma Algorithm (OMEGA) project, the BEAM Data Processor (BEAMDP) analyzes phase space files generated by BEAMnrc [135]. BEAMDP is a powerful tool that has the ability to derive beam fluence, spectra, mean energy, distribution of particle weights, particle scatter plots, combine multiple phase space files, and a number of other functions. This dissertation utilized BEAMDP for obtaining beam spectra at the location of dosimetry for the scintillator correction factors obtained in Chapter 8.

4.6 Summary

This chapter presented the details regarding the irradiators, dosimetry equipment, and software used throughout this dissertation. These materials form the basic building blocks that drive our research objectives. The next five chapters will present the meat on this body of work which utilize the materials discussed in this chapter.

Chapter 5

Multi-Institutional MicroCT Image Comparison of Image-Guided Small Animal Irradiators

"Sometimes I feel like I'm a seahorse, sometimes I think that I'm a horseshoe crab. I don't have anything in common."

–Slothrust

This chapter establishes quality assurance (QA) tolerance levels to recommend microCT imaging protocols for image quality standards in conformal image-guided small animal irradiators. Data was acquired through a multi-institutional study for the development of QA tolerance levels and imaging protocol recommendations. An exhaustive parameter study was also performed for the two commercial image-guided small animal irradiators to identify optimal imaging parameters for each respective irradiator.

5.1 Introduction

The use of conformal small animal irradiators advances the ability to treat human cancers with radiation through preclinical trials. Performing accurate irradiation on small animals gives a better understanding of radiation responses of normal and tumorous tissues, where preclinical studies on the effects of new treatment and fractionation schemes for major anatomical sites (e.g. brain, lung, pancreas, liver, colon, prostate) can be efficiently carried out in a controlled setting [13,14,17,36,83,126,166]. Coupling radiation with drugs, surgery, and/or nanoparticle delivery can help produce a valuable understanding of cross-modality treatments that otherwise would not be possible without small animal models [42, 122, 132, 137, 209]. Studies using the relatively short lifetimes of small animals are advantageous, as similar patient follow-up studies may take decades to acquire and can lack the regulation of a controlled setting.

Preclinical treatments require submillimeter precision to minimize dose to the small critical structures of the animal, where a close match between delivered and prescribed dose must be achieved. These submillimeter requirements for highly accurate and reproducible radiation guidance are facilitated by means of microCT imaging. Thus, high-resolution imaging is essential for image-guided small animal radiotherapy systems and there is a need for establishing standards in image quality. Unlike the AAPM TG-179 for the QA of CT-based image-guided accelerators [26], an equivalent does not yet exist for microCT-based image-guided small animal irradiators.

There are currently two companies manufacturing image-guided small animal irradiators: PXi and Xstrahl Inc. In this paper, microCT images of the commercial PXi X-RAD SmART and Xstrahl SARRP irradiators, as well as two in-house built systems, GE eXplore CT/RT 140 and GE eXplore CT120 (GE Healthcare, Milwaukee, WI), were investigated. A detailed summary of the specifications of each system are available [193], and briefly described in section 5.2.3.

Image quality characterization of small animal irradiators has been carried out in a past study presenting data from a single institution and irradiator [46]. Clarkson *et al.* covered a limited number of variable microCT imaging parameters and obtained image quality and reproducibility results from their image-guided small animal irradiator. This manuscript encompasses and compares data from eleven institutions and four

different image-guided small animal irradiators, acquired with a range of imaging protocols.

This work presents important steps towards comprehensive imaging QA for image-guided small animal radiotherapy. Here we respond to the lack of standardized imaging QA protocols for image-guided small animal irradiators and we illustrate a large range of image quality differences among institutions. To our knowledge, this is the first and most extensive multi-institutional study of its kind that presents microCT image quality of image-guided small animal irradiators and recommends imaging QA protocols and achievable tolerance levels.

5.2 Materials and Methods

A fully automated in-house QA software, SAPA, for quantitative analysis of the Micro-CT MCTP 610 phantom (Shelley Medical Imaging Technologies, London, ON, here referred to as the Shelley phantom) [60], was created in Matlab (The Mathworks, Nattick, MA). This phantom was specifically designed to be used as a device to assess image quality of microCT scanners. The Shelley phantom consists of six cylindrical polycarbonate plates containing CT number linearity, uniformity and noise, geometric accuracy, spatial resolution with slanted edge, spatial resolution with contrast coils, and CT number evaluation plates, as illustrated in **Figure 5.1**. The total phantom length and diameter are 9 and 7 cm, respectively.

5.2.1 SAPA

The SAPA software carries out quantitative analysis of CT linearity, SNR, uniformity and noise, geometric accuracy, spatial resolution using the MTF, and CT number evaluation, completely independent of the user. The SAPA GUI is presented in **Figure 5.2**. The quantification of all image quality metrics were carried out based on methods introduced in a past study [60],and are briefly described in section 5.2.2.

After the user selects the directory containing the phantom microCT images, the physical locations of the six QA plates within the Shelley phantom are automatically detected. SAPA then aligns the phantom in the same fashion for every scan regardless

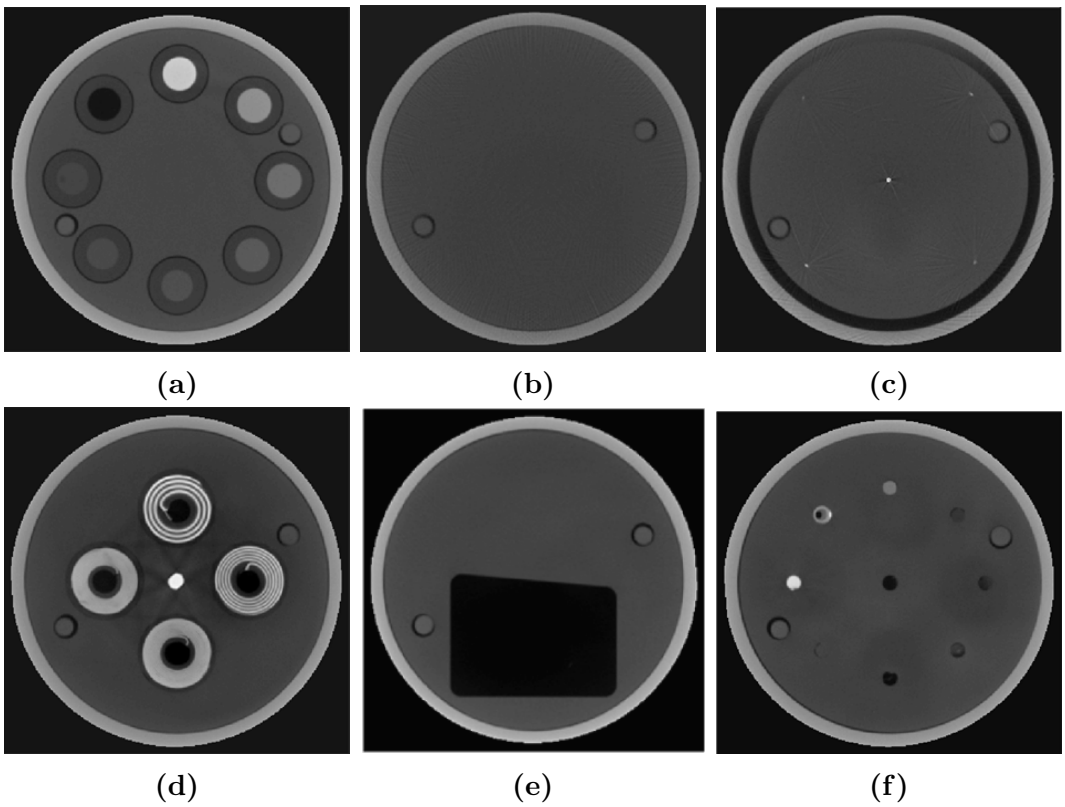

Figure 5.1: MicroCT images of the six quality assurance plates of the Shelley phantom after alignment in SAPA, illustrating the a) CT number linearity plate, b) uniformity and noise plate, c) geometric accuracy plate, d) spatial resolution coil plate, e) spatial resolution slanted edge plate, and f) CT number evaluation plate.

of the phantom's original orientation on the couch, to be displayed to the user in the slab order and orientation as shown in **Figure 5.1**. For this alignment, the images are rotated (the highest 30 mg/mL iodine concentration of the CT number linearity plate is positioned at 12 o'clock), cropped so the edge of the phantom is within 2 mm from the edge of the frame, and a mask is applied to the area outside the phantom to remove any outside artifacts. When needed, the images are then mirrored and the image order is reversed to achieve the standard phantom orientation for image analysis. In other words, the phantom may be scanned in any orientation and visual image quality assessment of any QA plate over multiple data sets can be easily performed in SAPA. Image quality parameters calculated after phantom alignment were within measurement error when compared to calculations without phantom alignment. All CT numbers are converted to HUs through linear interpolation using the air and water vials in the CT linearity plate, where air and water are set to -1000 and 0

HUs, respectively. SAPA then carries out each QA test by acquiring the necessary VOIs for each QA plate, as described in section 5.2.2 Quantitative QA results are then displayed in the GUI as shown in **Figure 5.2**. Each QA plate can be scrolled through in the viewer and the VOIs used for computation of each specific test are displayed. The user can also change the display window and level settings.

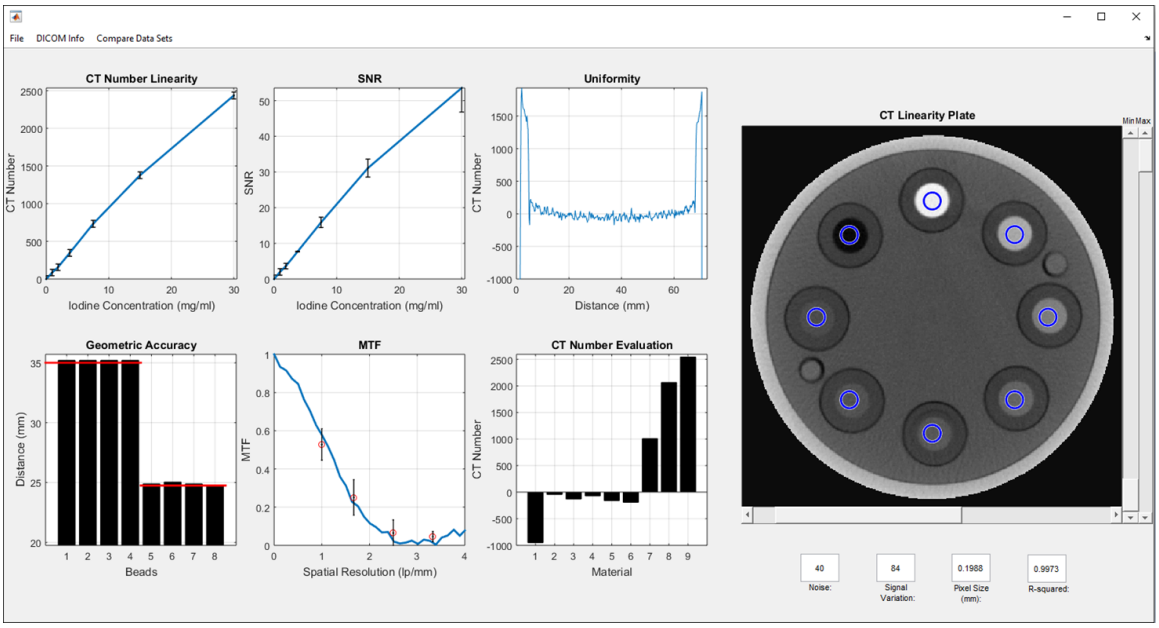

Figure 5.2: Screenshot of SAPA, our fully automated in-house QA softwares graphical user interface for QA analysis of the MCTP 610 Shelley phantom. Upon opening MicroCT scans in SAPA, image analysis of CT number linearity, SNR, uniformity, noise, geometric accuracy, MTF, and CT number evaluation are automatically calculated, independent of user, with an average computation time of less than 20 s. ROIs and MicroCT slices used for calculation are displayed to the user. Multiple analyses can be exported and compared to see if image quality degrades over time.

Additional functionalities of SAPA include the options to export the raw numerical QA data into a Microsoft Excel spreadsheet, obtain header information of scans, and save images of slices as TIFF files. SAPA can also automatically compare saved quantitative QA data from multiple datasets. This comparison can be used to display changes in a system's imaging functionality from its original performance and/or from the recommended tolerance levels presented in this study.

Users of the Shelley phantom also have the option of conducting image analysis for QA manually, or with image analysis software provided by the manufacturer of the Shelley Phantom (Model vmCT-SOFT). However, the manufacture's software is proprietary

and does not have the ability to directly compare QA results in the fashion that SAPA stores data over time.

5.2.2 Imaging Parameters

CT Number Linearity and SNR

CT number linearity was evaluated using the CT number linearity plate containing six vials of iodine solutions with concentrations of 0.9375, 1.875, 3.75, 7.5, 15, and 30 mgI/mL. The air and water vials of the CT number linearity plate were used for HU calibration, as described above. Signal intensities in HUs were obtained from a cylindrical VOI that was 3 mm in diameter and 3 mm in depth (throughout the chapter represented as 3Ø3 mm3 VOI) within each vial, and plotted as a function of iodine concentration. Next, the coefficient of determination (R^2) for a linear data fit was calculated, where a value of R^2=1 indicated that the data was perfectly linear. SNR was obtained as the ratio between mean signal intensity and signal variation expressed by means of HU standard deviation within the same VOIs.

Uniformity and Noise

Image uniformity was evaluated by plotting a line profile through the center of the uniformity plate. Signal uniformity was also obtained by calculating the signal intensity difference between four 5Ø3 mm^3 peripheral VOIs and a central 5Ø3 mm3 VOI. In addition, image noise was obtained as the average of the standard deviation within the five VOIs.

Geometric Accuracy

The geometric accuracy plate was designed with five 280 μm diameter tungsten-carbide beads to determine the in-plane voxel size of the reconstructed microCT volume. The respective distances of the beads were measured for the evaluation of geometric accuracy. Four of the corner beads are 35 mm apart and the central bead is located 24.75 mm from the four corner beads. The in-plane voxel size was determined

by dividing the known physical distance between neighboring beads by the measured distance between the centroid of the respective neighboring beads in voxels.

Spatial Resolution

Spatial resolution was obtained in two ways, using the resolution coil plate and the slanted edge plate. The resolution coil plate has four coils of alternating aluminum and plastic sheets with 500, 300, 200, and 150 μm thicknesses, corresponding to spatial resolution of 1, 1.67, 2.5, and 3.3 lp/mm, respectively. MTF can be determined by using the standard deviation of pixel values from ROIs within a cyclic bar pattern (e.g., each coil), as calculated by the following equation [59]

$$\mathrm{MTF}(f) = \frac{\pi\sqrt{2}}{4} . \frac{M(f)}{M_o}, \tag{5.1}$$

where *M(f)* is the average standard deviation of four 2Ø3 mm3 VOIs taken within each coil and corrected for noise, and M_o is half of the absolute difference between the aluminum and plastic HUs. MTF was also obtained with the slanted edge method [114], where the slanted edge is created by an air-polycarbonate plastic boundary and is tilted by 5° in order to create sub-pixel edge positions. A profile through the slanted edge defines the ESF, and when differentiated, the LSF is obtained. Finally, the MTF is determined by calculating the Fourier transform of the LSF. In SAPA, the MTF from the coil resolution plate is plotted with the MTF obtained from the slanted edge test (**Figure 5.2**). Unlike in the resolution coil test, the slanted edge MTF analysis results in continuous frequency values ranging from 0.0 to 3.3 lp/mm.

CT Number Evaluation and Image Contrast

Finally, the CT number evaluation plate was used to analyze the output of the system in HUs by means of nine tissue-equivalent materials embedded in the Shelley phantom. The mean HU of nine 1.5Ø3 mm3 VOIs of each material were plotted. Analysis of the CT number evaluation plate proved to be difficult, as the Shelley phantom's nine tissue-equivalent materials were sparse and non-uniform within and across slices. The vials often included a material non-uniformity, both within the center, edges, and

entire length of each vial, making accurate measurements challenging and problematic to reproduce. While the CT number evaluation plate data was plotted in SAPA, for QA purposes, iodine vials from the CT number linearity plate were used to assess changes in CT numbers and the 30 mgI/mL vial was used as the metric for image contrast.

5.2.3 Image-guided small animal irradiators

PXi X-RAD SmART

MicroCT imaging in the PXi X-RAD SmART system, previously sold as the 225cX system, is performed with a 360°-rotation of the C-arm gantry using CBCT geometry (**Figure 5.3a**). Focal spot x-ray beams of 3.0 and 0.4 mm are used for therapy and imaging, respectively, and are calibrated to a 30.7 cm SID and 64.5 cm SDD [46, 192]. The PXi X-RAD SmART system utilizes an amorphous silicon flat-panel detector with a pixel size of 200 μm (Perkin-Elmer, Wiesbaden, Germany) that captures x-rays generated with tube voltages generally between 40 and 100 kVp. The PXi X-RAD SmART system performs radiation therapy a tube voltage of 220 kVp and tube current of 13 mA, using 1 to 25 mm diameter circular and 5 x 5 to 40 x 40 mm^2 square field collimators as well as a motorized rotating collimator with a 4 Gy/min maximum output [46].

Xstrahl SARRP

MicroCT imaging on the Xstrahl SARRP is acquired in the so-called 'pancake' geometry (**Figure 5.3b**) with a stationary x-ray tube and detector with a 360° rotating couch. To obtain a more conventional CBCT geometry, the phantom may be placed standing on the couch (**Figure 5.3c**). The SID and SDD are 35 cm and 50 cm, respectively. The x-ray tube operates with a dual focal spot of 3.0 and 0.4 mm for therapy and imaging, respectively [186, 201]. The Xstrahl SARRP system utilizes the aforementioned Perkin-Elmer detector as well and acquires microCT images with tube voltages between 40 and 80 kVp. Alternatively, a Varian 2520DX panel with a pixel size of 127 μm can be used for imaging. Radiation therapy is performed a tube voltage of 220 kVp and tube current of 13 mA, using 0.5 to 10 mm diameter circular

and 3 x 3 to 10 x 10 mm^2 square collimators with a 4 Gy/min maximum output. A motorized variable collimator capable of rectangular field sizes from 1 x 1 mm^2 to 40 x 80 mm^2 is also available.

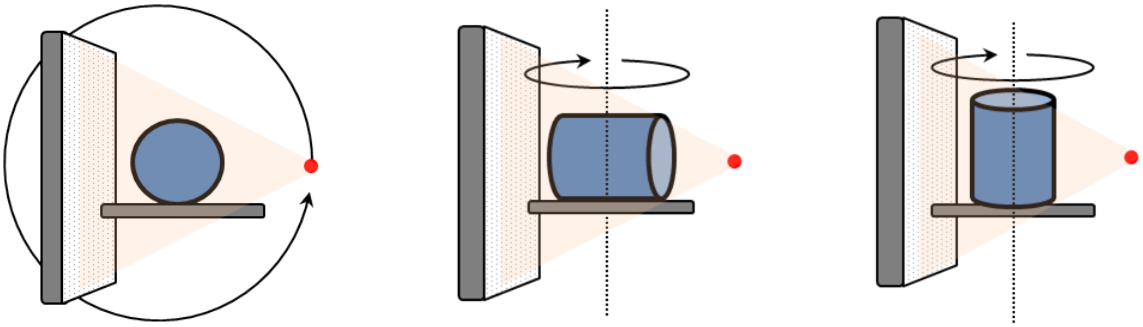

Figure 5.3: Illustrated is the a) PXi X-RAD SmART and conventional CBCT imaging geometry, with a stationary table as both source and detector rotate 360 around the short-axis of phantom. This is in comparison to the Xstrahl SARRP with stationary source and detector, as the table rotates 360 with b) phantom lying down in pancake geometry (photons transverse long and short-axes of phantom) and c) phantom standing up in standard geometry (photons transverse only short-axis of phantom), more similar to conventional CBCT geometry.

GE eXplore CT 120 and CT/RT 140

The GE eXplore CT120 (GE Healthcare, London, Ontario, Canada) was adapted to radiotherapy delivery by adding a two-stage iris collimation system [169]. This system utilizes a pulsed x-ray beam running a 10% duty cycle with a 0.3 mm focal spot for imaging, in contrast to using a continuous imaging beam on the PXi and Xstrahl units [213]. The amorphous silicon flat panel detector has a pixel size of 49 μm and the SID and SSD are 35.4 cm and a 45 cm, respectively. MicroCT imaging on the GE eXplore CT120 scanner is performed with tube voltages between 70 and 120 kVp and radiotherapy with the maximum tube voltage of 120 kVp and tube current of 60 mA, using 1 to 10 cm diameter circular collimation with 2 Gy/min maximum output. The GE eXplore CT/RT140 microCT imaging is performed in similar fashion to the imager of the GE eXplore CT120 scanner (Jensen *et al.* 2013). Radiotherapy is performed at 140 kVp with a 1.0 mm focal spot with a set of computerized independent jaws and the same SID as the eXplore CT120.

5.2.4 Multi-Institutional Study

To identify suitable imaging parameters and establish tolerance levels for microCT imaging QA tests of image-guided small animal irradiators, we analyzed microCT images of the same Shelley phantom scanned at eleven institutions. Each institution submitted multiple microCT data sets with varying imaging parameters, where the data sets acquired with imaging parameters routinely used for small animal radiotherapy were used in this study. Chosen imaging protocols for all institutions ranged from using manufacturer recommendations developed during irradiator commissioning, to institution-specific imaging research and techniques of past small animal studies, or a mixture of these. As stated above, four different irradiator units were involved in the study, the PXi X-RAD SmART, Xstrahl SARRP, GE Explore CT120, and GE Explore CT/RT 140. In no particular order, the eleven institutions involved in this study were: Dana-Farber Cancer Institute, University of Maryland, University of Western Ontario, University of Victoria, Princess Margaret Cancer Centre, University of California, Los Angeles, McGill University, MD Anderson Cancer Center, Stanford University, BC Cancer Agency-Vancouver Centre, and Xstrahl Inc. Imaging parameters used to acquire the presented data are summarized in **Table 5.1**.

Table 5.1: Imaging parameters and irradiators used in the multi-institutional study.

Institution	Irradiator	Voltage (kVp)	Added Filtration (mm Al)	Current (mA)	Total Imaging Time (s)	Current-Exposure Time (mAs)	Voxel Size (mm)
Institution 1	SmART	70	2.0	3.0	60	180	0.200
Institution 2	SARRP	60	1.0	0.8	240	192	0.200
Institution 3	eXplore 140	60	4.5[a]	63[b]	240[b]	1008[b]	0.205[c]
Institution 4	SmART	60	2.0	1.0	120	120	0.200
Institution 5	eXplore 120	70	4.5	40[b]	240[b]	480[b]	0.192
Institution 6	SARRP	65	1.0	0.9	60	54	0.350
Institution 7	SmART	60	2.0	4.0	20	80	0.150
Institution 8	SARRP	60	1.0	0.8	240	192	0.325
Institution 9	SARRP	60	1.0	0.7	57	40	0.275
Institution 10	SARRP	60	1.0	0.8	60	48	0.325
Institution 11	SmART	80	2.0	2.0	120	240	0.200

[a] Additional 0.38 mm Cu filtration used to reduce mouse imaging dose by approximately 10%.
[b] Pulsed beam with ˜10% duty cycle.
[c] Listed voxel sizes are identical in all three directions for all institutions, except Institution 3 (0.205 x 0.205 mm^2 in the transverse plane, 0.478 mm along the longitudinal axis).

We compared image quality parameters of the entire multi-institutional data set and established tolerance levels for each QA test based on the comparative performance of the systems, described in section 5.3.1. Note that the Shelley phantom was scanned in the 'pancake' geometry (**Figure 5.3b**, phantom lying on the couch), as opposed to the standard imaging geometry (**Figure 5.3c**, phantom standing on the couch) on all Xstrahl SARRP irradiators of the multi-institutional study. In order to investigate the effects of imaging geometry, we also compared image quality for the standard imaging geometry with the 'pancake' imaging geometry employed with the Xstrahl SARRP at two institutions. This comparison was done by laying the Shelley phantom on the couch for 'pancake' geometry and repeated using the same imaging parameters with the Shelley phantom standing on the couch achieving the standard imaging geometry.

5.2.5 Parameter Study

To further evaluate microCT imaging QA tests and identify the best imaging parameters, we performed an imaging parameter study on the two state-of-the-art commercial image-guided small animal irradiators, the PXi X-RAD SmART and the Xstrahl SARRP systems. In this investigation, a specific parameter, such as the x-ray tube voltage, current, or pixels size, was varied while all other parameters were maintained constant, to assess each parameter's effect on image quality in a systematic way.

PXi X-RAD SmART

The studied imaging parameters for the PXi X-RAD SmART system are summarized in **Table 5.2**. The constant settings for the imaging parameters employed in this study were: tube voltage of 70 kVp, tube current of 3 mA, imaging time of 60 s, voxel size of 0.20 mm, and imaging frame rate of 5 fps.

Xstrahl SARRP

The studied imaging parameters for the Xstrahl SARRP are also listed in **Table 5.2**. The constant settings for the imaging parameters employed on this system were: tube voltage of 60 kVp, tube current of 0.8 mA, imaging time of 240 s, voxel size of 0.325

mm, and imaging frame rate of 6 fps. The imaging parameter study in this paper used the standard geometry when scanning with the Xstrahl SARRP irradiator.

Table 5.2: Range of imaging parameters studied on the PXi X-RAD SmART and Xstrahl SARRP systems.

	Voltage (kVp)	Current (mA)	Total Imaging Time (s)	Current-Exposure Time (mAs)	Voxel Size (mm)	Frame Rate (fps)
SmART	50 - 100	1 - 10	30 - 240	90 - 720	0.100 - 0.500	1 - 15
SARRP	50 - 80	0.4 - 1.2	30 - 300	24 - 240	0.325	4 - 12

5.2.6 SAPA Validation

SAPA imaging parameter evaluation results were validated against hand calculations assisted with Fiji [176], a distribution of the open-source software ImageJ [177], and independent Matlab code. ROIs of approximately the same size used in SAPA were acquired using Fiji, and the QA results were obtained in the same fashion as described in section 5.2.2. for CT number linearity, SNR, uniformity and noise, geometric accuracy, MTF (resolution coil plate), and CT evaluation number. MTF (slanted edge plate) was acquired with independent Matlab code specifically designed to acquire the MTF of a slanted edge, where the user manually defines an ROI composed of approximately 50% air and 50% plastic within the slanged edge plate.

5.3 Results

MicroCT image quality parameters from the multi-institutional study performed with the Shelley phantom and analyzed with SAPA are plotted in **Figure 5.4**. CT number linearity, expressed in terms of R^2 of the linear fit, ranged from 0.9609 to 9953. The values of SNR for the 30 mgI/mL vial ranged among the data sets from 12 to 56, and noise levels also ranged from 35 to 110 HU. The spatial frequency for MTF = 0.2 ranged from 1.15 lp/mm to 1.82 lp/mm. The geometric accuracy, expressed as the difference between the nominal and measured voxel size, ranged from 0.1% to 2.2%. Image contrast for the 30 mgI/mL varied from 1585 to 2721 HU.

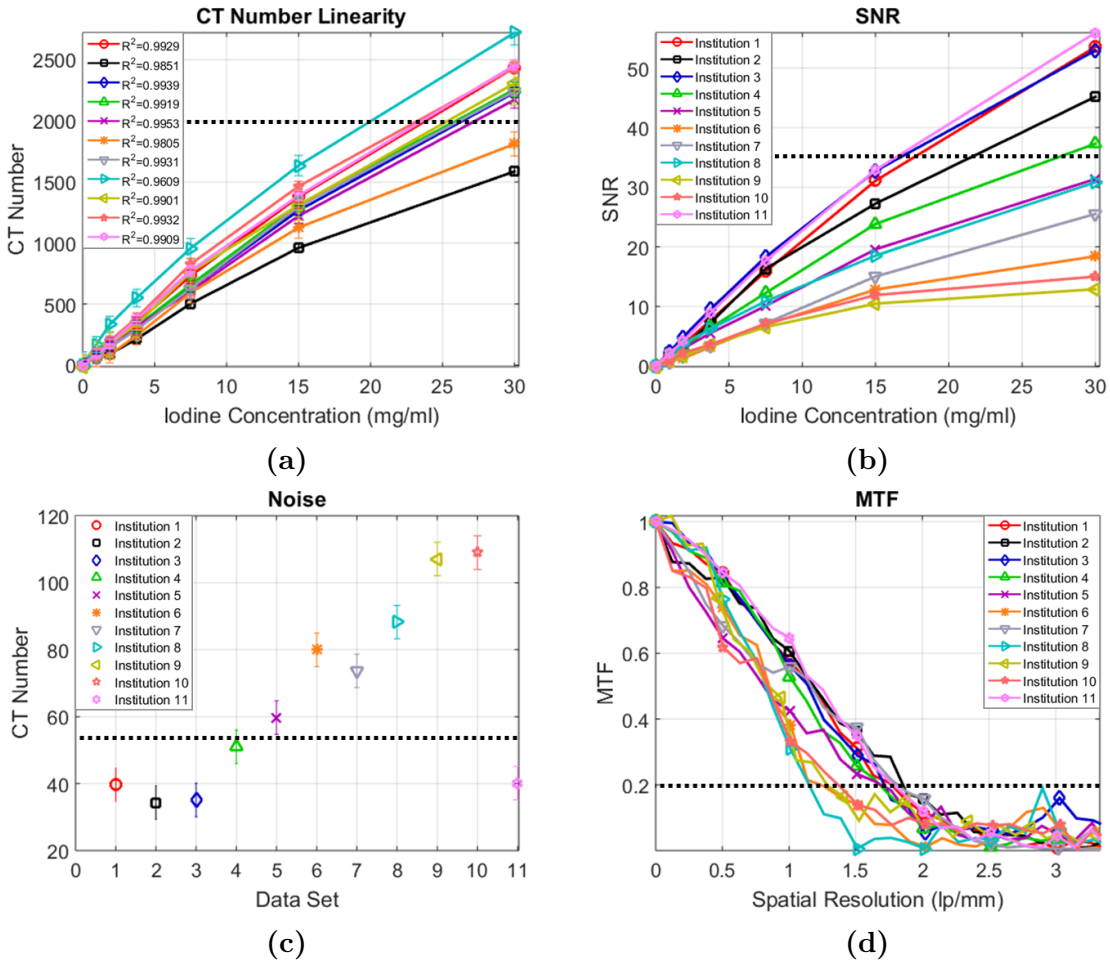

Figure 5.4: Multi-institutional study results for a) CT number linearity, b) SNR, c) noise, and d) slanted edge MTF acquired at eleven institutions. Tolerance levels for each QA test were established in Section 5.3.1 and are represented by the dashed horizontal lines.

5.3.1 Multi-Institutional Study: Tolerance Level Recommendations

Based on the multi-institutional study presented in **Figure 5.4**, tolerance levels for microCT QA tests were established for CT number linearity, SNR, noise, MTF (slanted edge), geometric accuracy, and image contrast and are summarized in **Table 5.3**. Tolerance levels were established based on the comparative performance of the institutions and the justification of their choice is described in the following paragraph.

Table 5.3: Recommended tolerance levels for image quality assurance of image-guided small animal irradiators.

CT# Linearity (R^2)	Noise	SNR	MTF	Geometric Accuracy	Contrast
		30 mgI ml^{-1}	0.2	Bead Distance, Voxels	30 mgI ml^{-1}
>0.990	<55 HU	>36	1.5 lp mm^{-1}	±0.20 mm, <1.5%	>2000 HU

CT linearity (**Figure 5.4a**) had an R^2 range between 0.9609 and 0.9953, where the poorest linearity (R2<0.990) occurred for data sets with the apparent outliers with lowest (HU<2000, Institutions 2 and 6) and highest (HU>2500, Institution 8) values for the 30 mgI/mL. As a result, CT linearity tolerance level of R^2>0.990 was established. SNR (**Figure 5.4b**) and noise (**Figure 5.4c**) tolerance levels were established in concert, as the two imaging parameters are related. SNR values of >36 were achieved at five institutions (Institutions 1, 2, 3, 4, 11), which corresponded to noise values of <55 HU at the same five institutions. It should be noted that based on a previous study [16], CT noise lower than 55 HU is required to keep MC dose calculation accuracy of the 220 kV SARRP beam within 5%. For our 2000 HU contrast tolerance level within the 30 mgI/mL vial, this correlates to an SNR of 36 (2000HU/55HU). Therefore we chose to set SNR and noise tolerance levels to be >36 and <55 HU, respectively. The MTF plot (**Figure 5.4d**) shows two noticeable groups of curves separated by 1.5 lp/mm at 20% MTF. The four lower-resolution curves were obtained with voxel sizes of 0.275 mm or greater and degradation in resolution could be observed with voxel sizes of 0.275 mm. As a result, spatial resolution tolerance level of >1.5 lp/mm at the 20% mark in MTF was established. Geometric accuracy was within a 1.5% difference (less than 0.20 mm) for all data sets except one (2.2% difference, Institution 7). Along with 0.20 mm as our recommendation for voxel size, a tolerance level of 1.5% was established. Finally, image contrast expressed as the CT number of the 30 mgI/ml vial ranged from 1585 to 2721 HUs. Two outliers with image contrast of <2000 HU could be identified in **Figure 5.4a**, and therefore the image contrast tolerance level was set as >2000 HU.

Table 5.4 summarizes the number of institutions passing the set QA tolerance levels for each test, as well as for the different irradiators. Note that microCT data sets acquired at four (Institution 1, 3, 4, 11) of the eleven institutions passed all set tolerance levels.

Table 5.4: Multi-institutional study summary: Institution and irradiator pass rate for set imaging QA tolerance levels.

Pass Rate	Linearity $R^2 > 0.990$	Noise < 55 HU	SNR > 36 30 mgI ml^{-1}	>1.5 lp mm^{-1} @ MTF=0.2	Geometric Accuracy $< 1.5\%$	Contrast > 2000 HU @ 30 mgI ml^{-1}
Institution	8/11	5/11	5/11	7/11	10/11	9/11
SmART	4/4	3/4	3/4	4/4	3/4	4/4
SARRP	2/5	1/5	1/5	1/5	5/5	3/5
eXplore	2/2	1/2	1/2	2/2	2/2	2/2

5.3.2 Imaging QA Protocol Recommendations

Based on an extensive image quality study of the two commercial irradiators, the PXi X-RAD SmART and the Xstrahl SARRP system, we recommend performing imaging QA with the Shelley phantom using the scanning protocols summarized in **Table 5.5**. These recommended parameters were deemed to be the optimal combination to ensure all imaging tolerance levels are met in a single scan. When the recommended parameters of **Table 5.5** were employed during additional data acquisitions at Institutions 1, 8, 10, and 11, all QA tests passed the set tolerance levels.

Table 5.5: Recommended QA imaging parameters using the Shelley phantom.

	Voltage (kVp)	Total Imaging Time (s)	Current (mA)	Voxel Size (mm)	Frame Rate (fps)
SmART	70	120	1.5	0.20	5
SARRP[a]	60	240	1.0	0.20	6

[a] We recommend scanning the Shelley phantom in the standard imaging geometry in the SARRP.

5.3.3 SARRP 'pancake' and Standard Imaging Geometry Comparison

Results comparing the 'pancake' imaging geometry (**Figure 5.3b**) with the Xstrahl SARRP standard imaging geometry (**Figure 5.3c**) using data acquired at two institutions are presented in (**Figure 5.5**).

Standard imaging geometry at both institutions produced passing linearity (R2> 0.990) where the 'pancake' imaging geometries failed. Image noise was 20% and 35%

lower in the standard geometry for institutions A and B, respectively. Likewise, SNR was 40% and 25% higher for the standard geometry. On the other hand, spatial resolution at MTF=0.2 was 30% and 8% higher in the 'pancake' geometry for Institutions A and B, respectively. Geometric accuracy was within error bars for all data sets.

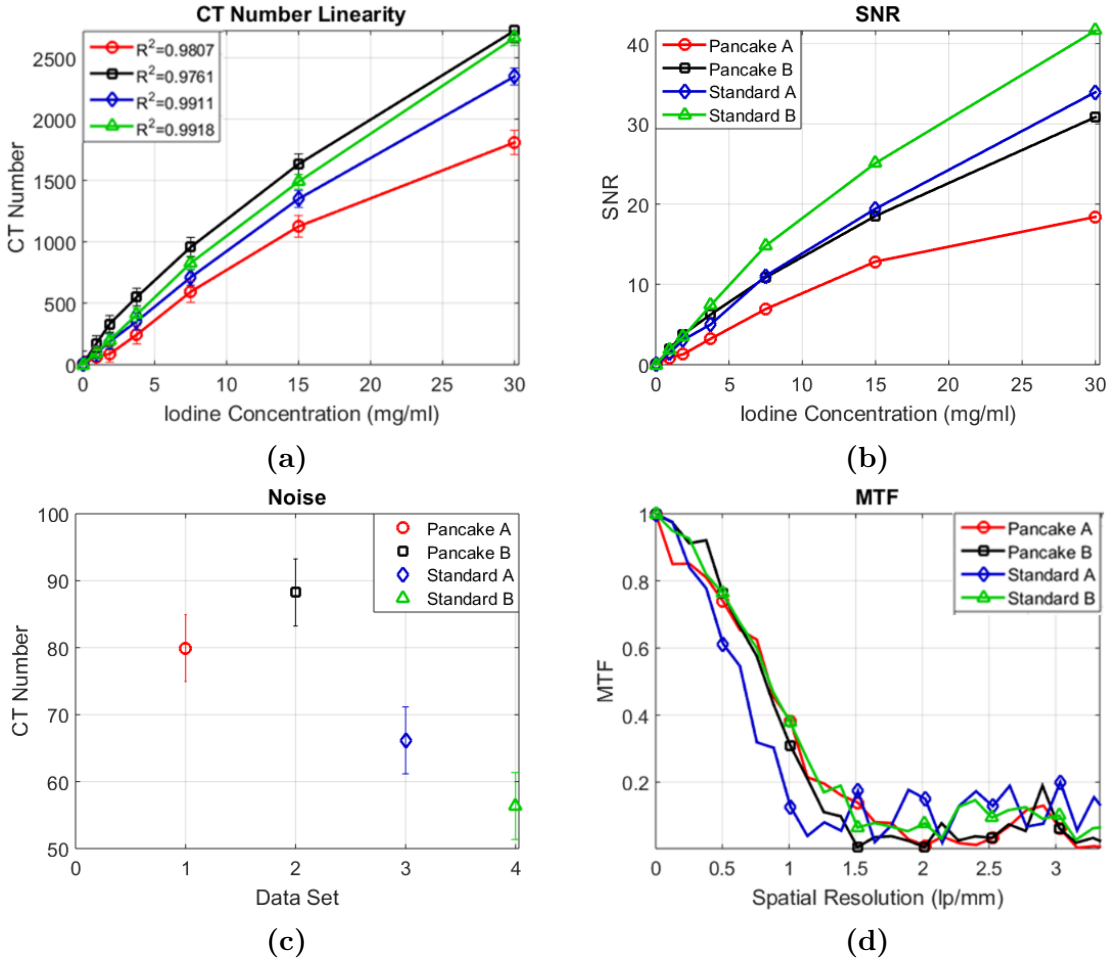

Figure 5.5: Comparison of the SARRP standard imaging geometry (standing phantom) vs pancake imaging geometry (lying phantom) for Institution A and Institution B: a) CT number linearity, b) SNR, c) noise, and d) slanted edge MTF.

5.3.4 Parameter Study

PXi X-RAD SmART

A comparison of image quality parameters for varying tube voltage, while maintaining all other parameters constant, is presented in **Figure 5.6**. All tube voltage (50-100

kVp) values resulted in good CT number linearity (R^2>0.991) with a tube voltage of 70 kVp producing the highest R^2 value. Decreasing tube voltage resulted in higher CT numbers due to the higher probability of photoelectric effect for lower x-ray energies. The 30 mgI/mL SNR was highest for the 70 and 80 kVp scans (SNR>50). Also, the SNR started to deteriorate above 80 kVp, likely due to saturation of the imager at too high of a tube voltage. Noise levels were inversely proportional to tube voltage. MTF and geometric accuracy were within statistical uncertainty for the different tube voltage datasets. Image contrast for all tube voltages except for 100 kVp passed the contrast tolerance of >2000 HU for the 30 mgI/mL vial.

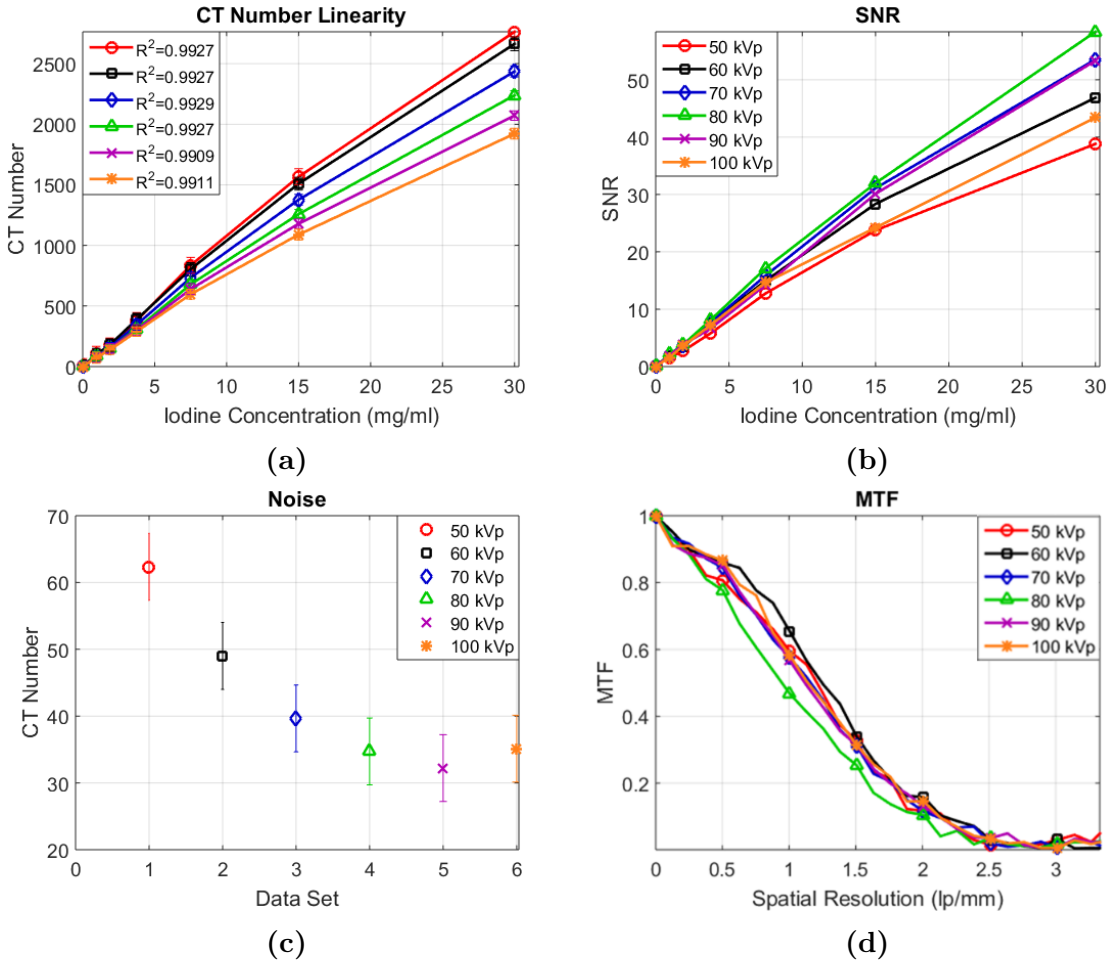

Figure 5.6: PXi X-RAD SmART imaging parameter study of a) CT number linearity, b) SNR, c) noise, and d) MTF plots as a function of varying tube voltage (50-100 kVp).

When varying current-exposure time (**Figure 5.7**), CT number linearity was unaffected, but higher current-exposure time resulted in higher SNR and lower-noise

images. MTF, geometric accuracy, and CT numbers were within statistical uncertainty for the varying current-exposure time scans. Qualitatively, streaking artifacts appeared in the scans acquired in 30 to 90 s, but disappeared for scan times of 120 s and longer. This was true regardless of the current-exposure time used, as a 60-second scan time with 10 mA (600 mAs) produced streaking artifacts while a 120-second scan time with 3 mA (360 mAs) did not. With the standard acquisition frame rate of 5 fps and a full 360° projection, this would correspond to a minimum of 600 frames per scan to avoid streaking artifacts.

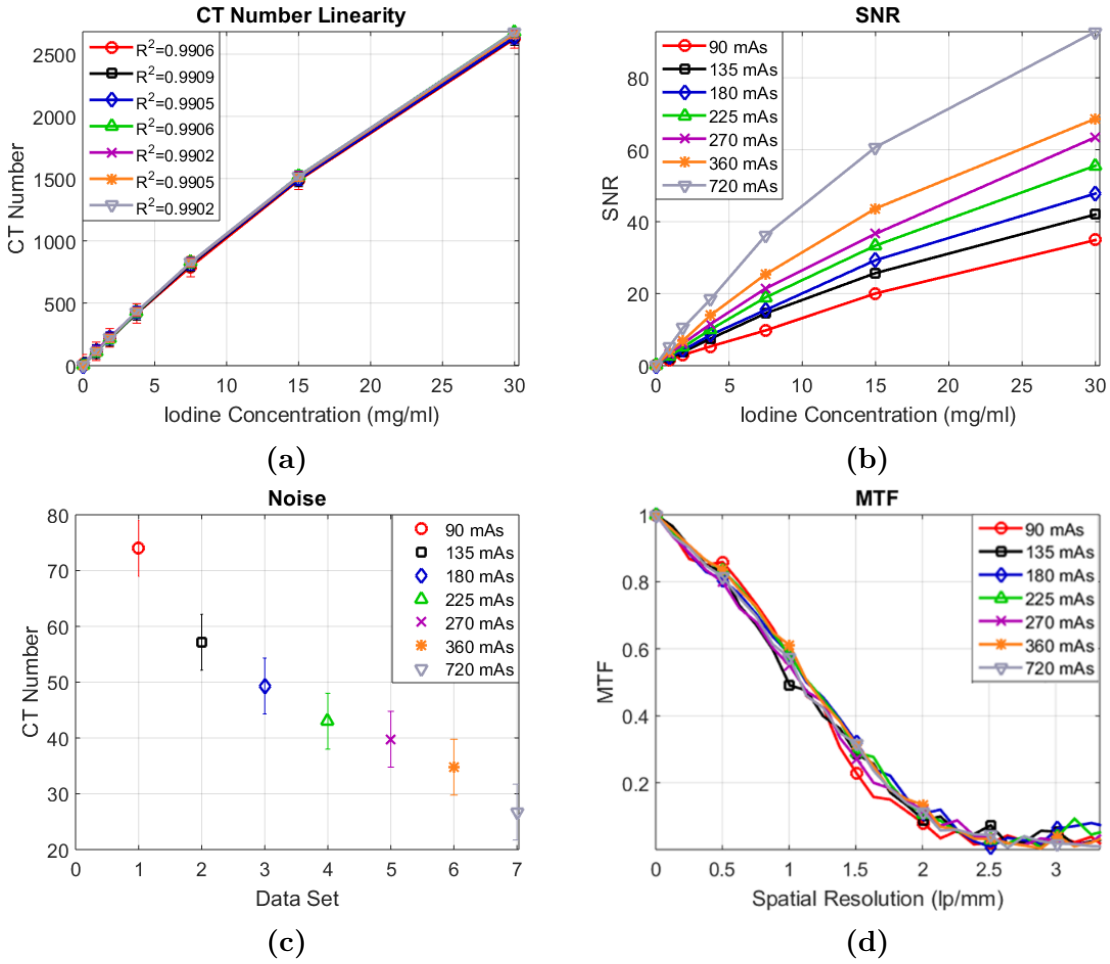

Figure 5.7: PXi X-RAD SmART imaging parameter study of a) CT linearity, b) SNR, c) noise, and d) MTF plots as a function of varying tube-exposure time (90-720 mAs).

When varying voxel size, CT linearity was statistically unaffected. Smaller voxel size was proportional to lower SNR, with the greatest degradation of SNR occurring for voxel sizes of less than 0.175 mm. Decreasing voxel size resulted in increased

noise and higher MTF values, with the greatest degradation in MTF and perceived spatial resolution occurring for voxel sizes larger than 0.250 mm. With the exception of increasing MTF, there was no benefit from decreasing the voxel size to less than 0.175 mm.

Xstrahl SARRP

Saturation of the CBCT detector panel occurred with parameter combinations higher than 80 kVp and 1 mA, and at 60 kVp and 1.5 mA for tube voltage and current, respectively. Thus, microCT imaging with parameters exceeding these combinations could not be performed on the SARRP system. This is in contrast to the PXi X-RAD SmART, which did not saturate for tube voltage and current combinations of 100 kVp and 3 mA, and 60 kVp and 10 mA.

An Xstrahl SARRP comparison of varying tube voltage while maintaining all other parameters constant is presented in **Figure 5.8**. All tube voltages resulted in good CT number linearity ($R^2 \geq 0.990$) except for the 50 kVp tube voltage. As expected, decreasing tube voltage resulted in higher CT numbers, lower SNR, and higher noise. MTF and geometric accuracy plots were within statistical uncertainty for all varying tube voltage datasets.

When the current-exposure time was varied (**Figure 5.9**), CT linearity was unaffected, but longer current-exposure times resulted in higher SNR and lower-noise images. MTF, geometric accuracy, and CT numbers were within statistical uncertainty for all studied current-exposure times scans. Visual inspection revealed noticeable image quality degradation due to noise for scans acquired in less than 180 s.

When the frame rate was varied (**Figure 5.10**), CT number linearity was statistically unaffected. Higher frame rates were proportional to higher SNR and lower noise. MTF, geometric accuracy, and CT numbers were within statistical uncertainty for all studied frame rate values. The Xstrahl SARRP system used for the parameter study was calibrated to work with a specific voxel size and we, therefore, could not obtain images for varying voxel size.

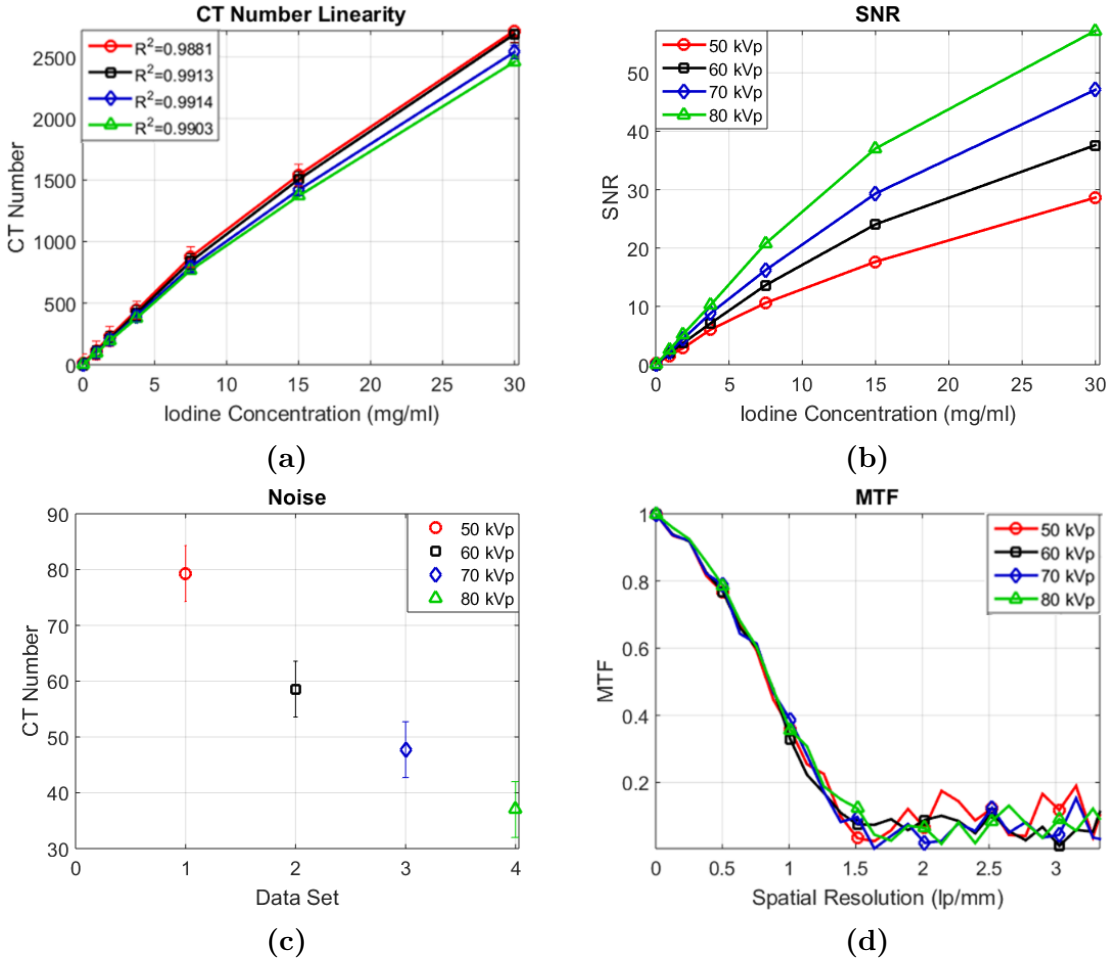

Figure 5.8: Xstrahl SARRP study for varying tube voltage (50-80 kVp): a) CT linearity, b) SNR, c) noise, and d) MTF plots.

5.3.5 SAPA Validation

QA test results determined by SAPA and independent calculations were compared and the differences are summarized in **Table 5.6**. Maximum difference between CT number linearity (R^2) as calculated by SAPA and Fiji was less than 0.0003. Noise and uniformity variations between the two methods were less than 5 HU. Geometric accuracy was calculated to be within ± 0.20 mm of bead distance (the voxel size). Differences between SAPA and manual MTF and contrast were 0.05 and 2.3%, respectively, and thus all in good agreement. Average SAPA computation time for complete QA analysis for a 0.20 mm voxel, 400-slice microCT data set was less than 20 s using an Intel Core i7-6700HQ CPU 2.60 GHz quad-core personal laptop.

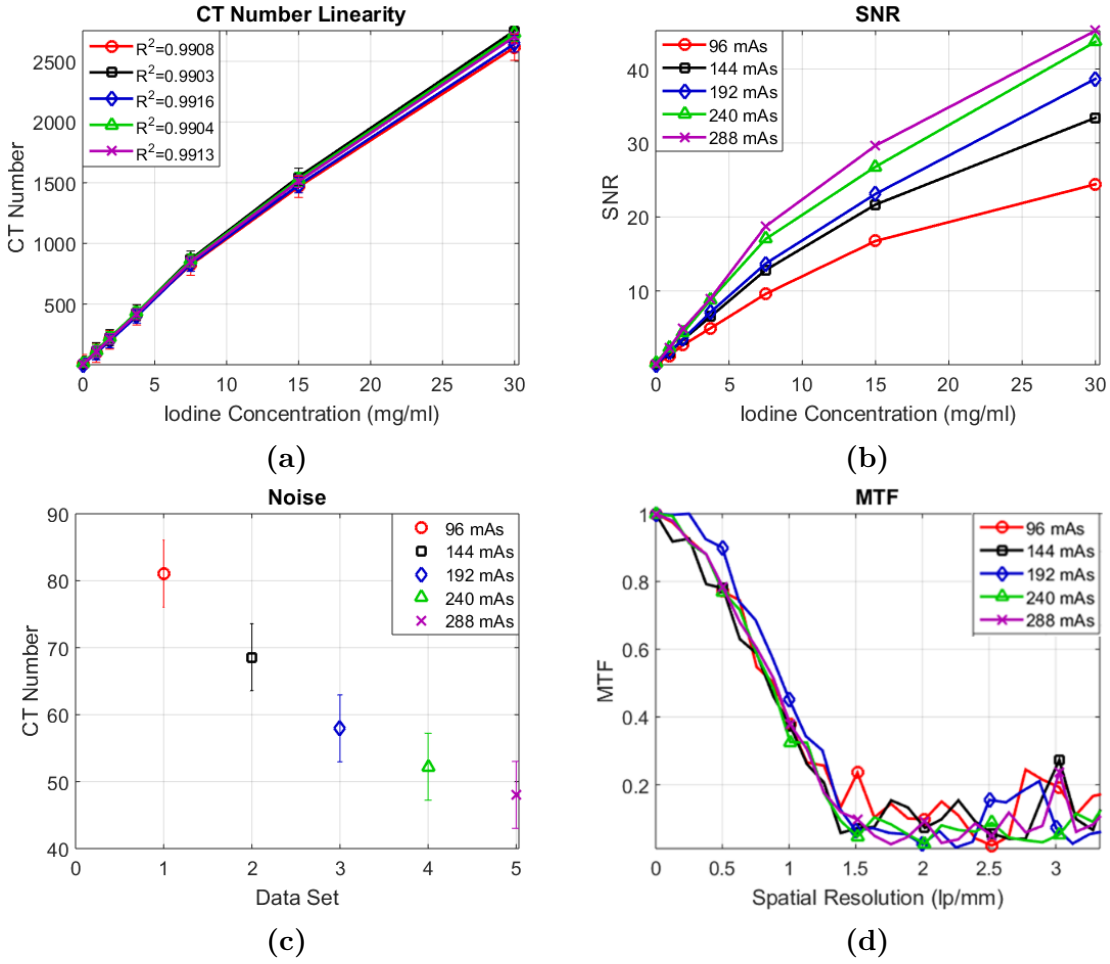

Figure 5.9: Xstrahl SARRP imaging parameter study of a) CT linearity, b) SNR, c) noise, and d) MTF plots as a function of varying mAs (96-288 mAs).

Table 5.6: Validation between SAPA and independent calculations.

	CT# Linearity (R^2)	Noise	SNR	MTF	Geometric Accuracy	Contrast
					Bead Distance, Voxel Size	30 mgI ml^{-1}
Difference	±0.0003	±5 HU	±3	±0.05	±0.20 mm, <1.0%	±10 HU

5.4 Discussion

MicroCT imaging of image-guided small animal irradiators has been investigated by analyzing the output of CT number linearity, SNR, noise and uniformity, geometric

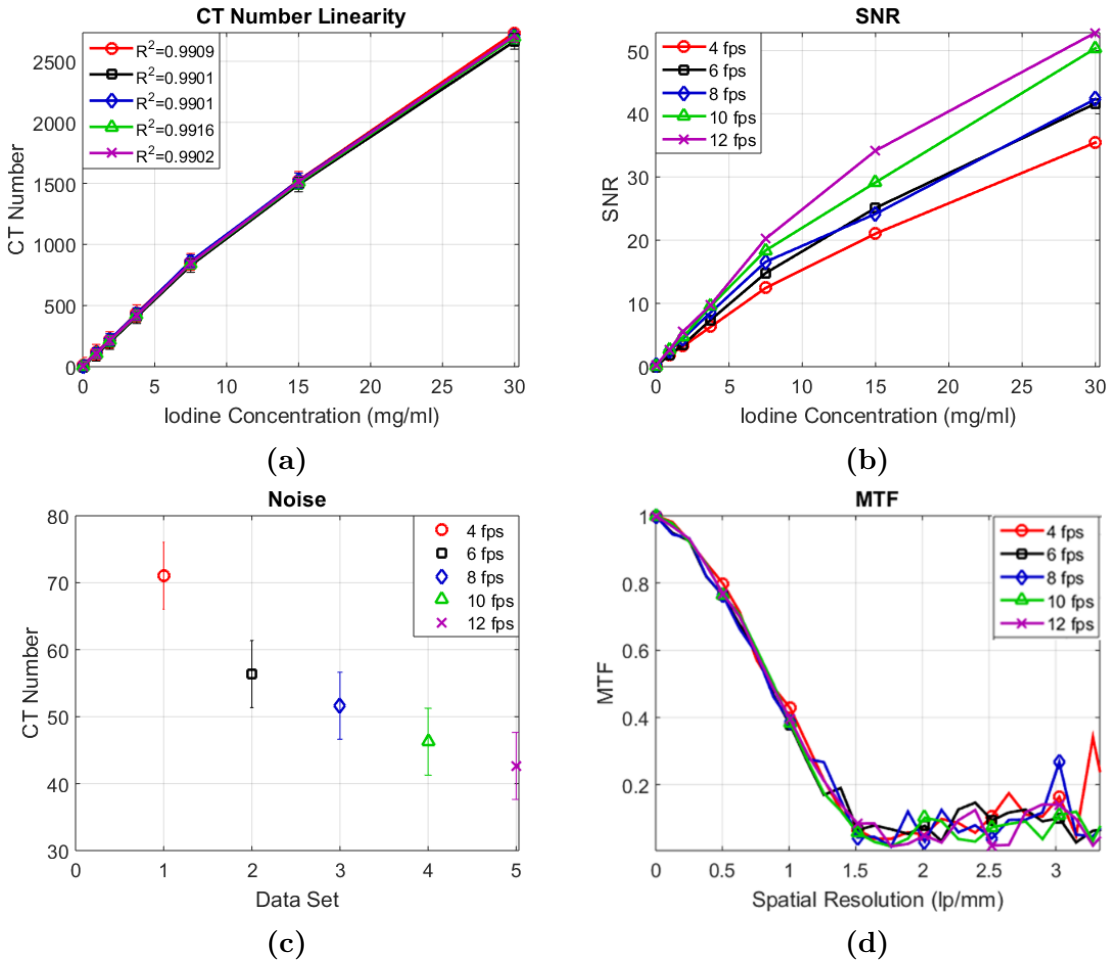

Figure 5.10: Xstrahl SARRP imaging parameter study varying the frames per second (fps) for a) CT linearity, b) SNR, c) noise, and d) MTF plots as a function of varying fps (4-12 fps).

accuracy, spatial resolution, and contrast using the Shelley microCT phantom in a multi-institutional study.

Examples of the varying image quality for data acquired at different institutions and with different protocols are presented in **Figure 5.11**. Displayed are the qualitative image difference of a scan from the uniformity plate that passed all tolerance levels (**Figure 5.11a**, Institution 4), and a scan that did not (**Figure 5.11b**, Institution 6), as a means for visual representation of acceptable image quality. Also presented are differences in the PXi X-RAD SmART image quality for images acquired in 60 s and 600 mAs (**Figure 5.11c**) and 120 s and 360 mAs (**Figure 5.11d**) with the same frame rate of 5 fps. Streaking artifacts were noticeable in all images acquired

with imaging times of less than 120 s, regardless of the current-exposure time. With the standard acquisition frame rate of 5 fps and a full 360° projection for the PXI X-RAD SmART, this would correspond to a minimum of 600 frames per scan to avoid streaking artifacts.

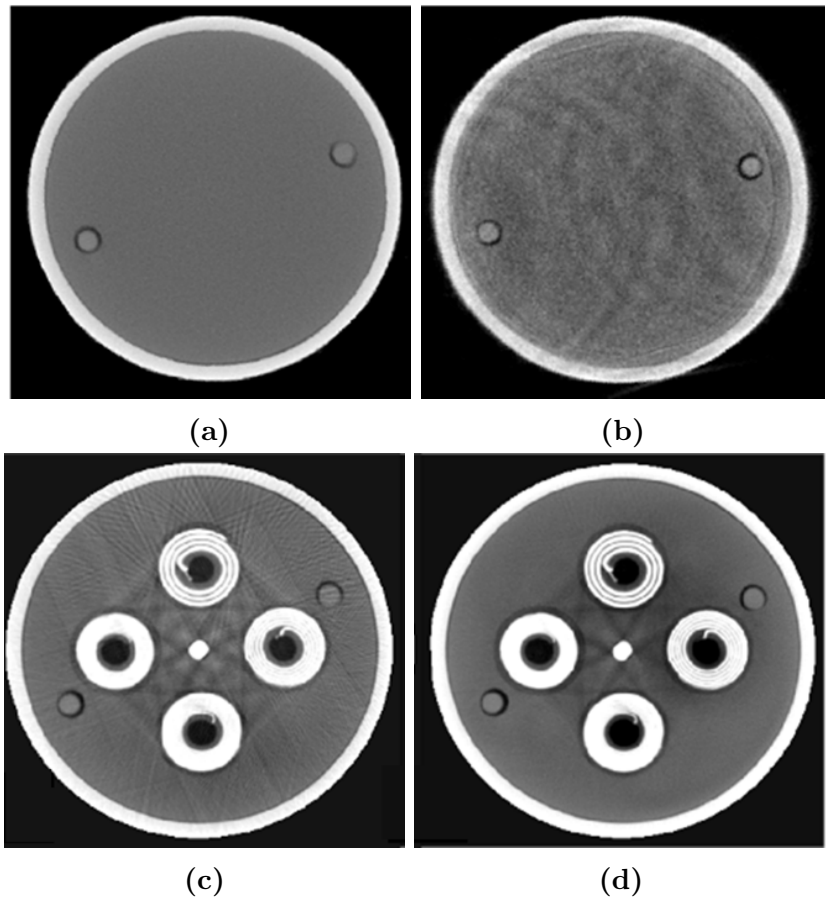

Figure 5.11: Uniformity plate scans displaying the image quality of a) a scan that passed all recommended tolerance levels (Institution 4), and b) a scan that did not (Institution 6). Streaking artifacts were present in an image c) acquired with 60 s imaging time but not in an image d) acquired with 120 s imaging time.

CT number linearity directly affects the accuracy of dose calculations, which are based on microCT images of small animals. SNR, spatial resolution, noise, and uniformity are parameters that impact the ease of proper identification of small animal anatomical structures and also affect the accuracy of dose calculations. Geometric accuracy and contrast are crucial for accurate spatial targeting and measurements of anatomical structures, which can be used to determine how a tumor is responding to treatment.

The minimum SNR and noise passing tolerance levels were obtained with current-exposure times of 120 and 240 mAs for the PXi X-RAD SmART and Xstrahl SARRP systems, respectively. One may shorten the scanning time and increase the tube current (while maintaining the minimum recommended current-exposure time) to minimize motion artifacts caused by physiological motion of the animal. It should be considered that for the PXi X-RAD SmART system, images acquired in less than 120 s produced streaking artifacts. On the Xstrahl SARRP system, imaging time of less than 240 s resulted in high noise (>70 HU). The only data set that did not pass geometric accuracy had a total scanning time of less than 30 s, possibly failing due to image blurring caused by the relatively fast scan.

A user could theoretically increase the current-exposure time indefinitely to increase SNR and lower noise, but imaging time and dose must be taken into account, specifically in regards to scanning a live animal. High imaging doses may change the animal immune response and other biological pathways that may alter the experimental outcome [30], so the lowest possible tube current (without compromising image quality) should be used with our recommended tube voltages. Thus, quantification of imaging dose should be an important part of system commissioning. Our recommended imaging parameters presented in **Table 5.3** result in an approximately 4 cGy imaging dose to an average size mouse with the Xstrahl SARRP system based on the user's manual, which states an imaging dose range between 1.2 cGy and 4.8 cGy. The manual of the PXi X-RAD SmART quotes a 'typical' imaging dose to be between 1 to 10 cGy to the center of a 30 mm thick small animal. MicroCT imaging dose to the various organs of small animals with varying imaging parameters in these commercial systems is not well established, and is currently being extensively examined in another study within our research group.

Due to the saturation of the Xstrahl SARRP detector, we were unable to obtain data with increased x-ray tube and current combinations higher than 80 kVp and 1 mA, and 60 kVp and 1.4 mA. In order to keep image noise lower than the recommended value of 55 HU, a minimum current-exposure ti***m***e of 240 mAs is recommended for the Xstrahl SARRP, and 180 mAs for the PXi X-RAD SmART. In an additional experiment, when the frame rate of the Xstrahl SARRP was increased from 6 to 12 fps, noise was lowered by 20%. It is also worth noting that Xstrahl SARRP images with voxel sizes of 0.275 mm and larger failed the spatial resolution test (MTF(0.2) $<$ 1.5 lp/mm). With the recommended voxel size of 200 μm, the highest achievable

spatial resolution would be 2.5 lp/mm. We have experimentally verified, that at 20% MTF, the practically achievable spatial resolution was approximately 1.75 lp/mm for most systems. Assuming the small sizes of mouse anatomical structures in the order of 300-400 μm (e.g. for skull and vertebrae thickness), we have decided to set the passing spatial resolution to 1.5 lp/mm, corresponding to resolving structures of 333 μm in size. It is important to have a high resolving power for bony structures not only for targeting and structure avoiding purposes, but also for dose calculations.

This work presents recommendations for imaging QA protocols for the two commercial systems for the benefit of approximately one hundred institutions owning them. We did not develop recommendations for QA imaging parameters for the two in-house small animal systems, because of their limited number of users and lack of multi-institutional data.

For the Xstrahl SARRP system, the standard imaging geometry (**Figure 5.3c**) instead of the more natural 'pancake' geometry (**Figure 5.3b**, phantom laying on the SARRP couch) is recommend for imaging QA with the Shelley phantom using the Xstrahl SARRP system. In the 'pancake' geometry, the phantom rotates with respect to a stationary source, causing photons to traverse the longest part of the phantom. This increased attenuation and scatter, causing photon starvation artifacts that resulted in poorer image quality: scanning in the 'pancake' geometry consistently produced poorer CT number linearity (i.e., R^2_p=0.976, R^2_s=0.992), and up to 40% lower SNR and 35% higher noise, when compared to the standard imaging geometry. While small animals are often imaged and irradiated in the 'pancake' geometry, CT number linearity, SNR, and noise are poorer and less reproducible compared to the standard geometry. For this reason, we recommend scanning the Shelley phantom using standard geometry for the purpose of accurately quantifying image quality over time. Additionally, failing spatial resolution and noise were due to large voxel sizes (>0.275mm), and insufficient tube current and scanning times, respectively. It should be noted that scanning small animals in the 'pancake' geometry would likely produce satisfactory image quality due to their smaller size compared to the Shelley phantom.

Quality control programs are a crucial part of the clinical radiotherapy process, and the same is true of the preclinical radiation therapy process. An important piece of a quality control program is having tolerances for the tests that are performed. Despite the fact that these commercial small animal systems have been available

for many years, there are no other (to our knowledge) studies which establish these specifications based on what can/is actually being achieved by these systems.

Users of the commercially available PXi X-RAD SmART and Xstrahl SARRP systems are encouraged to use QA imaging protocols summarized in **Table 5.5** for routine imaging QA with the Shelley phantom. With the recommended scanning protocols, the imaging tolerance levels presented in **Table 5.3** should be met for each test. Most importantly, a corrective action such as imaging system recalibration should be taken if tolerance levels cannot be met when the recommended imaging protocols are used.

5.5 Conclusions

We have developed the small animal phantom analyzer (SAPA), automated image analysis software, tailored to microCT image quality analysis of the Shelley Micro-CT MCTP 610 phantom. Thanks to the multi-institutional data acquisition facilitated by the AAPM Working Group on Small Animal Irradiator Devices, we have analyzed microCT image quality from eleven institutions with image-guided small animal irradiators, and recommended imaging protocols and tolerance levels for routine image quality assurance tests. This analysis provides a number of metrics to determine what is practically achievable for pre-treatment image quality in the interest of small animal radiotherapy. These metrics set a benchmark for what current users consider as acceptable quality, as well as present objective benchmarks to be met by updates to current and future small animal systems.

SAPA can be conveniently used to rapidly perform imaging quality assurance tests using the Shelley phantom on any image-guided small animal irradiator, as well as microCT scanners. Additionally, SAPA can accumulate results over time and display possible changes in imaging functionality from its original performance and/or from the recommended tolerance levels presented in this work. This allows for corrective action to be made should image quality degrade over time. Upon request, SAPA will be distributed to users of image-guided small animal irradiators.

5.6 Acknowledgments

I would like to thank Jessica Perez for first introducing me to and assisting me with using the PXi X-RAD SmART irradiator, and all of the researchers involved in acquiring the microCT images presented in this study, including James Stewart, Simon Vallires, and Paul DeJean. I would also like to thank those who permitted us to use their image-guided small animal irradiators for this study, namely Ross Berbeco, Jan Seuntjens, Laurence Court, and Cheryl Duzenli. The purchase of the Shelley phantom was supported by the AAPM Working Group on Conformal Small Animal Irradiator Devices. The presented work was partly supported by an NSERC Discovery Grant.

5.7 Summary

This chapter developed QA standards and tolerance levels for microCT imaging in conformal image-guided small animal irradiators. Optimal microCT imaging parameters for the two commercial image guided small animal irradiators were also established. While it is important to obtain high quality images within image-guided small animal irradiators, the dose delivered during these imaging procedures must also be taken into consideration. The next chapter will now determine the amount of imaging dose delivered in the commercial Xstrahl SARRP using MC methods.

Chapter 6

MicroCT Imaging Dose to Mouse Organs using a Validated Monte Carlo Model of the Small Animal Radiation Research Platform (SARRP)

"I've been back here all this time, can you believe it? I've been out since from the fall."

–Dinosaur Jr.

After establishing QA tolerance levels for obtaining high quality images in image-guided small animal irradiators, this chapter now delves into determining the dose delivered by these imaging protocols. The amount of microCT imaging dose delivered to various sized mice for a myriad of imaging parameters will now be examined. Quantifying the scattering contributions from the small confines of an image-guided small animal irradiator will also be examined.

6.1 Introduction

Preclinical studies are useful for advancing our understanding of radiation induced effects through translational research. Such studies may be carried out using image-guided small animal irradiators that use kilovoltage x-ray beams for both therapy and image guidance. Imaging is also used to observe changes to both tumor and normal tissues exposed to different radiotherapy fractionation schemes and techniques. MicroCT imaging dose to small animals from these irradiators, especially from serial scans, may be high enough to affect the immune system and biological pathways of the animal, resulting in changes to the experimental outcome and compromise the results of a study [30, 40, 198]. Imaging dose should thus be low enough to not interfere with the biological model and tumor growth, with whole-body radiation doses not showing deterministic effects below 10 cGy [193].

Previous studies have analyzed microCT imaging dose to mice with various imaging protocols and beam filtrations with non-commercial small animal irradiators [30, 32, 143, 183]. These studies investigated microCT imaging dose using cylindrical water phantoms, plastic phantoms, and heterogeneous mouse phantoms. Studies that included actual mice to establish dose to organs and tissues experimentally with various TLDs have been done [40,53,67,198]. MicroCT mouse organ dose from a dedicated GE microCT scanner to lung, bone, and soft tissue was previously established using MC simulations [32]. In that study, all bone and soft tissues were grouped together (except lung), and organ doses were approximated from spherical regions of interest within the organs.

This study investigates imaging dose delivered by the Small Animal Radiation Research Platform (SARRP, Xstrahl Inc., Suwanee, GA), one of the two commercial state-of-the-art image-guided small animal irradiators. MicroCT imaging dose to a mouse is calculated using a validated Monte Carlo (MC) model of the SARRP. Absorbed dose is established to eight different mouse organs and a subcutaneous tumor segmented using the entire 3-dimensional mouse volume obtained from a microCT scan. CT numbers of each organ were converted into mass densities using a mouse phantom with tissues segmented from the microCT mouse scan [15,16]. Organ dose is then calculated for 15-35 g mice using a voxelization method, in comparison to previous studies that reported microCT imaging dose to only a single mouse [32,40,159,183] and studies that used multiple mice but of approximately the same size [53, 67]. A

previous work similarly assigns material densities and segments organs for dose computations for the other commercial small animal irradiator, the PXi X-RAD SmART (PXi, North Brandford, CT) [159]. This work investigates dose delivered from the therapy beam, while our work focuses on imaging dose.

In addition, the scatter contribution to HVL measurement within the relatively small confines of the self-shielding cabinet is determined. Kilovoltage x-ray beam output correction factors rely on accurately obtaining HVL through only the primary beam in a scatter free environment [110,144] to accurately determine dose output using the AAPM TG-61 [136].

6.2 Materials and Methods

6.2.1 Xstrahl SARRP Irradiator

The SARRP operates at a SID of 35 cm with a dual x-ray tube focal spot of 3.0 mm (large) and 0.4 mm (small) for the 220 kVp therapy and 40-80 kVp imaging beams, respectively [186, 201]. MicroCT imaging is acquired in pancake geometry utilizing a stationary x-ray tube and detector with a 360° rotating couch, and is performed with 40-80 kVp imaging beams with 0.8 mm Be internal filtration and 1 mm Al added filtration [111]. The standard imaging protocol of our SARRP, which is not consistent for all SARRP units, consists of 60 kVp tube voltage, 0.8 mA beam current and 1-minute scanning time. The 220 kVp therapy beam can be collimated to 0.5 mm circular fields to 10 x 10 mm^2 square fields and is filtered with 0.15 mm Cu added filtration.

6.2.2 Absolute Dose and HVL Measurements

Absolute dose and HVL measurements were conducted to characterize the quality of our SARRP beams. Absolute dose measurements were obtained with a 0.6 cc PTW 30013 Farmer-type ionization chamber (PTW, Freiburg, Germany) for 220 kVp tube potential and 13 mA tube current and for 40, 50, 60, 70, and 80 kVp tube potential at 13, 12, 10, 9, and 8 mA tube current, respectively, with a one minute irradiation time

and open beam. According to the AAPM TG-61 [136], cylindrical type ionization chambers have a nearly constant energy response for energies in the range of 40 to 300 kVp, which made this type of chamber optimal for our study.

Measurements were taken at a 2 cm depth of a 30 x 30 x 5 cm^3 slab of solid water at isocenter (**Figure 6.1**), where dose was found using AAPM TG-61 protocol using the following equation described by [136],

$$D_{w,z=2cm} = MN_k P_{Q,cham} P_{sheath} \left[\left(\frac{\mu_{en}}{\rho} \right)^{w}_{air} \right]_{water}. \tag{6.1}$$

First and second HVL measurements were also acquired following the AAPM TG-61 protocol as best as possible within the small confines of the SARRP cabinet, where a PTW 31014 (0.015 cc) PinPoint chamber (PTW, Freiburg, Germany) was used for all HVL measurements. HVLs were acquired for 220, 40, 50, 60, 70, and 80 kVp tube potentials at 13, 13, 12, 10, 9, and 8 mA tube currents, respectively, with a two minute irradiation time. The SDD was set to 50 cm which was a practical measurement distance taking into account the space constraints of the SARRP cabinet. The gantry angle was set at 0° (12 oclock position), and attenuating materials were placed immediately below the head of the irradiator, held in place by a stand (**Figure 6.1a**). HVL was measured with open beams with Cu (220 kVp therapy beam) and Al (40 - 80 kVp imaging beams) filters. Polynomial interpolation in MATLAB (MathWorks Inc., Natick, MA) was used to determine the first and second HVLs from attenuation measurements.

6.2.3 Monte Carlo Simulations

SARRP Monte Carlo Model

A MC model of the SARRP was created in BEAMnrc [171] of the EGSnrc MC code [117,118], with dose computed in DOSXYZnrc [194]. The 220 kVp therapy and 40-80 kVp imaging beams were modeled and validated with depth dose and profile (therapy beam only) measurements in homogeneous and heterogeneous phantoms, described in **Appendix B**.

A schematic drawing of the MC model of the SARRP is shown in **Figure 6.2**, il-

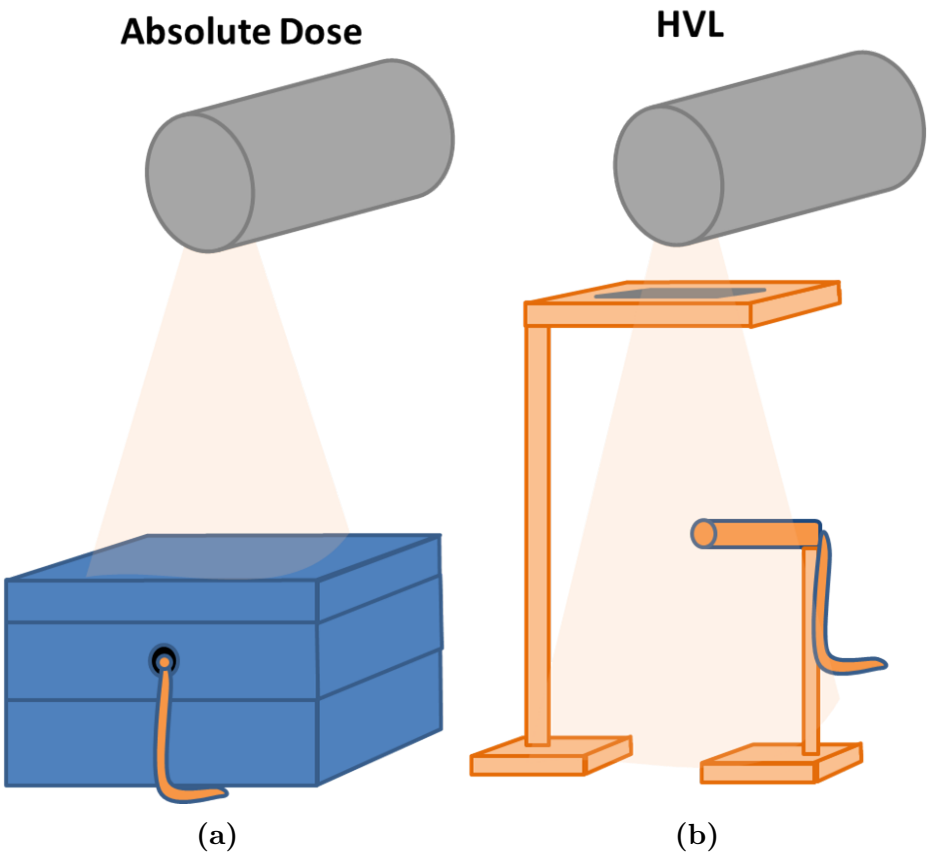

Figure 6.1: Experimental setup for a) absolute dose and b) HVL measurements.

lustrating the geometries used to approximate the actual components of the system. Photons were generated using 3 x 10^9 histories (1 x 10^{10} histories for HVL and mouse organ dose computations). For the therapy beam, phase-space files were scored immediately below the nozzle (30 cm source-to-phase space distance), and for imaging beams the phase-space files were scored immediately below the head of the irradiator (7.3 cm source-to-phase space distance).

MC output for all square nozzles were directly converted to dose rate in Gy/min from first-principles,

$$D(\text{Gy/min}) = \frac{MC \cdot I \cdot t}{1.60\,\text{x}\,10^{-19}\,\text{C}}, \tag{6.2}$$

where MC is the MC output in Gy/particle, I is the tube current in Amperes, t is the exposure time in seconds, and divided by the charge of an electron in Coulombs.

However, all smaller circular nozzles ($\leq$ 1 mm diameter) were normalized to the first depth dose data point at 0.14 mm, creating a nozzle-size and SSD dependent scale factor that was applied to all circular nozzle depth doses and profiles. All MC simulations ran on an Intel Core i7-6700HQ CPU 2.6 GHz quad-core personal laptop.

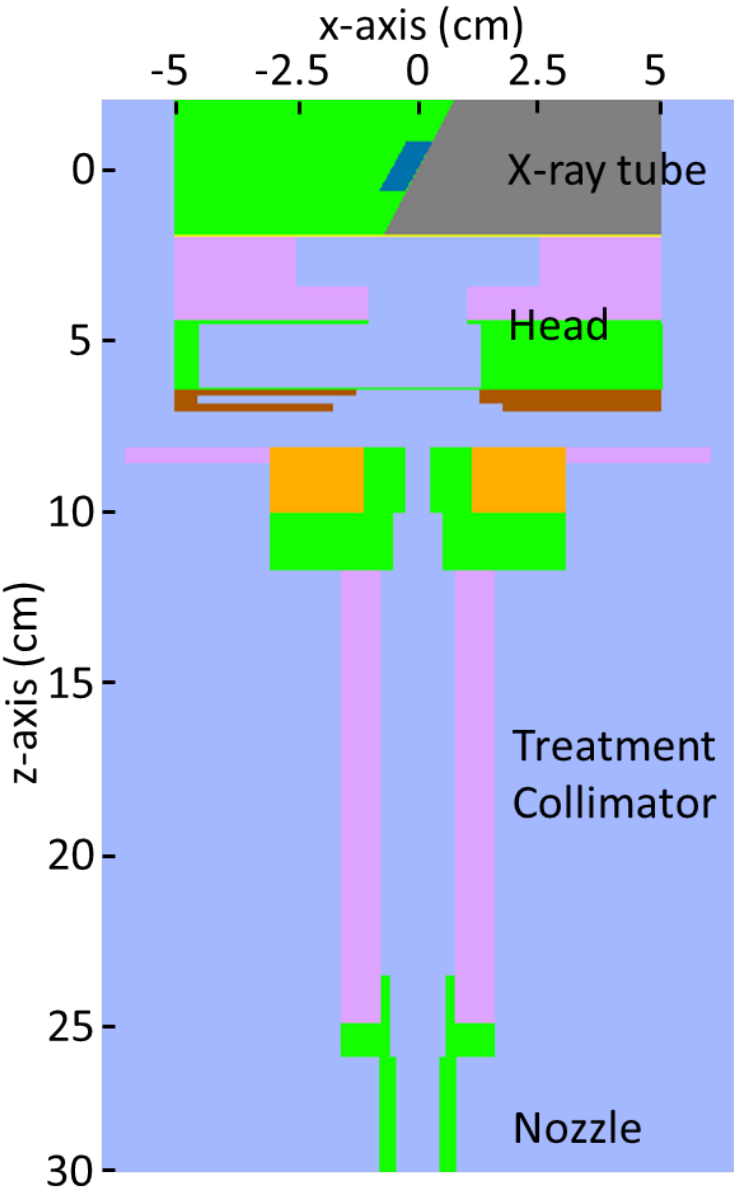

Figure 6.2: Our BEAMnrc in-house MC model of the SARRP, illustrating the x-ray tube, internal, and external collimation.

Absolute Dose and HVL

Absolute dose was computed using a CM CHAMBER that was inserted into BEAMnrc at a 2 cm depth in a virtual 30 x 30 x 4 cm^3 water phantom. A 35 cm SDD was used with the same tube voltages used as measurement: 40, 50, 60, 70, 80, and 220 kVp. Dose was calculated in a 1 cm^3 cube voxel approximating the ionization chamber.

First and second HVLs were calculated in BEAMnrc by creating attenuating material using the SLAB CM directly below the phase space file, and placing a CHAMBER CM at a 50 cm SDD. In the same fashion as measurement, output of the o***p***en beam for each tube potential was first calculated. Then Cu SLAB CM (220 kVp therapy beam) and Al SLAB CM (40 - 80 kVp imaging beams) were added with increasing thicknesses until one-half and one-fourth of the outputs of the open beams were achieved, for the first and second HVLs, respectively.

Imaging Dose to Mouse Organs

We scanned a 32-g female NOD.CB17-PRKDCSCID/J strain mouse (The Jackson Laboratory, Bar Harbor, Maine) with the SARRP microCT using a 60 kVp, 0.8 mA and 4-minute imaging protocol with a 0.275 x 0.275 x 0.275 mm^3 voxel size. The mouse was approximately 2.4 x 2.6 cm^2 in diameter (central-axis cross-section) and 9.1 cm in length (nose to base of tail). An orthotopic tumor was implanted on its left flank, which was approximately 9.8 x 10.4 mm^2 in diameter, and 6.9 mm in length. We segmented the microCT image (**Figure 6.3**) in OsiriX (Pixmeo SARL, Switzerland) into nine tissues (**Figure 6.3b** and **6.3c**): tumor, cranium, ribs, spine, brain, kidney, heart, lungs, and body (external contour). The mean mass densities of each tissue based on a microCT calibration curve were then calculated and are presented in **Table 6.1**. This was done to obtain mouse-specific mass densities, in contrast to using the ICRU-44 human density values [76], which have been known to deviate from mouse tissues [16].

Table 6.1: Mouse-specific organ mean mass densities.

Mouse Organ	Cranium	Ribs	Spine	Brain	Kidney	Heart	Lungs
Mass Density (g/cm^3)	1.82	1.44	1.61	0.99	1.16	0.97	0.58

The mouse-model was then input into DOSXYZnrc for imaging dose computation to the entire mouse volume, and evaluated for both pancake and standard imaging geometries within the SARRP (**Figure 6.3d** and **6.3e**). Source type 8 was used in DOSXYZnrc to have the imaging beam rotate 360° around the mouse. To obtain dose D_α for any combination of tube current I_α and imaging time t for a given tube voltage, one may use the following equation,

$$D_\alpha(\text{cGy}) = D_\beta(\text{cGy})\frac{I_\alpha t_\alpha}{I_\beta t_\beta}, \tag{6.3}$$

where D_β is a reference imaging dose in cGy for a given beam energy (kVp), and $I_\beta t_\beta$ is the product of the reference tube current and imaging time, also known as current-exposure time (mAs). The 40-80 kVp imaging beam doses were then established in DOSXYZnrc, and tabulated for our reference imaging protocol (our standard protocol) of 0.8 mA tube current and 60 second imaging time ($I_\beta t_\beta$=48 mAs).

Imaging Dose for Varying Mouse Sizes

Organ dose is influenced by mouse size and weight, thus simulations were performed modeling mice weights ranging from 15 to 35 g (7.1 to 9.4 cm long, respectively), using a technique similar to Boone *et al.* 2004. To compare the effects of only varying mouse size in a controlled and systematic way, free from other biological variables, voxel size was varied according to a scaling factor κ, defined as

$$\kappa = \sqrt[3]{\frac{m'}{m}} \tag{6.4}$$

where $m = 32$ g and is the mass of our mouse shown in **Figure 6.3**, and m' is the desired mouse mass. Scaling factors are applied to the entire volume of our 32 g mouse to simulate 15, 20, 25, 30, and 35 g mice (7.1 to 9.4 cm mouse length range) and input into DOSXYZnrc for organ dose computation for both pancake and standard imaging geometries.

To test the validity of this approach we measured the mass, diameter in two dimensions (central-axis cross-section), and length (nose to base of tail) of different mice of

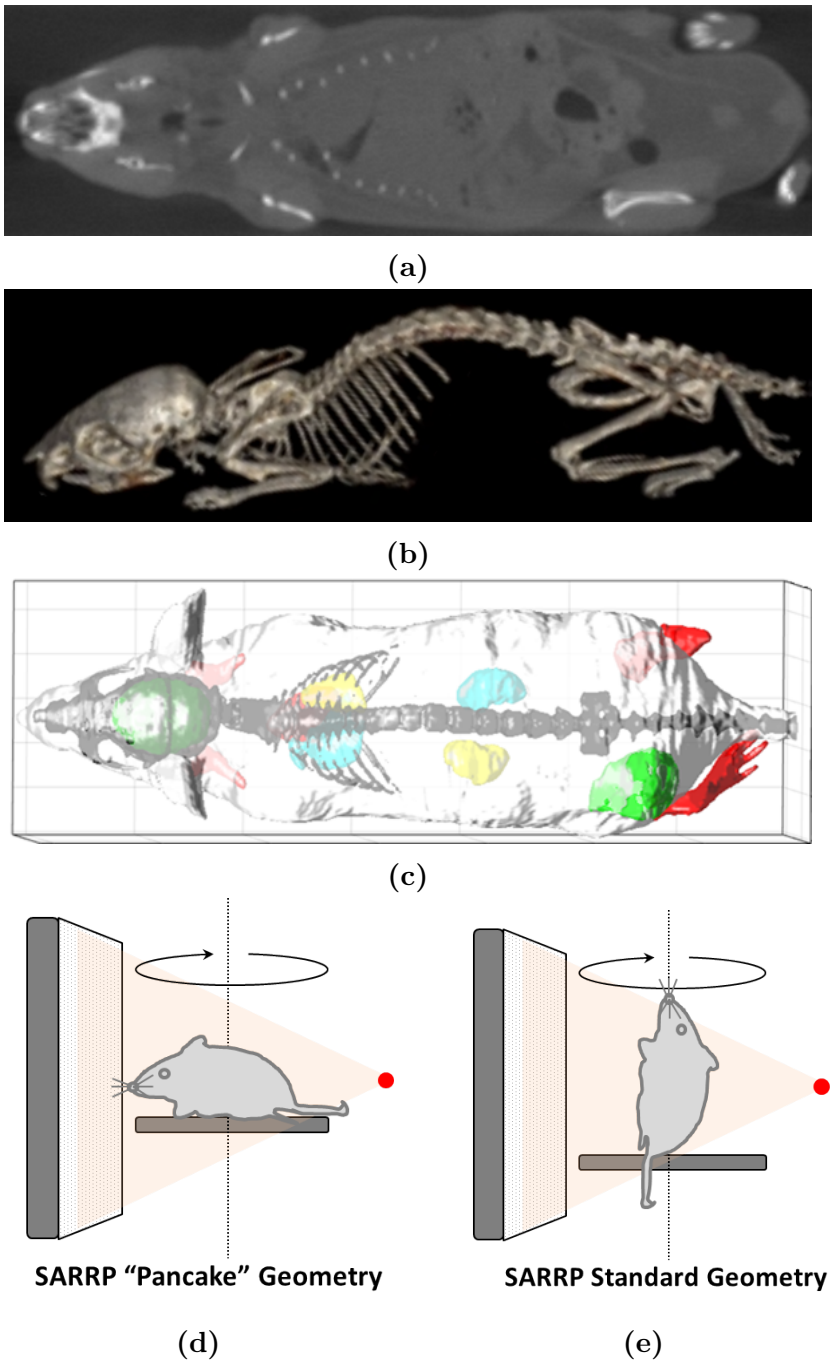

Figure 6.3: a) Micro-CT scan of a mouse obtained within the SARRP was used in b) OsiriX to segment tissues (segmented skeletal system shown), including c) body, tumor, cranium, ribs, spine, brain, kidney, heart, and lungs of the entire mouse volume. Micro-CT imaging dose was calculated for the mouse-model in d) pancake geometry (lying on couch) and e) standard geometry (standing on couch) with a stationary source and detector as the table rotates 360.

the same aforementioned strain, ranging from 20 to 27 g, and compared the dimensions to those of our voxel-rescaled mice for the same weights. Maximum deviation between dimensions of voxel-rescaled and actual mice for each weight was 3 mm in diameter, and 2 mm in length.

6.3 Imaging Dose with Off-Center Positioning Shifts

Imaging isocenter in the egsphant mouse phantom in DOSXYZnrc was shifted by 1 and 3 cm in the ± x-, y-, and z-directions (left/right, superior/inferior, posterior/anterior, respectively) from the center of the mouse to quantify the effects of imaging dose with off-center positioning shifts/misalignment during microCT imaging. Dose to mouse organs were established in the pancake geometry following the methods applied to the 32 g mouse.

6.4 Scatter Contributions to HVL

To analyze the effect of changing beam quality due to possible scatter contributions to HVL for the 220 kVp therapy beam, we ran BEAMnrc MC simulations while modeling the internal walls of the SARRP. Only the walls (PYRAMIDS and CONESTAK CMs) and the bottom stage (CONESTAK CM) were modeled. HVL was both measured and calculated at a 50 cm SDD, which was the practical measurement distance taking into account the space constraints of the SARRP. These HVL measurement and calculations were compared to a DOSXYZnrc simulation of the 100 cm SDD, scatter free narrow-beam (3 cm beam diameter) geometry recommended by the AAPM TG-61 protocol modeled without the internal walls.

6.4.1 Image Noise Considerations

To maintain equivalent image noise across the studied tube voltages, microCT scans of a mouse were obtained using 40, 50, 60, 70, and 80 kVp tube voltages with 60 second scan times and a 0.8 mA tube current. Using analysis software Fiji [176], the standard deviation of four ROIs were averaged in soft tissue within the same

slice of each scan to obtain noise. Using the 60 kVp noise as a baseline, we obtain a noise-scaling factor η_λ defined by

$$\eta_\lambda = \left(\frac{N_\lambda}{N_{60}}\right)^2, \tag{6.5}$$

where N_λ is the noise of any given tube voltage and N_{60} is the 60 kVp noise. For the 40-80 kVp noise to match that of the 60 kVp imaging beam, the current-exposure time of each imaging beam (mAs_λ) must be $\eta_\lambda \cdot mAs_{60}$. Since current-exposure time directly relates to imaging dose, the dose for each tube voltage scales linearly with η_λ. To validate this approach, η_λ was applied to three separate 60 s scans at 50, 60, and 70 kVp tube voltages, and noise was measured

6.5 Results

6.5.1 Absolute Dose and HVL

The results of absolute dose measurements and MC simulations are displayed in **Table 6.2**. The differences between measured and simulated absolute doses were 2.3% and 2.9% for the 220 kVp therapy beam and 40–80 kVp imaging beams, respectively, demonstrating good agreement between MC simulations and measurements for all energies.

Table 6.2: Measured and simulated absolute dose rate of the 220 kVp therapy (Gy/min) and 40-80 kVp imaging beams (cGy/min).

Tube Voltage (kVp)	Tube Current (mA)	Measured (cGy/min)	MC (cGy/min)	% Difference
220	13	3.63 Gy/min	3.55 Gy/min	2.2%
80	1	5.75	5.63	2.2%
70	1	4.56	4.44	2.4%
60	1	3.40	3.30	2.9%
50	1	2.25	2.25	0.4%
40	1	1.23	1.23	0.3%

HVL measurement and simulation results are displayed in **Table 6.3**. Simulations for all beam energies for the first and second HVLs were in good agreement with

measurement, with the largest deviations being 6% (0.04 mm Cu) for the 220 kVp therapy beam and 1% (0.02 mm Al) for all imaging beams.

Table 6.3: Measured and MC-simulated HVL values as a function of tube voltage. Note that HVL is in mm Cu for the treatment beam, and in mm Al for imaging beams.

1^{st} HVL (mm Al)	220 kVp	80 kVp	70 kVp	60 kVp	50 kVp	40 kVp
Measured	0.67 mm Cu	1.53	1.34	1.17	1.02	0.83
MC	0.71 mm Cu	1.54	1.34	1.18	1.04	0.83
% Difference	6.0%	0.7%	0.4%	0.9%	2.0%	0.6%
2^{nd} HVL (mm Al)	220 kVp	80 kVp	70 kVp	60 kVp	50 kVp	40 kVp
Measured	2.24 mm Cu	4.50	3.68	3.17	2.66	2.03
MC	2.31 mm Cu	4.48	3.66	3.16	2.65	2.01
% Difference	3.1%	0.4%	0.5%	0.3%	0.4%	1.0%

6.5.2 Imaging Dose to Mouse Organs

Imaging doses to nine mouse tissues are displayed in **Table 6.4** for 40–80 kVp imaging beams for the SARRP pancake imaging geometry for a 32 g mouse. For comparison, 60 kVp imaging dose is also listed for the standard imaging geometry. Mouse dimensions are reported as diameters (along the central-axis cross-section of the mice) and length (nose to base of tail).

For a standard protocol of 60 kVp, 0.8 mA, 1 minute microCT scan, maximum mean organ doses to bony and non-bony structures were 9.6 cGy (cranium) and 3.3 cGy (tumor), respectively. Maximum dose was in the cranium, and was as high as 20 cGy for both imaging geometries. We found that mean body dose was 18% higher in standard geometry compared to pancake geometry. Dose distributions within the mouse were different between imaging geometries, as the top of the cranium received higher dose than the bottom in pancake geometry, while the cranium dose was more uniform in standard geometry (**Figure 6.4**). Body dose distributions in pancake geometry were non-uniform, with skin dose 50% higher than dose in the center of the body. Body dose distributions in standard geometry were more uniform, with skin dose 25% higher than dose in the center of the body for all tube voltages.

Table 6.4: Mean organ doses (cGy) within the SARRP for a 32g mouse for 40-80 kVp imaging beams, with a standard protocol of 0.8 mA tube current and 60 second imaging time in pancake geometry, and mean organ doses for the 60 kVp imaging beam in standard geometry with its corresponding difference from pancake geometry. Note, percentage difference between standard (x) and pancake (y) geometries are calculated by, (x - y)/((x + y)/2)*100.

32g Mouse									
2.4 x 2.6 x 9.1 cm^3	Body	Tumor	Cranium	Ribs	Spine	Brain	Kidney	Heart	Lung
40 kVp	1.40	1.49	3.68	3.41	2.95	1.14	1.06	1.00	0.97
50 kVp	2.34	2.37	6.58	5.95	5.19	1.99	1.83	1.73	1.72
60 kVp	3.32	3.27	9.64	8.59	7.52	2.90	2.64	2.49	2.52
70 kVp	4.32	4.17	12.74	11.23	9.88	3.85	3.47	3.30	3.35
80 kVp	5.36	5.08	15.87	13.88	12.26	4.84	4.35	4.14	4.23
60 kVp (Standard)	3.98	3.57	11.21	10.99	9.74	3.30	3.37	3.38	3.32
Difference (%)	18.1	8.8	15.1	24.5	25.7	12.9	24.3	30.3	27.4

6.5.3 Imaging Dose for Varying Mouse Sizes

SARRP microCT imaging dose to organs of 15 - 35 g mice for 40–80 kVp tube voltages are presented in **Table 6.5**. For a given tube voltage, dose to organs decreases by 2 - 6% for every 5 g increase in mouse size, with a greater difference seen at lower tube voltages. For a given mouse size, every 10 kVp increases dose to organs by approximately 43, 31, 24, and 19% for 40 to 50, 50 to 60, 60 to 70, and 70 to 80 kVp, respectively. Percentage differences between pancake and standard geometries are approximately the same as reported in **Table 6.4** for all tube voltages.

6.5.4 Imaging Dose with Off-Center Positioning Shifts

Differences in microCT imaging dose with off-center positioning shifts, including body, tumor, and maximum differences of all organs, are summarized in **Table 6.6**. Maximum percentage differences to the body, tumor, and mean organ doses are 0, 1.5, and 0.8%, respectively, for a 1 cm shift, and 0.6, 4.9, and 3.5%, respectively, for a 3 cm shift. Percentage differences in imaging dose between shifted (x) and non-shifted (y) simulations are calculated by, ((x - y)/y)*100.

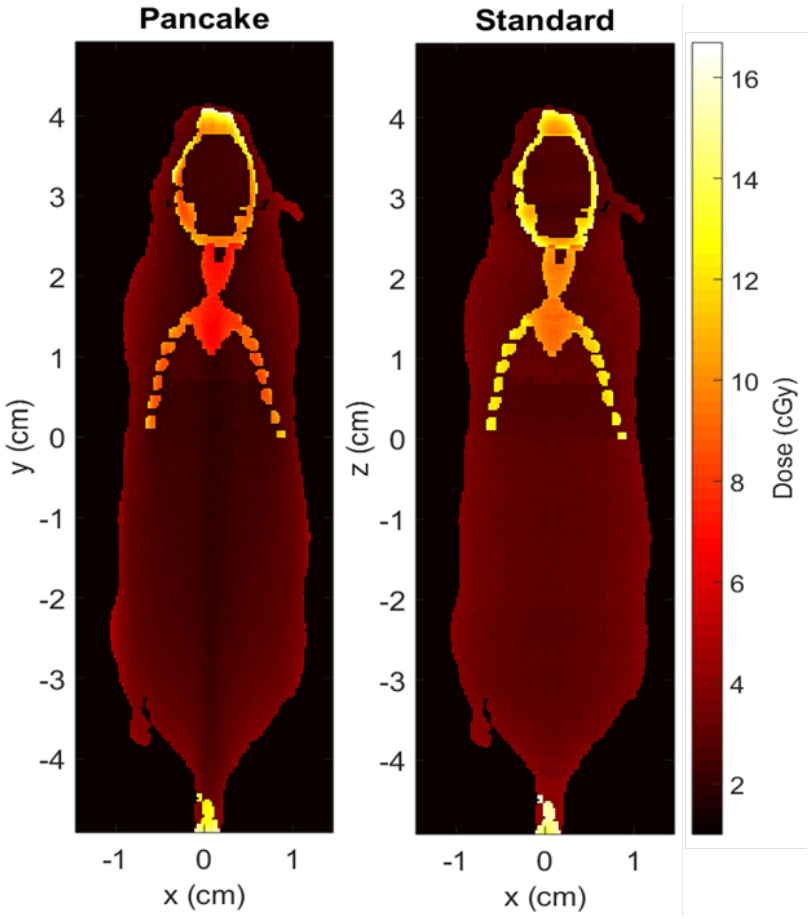

Figure 6.4: MC-calculated dose distribution to a 32-g mouse for our SARRP standard microCT imaging protocol of 60 kVp, 0.8 mA, and 1 minute scan time, for pancake and standard imaging geometries.

6.5.5 Image Noise Considerations

Based on microCT images of the same mouse acquired at the studied tube voltages, noise, noise-scaling factors (obtained using **Equation 6.5**), and corresponding dose to body are presented in **Table 6.7**. Noise-scaling factors can be applied to both current-exposure time and organ doses (**Table 6.5**), in order to maintain equivalent image noise across tube voltages. For example, for a 60 second scan to a 20 g mouse, the scaled tube current would be $\eta_{40} \cdot 0.8$ mA $= 2$ mA, with resulting body dose of, $\eta_{40} \cdot 1.50$ cGy $= 3.75$ cGy.

Table 6.5: Mean SARRP microCT imaging doses (cGy) for 15–35g mice acquired with 40-80 kVp tube voltages with a standard protocol of 0.8 mA tube current and 60 second imaging time in pancake geometry. **Equation 6.3** can be used to convert imaging dose for any current-exposure time for a given tube voltage.

15g Mouse									
1.9 x 2.0 x 7.1 cm^3	Body	Tumor	Cranium	Ribs	Spine	Brain	Kidney	Heart	Lung
40 kVp	1.57	1.60	4.37	4.01	3.47	1.32	1.24	1.15	1.16
50 kVp	2.59	2.53	7.62	6.83	5.94	2.26	2.07	1.95	1.99
60 kVp	3.64	3.46	10.98	9.71	8.49	3.25	2.95	2.78	2.87
70 kVp	4.70	4.39	14.36	12.56	11.04	4.26	3.84	3.65	3.77
80 kVp	5.79	5.34	17.73	15.41	13.59	5.31	4.77	4.55	4.71
20g Mouse									
2.1 x 2.2 x 7.8 cm^3	Body	Tumor	Cranium	Ribs	Spine	Brain	Kidney	Heart	Lung
40 kVp	1.50	1.55	4.10	3.78	3.27	1.25	1.17	1.09	1.09
50 kVp	2.50	2.47	7.22	6.50	5.66	2.16	1.98	1.86	1.89
60 kVp	3.52	3.39	10.47	9.28	8.12	3.12	2.83	2.67	2.74
70 kVp	4.56	4.31	13.73	12.06	10.60	4.11	3.70	3.51	3.61
80 kVp	5.63	5.25	17.02	14.84	13.09	5.13	4.61	4.39	4.53
25g Mouse									
2.2 x 2.4 x 8.4 cm^3	Body	Tumor	Cranium	Ribs	Spine	Brain	Kidney	Heart	Lung
40 kVp	1.45	1.52	3.90	3.61	3.12	1.20	1.12	1.05	1.03
50 kVp	2.42	2.42	6.91	6.24	5.43	2.08	1.91	1.80	1.81
60 kVp	3.43	3.33	10.07	8.95	7.84	3.01	2.74	2.59	2.63
70 kVp	4.45	4.24	13.26	11.67	10.26	3.98	3.59	3.41	3.49
80 kVp	5.50	5.17	16.47	14.39	12.70	5.00	4.49	4.28	4.39
30g Mouse									
2.3 x 2.5 x 8.9 cm^3	Body	Tumor	Cranium	Ribs	Spine	Brain	Kidney	Heart	Lung
40 kVp	1.41	1.50	3.74	3.46	3.00	1.15	1.08	1.01	0.99
50 kVp	2.36	2.38	6.67	6.03	5.25	2.01	1.85	1.74	1.74
60 kVp	3.35	3.28	9.76	8.68	7.60	2.93	2.66	2.52	2.55
70 kVp	4.36	4.19	12.88	11.34	9.98	3.88	3.50	3.33	3.39
80 kVp	5.40	5.11	16.02	14.02	12.38	4.88	4.39	4.18	4.27
35g Mouse									
2.5 x 2.7 x 9.4 cm^3	Body	Tumor	Cranium	Ribs	Spine	Brain	Kidney	Heart	Lung
40 kVp	1.38	1.47	3.61	3.35	2.89	1.12	1.04	0.98	0.95
50 kVp	2.31	2.35	6.46	5.85	5.10	1.96	1.80	1.70	1.69
60 kVp	3.28	3.24	9.49	8.45	7.41	2.86	2.60	2.46	2.48
70 kVp	4.28	4.14	12.55	11.06	9.74	3.80	3.42	3.26	3.30
80 kVp	5.31	5.05	15.65	13.70	12.10	4.79	4.30	4.10	4.18

Table 6.6: Percentage imaging dose differences from 1 and 3 cm off-center positioning shifts.

	Body (%)	Tumor (%)	Organs (%)
Shift Direction	1cm / 3cm	1cm / 3cm	1cm / 3cm
Superior	0 / -0.3	0 / 0	-0.7 / -2.5
Inferior	0 / -0.6	-0.3 / -0.3	-0.3 / -3.5
Left	0 / -0.3	-0.9 / -2.5	-0.8 / -1.5
Right	0 / 0.3	0.6/ 2.5	0.7 / 2.5
Posterior	0 / -0.6	-1.5 / -4.9	-0.4 / -1.6
Anterior	0 / -0.6	1.2 / 3.1	-0.8 / -1.9

Table 6.7: Noise for microCT mice images acquired at 40-80 kVp, 0.8 mA, and 60 second scan times, with noise-scaling factors (η_λ). Also presented are scaled tube currents to match imaging noise across tube voltages for a 60 second scan, with corresponding scaled dose to body for a 20 g mouse.

	40 kVp	50 kVp	60 kVp	70 kVp	80 kVp
Image Noise (HU)	142	103	90	81	65
Noise-Scaling Factor (η_λ)	2.5	1.3	1.0	0.8	0.5
Scaled Tube Current (mA)	2	1	0.8	0.6	0.4
Scaled Dose to Body (cGy)	3.75	3.25	3.52	3.65	2.82

6.5.6 Scatter contributions to HVL

MC-calculated HVL with scatter contribution due to the internal walls of the SARRP for the 220 kVp therapy beam at a 50 cm SDD was HVL = 0.71 mm Cu. MC simulation of the 100 cm SDD, scatter free narrow-beam geometry recommended by the AAPM TG-61 protocol resulted in HVL = 0.75 mm Cu (**Table 6.8**), causing a 5.3% difference in HVL determination. This is also compared to a measured HVL of 0.67mm Cu at a 50 cm SDD, which is a 10.7% difference from the MC simulated AAPM TG-61 protocol geometry. MC simulated HVLs were calculated with a 0.4% statistical uncertainty.

6.6 Discussion

MicroCT imaging dose to the body of the mouse was 18% less in pancake geometry than in standard geometry due to photon attenuation, where photons transverse a

greater thickness of tissue in pancake compared to standard geometry. Note, however, that the photon attenuation may lead to degradation in microCT image quality in larger animals when scanning in pancake geometry [111].

The tumor located on the left flank of an average 20 g mouse received an imaging dose of 3.4 cGy using our standard SARRP microCT imaging protocol of 60 kVp, 0.8 mA, and 1 minute scan time. This is likely not enough dose to compromise tumor growth and outcome as both total body and tumor dose was below 10 cGy [193]. Tumor imaging dose of 3.4 cGy is also much lower than the common 1 to 20 Gy treatment doses given in small animal irradiators to treat mouse tumors [78, 80, 81]. However, increasing current-exposure combinations above 323, 203, 147, 116, and 95 mAs for 40, 50, 60, 70, and 80 kVp tube voltages, respectively, will increase the tumor and body doses above 10 cGy. For typical scan parameters of 60 kVp and 0.8 mA, three serial scans or a single three-minute scan would result in tumor and body doses above 10 cGy for an average size 20 g mouse. Interestingly, studies giving 10 and 30 cGy radiation doses to mouse tumors have been shown to protect endothelial cells against apoptosis and promote tumor growth [188,211], further establishing that imaging dose to mice tumors should be less than 10 cGy to not affect the biological processes in the tumor. A common tumor location and scan protocol was chosen for this study on the basis that our tumor and organ dose results would be relevant to the greatest number of researchers performing translational research. For orthotopic tumors, tumor dose will likely be similar to the tissue/organ that surrounds it.

Table 6.8: MC-calculated HVL for the scatter free AAPM TG-61 geometry, measured HVL, and MC-calculated HVL with the internal walls of the SARRP, completed for the 220 kVp therapy beam.

	100 cm SDD MC AAPM TG-61	50 cm SDD MC with Walls	50 cm SDD Measurement
HVL (mm Cu)	0.75	0.71	0.67

We found that smaller mice under the same conditions receive higher imaging dose, approximately 2 - 6% for every 5 g weight decrease, and that a 10 kVp increase from the standard 60 kVp tube voltage results in a 24% increase in imaging dose. If a users imaging protocol for single or serial scans produces tumor or body doses above 10 cGy, one may reduce tube voltage from 60 to 50 kVp (if resulting imaging quality is satisfactory) to decrease the mouse imaging dose by 31%, or reduce current-exposure

time. A 1 or 3 cm positioning shift/miss-alignment in imaging from the center of the mouse will not greatly affect body or organ doses, but may increase flank tumor dose by more than 5% if tumor is positioned at the center of the beam.

Accuracy in segmentation may be limited if imaging resolution is lower than the size of the organ being segmented. The microCT scan resolution we used was 0.275 x 0.275 x 0.275 mm^3, where the dimensions of the smallest non-bony organ was approximately 4.5 x 5 x 4 mm^3, and thus partial volume effects would have a negligible effect on overall mean dose to non-bony organs analyzed. For bony structures, the smallest segmented volume was approximately 0.3 x 0.5 x 0.4 mm^3, where our scanning resolution was 0.275 mm. Partial volume effects would have a minimal effect on overall mean dose to bony organs analyzed. Increasing resolution further would likely minimally affect mean organ doses, add computation time, and result in greater image noise. Previous studies used microCT images (or down-sampled images due to large computation times) with a 0.4 x 0.4 x 0.4 mm^3 voxel resolution [32, 159, 183].

Due to modeling limitations in BEAMnrc, not all components of the inside of the SARRP cabinet were modeled in the HVL study, and may explain the difference between experimentally measured and MC-calculated HVL at a 50 cm SDD in the presence of the inner walls. MC-calculated HVL using the AAPM TG-61 recommended geometry at a 100 cm SDD produced an HVL 11% higher than experimental measurement at a 50 cm SDD. This produced changes to the HVL-dependent correction factors in the AAPM TG-61, i.e., the mass energy-absorption coefficient ratio, backscatter factor for the in-air method, and chamber correction factor for the in-phantom method. This resulted in changes to absorbed dose to water calculations of 0.5% (in-air method) and 0.3% (in-phantom method) for both open and 10 x 10 mm^2 collimated beams. This illustrates that the change in HVL due to scatter has a minimal effect on absorbed dose calculations for the 220 kVp therapy beam. MC-calculated HVL with and without the internal shielding of the SARRP at a 50 cm SDD were identical, which is in agreement with previous studies of cabinet irradiators [11,144]. This suggests that a large portion of scatter is produced within the head of the irradiator for the relatively short SDD, rather than backscatter from internal walls.

6.7 Conclusions

Our MC model was used to establish imaging dose to 15 - 35 g mouse organs for 40–80 kVp imaging beams using a segmented microCT scan. The standard 60 kVp scan protocol acquired with 0.8 mA tube current and 1-minute imaging time for a 20 g mouse resulted in a mean body dose of 3.5 cGy, which is within a whole body dose limit of 10 cGy for preventing deterministic effects. However, current-exposure combinations above 323, 203, 147, 116, and 95 mAs for 40, 50, 60, 70, and 80 kVp tube voltages, respectively, will increase the both the body and tumor doses above 10 cGy. Three serial scans or a single three minute scan will also result in body and tumor doses above 10 cGy. HVL measurements modeling the internal walls of the SARRP resulted in a 0.5% change to absorbed dose calculations with respect to the scatter-free geometry recommended by the AAPM TG-61 protocol, which shows that measuring HVL within the SARRP cabinet is acceptable. Upon request, our validated therapy and imaging phase-space files of the SARRP will be distributed.

6.8 Acknowledgments

We would like to thank Eisa Alyaqoub for his contributions toward tissue segmentation of our microCT scan, Samantha Van Nest for her invaluable knowledge and assistance with the mice used in this study, and Bo Lu from the University of Florida for analyzing film data. This work was partly supported by an NSERC Discovery Grant and the Canada Research Chair program.

6.9 Summary

This chapter established imaging dose to mouse organs using a validated MC model of the Xstrahl SARRP, including quantifying the effects of scatter from the internal walls on animal therapy dose determination. The MC model was also extensively validated with a series of homogeneous and heterogeneous phantom measurements found in **Appendix B**. While the previous chapter established image quality standards in image-guided small animal irradiators and this chapter determined the dose delivered

from such imaging parameters, the next chapter will merge these two chapters by establishing imaging dose to mouse organs based on varying microCT image quality scans of a mouse. The next chapter will now compare the visual image quality for a large range of microCT image quality scans of a mouse with the corresponding organ doses conveniently reported alongside the respective images.

Chapter 7

MicroCT Imaging Dose to Mouse Organs as a Function of Imaging Protocol

"Still when I see branches in the wind, the tumultuous place where I live, calls out revealing, 'Can you see the river in the branches?'"

–Mount Eerie

Chapter 5 described image quality standards and tolerance levels for the QA of image-guided small animal irradiators. MicroCT imaging dose to mouse organs was then presented in Chapter 6 for a commercial image-guided small animal irradiator. This established both the dose to organs and the imaging protocols necessary to keep whole body imaging dose under 10 cGy to prevent deterministic radiation effects from occurring [109]. This chapter aims to combine these two studies to report the microCT dose to mouse organs as a function of imaging protocol with image quality defined by noise. This will give users of image-guided small animal irradiators a baseline for what imaging dose is being given for varying image quality scans. This may guide the user to make informed decisions regarding the balance of imaging noise and low imaging dose, especially important for studies requiring serial microCT scans where imaging dose will be compounded.

7.1 Introduction

The microCT imaging parameters used to obtain images of mice within image-guided radiation therapy (IGRT) systems have been largely overlooked in regards to the amount of imaging dose given for varying image quality scans. A large portion of users of commercial image-guided small animal irradiators, specifically the SARRP, chose microCT imaging parameters (kVp, mAs, fps) based on what Xstrahl, the company that manufactures and installs the SARRP, recommends. Many institutions that employ the SARRP use a standard imaging protocol consisting of a 60 kVp tube voltage, 60 second scan time and 0.8 mA $\pm$0.2 (~48 mAs), and 6 fps frame rate, because this protocol is programed into the imaging software. To the author's knowledge, there are currently no published studies providing any quantitative evidence on why this may or may not be the optimal imaging parameters. Many people use this protocol without questioning, with few institutions conducting studies on which imaging parameters are best for their specific studies, and almost none documenting a comprehensive analysis of imaging dose for varying imaging parameters outside of Boone *et al* 2004 [30] and Johnstone and Bazalova-Carter 2018 [109]. This chapter expands the latter study by now incorporating mouse microCT images with the corresponding absorbed dose to organ values obtained in the Xstrahl SARRP.

7.2 Materials and Methods

7.2.1 MicroCT Scanning and Normalization

MicroCT images were acquired in the SARRP with the 32 g mouse of Chapter 6 and presented in the axial and coronal planes. During the same study, a smaller 20 g mouse was also scanned but not used for the study. Both 32 and 20 g mice were female NOD.CB17-PRKDCSCID/J strain mice (The Jackson Laboratory, Bar Harbor, Maine) with dimensions (length, width, height) of 9.1 x 2.4 x 2.6 cm^3 and 7.8 x 2.1 x 2.2 cm^3, respectively. This strain of mice are immune deficient and are unique in that they have a genetic DNA repair mutation that makes them more sensitive to ionizing radiation, accept xenogeneic grafts, and are ideal for cell transfer experiments. Those who use this strain of mice must know they are more radiosensitive and should

take this into consideration for their studies. Both mice also had flank tumors of approximately 1 cm in diameter. Axial, coronal, and sagittal planes are presented in this chapter to give the reader a complete picture of mouse microCT image quality in all three dimensions. The two mice used in this chapter were scanned immediately after being sacrificed during another study [80] so that the internal organs were still representative of a live mouse. The mice were scanned with various imaging protocols ranging from 40-80 kVp tube voltages, 24-288 mAs current-exposure times, and 6-12 fps frame rates. The noise from all presented images including the corresponding microCT imaging dose absorbed to the following tissues and organs are reported: body, tumor, cranium, ribs, spine brain, kidney, heart, and lungs. MicroCT scans were acquired with a 0.275 mm^3 voxel size.

Since microCT scans taken within the SARRP are currently not normalized to appropriate HUs, each original data set contained different pixel values and could not be directly compared to one another. In order to properly compare data sets, HUs for all images were normalized in Matlab (The Mathworks, Nattick, MA). HU normalization was completed by in-house Matlab code written to obtain air and soft tissue ROIs at approximately the same locations for every scan. For each scan, the central slice was used with the location of air taken outside of the mouse, and the location of water ROIs displayed in **Figure 7.7**. The raw a***i***r and soft tissue pixel numbers were polynomial fitted to -1,000 and 0 HUs, respectively, with the fit applied to all pixel values for a respective scan using polynomial evaluation.

Using Fiji [176], all data sets were then applied the same window and level values of 4969 and 2520, respectively. All images presented in this chapter are of the same central slice to produce a consistent image comparison across all data sets. Noise measurements were obtained in Fiji and acquired within the same central slice for all data sets of a given comparison. A 4 mm diameter circular ROI was used within soft tissue with noise averaged over four ROI measurements (ROI locations illustrated in **Figure 7.7**). Uncertainty in noise measurements was $\pm 7\%$ as determined by acquiring multiple ROI values in the same region to quantify the variation in signal, as there were relatively abrupt signal changes within the soft tissue. Suboptimal imaging noise will be defined as imaging noise > 55 HU in soft tissue, as it is recommended to keep noise below this tolerance level to keep MC dose calculation accuracy to within 5% [16, 111], while delivering a body dose of only 2.49 cGy.

7.2.2 MicroCT Image Quality and Corresponding Imaging Dose

Varying Current-Exposure Time

MicroCT images for the same axial slice of the 32 g mouse are presented with current-exposure times of 24, 36, 48, 72, 96, 144, 192, and 288 mAs. This provides a systematic way for objectively comparing the dose absorbed within the mouse with the visual image quality and noise produced for respective image quality parameters.

Doubling the Standard Frame Rate

Frame rate is the number of 2D projections acquired by the flat panel detector per unit time. A frame rate of 12 fps in the coronal plane is compared in the 32 g mouse for varying image quality scans obtained at a tube voltage of 60 kVp. Current-exposure times used were 24, 36, 48, 60, 72, and 144 mAs. Analyzing a frame rate of 12 fps at a 60 kVp tube voltage was completed to analyze its effect on visual image quality and noise compared to standard image acquisitions using 6 fps at 60 kVp. An advantage of increasing the frame rate from 6 to 12 fps is to reduce imaging noise without adding any extra imaging dose to the mouse, as the amount of projections acquired by the detector during a given amount of time is independent on the beam quality (or dose). Also, while it is true that a higher frame rate contains a higher amount of noise per frame as there is less information available per frame, the noise drops approximately by the square root of the number of total frames used. This is the reason why increasing the frame rate reduces the amount of noise in a scan.

Setting the frames per second, *fps*, within the SARRP software was acquired using

$$fps = \frac{\Pi}{t}, \tag{7.1}$$

where Π is the number of 2D projections (or total frames) and t is the total scanning time in seconds. For example, if a frame rate of 12 fps is needed, then the user can input 720 2D projections for a 60 second scan. This is in comparison to a standard 6 fps scan that uses 360 2D projections during a 60 second microCT scan. Note that

the "Force 6 FPS" option must be unchecked in the SARRP software to change the frame rate.

Image Noise Considerations

To display another imaging plane of the 32 g mouse, a coronal slice of the 32 g mouse is compared after applying the noise-scaling factors of **Table 6.7**. Current-exposure times used to apply the same noise across tube voltages of 50, 60, and 70 kVp were 60, 48, and 36 mAs, respectively. This experiment was carried out to experimentally validate the noise-scaling factors calculated in Chapter 6.

Varying Tube Voltage

Every time the tube voltage was changed, the flat panel detector was recalibrated with a flood field correction to correct for the change in detector gain. To illustrate absorbed dose compared to the visual image quality and noise across 40-80 kVp tube voltages at a constant current-exposure time of 60 mAs, sagittal slices are displayed with the smaller 20 g mouse. Holding the current-exposure time constant allows for observing the direct contribution that changing tube voltages have in visual imaging quality, noise, and absorbed dose. An additional high dose ($>$ 10 cGy body dose) very low noise ($<$ 20 HU) scan is included as a comparison to the higher noise scans. The 20 g mouse is presented to illustrate microCT image quality for a much smaller mouse (in contrast to the larger 32 g mouse).

7.3 Results

7.3.1 Varying Current-Exposure Time

Imaging noise and imaging dose to organs using a constant 50 kVp tube voltage and varying current-exposure time are displayed in the axial plane in **Figure 7.1**. Imaging with a 50 kVp tube voltage produces suboptimal noisy images (noise $>$ 55 HU) when less than approximately a 96 mAs current-exposure time is used. Within the imaging scans analyzed, the optimal combination of low imaging noise and a body

dose less than 5 cGy for a single scan at a 50 kVp tube voltage is produced at a 96 mAs current-exposure time.

Imaging noise and imaging dose to organs using a constant 60 kVp tube voltage and varying current-exposure time are displayed in **Figure 7.2**. It can be seen that imaging with a 60 kVp tube voltage produces suboptimal noisy images when a current-exposure time of less than 72 mAs is used. Within the imaging scans analyzed, the optimal combination of low imaging noise and a body dose less than 5 cGy for a single scan at a 60 kVp tube voltage is produced at a 72 mAs current-exposure time.

Imaging noise and imaging dose to organs using a constant 70 kVp tube voltage and varying current-exposure time are displayed in **Figure 7.3**. From interpolating the imaging scans analyzed, imaging with a 70 kVp tube voltage produces suboptimal noisy images when a current-exposure time of approximately 65 mAs and less are used. The optimal combination of low imaging noise and body doses less than 5 cGy for a single scan at a 70 kVp tube voltage is produced between current-exposure times of approximately 65 mAs and 70 mAs using interpolation.

For all tube voltages analyzed, image noise becomes marginally lower with significantly higher body dose when current-exposure times greater than 96 mAs are used (with 96 mAs being an acceptable maximum threshold when using a 50 kVp tube voltage to keep body dose below 5cGy), with this trend is illustrated in **Figure 7.4**. We can see that increasing the current-exposure time between 24 to 288 mAs for 50 to 70 kVp tube voltages results in an exponential reduction in image noise and a linear increase in body dose. Image noise becomes very low (less than 20 HU) at a current-exposure time of 288 mAs (equivalent to a 240 second scan at 1.2 mA) for all tube voltages presented, but at the cost of high body doses of 14, 20, and 25 cGy for 50, 60, and 70 kVp tube voltages, respectively. In addition, very high rib doses of greater than 0.5 Gy are given when a 288 mAs current-exposure time is used at 60 and 70 kVp tube voltages.

The measured noise in each image should be proportional to 1/sqrt(mAs). It was found that the general trend of the measured noise was indeed proportional to 1/sqrt(mAs) when normalized for tube currents above 50 mAs, but the noise was over 20% higher than expected for lower tube currents, most likely because of scatter and a lack of photons reaching the detector due to the pancake geometry within the Xstrahl SARRP.

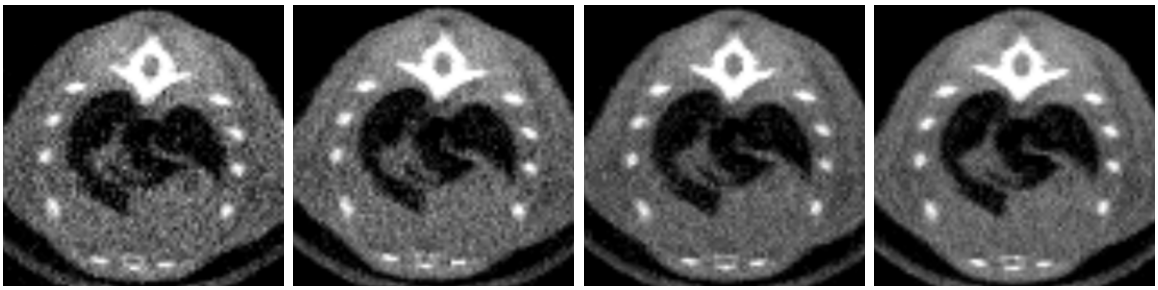

(a) 50 kVp, 24 mAs
Noise: 158 HU
Body: 1.17 cGy
Lungs: 0.86 cGy
Heart: 0.87 cGy
Spine: 2.60 cGy
Ribs: 2.98 cGy
Tumor: 1.19 cGy‡
Cranium: 3.29 cGy‡
Brain: 1.00 cGy‡
Kidney: 0.92 cGy‡

(b) 50 kVp, 36 mAs
Noise: 135 HU
Body: 1.76 cGy
Lungs: 1.29 cGy
Heart: 1.30 cGy
Spine: 3.89 cGy
Ribs: 4.46 cGy
Tumor: 1.78 cGy‡
Cranium: 4.94 cGy‡
Brain: 1.49 cGy‡
Kidney: 1.37 cGy‡

(c) 50 kVp, 48 mAs
Noise: 106 HU
Body: 2.34 cGy
Lungs: 1.72 cGy
Heart: 1.73 cGy
Spine: 5.19 cGy
Ribs: 5.95 cGy
Tumor: 2.37 cGy‡
Cranium: 6.58 cGy‡
Brain: 1.99 cGy‡
Kidney: 1.83 cGy‡

(d) 50 kVp, 72 mAs
Noise: 71 HU
Body: 3.51 cGy
Lungs: 2.58 cGy
Heart: 2.60 cGy
Spine: 7.79 cGy
Ribs: 8.93 cGy
Tumor: 3.56 cGy‡
Cranium: 9.87 cGy‡
Brain: 2.99 cGy‡
Kidney: 2.75 cGy‡

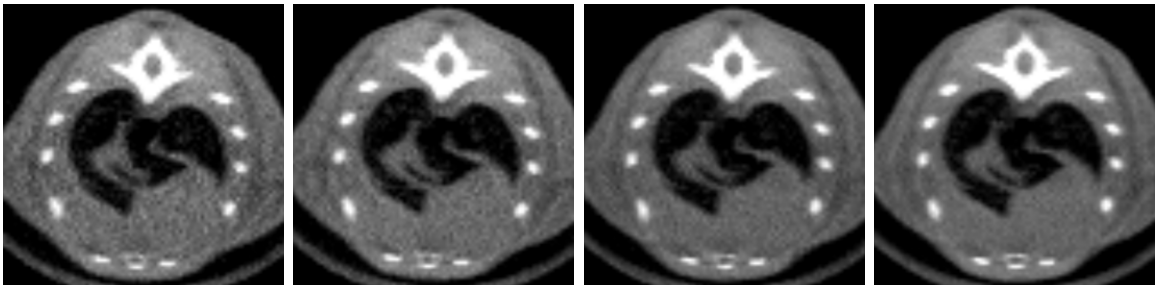

(e) 50 kVp, 96 mAs
Noise: 58 HU
Body: 4.68 cGy
Lungs: 3.44 cGy
Heart: 3.46 cGy
Spine: 10.38 cGy
Ribs: 11.90 cGy
Tumor: 4.74 cGy‡
Cranium: 13.16 cGy‡
Brain: 3.98 cGy‡
Kidney: 3.66 cGy‡

(f) 50 kVp, 144 mAs
Noise: 41 HU
Body: 7.02 cGy
Lungs: 5.16 cGy
Heart: 5.19 cGy
Spine: 15.57 cGy
Ribs: 17.85 cGy
Tumor: 7.11 cGy‡
Cranium: 19.74 cGy‡
Brain: 5.97 cGy‡
Kidney: 5.49 cGy‡

(g) 50 kVp, 192 mAs
Noise: 29 HU
Body: 9.36 cGy
Lungs: 6.88 cGy
Heart: 6.92 cGy
Spine: 20.76 cGy
Ribs: 23.80 cGy
Tumor: 9.48 cGy‡
Cranium: 26.32 cGy‡
Brain: 7.96 cGy‡
Kidney: 7.32 cGy‡

(h) 50 kVp, 288 mAs
Noise: 18 HU
Body: 14.04 cGy
Lungs: 10.32 cGy
Heart: 10.38 cGy
Spine: 31.14 cGy
Ribs: 35.70 cGy
Tumor: 14.22 cGy‡
Cranium: 39.48 cGy‡
Brain: 11.94 cGy‡
Kidney: 10.98 cGy‡

Figure 7.1: Demonstration of visual microCT image quality with corresponding dose to organs for a 32 g mouse in the axial plane, using a constant tube voltage of 50 kVp with current-exposure time variations of a) 24, b) 36, c) 48, d) 72, e) 96, f) 144, g) 192, and h) 288 mAs. ‡Tissue not in image.

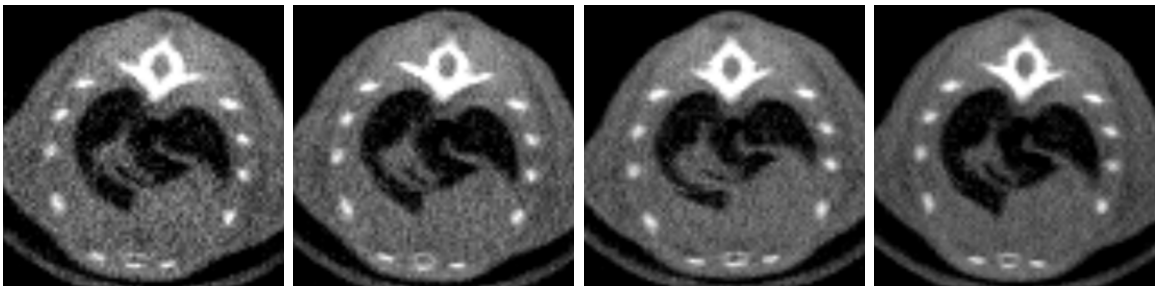

(a) 60 kVp, 24 mAs
Noise: 139 HU
Body: 1.66 cGy
Lungs: 1.26 cGy
Heart: 1.25 cGy
Spine: 3.76 cGy
Ribs: 4.30 cGy
Tumor: 1.64 cGy‡
Cranium: 4.82 cGy‡
Brain: 1.45 cGy‡
Kidney: 1.32 cGy‡

(b) 60 kVp, 36 mAs
Noise: 119 HU
Body: 2.49 cGy
Lungs: 1.89 cGy
Heart: 1.87 cGy
Spine: 5.64 cGy
Ribs: 6.44 cGy
Tumor: 2.45 cGy‡
Cranium: 7.23 cGy‡
Brain: 2.18 cGy‡
Kidney: 1.98 cGy‡

(c) 60 kVp, 48 mAs
Noise: 93 HU
Body: 3.32 cGy
Lungs: 2.52 cGy
Heart: 2.49 cGy
Spine: 7.52 cGy
Ribs: 8.59 cGy
Tumor: 3.27 cGy‡
Cranium: 9.64 cGy‡
Brain: 2.90 cGy‡
Kidney: 2.64 cGy‡

(d) 60 kVp, 72 mAs
Noise: 54 HU
Body: 4.98 cGy
Lungs: 3.78 cGy
Heart: 3.74 cGy
Spine: 11.28 cGy
Ribs: 12.89 cGy
Tumor: 4.91 cGy‡
Cranium: 14.46 cGy‡
Brain: 4.35 cGy‡
Kidney: 3.96 cGy‡

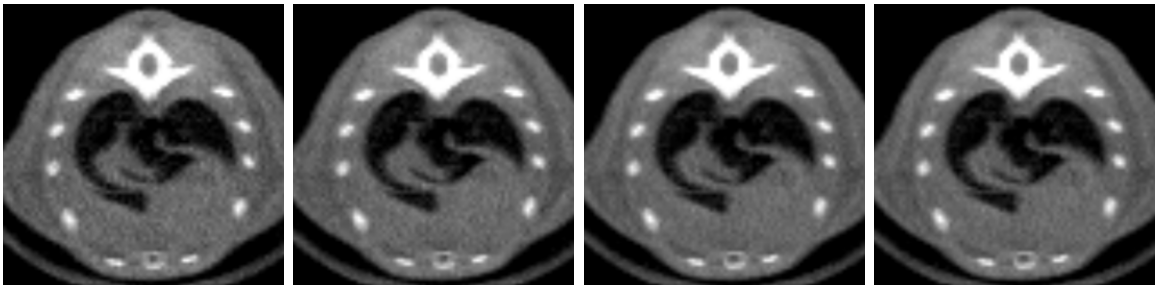

(e) 60 kVp, 96 mAs
Noise: 39 HU
Body: 6.64 cGy
Lungs: 5.04 cGy
Heart: 4.98 cGy
Spine: 15.04 cGy
Ribs: 17.18 cGy
Tumor: 6.54 cGy‡
Cranium: 19.28 cGy‡
Brain: 5.80 cGy‡
Kidney: 5.28 cGy‡

(f) 60 kVp, 144 mAs
Noise: 30 HU
Body: 9.96 cGy
Lungs: 7.56 cGy
Heart: 7.47 cGy
Spine: 22.56 cGy
Ribs: 25.77 cGy
Tumor: 9.81 cGy‡
Cranium: 28.92 cGy‡
Brain: 8.70 cGy‡
Kidney: 7.92 cGy‡

(g) 60 kVp, 192 mAs
Noise: 21 HU
Body: 13.28 cGy
Lungs: 10.08 cGy
Heart: 9.96 cGy
Spine: 30.08 cGy
Ribs: 34.36 cGy
Tumor: 13.08 cGy‡
Cranium: 38.56 cGy‡
Brain: 11.60 cGy‡
Kidney: 10.56 cGy‡

(h) 60 kVp, 288 mAs
Noise: 14 HU
Body: 19.92 cGy
Lungs: 15.12 cGy
Heart: 14.94 cGy
Spine: 45.12 cGy
Ribs: 51.54 cGy
Tumor: 19.62 cGy‡
Cranium: 57.84 cGy‡
Brain: 17.40 cGy‡
Kidney: 15.84 cGy‡

Figure 7.2: Demonstration of visual microCT image quality with corresponding dose to organs for a 32 g mouse in the axial plane, using a constant tube voltage of 60 kVp with current-exposure time variations of a) 24, b) 36, c) 48, d) 72, e) 96, f) 144, g) 192, and h) 288 mAs. ‡Tissue not in image.

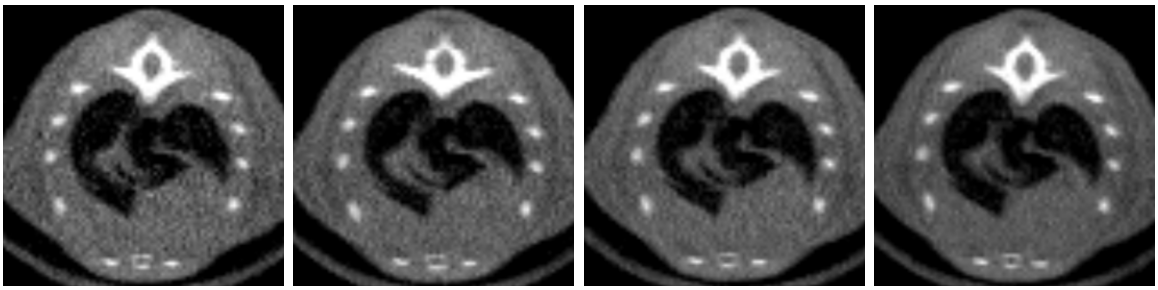

(a) 70 kVp, 24 mAs
Noise: 116 HU
Body: 2.16 cGy
Lungs: 1.68 cGy
Heart: 1.65 cGy
Spine: 4.94 cGy
Ribs: 5.62 cGy
Tumor: 2.09 cGy‡
Cranium: 6.37 cGy‡
Brain: 1.93 cGy‡
Kidney: 1.74 cGy‡

(b) 70 kVp, 36 mAs
Noise: 91 HU
Body: 3.24 cGy
Lungs: 2.51 cGy
Heart: 2.48 cGy
Spine: 7.41 cGy
Ribs: 8.42 cGy
Tumor: 3.13 cGy‡
Cranium: 9.56 cGy‡
Brain: 2.89 cGy‡
Kidney: 2.60 cGy‡

(c) 70 kVp, 48 mAs
Noise: 79 HU
Body: 4.32 cGy
Lungs: 3.35 cGy
Heart: 3.30 cGy
Spine: 9.88 cGy
Ribs: 11.23 cGy
Tumor: 4.17 cGy‡
Cranium: 12.74 cGy‡
Brain: 3.85 cGy‡
Kidney: 3.47 cGy‡

(d) 70 kVp, 72 mAs
Noise: 46 HU
Body: 6.48 cGy
Lungs: 5.03 cGy
Heart: 5.78 cGy
Spine: 14.82 cGy
Ribs: 16.85 cGy
Tumor: 6.26 cGy‡
Cranium: 19.11 cGy‡
Brain: 1.00 cGy‡
Kidney: 5.21 cGy‡

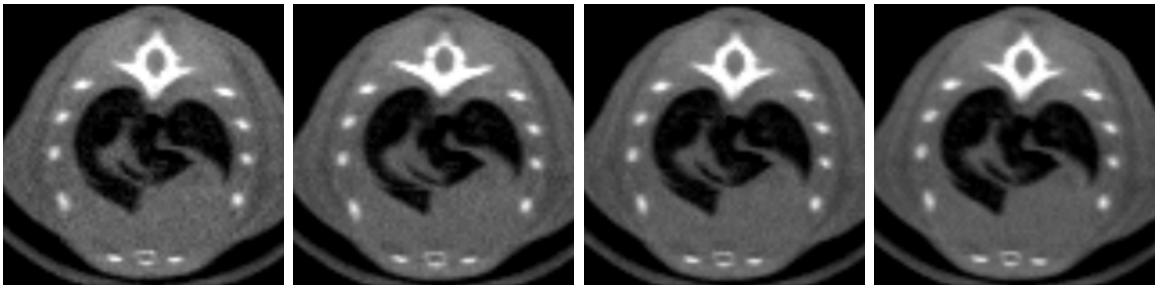

(e) 70 kVp, 96 mAs
Noise: 26 HU
Body: 8.64 cGy
Lungs: 6.70 cGy
Heart: 6.60 cGy
Spine: 19.76 cGy
Ribs: 22.46 cGy
Tumor: 8.34 cGy‡
Cranium: 25.48 cGy‡
Brain: 7.70 cGy‡
Kidney: 6.94 cGy‡

(f) 70 kVp, 144 mAs
Noise: 19 HU
Body: 12.96 cGy
Lungs: 10.05 cGy
Heart: 9.90 cGy
Spine: 29.64 cGy
Ribs: 33.69 cGy
Tumor: 12.51 cGy‡
Cranium: 38.22 cGy‡
Brain: 11.55 cGy‡
Kidney: 10.41 cGy‡

(g) 70 kVp, 192 mAs
Noise: 15 HU
Body: 17.28 cGy
Lungs: 13.40 cGy
Heart: 13.20 cGy
Spine: 39.52 cGy
Ribs: 44.92 cGy
Tumor: 16.68 cGy‡
Cranium: 50.96 cGy‡
Brain: 15.40 cGy‡
Kidney: 13.88 cGy‡

(h) 70 kVp, 288 mAs
Noise: 11 HU
Body: 25.92 cGy
Lungs: 20.10 cGy
Heart: 19.80 cGy
Spine: 59.28 cGy
Ribs: 67.38 cGy
Tumor: 25.02 cGy‡
Cranium: 76.44 cGy‡
Brain: 23.10 cGy‡
Kidney: 20.82 cGy‡

Figure 7.3: Demonstration of visual microCT image quality with corresponding dose to organs for a 32 g mouse in the axial plane, using a constant tube voltage of 70 kVp with current-exposure time variations of a) 24, b) 36, c) 48, d) 72, e) 96, f) 144, g) 192, and h) 288 mAs. ‡Tissue not in image.

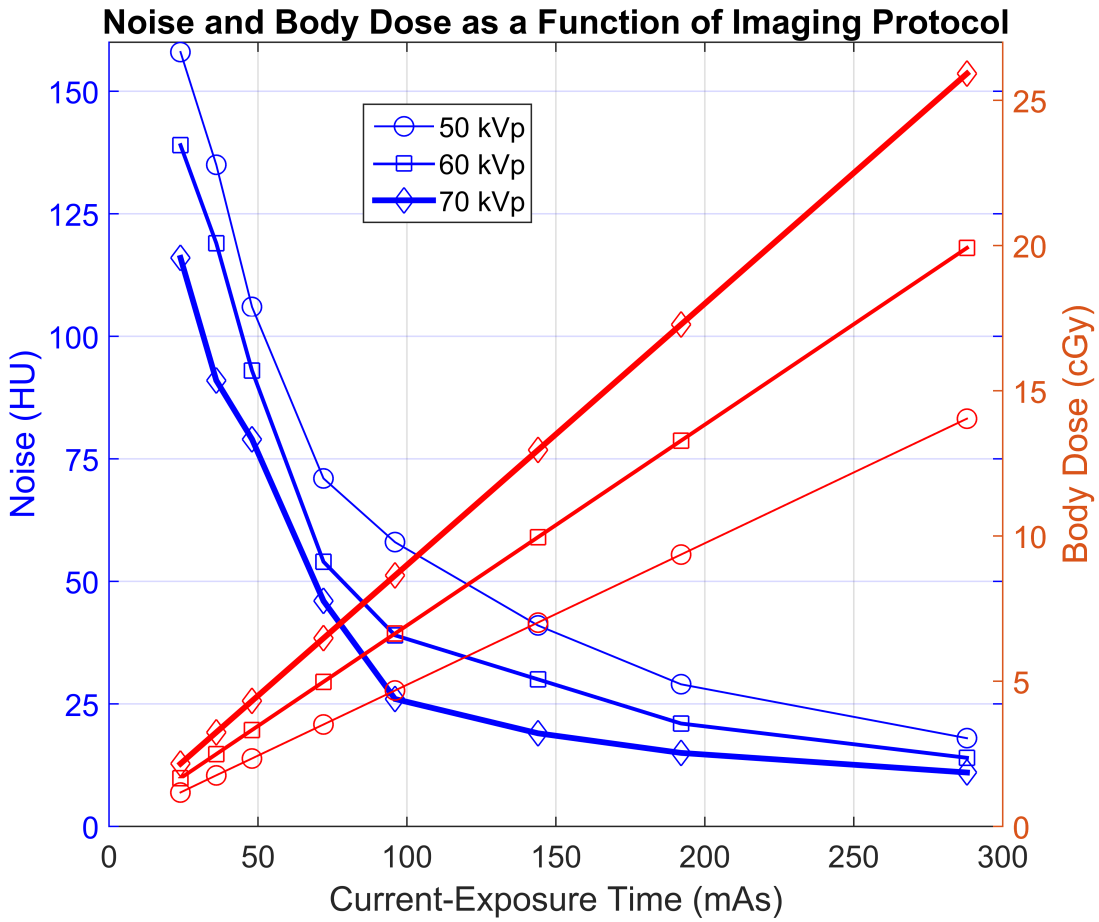

Figure 7.4: Image noise and body dose to a 32 g mouse as a function of imaging protocol for 50 (circles), 60 (squares), and 70 (diamonds) kVp tube voltages over a range of current-exposure times. Blue and Red curves illustrate image noise and body dose, respectively.

7.3.2 Doubling the Standard Frame Rate

Figure 7.5 displays images acquired in the axial plane with a frame rate of 12 fps for current-exposure times between 24-144 mAs with a standard 60 kVp tube voltage. We find that image noise for a 60 kVp tube voltage for a respective current-exposure time at 12 fps was significantly reduced when compared to the same imaging parameters but with the standard frame rate of 6 fps. As illustrated in **Figure 7.6**, the image noise for all 12 fps data sets were at least 45% lower than the 6 fps data sets when using the same current-exposure times at a 60 kVp tube voltage, while the body doses were the same for each respective 6 and 12 fps scans. Doubling the frame rate did not show any signs of artifacts within the image, and gives the same amount of imaging dose as using a frame rate of 6 fps.

Note, that the 24 and 36 mAs current-exposure time scans at 12 fps were acquired using a 30 second scan time, while the scans at 6 fps were acquired using a 60 second scan time. While the scan times were different between these two scans, the current-exposure time and tube voltage between the 6 and 12 fps scans were the same. It can be expected that the noise obtained for a given current-exposure time and tube voltage, regardless of scanning time, will be the same.

What this comparison does show, however, is that at a 60 kVp tube voltage and 36 mAs current-exposure time, scanning with a faster 30 second scan time at 12 fps produced 46% less noise while delivering the same imaging dose (2.49 body dose) compared to scanning with a 60 second scan time at 6 fps. Additionally, this scanning protocol using 12 fps, 30 second scant time, 1.2 mA tube current, and 60 kVp tube voltage produces an image with 55 HU of noise which is within the maximum noise allowed to keep MC dose calculation accuracy to within 5% [16, 111]. It can be specially noted that this faster protocol when compared to a common standard imaging protocol for the Xstrahl SARRP (60 kVp, 0.8 mA, 60 second scan time, 6 fps) reduced imaging noise by 60% and reduced imaging dose to all organs by 25%.

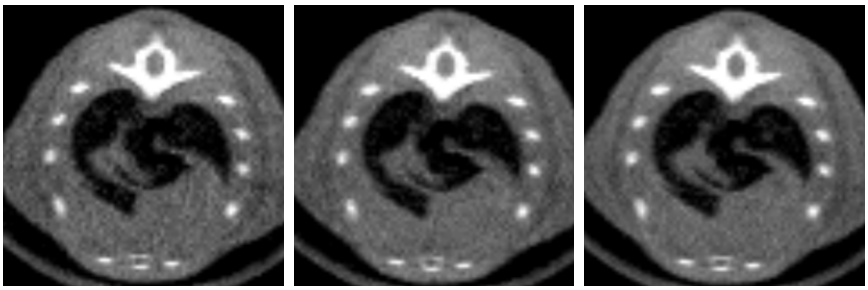

(a) 60 kVp, 24 mAs*, 12 fps
Noise: 88 HU
Body: 1.66 cGy
Lungs: 1.26 cGy
Heart: 1.25 cGy
Spine: 3.76 cGy
Ribs: 4.30 cGy
Tumor: 1.64 cGy‡
Cranium: 4.82 cGy‡
Brain: 1.45 cGy‡
Kidney: 1.32 cGy‡

(b) 60 kVp, 36 mAs*, 12 fps
Noise: 55 HU
Body: 2.49 cGy
Lungs: 1.89 cGy
Heart: 1.87 cGy
Spine: 5.64 cGy
Ribs: 6.44 cGy
Tumor: 2.45 cGy‡
Cranium: 7.23 cGy‡
Brain: 2.18 cGy‡
Kidney: 1.98 cGy‡

(c) 60 kVp, 48 mAs, 12 fps
Noise: 43 HU
Body: 3.32 cGy
Lungs: 2.52 cGy
Heart: 2.49 cGy
Spine: 7.52 cGy
Ribs: 8.59 cGy
Tumor: 3.27 cGy‡
Cranium: 9.64 cGy‡
Brain: 2.90 cGy‡
Kidney: 2.64 cGy‡

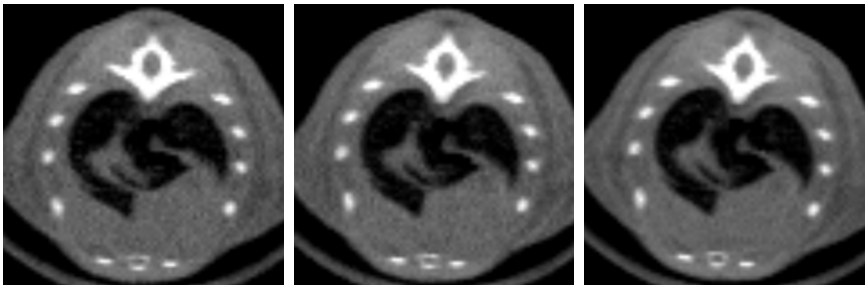

(d) 60 kVp, 60 mAs, 12 fps
Noise: 33 HU
Body: 4.15 cGy
Lungs: 3.15 cGy
Heart: 3.11 cGy
Spine: 9.40 cGy
Ribs: 10.74 cGy
Tumor: 4.09 cGy‡
Cranium: 12.05 cGy‡
Brain: 3.63 cGy‡
Kidney: 3.30 cGy‡

(e) 60 kVp, 72 mAs, 12 fps
Noise: 29 HU
Body: 4.98 cGy
Lungs: 3.78 cGy
Heart: 3.74 cGy
Spine: 11.28 cGy
Ribs: 12.89 cGy
Tumor: 4.91 cGy‡
Cranium: 14.46 cGy‡
Brain: 4.35 cGy‡
Kidney: 3.96 cGy‡

(f) 60 kVp, 144 mAs, 12 fps
Noise: 23 HU
Body: 9.96 cGy
Lungs: 7.56 cGy
Heart: 7.47 cGy
Spine: 22.56 cGy
Ribs: 25.77 cGy
Tumor: 9.81 cGy‡
Cranium: 28.92 cGy‡
Brain: 8.70 cGy‡
Kidney: 7.92 cGy‡

Figure 7.5: Demonstration of visual microCT image quality with corresponding dose to organs for a 32 g mouse in the axial plane, using a constant frame rate of 12 fps (standard is 6 fps) and constant tube voltage of 60 kVp with current-exposure time variations of a) 24, b) 36, c) 48, d) 60, e) 72, and f) 144 mAs. *30 second scan time used. ‡Tissue not in image.

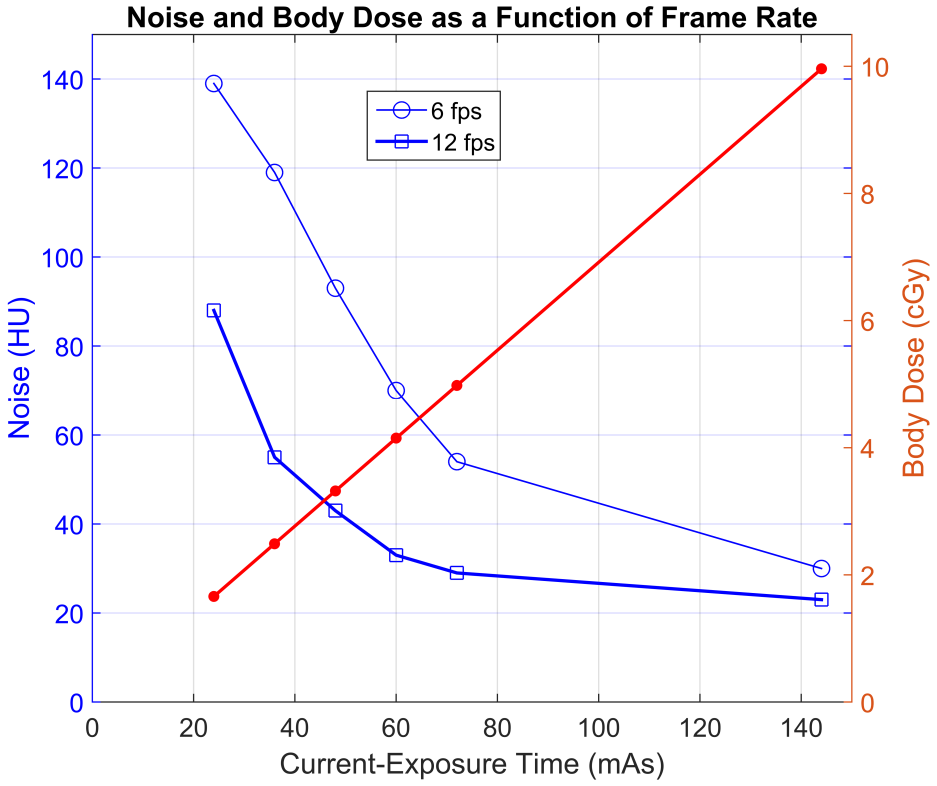

Figure 7.6: Image noise and body dose to a 32 g mouse at a 60 kVp tube voltage as a function of 6 (circles) and 12 (square) fps microCT scans over a range of current-exposure times. The Red curve illustrates body dose for both 6 and 12 fps scans.

7.3.3 Image Noise Considerations

The noise-scaling factors of **Table 6.7** were used on the 32 g mouse of Section 6.2.3 to acquire three separate 60 second scans at 50, 60, and 70 kVp, shown in the coronal plane in **Figure 7.7**. We find that the percentage difference in noise was within a 7% difference between the 50 and 60 kVp tube voltage scans, and within a 3% difference between the 60 and 70 kVp tube voltage scans. Before the noise-scaling factor was applied, the noise within the 50 and 70 kVp tube voltage scans compared to the 60 kVp tube voltage scan were 14% and -18%, respectively. This illustrates that the noise-scaling factor appropriately normalized the noise for the 70 kVp tube voltage, but only approximately normalized the image noise for the 50 kVp scan.

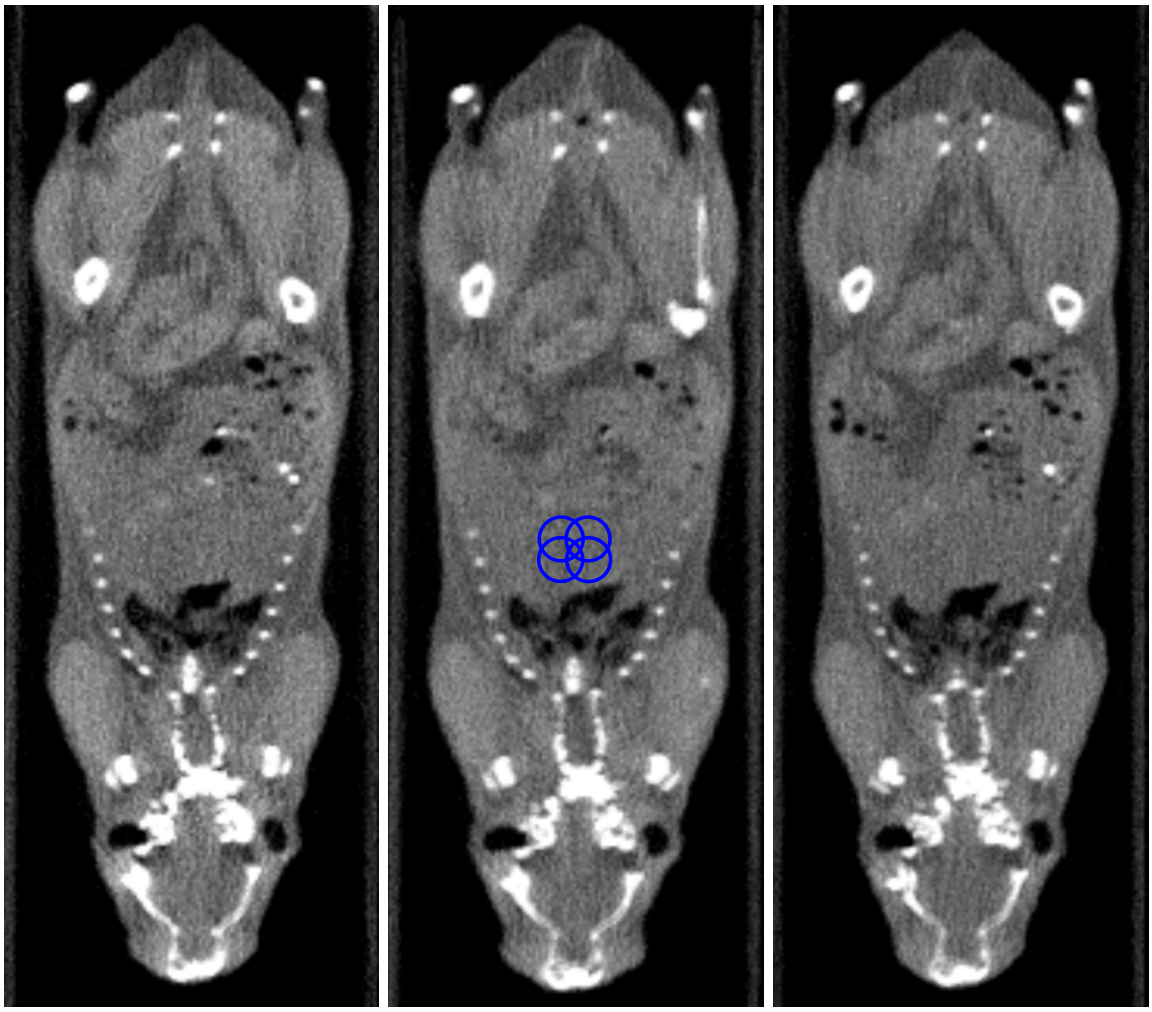

(a) 50 kVp, 60 mAs
Noise: 99 HU
Body: 2.93 cGy,
Tumor: 2.96 cGy,
Cranium: 8.23 cGy,
Ribs: 7.44 cGy,
Spine: 6.49 cGy,
Brain: 2.49 cGy,
Kidney: 2.29 cGy,
Heart: 2.16 cGy,
Lungs: 2.15 cGy

(b) 60 kVp, 48 mAs,
Noise: 93 HU
Body: 3.32 cGy,
Tumor: 3.27 cGy,
Cranium: 9.64 cGy,
Ribs: 8.59 cGy,
Spine: 7.52 cGy,
Brain: 2.90 cGy,
Kidney: 2.64 cGy,
Heart: 2.49 cGy,
Lungs: 2.52 cGy

(c) 70 kVp, 36 mAs,
Noise: 91 HU
Body: 3.24 cGy,
Tumor: 3.13 cGy,
Cranium: 9.56 cGy,
Ribs: 8.42 cGy,
Spine: 7.41 cGy,
Brain: 2.89 cGy,
Kidney: 2.60 cGy,
Heart: 2.48 cGy,
Lungs: 2.51 cGy

Figure 7.7: Demonstration of the effects of the noise-scaling factor η_λ to microCT image quality of a 32 g mouse in the coronal plane, using a 60 s scan time with tube voltage and exposure-current times of a) 50 kVp and 60 mAs, b) 60 kVp and 48 mAs, and c) 70 kVp and 36 mAs. ROIs (4 blue circles) used for noise measurements shown.

Due to the relatively high ±7% signal variation in the soft tissue ROIs, it was difficult to obtain consistent measurements, with the measurement uncertainty most likely caused by the statistical nature of x-ray absorption in tissue and photon starvation.

7.3.4 Varying Tube Voltage

Displayed in **Figure 7.8** are 40-80 kVp tube voltages with a constant current-exposure time of 60 mAs with the smaller 20 g mouse in the sagittal plane. Between 50 and 80 kVp tube voltages, we find that the imaging noise varies by approximately 10 to 20 HU every 10 kVp change in tube voltage. We also find that there is a larger 40 HU noise change between 40 and 50 kVp tube voltages. While holding all other imaging parameters constant, increasing the tube voltage from 40-50, 50-60, 60-70, and 70-80 kVp increases imaging dose to the body by 65%, 40%, 30%, and 25%, respectively, while reducing image noise by 30%, 23%, 22%, and 18%, respectively. This trend is illustrated in **Figure 7.9**. The microCT scan found in **Figure 7.8f** is displayed to illustrate a high dose ($>$ 10 cGy body dose), very low noise scan ($<$ 20 HU noise) compared to lower doses.

It was expected that the dose to bone should be larger at lower kVp tube voltages owing to a higher amount of dose absorbed due to the photoelectric effect. This is not the case in the calculated dose obtained through our MC methods, and this is most likely due to the unique pancake imaging geometry within the Xstrahl SARRP. Since the photons are attenuated through the long access of the mouse, including photons that scatter out of the area, a large number of the incident photons will not make it to the bone tissue to attribute to the bone dose, with this phenomena being more evident at lower tube voltages. Using the mean energies of the 40 and 80 kVp imaging beams with the NIST mass attenuation coefficient table for water, and using equation $N(x) = N_0 e^{-\mu x}$, we find that while there is more photoelectric effect for the 40 kVp imaging beam, more than a magnitude more photons will reach the bone in the 80 kVp imaging beam to deposit more dose.

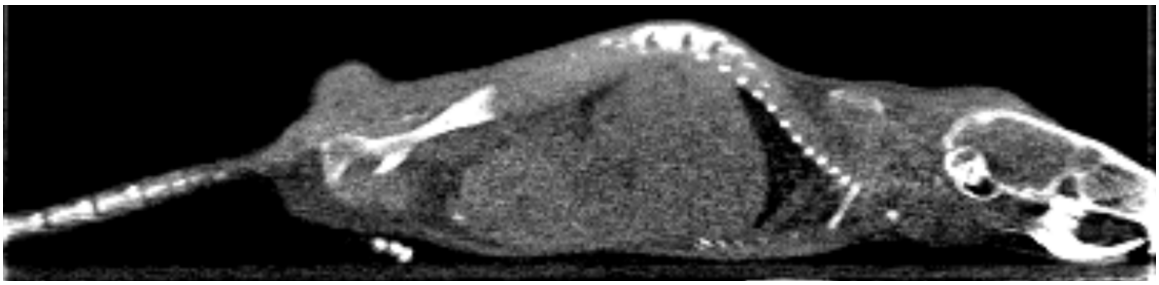

(a) 40 kVp, 60 mAs, *Noise: 136 HU*
Body: 1.88 cGy, Tumor: 1.94 cGy, Cranium: 5.13 cGy, Ribs: 4.73 cGy, Spine: 4.09 cGy, Brain: 1.56 cGy, Kidney: 1.46, Heart: 1.36, Lungs: 1.36 cGy

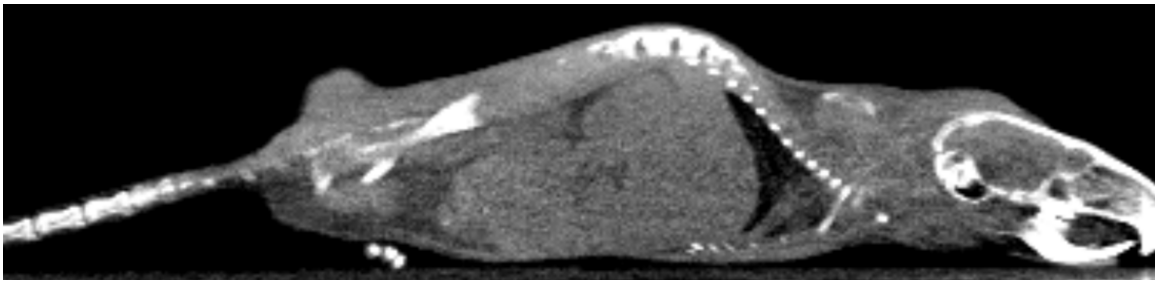

(b) 50 kVp, 60 mAs, *Noise: 95 HU*
Body: 3.13 cGy, Tumor: 3.09 cGy, Cranium: 9.03 cGy, Ribs: 8.13 cGy, Spine: 7.08 cGy, Brain: 2.70 cGy, Kidney: 2.48, Heart: 2.33, Lungs: 2.36 cGy

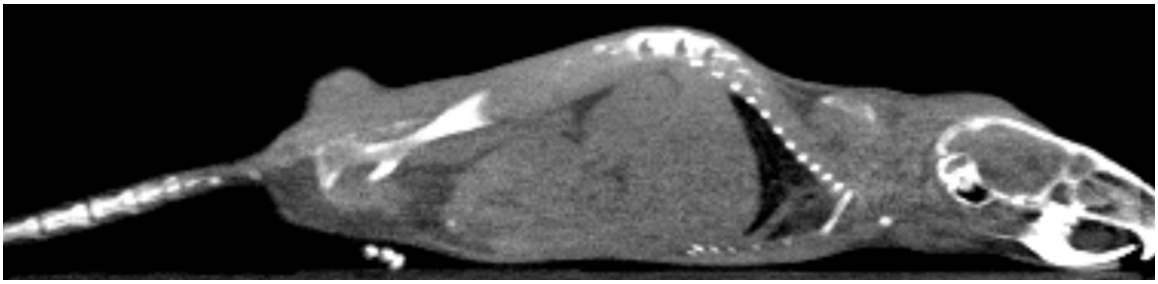

(c) 60 kVp, 60 mAs, *Noise: 73 HU*
Body: 4.40 cGy, Tumor: 4.24 cGy, Cranium: 13.09 cGy, Ribs: 11.60 cGy, Spine: 10.15 cGy, Brain: 3.90 cGy, Kidney: 3.54, Heart: 3.34, Lungs: 3.43 cGy

Figure 7.8: Demonstration of visual microCT image quality with corresponding dose to organs for a 20 g mouse in the sagittal plane, using a constant current-exposure time of 60 mAs with tube voltage variations of a) 40, b) 50, c) 60, d) 70, e) 80, and f) 80 (240 mAs) kVp. (Continued on next page...)

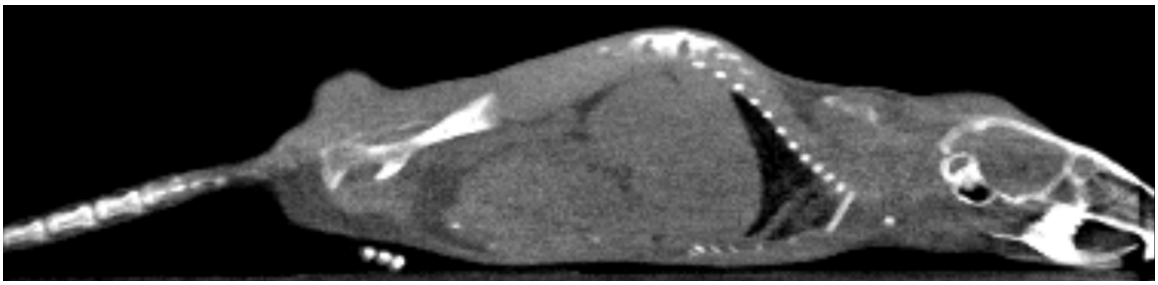

(d) 70 kVp, 60 mAs, *Noise: 57 HU*
Body: 5.70 cGy, Tumor: 5.39 cGy, Cranium: 17.16 cGy, Ribs: 15.08 cGy, Spine: 13.25 cGy, Brain: 5.14 cGy, Kidney: 4.63, Heart: 4.39, Lungs: 4.51 cGy

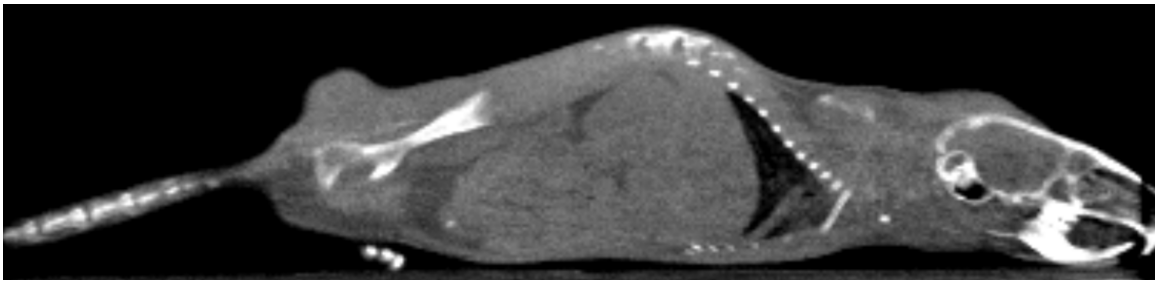

(e) 80 kVp, 60 mAs, *Noise: 47 HU*
Body: 7.04 cGy, Tumor: 6.56 cGy, Cranium: 21.28 cGy, Ribs: 18.55 cGy, Spine: 16.36 cGy, Brain: 6.41 cGy, Kidney: 5.76, Heart: 5.49, Lungs: 5.66 cGy

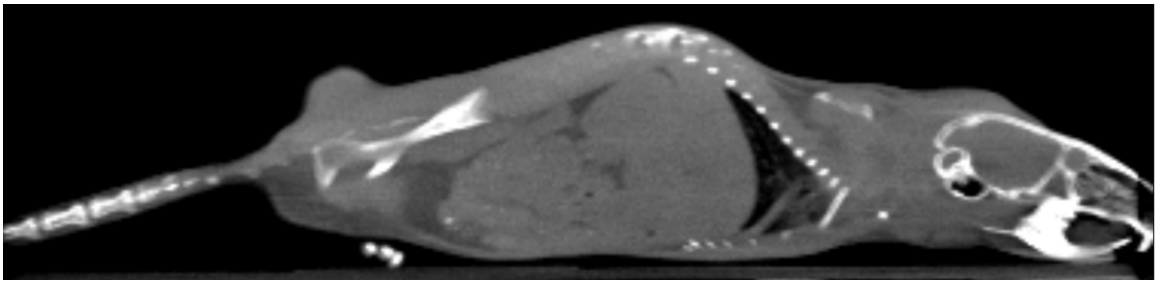

(f) 80 kVp, 240 mAs, *Noise: 14 HU*
Body: 28.15 cGy, Tumor: 26.25 cGy, Cranium: 85.10 cGy, Ribs: 74.20 cGy, Spine: 65.45 cGy, Brain: 25.65 cGy, Kidney: 23.05, Heart: 21.95, Lungs: 22.65 cGy

Figure 7.8: ...Figure continued from previous page.

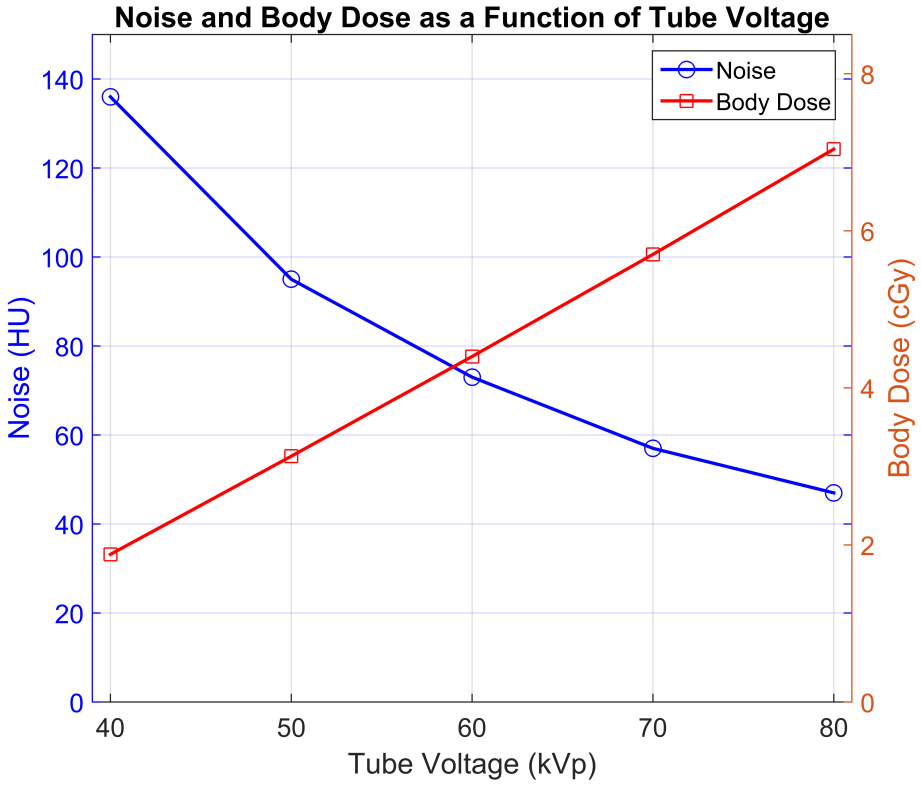

Figure 7.9: Image noise and body dose to a 20 g mouse as a function of tube voltage with constant 60 mAs current-exposure time and 6 fps microCT scans. The Blue and Red curves illustrate image noise and body dose, respectively.

7.4 Discussion

High quality and low noise images may not be needed to locate flank tumors for radiation treatment planning, but high quality images are indeed needed for small tumors (i.e., 1-3 mm) located within the body. We did not have access to mice with non-subcutaneous tumors. For flank tumor irradiations, it may be sufficient to acquire a lower quality image using 40 kVp and 60 mAs in order to give as little dose to the animal as possible. However, further studies must be conducted to analyze the dose calculation accuracy of the SARRP by comparing calculated dose between a very noisy scan (such as in **Figure 7.8a**) with medium and low noise scans (such as in **Figures 7.8d** and **7.8f**, respectively).

If the amount of time a mouse is under anesthesia is a concern, or if imaging dose

is a concern, it is recommended to scan mice within the SARRP with the following imaging parameters: A 30 second scan time, frame rate of 12 fps, 1.2 mA tube current, 60 kVp tube voltage, and 0.275 mm^3 voxel size. This protocol will produce imaging noise of 55 HU, which is recommended to keep MC dose calculation accuracy to within 5% [16, 111].

For 50-70 kVp tube voltage scans, it is recommended that the current-exposure time never exceed 96 mAs for a single scan in order to keep image noise less than 55 HU when imagine dose is a concern. Imaging dose and noise are also associated with the size of the mouse. In general, a larger mouse will obtain higher noise and overall less total body dose compared to a smaller mouse when using the same imaging parameters.

Image quality with varying voxel sizes could not be assessed with the current software. Changing voxel sizes within the SARRP requires the user to access a password-protected interface within the software to change the reconstruction parameters. Changing the voxel size was accomplished in this fashion; however, this created substantial artifacts in the image that was not representative of the true scanned object. This process corrupted the data set when manually changing the reconstruction protocol outside of the calibrated voxel sizes. For our specific SARRP irradiator, the calibrated voxel options are 0.275 mm^3 ("Mouse Cropped") and 0.325 mm^3 ("Mouse Fullfield").

7.5 Conclusions

This chapter presented how imaging dose affects the image quality and noise of microCT mouse scans within the SARRP. Two mice, large and small, were scanned with many different imaging protocols and microCT images were presented together with imaging dose to organs as calculated in Chapter 6. A visual story merging microCT image quality and imaging dose was demonstrated. The readers may use this information to find what imaging dose corresponds to which imaging parameters to make an informed decision on what imaging parameters are best to use for their specific study.

7.6 Summary

MicroCT imaging dose to mouse organs were calculated for various imaging protocols with the corresponding noise and microCT images to accompany them. Imaging dose thus far has been calculated through MC methods. The next chapter will now look into experimentally measuring absorbed dose in an image-guided small animal irradiator using a novel scintillating dosimeter.

Chapter 8

Characterization of a Plastic Scintillating Detector for the Small Animal Radiation Research Platform (SARRP)

"I used to walk like a giant on the land, now I feel like a leaf floating in a stream."

–Neil Young

Building from the calculated dose obtained through MC methods of the previous chapter, this chapter now aims to experimentally measure dose in an image-guided small animal irradiator. Unlike common dosimeters that only have the ability to measure dose in large fields, preclinical irradiators demand measurements to be made within small fields. Presented is a small novel scintillating dosimeter to be characterized for the small fields and low energies found in preclinical irradiators. This presents the first steps towards real-time *in-vivo* small field dosimetry in small animal irradiators.

8.1 Introduction

Image-guided small animal irradiators advance our ability to treat cancers through translational research. Performing accurate irradiations on small a***n***imals improves our understanding of radiation responses to human tumors. These preclinical studies require small fields ($\leq$ 1 x 1 cm^2) which make high spatial resolution dosimetry vital in guaranteeing a high degree of accuracy and precision for treatment verification and quality assurance. Current ionization chambers, diodes, thermoluminescent dosimeters (TLDs), radiochromic films, chemical, and gel dosimeters do not simultaneously provide real-time output and the high spatial resolution needed for small field dosimetry. Pinpoint ionization chambers are not small enough to be suitable for fields less than 2 x 2 cm^2 field size as reported by PTW (PTW, Freiburg, Germany); however a smaller (2 mm diameter) prototype ionization chamber is being developed but has not been validated for kilovoltage x-ray beams [167]. Additionally, to the author's knowledge, small diamond detectors have not been validated for field sizes smaller than 5 mm [22, 50, 51, 61].

Plastic scintillator detectors have an advantage of being near water-equivalent, versatile, and provide real-time output with high spatial resolution, and have been previously characterized for high energy beams [19, 20, 54, 158, 184]. Their small size and precision makes their use optimal for small fields [6, 6, 124, 129], and have been previously validated in-vivo for radiotherapy [203]. Lower energy beams have been examined using scintillators for superficial and orthovoltage x-ray units, computed tomography (CT) scans, brachytherapy, and radiography [29, 85, 123, 128, 155, 199, 208, 208].

Unlike at high energies, an energy dependence exists for the scintillation efficiency of polystyrene at the low energies used in small animal irradiators ($\leq$ 250 kVp), especially with imaging beams ($\leq$ 80 kVp) [199]. The x-ray absorption properties of plastic scintillators are different to that of air, and can be quantified using the mass energy-absorption coefficient ratio between polystyrene and air. Accurate x-ray spectra of the beam must be obtained to convert this ratio into spectrally-weighted, poly-energetic mass energy-absorption coefficients to properly convert absorbed dose in the scintillator to air kerma [29,199]. Also, a decrease in sensitivity is produced from high LET electrons liberated within the scintillator that reduce scintillation efficiency through ionization quenching. Quenching models have been used to describe this phenomenon [24, 25, 49, 71, 156], with the Birks model [25] being the most commonly

used.

Previous studies have characterized plastic scintillators for low energy beams by correcting scintillator sensitivity for different x-ray beam energies [29, 125]. Boivin *et. al* [29] used radiation sources from a Gulmay CP 320 x-ray generator, a ^{137}Cs source, and a ^{60}Co source, using scintillators with 1 mm diameter, 10 mm long active volumes. Le Deroff *et. al* [125] used a scintillator with a 1 mm diameter, 15 mm long active volume, irradiated with the X-RAD 225Cx small animal irradiator (Precision X-Ray, Inc., North Branford, CT). Calculations of their sensitivity correction factors were approximate, where only the mean photon energy was used for spectral corrections.

We present the characterization of a small (1 mm diameter, 1 mm long active volume) plastic scintillator dosimeter for the 40–80 kVp imaging beams and 220 kVp therapy beam of the Small Animal Radiation Research Platform (SARRP, Xstrahl Inc., Suwanee, GA). Our validated in-house Monte Carlo (MC) model of the SARRP [109] was used to obtain accurate beam spectra for spectral corrections in conjunction with mass energy-absorption coefficients. Scintillator sensitivity and linearity was characterized, as well as beam profile measurements and computed correction factors validated using MC simulations. This work presents steps towards implementing a small, high resolution, real-time dosimeter for the use of small fields and low energies used in small animal irradiators.

8.2 Materials and Methods

8.2.1 Scintillator Dosimeter System

A schematic of the plastic scintillation detector (PSD) system is illustrated in **Figure 8.1**. The PSD consisted of a polystyrene scintillating fiber (BCF-60, Saint-Gobain Crystals, Nemours, France) fiber with a 1-mm diameter, 1-mm long active volume emitting green light. The active volume was protected by a 0.015-mm thick polymethyl methacrylate (PMMA) cladding. This was optically coupled to a 1-mm diameter, 15-m long cladded PMMA optical fiber (Eska GH-4001, Mitsubishi International Corporation, NY), and made light-tight by a 0.6-mm thick black polyethylene jacket. The optical fiber was terminated by a SMA connector and connected through a fiber

adapter to an H10721 photomultiplier tube (PMT, Hamamatsu Photonics, Hamamatsu, Japan). The PMT was connected to a PTW UNIDOS E electrometer (PTW, Freiburg, Germany) outputting μC-sensitive charge readings in real time. The measured charge was used as a surrogate for the light generated within the scintillator.

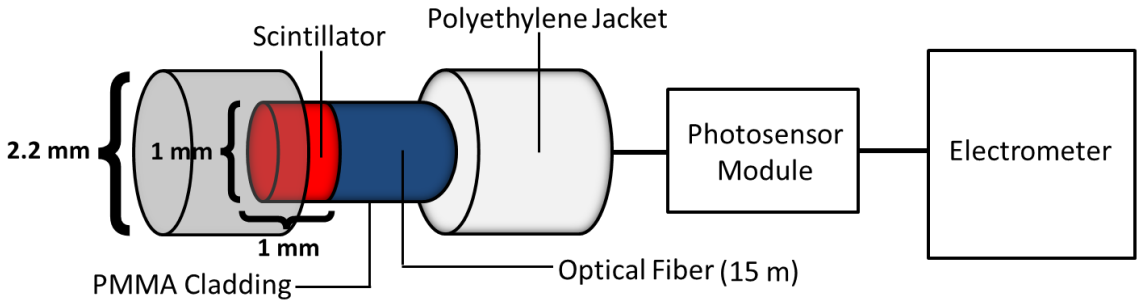

Figure 8.1: Cross-section of the polystyrene scintillator coupled to an optical fiber, surrounded by a polyethylene jacket, transmitting light to a photomultiplier tube module with charges collected by an electrometer.

8.2.2 Small Animal Irradiator

The SARRP used in this study operates with 220 kVp (therapy) and 40, 50, 60, 70, and 80 kVp (imaging) beam energies with focal spot sizes of 3.0 and 0.4 mm for therapy and imaging beams, respectively [186, 201]. The SARRP x-ray beam has a 0.8 mm Be internal filtration. All therapy and imaging beam measurements were acquired with 13 and 1 mA, respectively. A source-to-isocenter distance (SID) of 35 cm is used for all measurements unless otherwise noted. The 220 kVp therapy beam uses a 0.15 mm Cu external filtration, with beams usually collimated with 10 x 10, 5 x 5, and 3 x 3 mm^2 square and a 1 mm diameter circular field sizes. MicroCT imaging is acquired using 40, 50, 60, 70, and 80 kVp beam energies with 1 mm Al external filtration, uncollimated (approximately 15 x 15 cm^2 field size at isocenter), and with a 360° rotating couch and stationary x-ray tube [111]. Therapy and imaging beams qualities were measured in our previous study and are listed in **Table 8.1** [109]. The distance from the source to the bottom of the collimator nozzles for the therapy beam were at a fixed 30 cm distance, and a 7.3 cm distance from the source to the bottom of the irradiator head for the open imaging beams.

Table 8.1: Measured beam characteristics for the therapy (220 kVp) and imaging (40–80 kVp) beams used for scintillator measurements.

Tube Voltage (kvp)	220 kVp	80 kVp	70 kVp	60 kVp	50 kVp	40 kVp
Tube Current (mA)	13.0	1.0	1.0	1.0	1.0	1.0
Added Filtration (mm Al)	0.15 Cu	1.0	1.0	1.0	1.0	1.0
HVL (mm Al)	0.67 Cu	1.53	1.34	1.17	1.02	0.83
Dose Rate (cGy/min)	363	5.75	4.56	3.40	2.25	1.23

8.2.3 Setup

The scintillator was irradiated at a 35 cm source-to-detector distance (SDD) for all therapy and imaging beam measurements at isocenter, with the x-ray source positioned at a 0° gantry angle. The treatment couch was replaced by a 5 mm thick foam (polystyrene) block (**Figure 8.2**). The scintillator was centered by attaching the 1 mm diameter collimator and shifting the scintillator in the x-y plane (plane perpendicular to the beam axis) using the SARRP positioning software until the highest scintillator response for the therapy beam was obtained. Centering along the z-axis (plane along the beam axis) was accomplished by using plastic SDD pointers machined in-house. The SDD pointers were machined within a ± 30 μm accuracy to the desired length, allowing for z-axis placement of the detector to be estimated less than a 0.1 mm uncertainty, which had a negligible effect on scintillator positioning uncertainty in the z-direction.

Air kerma measurements were performed to help characterize the scintillators output (μC), sensitivity (output charge per unit dose), linearity, and in-air profile measurements. The scintillator probe was replaced by a 0.6 cc PTW 30013 farmer-type ionization chamber (PTW, Freiburg, Germany) and held in-air by a stand at isocenter.

8.2.4 Irradiations

Dark current readings (approximately 3.9 nA) were subtracted from each measurement. The dark current contribution was 2.9% of the total signal for the 220 kVp therapy beam, and ranged from 19.9% to 33.2% for the 80 and 40 kVp imaging beams, respectively. We started collecting electrometer measurements 5 seconds af-

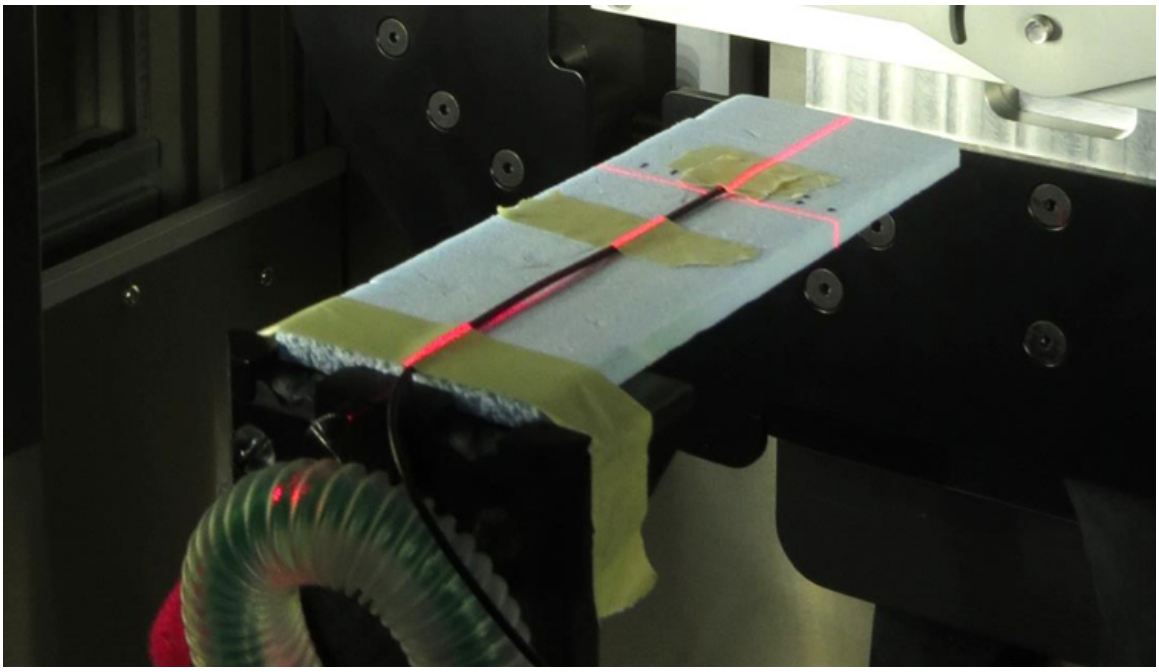

Figure 8.2: Experimental setup for scintillator dosimetry within the SARRP, with scintillator probe on foam block secured to table column (table removed).

ter the initial beam ramp-up to allow for the beam to stabilize. An average of three successive readings were performed for all scintillator and ionization chamber measurements. Contributions to the signal encountered by the stem effect was small, and found to be only 0.1% of the entire signal. Setup uncertainty was estimated by obtaining the standard deviation from different scintillator readings after taking down and reassembling the setup.

Scintillator Sensitivity

Scintillator sensitivity was obtained from measurement of the scintillator response and air kerma (in Gy) at isocenter with uncollimated fields for all therapy and imaging beams. Air kerma was obtained using a 0.6 cc PTW 30013 farmer-type ionization chamber, irradiated 0–50 Gy and 0–5 Gy for therapy and imaging beams, respectively, with measurements corrected according to the American Association of Physicists in Medicine Task Group 61 (AAPM TG-61) [136]. The scintillator was then irradiated for the same amount of time as the ionization chamber.

Scintillator response as a function of tube current was also obtained in the same fash-

ion as sensitivity readings. The scintillator and ionization chamber were irradiated up to the maximum tube currents of the 220 kVp therapy (13 mA) and 40, 50 , 60, 70, and 80 kVp imaging beams (16, 12, 10, 9, and 8 mA, respectively), using 1-minute irradiation times.

Beam Profiles

Therapy beam profiles were acquired in-air using the scintillator with 5 x 5 mm^2 and 3 x 3 mm^2 square fields with the scintillator positioned at 35, 37, and 39 cm SDDs. Off-axis resolution was 0.25 mm, and a 10-second irradiation time was used for each measurement point. High positioning accuracy was achieved by moving the couch column controlled by the SARRP software, with a position accuracy shown to be 0.2 mm [140].

Profile measurements were also acquired using EBT3 film to assess volume averaging effects, with results displayed in the Discussions section. EBT3 film was placed in-air (extending beyond the foam couch) at the 35 cm source-to-isocenter distance and irradiated with the 5 x 5 and 3 x 3 mm^2 square beams, and the 1 mm circular beam for 100 seconds. The film results were normalized to an equivalent 10 second irradiation time to match scintillator readings. After 24 hours, the film was scanned using an Epson model 10000XL scanner at 600 dpi, with the film previously calibrated for the 220 kVp therapy beam [109]. For additional verification, film was simulated in DOSXYZnrc as a 0.350 mm thick, 3 x 3 cm^2 sheet of water under the same irradiation geometry. All profiles were compared.

8.2.5 Monte Carlo Simulations

A previously validated in-house MC model [109] of the SARRP was created in BEAMnrc [170] using the EGSnrc MC code [118] and used to characterize our scintillator. MC-derived spectra were used to obtain mass energy-absorption coefficients to correct scintillator output, and scintillator profile measurements were compared to MC simulations for measurement validation. All MC simulations ran on an Intel Core i7-6700HQ CPU 2.6 GHz quad-core personal laptop.

Spectral Correction with Birks Model

Due to the need for spectra-weighted mass energy-absorption coefficients to correct the response of polystyrene [29,199], an accurate model of the spectra of the measured beam must be obtained. In addition, the model must also account for situations that may change the original spectra of the beam at the location of dosimetry, such as changes in media between the source and detector, detector off-axis position, distance from the source, and beam collimation. These changes to the original spectra cannot easily be accounted for using analytical software such as SpekCalc [162]. Our MC model generated spectra by creating phase space files at the point of dosimetry, between the polystyrene active volume and polyethylene jacket interface, and inputting them into BEAMdp [135]. Spectra were obtained at all points of dosimetry described in sections 8.2.4 and 8.2.4. Correction to scintillator output ε_λ was obtained by

$$\varepsilon_\lambda = \alpha_\lambda \left[P_{sheath,\lambda}\psi_\lambda\right]^{-1}, \tag{8.1}$$

where λ is a given beam energy in kVp, α_λ is the ionization quenching factor (for the active scintillator volume) defined by the Birks quenching model [25] and obtained from Boivin *et. al* [29], and ψ_λ is the MC spectral correction coefficient. The spectral contribution is corrected from unity (spectra at calibration conditions) to a value between 0 and 1 as determined by ψ_λ. The attenuation coefficient from the polyethylene jacket $P_{sheath,\lambda}$ is defined as

$$P_{sheath,\lambda} = \int_0^\infty \phi_\lambda(\nu) e^{-\frac{\mu}{\rho}(\nu)x} d\nu, \tag{8.2}$$

where $\phi_\lambda(\nu)$ is the photon fluence of the spectra for a given photon energy $h\nu$ [128], $\frac{\mu}{\rho}(\nu)$ is the polyethylene mass attenuation coefficient applied to every respective energy bin of the spectra, x is average jacket thickness in the beam direction (0.61 mm) and ρ is the density of polyethylene (0.940 g cm^{-3}). MC spectral correction ψ_λ is the convolution of the complete photon energy fluence with every respective energy bin of the spectra, defined as

$$\psi_\lambda = \frac{\int_0^\infty \left(\frac{\mu_{en}}{\rho}(\nu)\right)_{scint} \phi_\lambda(\nu) d\nu}{\int_0^\infty \left(\frac{\mu_{en}}{\rho}(\nu)\right)_{med} \phi_\lambda(\nu) d\nu}, \tag{8.3}$$

where $\frac{\mu_{\text{en}}}{\rho}(\nu)$ are the mono-energetic mass energy-absorption coefficients of the scintillator material (polystyrene) and outside medium (air), obtained from the the National Institute of Standards and Technology (NIST) tables [94].

Spectral Correction with Air Kerma Calibration

An empirical method was also analyzed to account for ionization quenching as well as any physical process leading to energy absorption within the detector volume. The air kerma calibration correction $\xi_{\lambda,\,m}$, is defined by

$$\xi_{\lambda,m} = N_{\lambda,c} \left[\frac{P_{sheath,\lambda,m} \psi_{\lambda,m}}{P_{sheath,\lambda,c} \psi_{\lambda,c}} \right]^{-1}, \tag{8.4}$$

where c denotes measurement conditions used for scintillator air kerma calibration, obtained with an uncollimated beam at isocenter, and m denotes scintillator measurement. The air kerma calibration factor $N_{\lambda,\,c}$ is expressed in Gy C^{-1}, and $\frac{\psi_{\lambda,\,m}}{\psi_{\lambda,\,c}}$ is the ratio of MC spectral corrections for measurement and calibration conditions, computed as described in **Equation 8.3**.

The air kerma calibration factor, for a given beam energy λ, is defined as $N_{\lambda,\,c} = \frac{K_{\lambda,\,c}}{M_{\lambda,\,c}}$, where air kerma $K_{\lambda,\,c}$ is obtained with the ionization chamber at isocenter (calibration point), and the scintillator reading $M_{\lambda,\,c}$ is calibrated by obtaining scintillator measurement at the same calibration point. Any photon attenuation by the ionization chamber wall for air kerma measurements are corrected for by the chamber calibration performed at the National Research Council (NRC). All air kerma measurements with the ionization chamber and corresponding scintillator measurements were acquired for the same amount of time. The correction obtained using $\xi_{\lambda,\,m}$, for a given beam energy, bypasses the need to obtain complex ionization quenching factors by instead using an air kerma calibration factor, and corrects any changes to the photon spectra that deviate from the calibration conditions for in-air measurements off-axis and with distance from the source. This effectively calibrates the scintillator

output to dose with a single calibration measurement for a given tube voltage.

Profiles

Therapy beam profile simulations were acquired with 5 x 5 and 3 x 3 mm^2 square collimated fields at 35, 37, and 39 cm SDDs using 10 s irradiation times for each measurement location. A single air kerma calibration measurement was completed for all profile measurements using an open 220 kVp therapy beam at isocenter. This single calibration measurement was conducted every session. Each measurement point was then corrected spectrally for off-axis, collimation, and distance from the source relative to the calibration geometry through MC methods as described in section 8.2.5. All off-axis MC simulations used an active volume voxel size of 1 mm diameter and 1 mm length for the 5 x 5 and 3 x 3 mm^2 field sizes, moved in 0.20 mm increments. The polyethylene jacket and polystyrene scintillator were fully modeled to-scale of the actual scintillator in DOSXYZnrc [194] with simulations computing absorbed dose in Gy/particle. MC dose was directly converted into dose rate D_{MC}(Gy/min) from first-principles,

$$D(Gy/min) = \frac{MC \cdot I \cdot t}{q}, \tag{8.5}$$

where MC is the raw MC output in Gy/particle, I is the tube current in Amperes, t is the exposure time in seconds, and q is the charge of an electron in Coulombs. Absolute dose to the scintillator for profile measurements was determined by

$$D_{scint}(Gy) = \xi_{\lambda,m} M_{\lambda,m}, \tag{8.6}$$

where $\xi_{\lambda,\,m}$ is the correction factor defined in section 8.2.5, and $M_{\lambda,\,m}$ is the scintillator reading in Coulombs for a given beam energy, corrected for scatter contributions and dark current described in sections 8.2.3 and 8.2.4, respectively. Scintillator measurements were compared with MC simulations to validate our corrected scintillator profile measurements.

8.3 Results

8.3.1 Scintillator Response

Scintillator response as a function of air kerma for therapy and imaging beams are established. The difference in sensitivity between the therapy and 60 kVp imaging beam was 52.3%. It will be shown in section 8.3.2 how this difference can be partly corrected for. Scintillator correction factors and sensitivities for therapy and imaging energies are shown in **Table 8.2**.

Scintillator response as a function of tube current for therapy and imaging beams are displayed in **Figure 8.3**, as R^2 values for all beams were ≥ 0.999, with an average variance between three successive measurements of 0.3%, showing excellent scintillator linearity and precision. Increasing the tube current increases the dose rate, thus **Figure 8.3** illustrates that the scintillator response is independent of dose rate for a given tube voltage. Both ionization chamber and scintillator measurements were within a 0.3% variance between successive measurements. The positioning of the scintillator was more challenging to reproduce due to its small volume. Taking down and repositioning the scintillator setup over the course of three weeks produced a maximum change in output of 3%, while the relative ease of setup for the ionization chamber allowed for the setup uncertainty of 0.4%. This would add a 3% measurement uncertainty to the scintillator results presented.

Table 8.2: Scintillator sensitivity at isocenter before and after applying correction factor ε.

Tube Voltage (kvp)	220 kVp	80 kVp	70 kVp	60 kVp	50 kVp	40 kVp
Correction Factor ε	1.34	2.20	2.25	2.29	2.36	2.40
Sensitivity (μC/Gy)	2.41	1.32	1.29	1.26	1.23	1.21
Corrected Sensitivity (μC/Gy)	3.22	2.91	2.90	2.89	2.90	2.90

8.3.2 Spectral Correction with Birks Model

MC-calculated spectra for uncollimated therapy and imaging beams at isocenter are displayed in **Figure 8.4**. After applying the spectral correction factor ε_λ using **Equation 8.1** for therapy and imaging beams, we obtained the corrected scintillator output

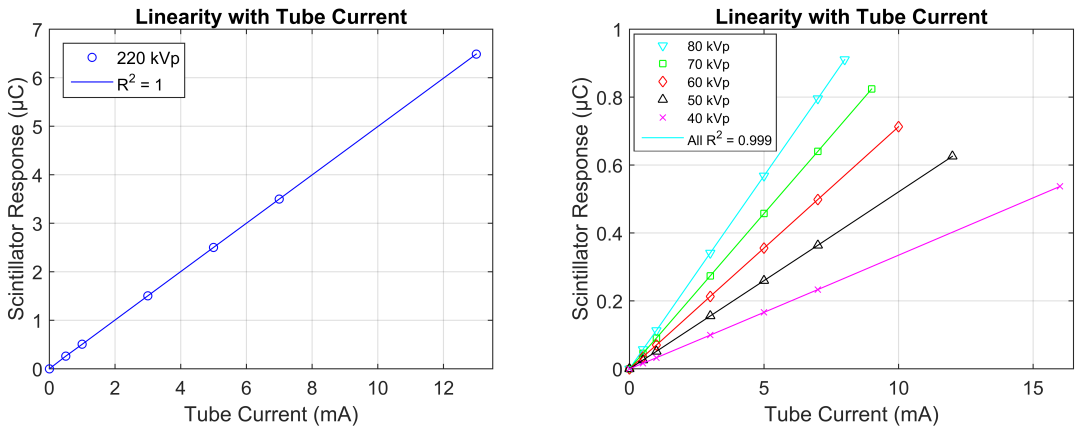

Figure 8.3: Scintillator response as a function of tube current demonstrating its independence on dose rate for the a) 220 kVp therapy beam and b) 40–80 kVp imaging beams for a 1-minute irradiation time.

shown in **Table 8.2**. The maximum percentage difference in scintillator sensitivity between imaging beams decreased from 8.3% to 0.7%. Percentage difference in sensitivity between the therapy and 60 kVp imaging beams was reduced from 52.3% to 10.2%. The variation of quenching factors is relatively well defined between the 40–80 kVp imaging energies, but the quenching factor becomes less defined and volatile for the 220 kVp energy, making it difficult to determine a proper quenching factor for the 220 kVp therapy beam. This illustrates that using the Birks quenching model for beam energies between 40–80 kVp corrects sensitivity appropriately; however, it does not fully correct our sensitivity for the 220 kVp beam. Due to this, the results of a different spectral correction using air kerma calibrations are shown in section 8.3.3.

8.3.3 Spectral Correction with Air Kerma Calibration

Mean differences in sensitivity between the therapy and 60 kVp imaging beams for the uncorrected measurements (**Figure 8.5a**), spectrally corrected measurements without the Birks quenching factor (**Figure 8.5b**), spectrally corrected measurements with the Birks quenching factor (**Figure 8.5c**), and spectrally corrected dose response with air kerma calibrations (**Figure 8.5d**) were 52.3%, 13.2%, 10.2%, and 0.3%, respectively. Thus, the air kerma calibration method produced excellent results.

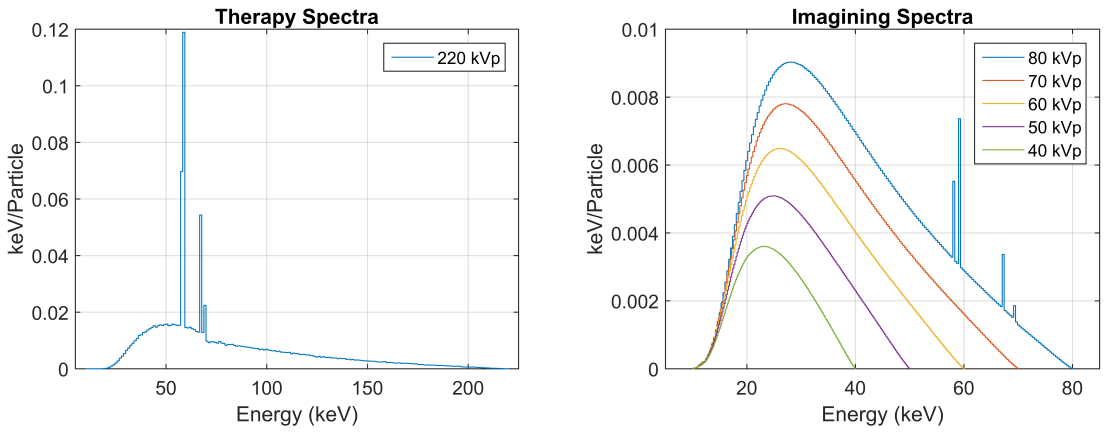

(a) **(b)**

Figure 8.4: MC-calculated spectra at isocenter for uncollimated a) therapy and b) imaging beams.

8.3.4 Profiles

Off-axis energy spectra obtained for the 220 kVp therapy beam and 3 x 3 mm^2 field size used for spectral corrections are shown in **Figure 8.6**. This illustrates the MC calculated spectra used for obtaining our off-axis profile measurement corrections for the air kerma calibration method. It also illustrates the amount of spectral changes that are incurred off-axis for a given field size. Spectra obtained off-axis resulted in reduced amplitude, but retained the central-axis spectra shape. The central axis spectral amplitude reduces to 50% at approximately 1.1 mm out from the central axis, and then rapidly after that. Relative to the center of the beam for the open, 5 x 5, and 3 x 3 mm^2 field sizes, Φ_{220} increased away from the center of the beam by approximately 0.5% at 80% of the central axis, and increased by 1.5% at FWHM. Maximum differences in Φ_{220} on the central axis at 35 and 39 cm SDDs for the open, 5 x 5, and 3 x 3 mm^2 field sizes were 0.1%. This suggests that the effect of spectral changes in-air with distance from the source for all field sizes is minimal along the central axis.

Corrected scintillator profile measurements plotted with MC simulations are illustrated in **Figure 8.7**. Average variance between three successive measurements was 0.6% for the 10-second irradiations. Mean and maximum percentage differences between measurement and MC simulations were 2.4% and 3.5%, respectively, for the 5 x 5 and 3 x 3 mm^2 field sizes at all three SDDs. The percentage differences in FWHM

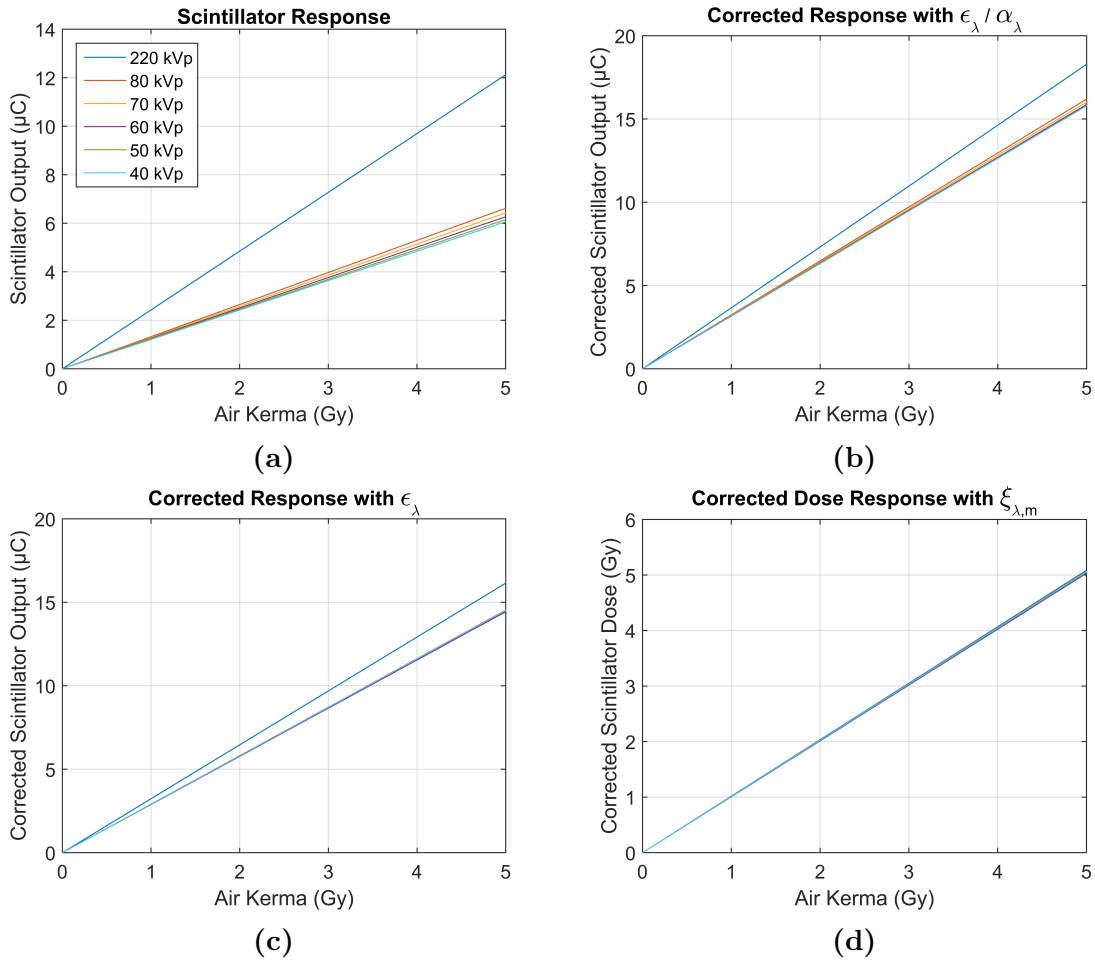

Figure 8.5: Scintillator response as a function of air kerma at isocenter a) before applying correction factors, b) after applying spectral correction without Birks quenching factor (α_λ), c) after applying spectral correction with α_λ, and d) after spectral correction with air kerma calibration.

between measurement and simulation for the 5 x 5 and 3 x 3 mm^2 field sizes at all three SDDs never exceeded 1.7%, showing good agreement in the penumbra region. Great care must be taken into positioning the scintillator for such small field sizes, as a 0.1 mm misalignment in scintillator position changed the FWHM dose by 4%. The 0.2 mm scintillator positioning shifts for profile measurements were a function of the ability of the SARRP positioning software. This positioning constraint is in contrast to high resolution 3D volumetric scintillator dosimeters that would not need to be translated [21].

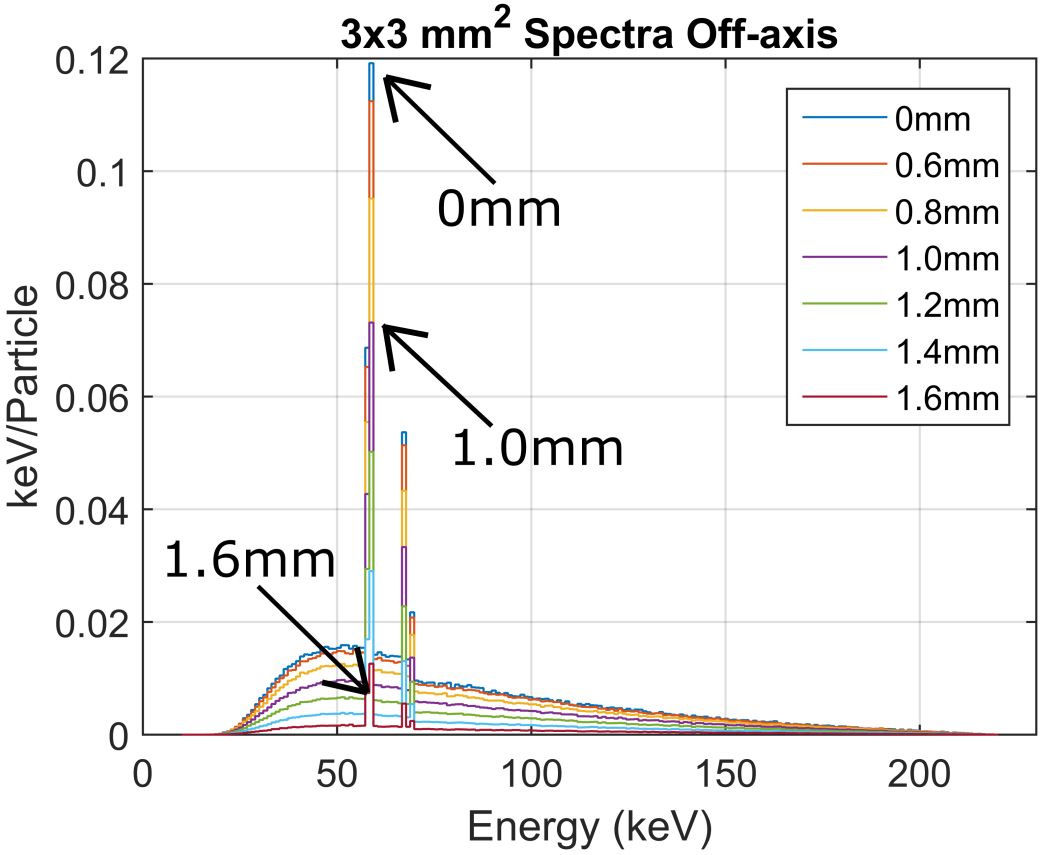

Figure 8.6: MC-computed off-axis spectral changes for the 220 kVp therapy beam and 3 x 3 mm^2 field size. Locations of obtained spectra, relative to the center of the beam, are displayed in the legend.

8.4 Discussion

Our small 1 mm diameter, 1 mm long polystyrene scintillator detector has been characterized for use in a small animal irradiator. We have obtained poly-energetic mass energy-absorption coefficients using MC simulations in conjunction with NIST tables to correct scintillator sensitivities for the 220 kVp therapy and 40–80 kVp imaging energies. This calibration method successfully corrected scintillator output, and produced agreement to within a mean relative difference of 2.4% between measurement and MC simulated in-air profiles for 5 x 5 and 3 x 3 mm^2 field sizes at 35, 37, and 39 cm SDDs. The in-house MC model in conjunction with the high precision, high resolution, small PSD will allow for resolution previously only achievable through radiographic film.

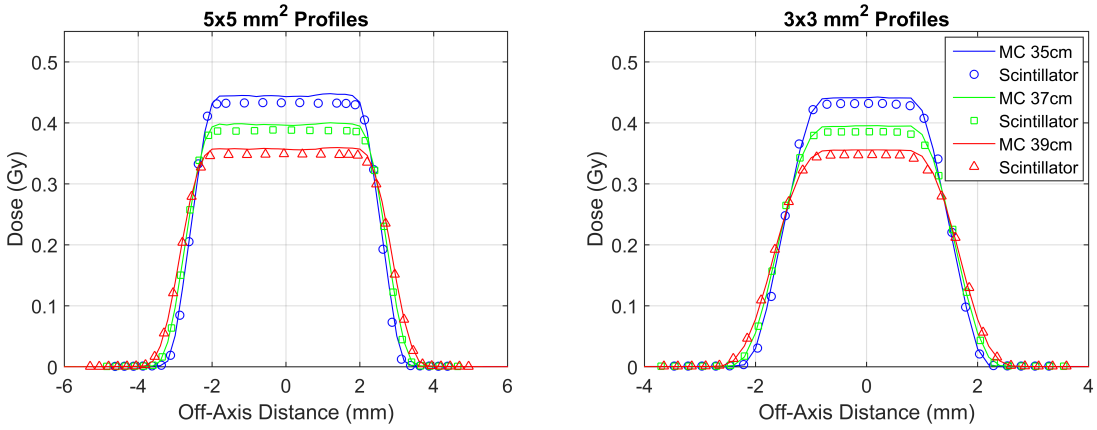

(a) **(b)**

Figure 8.7: MC-computed and scintillator measured in-air 220 kVp therapy beam profiles at 35, 37, and 39 cm SDDs for a) 5 x 5 and b) 3 x 3 mm^2 field sizes.

For field sizes larger than 5 x 5 mm^2, it has been shown that PSDs mitigate the partial volume effect for field sizes that are larger than the detector. MC simulations showed that PSDs obtain the closest agreement to a theoretical perfect detector compared to a number of ionization chambers, diamond, and diode dosimeters [70,115,152]. It was found that non-PSD dosimeters deviated in dose measurements by 7.4% to 35.0% due to the partial volume effect, where the PSD produced a maximum 1.7% deviation due to volume averaging for similar geometries and field sizes used in this study [18, 70]. Moreover, experimental measurements by Ralston *et al.* [165] and Morin *et al.* [146] have shown that PSDs are accurate enough in small field dosimetry to experimentally obtain correction factors for larger dosimeters.

The MC model of the scintillator is the same in dimensions as the scintillator used for experimental measurement (1 mm diameter and 1 mm length polystyrene active volume, with a surrounding 0.6 mm thickness in polyethylene sheath). This means that the MC profiles obtained in **Figure 8.7** are effectively modeling the volume averaging experienced by the experimental scintillator measurements.

However, to quantify the volume averaging effect, scintillator profile measurements for the 5 x 5 and 3 x 3 mm^2 square beam and smaller 1 mm circular beam were compared to EBT3 film measurement and MC film simulations in **Figure 8.8**. The mean difference between film measurement and MC film simulations compared to scintillator measurement for doses higher than 80% of D_{max} were 2.5% and 3.6% for

the 5 x 5 and 3 x 3 mm^2 field sizes, respectively. The difference in beam size between film measurement and scintillator measurement at 80%, 50%, and 20% of D_{max} are shown in **Table 8.3**. Small volume averaging can be noted in the penumbra edges of the 5 x 5 and 3 x 3 mm^2 fields. Scintillator measurements dropped off quicker at the beginning of the 80% beam penumbra and widened at the end of the 20% beam penumbra. This illustrates that volume averaging at the penumbra edges needs to be considered when measuring 5 x 5 and 3 x 3 mm^2 field sizes using a 1 mm diameter scintillator.

Table 8.3: Difference in beam sizes between film measurement and scintillator measurement at 80%, 50%, and 20% of D_{max} for the 5 x 5 and 3 x 3 mm^2 square, and 1 mm diameter beams in-air at a 35 cm SDD. The relative difference between film measurement (x) and scintillator measurement (y) is defined as (y - x) / x * 100%.

	5 x 5 mm^2 Square Beam			3 x 3 mm^2 Square Beam			1 mm Circular Beam		
Difference	80%	50%	20%	80%	50%	20%	80%	50%	20%
Absolute (mm)	-0.28	0.11	0.32	-0.20	0.04	0.21	-0.10	0.07	0.05
Relative (%)	-5.7	2.1	5.8	-7.6	1.3	6.1	-13.7	-6.1	3.2

To illustrate major volume averaging in the smaller 1 mm diameter field size (**Figure 8.8c**), a large discrepancy in central axis dose between scintillator measurement with both film measurement and simulation is demonstrated, showing a 20% lower scintillator response compared to film measurement and simulation. This discrepancy can be explained by previous studies showing that a lower response in central axis output for relatively large detectors in small fields can be attributed to volume averaging [134, 205]. It was expected that the penumbra of the 1 mm diameter profile measurements obtained with the scintillator would be wider than in the film data, as was the case at the end of the 20% penumbra region. However, the 80%–20% beam penumbra for the scintillator measurement was 0.47 mm, where this was at most 0.08 mm wider than the EBT3 film measurement and MC-simulated beam penumbra. These results quantify the large volume averaging effect that a 1 mm diameter plastic scintillator encounters when measuring small fields.

We compared in-air EBT3 film profile data (**Figure 8.8**) to a recent study that presented profiles at a 2 cm depth in solid water at a 35 cm SDD acquired with EBT3 film measurements [196]. The 50%–50% (field size) / 80%–20% (penumbra) film measurement from our study for the 5 x 5, 3 x 3 mm^2 square, and 1 mm circular diameter profiles were 5.09/0.35, 3.03/0.38, and 1.16/0.39 mm, respectively, compared

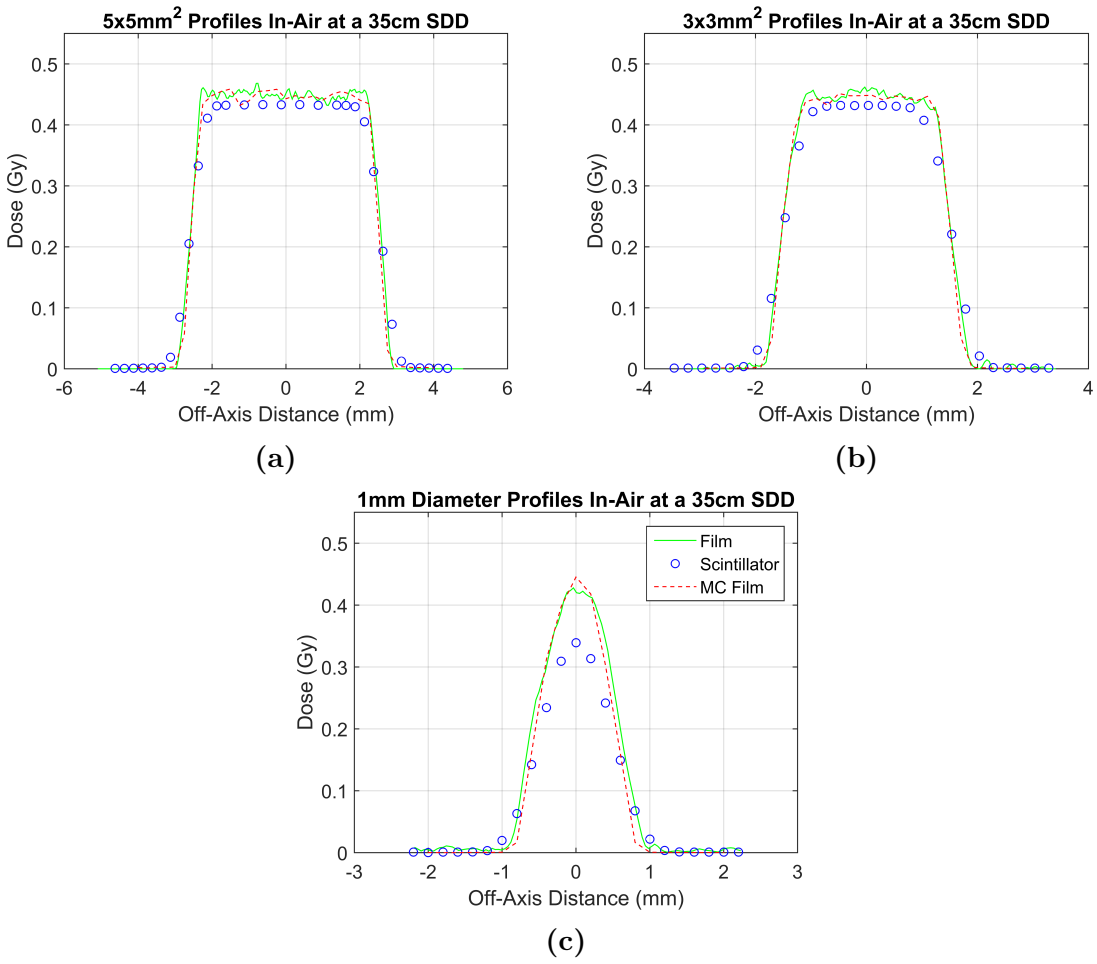

Figure 8.8: Comparison between scintillator measurement, EBT3 film measurement, and MC film simulations for a) 5 x 5, b) 3 x 3 mm^2 square, and c) 1 mm diameter profiles at a 35 cm SDD in-air.

to 5.04/0.23, 2.99/0.37, and 1.10 /0.36 mm, respectively, of the previous study.

A 10.2% discrepancy in correcting our scintillator sensitivity remained when using the Birks' quenching model. It has been shown that plastic scintillators have an energy dependence in the low kilovoltage energy range that can be described by ionization quenching, but obtaining ionization quenching factors is not straightforward. The most widely used method to quantify and correct for decreased light production at lower beam energies is through complex analysis of the Birks' quenching model [25]. Although the Birks quenching model is robust, further analysis has shown that no single Birks parameter (kB) can be used for all kilovoltage beam energies, and a variation of this parameter must be used to more accurately account for ionization

quenching [29].

A diversity in reported kB values [29, 71, 84, 104, 185, 195] has raised doubts about the validity of the Birks quenching model, where Williamson *et al.* [199] expressed concerns as the Birks quenching model failed to account for their measurements. While the Birks quenching model agreed with our measurements to within 10.2%, Boivin *et al.* [29] found a combination of kB values to agree within 5% of their measurements. This illustrates that ionization quenching may be more complex than previously thought, or possibly other contributions to the response of polystyrene scintillators may exist at low photon energies.

In a recent study, it was shown that a temperature dependence exists in BCF-60 scintillating fibers, and that increasing temperatures produced a decrease in light yield [154]. The authors stressed the need for more comprehensive studies to fully understand the physical mechanisms of light yield production in plastic scintillators. Due to our SARRP irradiator being housed with immune compromised mice in a temperature-controlled quarantined room, temperatures during all scintillator measurements were 22 $\pm$ 1° C. This small variation in temperature would produce a maximum $\pm$ 1% output difference in our measurements, and therefore can't alone account for the 10.2% difference we observed.

The complexities of ionization quenching may be avoided by instead applying air-kerma calibration factors as shown in **Equation 8.4**. This provides the advantage of bypassing the need for obtaining ionization quenching factors by simply calibrating the scintillator sensitivity in-air at isocenter for a given beam energy, and applying the ratio of mass energy-absorption coefficients between the measurement location and calibration location.

Due to backscatter, it was found that the presence of the foam block increased the scintillator readings by 13% and 15% for the therapy and imaging energies, respectively. It was found that the backscatter contribution from the 5 mm thick foam block was within a 2.6% difference of the backscatter produced by a 5 mm thick solid water slab. The relatively high backscatter can be attributed to a 4% greater effective atomic number in the dense polystyrene (foam) compared to that of water [121]. It has been previously shown that a 5 mm slab of solid water under similar geometries used in this study produced approximately 11% backscatter [62]. This suggests that the backscatter produced by the foam at low kV energies for the thin 5 mm block

thickness is comparable to water. Scintillator readings with the foam block were then reduced by backscatter readings in order to obtain the response of the scintillator without the foam. The scintillator was extended by 5 cm into the air to remove scatter contributions. The scintillator would sag/shift during couch shifts and profile measurements, so the foam block was used to provide reproducible measurements.

8.5 Conclusions

A plastic scintillator dosimeter system with a 1 mm diameter, 1 mm long active volume has been characterized for therapy and imaging beams of the Small Animal Radiation Research Platform (SARRP). The presented dosimeter system has been shown to have linearity, precision, and resolution for kilovoltage x-ray beams, making it an important detector for small fields. Spectral corrections have been obtained using a validated in-house Monte Carlo model together with NIST mass energy-absorption coefficients to correct scintillator energy response for conditions that modify the primary energy spectra of the beam. Future work will include expanding scintillator calibration and measurements for water and heterogeneous phantoms, *in-vivo* applications, and including a smaller 0.5 mm diameter scintillator. This dosimeter system presents steps towards implementing possible real-time measurements for dosimetric quality assurance and treatment and imaging dose verification for small animal irradiators.

8.6 Acknowledgments

I would like to thank Stephen Gray for his contributions towards scintillator dosimetry setup, and Dr. Samantha Van Nest for her invaluable help and discussions. This work was partly supported by NSERC Discovery Grants #435510-2013 and the Canada Research Chair program.

8.7 Summary

Presented was the characterization of a novel plastic scintillating dosimeter for the small fields and low energies found in an image-guided small animal irradiator. In combination with correction factors obtained through MC methods and measurement, the scintillator output was corrected and sub-cm field sizes were measured. This now brings us full circle from first determining microCT image quality, establishing the dose deposited from microCT scans of varying imaging protocols, to now experimentally measuring the dose delivered by an image-guided small animal irradiator.

To conclude the research of this dissertation, we will now discuss methods for maintaining a quality assurance program for an image-guided small animal irradiator. This is important, as the output and mechanical operations of an irradiator unit must be properly monitored on a regular basis to assure that the proper amount of radiation is being delivered to the location of interest as prescribed.

Chapter 9

SARRP Quality Assurance

"And how long have you been writing for?"

–Godspeed You! Black Emperor

Therapeutic and imaging x-ray devices require systematic and regular monitoring to assess any changes that may occur to the radiation output and mechanical operation over time. This monitoring is established through quality assurance (QA), where daily, weekly, monthly, or annual measurements are made to verify that the output and mechanical properties are consistent to what is expected. This is imperative, as any unforeseen changes to the radiation beam delivered can jeopardize the expected outcome of an experiment. Degradation of image quality needs to be assessed as well, where high quality images are required for the radiation dose prescribed to be accurately delivered to the target. Radiation output and mechanical quality are different between machines, even between the same models, so baseline measurements must be performed to establish machine-specific performance. The inaugural baseline measurements are usually performed during commissioning when a machine is first acquired, where commissioning data is held as the gold standard to what future QA measurements are compared to. The QA tests performed in this chapter are recommended to be completed on a monthly or annual basis, as described below.

9.1 Monthly QA

9.1.1 Absolute Dose

Absolute dose measurements should be completed on a monthly basis to ensure that the output of the SARRP is not changing with time. Absolute dose measurements are to be carried out following the methods of section 6.2.2. Briefly, an ionization chamber is placed at the 35 cm SDD isocenter, with the ionization chamber located at a 2 cm depth within the solid water at a 33 cm SSD. This is to be carried out for the 220 and 60 kVp therapy and imaging beams, respectively, for a one-minute irradiation time. The raw ionization chamber output is then corrected for temperature, pressure, ion recombination, polarity effect, and electrometer accuracy based on **Equation 6.1** found in the AAPM TG-61 protocol. **Table 9.1** displays our annals of absolute dose measurements (labeled in-water) from the time of commissioning the SARRP at UVIC on August 16th, 2016, to the most recent measurements on April 22nd, 2018.

In **Table 9.1**, large fluctuations of up to 11% can be seen in the in-water dose column which was due to limitations in our setup reproducibility. The initial, reproducible jig lent to UVIC from Xstrahl for the commissioning of our SARRP was returned shortly after commissioning. Due to the large (30 x 30 x 4.5 cm^3) and heavy solid water slabs available to UVIC to house a PTW ionization chamber for our in-house absolute dose measurements, it was impossible to place the ionization chamber at isocenter within the solid water on the SARRP couch. This was because the SARRP couch could not support the weight of the large solid water slabs, as it was designed for the much lighter weight of small animals. In order to support the solid water slabs, the slabs were placed on top of a biohazard bin that was placed at the bottom of the SARRP stage. While this successfully supported the solid water slabs, there was a slight bow at the bottom of the stage that prevented a reproducible setup. The difference from the commissioning dose rate of 3.63 Gy/min to the 3.47 - 3.52 Gy/min range, illustrated in **Figure 9.1**, is due to a difference in setup from the Xstrahl commissioning jig, namely the non-level nature of out in-house setup, and the amount of extra backscatter produced by Xstrahl's jig compared to our biohazard bucket that the solid water rested on.

Table 9.1: Absolute Dose in-water (33 cm SSD at 2 cm depth) and in-air (35 cm SDD) air kerma for the 220 kVp therapy (and 60 kVp imaging beam where noted), including absolute dose in-water (84 cm SSD at a 0.5 cm depth) and in-air (84.5 cm SDD) air kerma for whole-body mouse irradiations at the bottom of the SARRP, using a PTW ionization chamber. HVL measurements were acquired at a 50 cm SDD, and commissioning date was August 16th, 2016. Note: The therapy beam parameters were 220 kVp, 13 mA, one minute irradiation, while imaging beam parameters were 60 kVp, 1 mA, one minute irradiation.

	Isocenter			
QA Date	In-Water (Gy/min)	In-Air (Gy/min)	1^{st}HVL (mm)	2^{nd}HVL (mm)
Commissioning	3.63	–	0.67 Cu	2.24 Cu
April 6th, 2017	3.24	2.65	–	–
May 5th, 2017	3.47	2.70	–	–
June 13th, 2017	3.47	2.68	–	–
August 14th, 2017	3.52	2.70	–	–
April 22nd, 2018	3.46*	2.66	0.69 Cu	2.38 Cu
May 5th, 2017 (No Filter)	5.54	18.85	–	–
	Imaging Beam			
September 9th, 2016	3.40 (cGy/min)	–	1.17 Al	3.17 mm Al
April 22nd, 2018	3.86 (cGy/min)*	5.45 (cGy/min)	1.26 Al	3.37 Al
	Whole-Body Irradiations			
September 9th, 2016	0.67	0.57	–	–
April 22nd, 2018	0.67	0.58	–	–

*Absorbed dose measurement obtained with EBT3 film in solid water (33 SSD at a 2 cm depth).

On April 22nd, 2018, EBT3 film was used at a 2.1 cm depth of a much smaller and lighter 6 x 6 x 4.2 cm^3 solid water phantom at a 33 cm SSD to obtain a reproducible setup for absolute dose measurements. EBT3 film was used as described in **Appendix B**. Due the cost and time consuming nature in calibrating film for a given beam energy, air kerma measurements are instead recommended, unless a small lightweight solid water slab specially machined for a pinpoint chamber can be obtained in the future. For the imaging beam, the increase in absolute dose from 2016 to 2018 may be attributed to a difference in dosimeter, as film was used in 2018, where low kV film calibrations have been known to be challenging. Unfortunately, no in-air imaging beam outputs at isocenter were taken before April 22nd 2018 to serve as a comparison.

Additional measurements were taken with the therapy beam, without the external Cu filter on May 5th, 2017, to serve as a baseline for output without external filtration

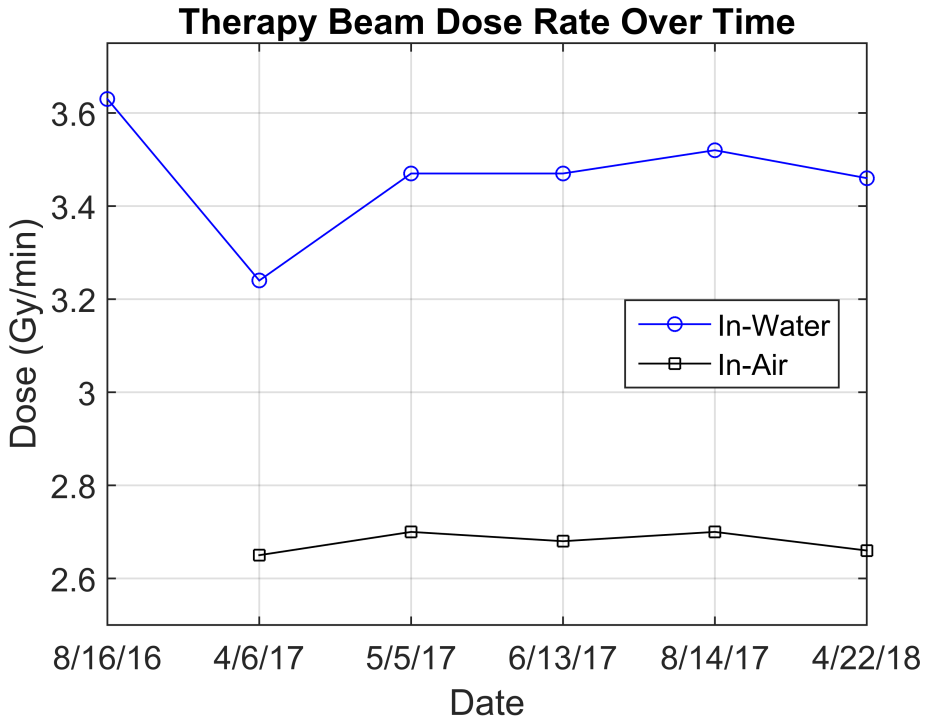

Figure 9.1: In-Water (33 cm SSD at 2 cm depth in solid water) and In-air (35 cm SDD) dose rate for the 220 kVp therapy beam, irradiated for 60 seconds. Dose rates obtained between August 2016 to April 2018.

to be compared to future output measurements. The purpose of this will be to assess if output changes over time independent of the filter (as our filter has been changed in the past). Also, TBI irradiation experiments are occasionally performed at the bottom stage of the SARRP, with stage bottom 85 cm from the x-ray source, with dose rate obtained by placing an ionization chamber at a 0.5 cm depth in a 30 x 30 x 1 cm^3 solid water phantom at the stage bottom. HVL is also presented, but will be discussed bellow under annual QA in section 9.2.1.

9.1.2 Air Kerma

In light of the difficulties in absolute dose measurement setup with our available resources, air kerma measurements are recommended in place of absolute dose in solid water within the SARRP. In-air measurements are presented in **Table 9.1**. Air kerma measurements are obtained by holding an ionization chamber in-air at isocenter with a stand, and irradiating for one minute for the 220 and 60 kVp therapy

and imaging beams, respectively. The output is then corrected based on the in-air method found in the AAPM TG-61 protocol. This more simplistic setup is highly reproducible within the SARRP, with its reproducibility illustrated by the consistent in-air readings shown in **Figure 9.1**. Initially, it was thought on April 6th, 2017, that our dose rate had changed drastically due to our filter being changed, however on May 5th, 2017 it was verified through consistent air kerma measurement that the change in in-water dose was due to a non-reproducible setup and not a change in dose rate, as the air kerma remained consistent. Thus, based on the more consistent in-air dose rate measurements compared to the in-water dose rate measurements illustrated in **Figure 9.1**, it is recommended that in-air dose rate measurements be performed to verify the Xstrahl SARRP dose rate for monthly QA.

9.1.3 Image Quality

Treatment planning and image-guided treatment delivery can be limited by the quality of the microCT scan obtained. A lack of spatial resolution or too much noise can negatively affect the ability to properly locate a tumor, segment critical structures, deliver the prescribed dose, and overall degrade the quality of a treatment. In order to catch degradation of imaging quality before it becomes an issue, image quality must be assessed on a regular basis.

Following the microCT imaging quality tests presented in section 5.2.2 using the same Shelley phantom, a new microCT scan was taken at UVIC nearly two years after the original scan. The Shelley phantom scan on April 22nd 2018 was then compared to the original scan on June 13th 2016. The comparison is displayed in **Figure 9.2**. Both data sets were acquired using an imaging protocol of 60 kVp, 0.8 mA, 60 second scan time, 6 fps, 0.325 voxel size, and pancake geometry.

CT Number Linearity, SNR, Noise, MTF, and geometric accuracy, resulted in percentage differences of 19.9%, 16.9%, 17.2%, 4.7%, and <0.3%, respectively, with R^2 values of 0.992 (2016) and 0.962 (2018). These large percentage differences illustrate that the microCT data is much nosier than two years ago. This difference may be due to the liquid in the vials further evaporating and larger air bubbles being formed since our first scan, which may have possibly lead to changes in liquid concentration per vial. The CT linearity and SNR percentage differences are with respect to the 30

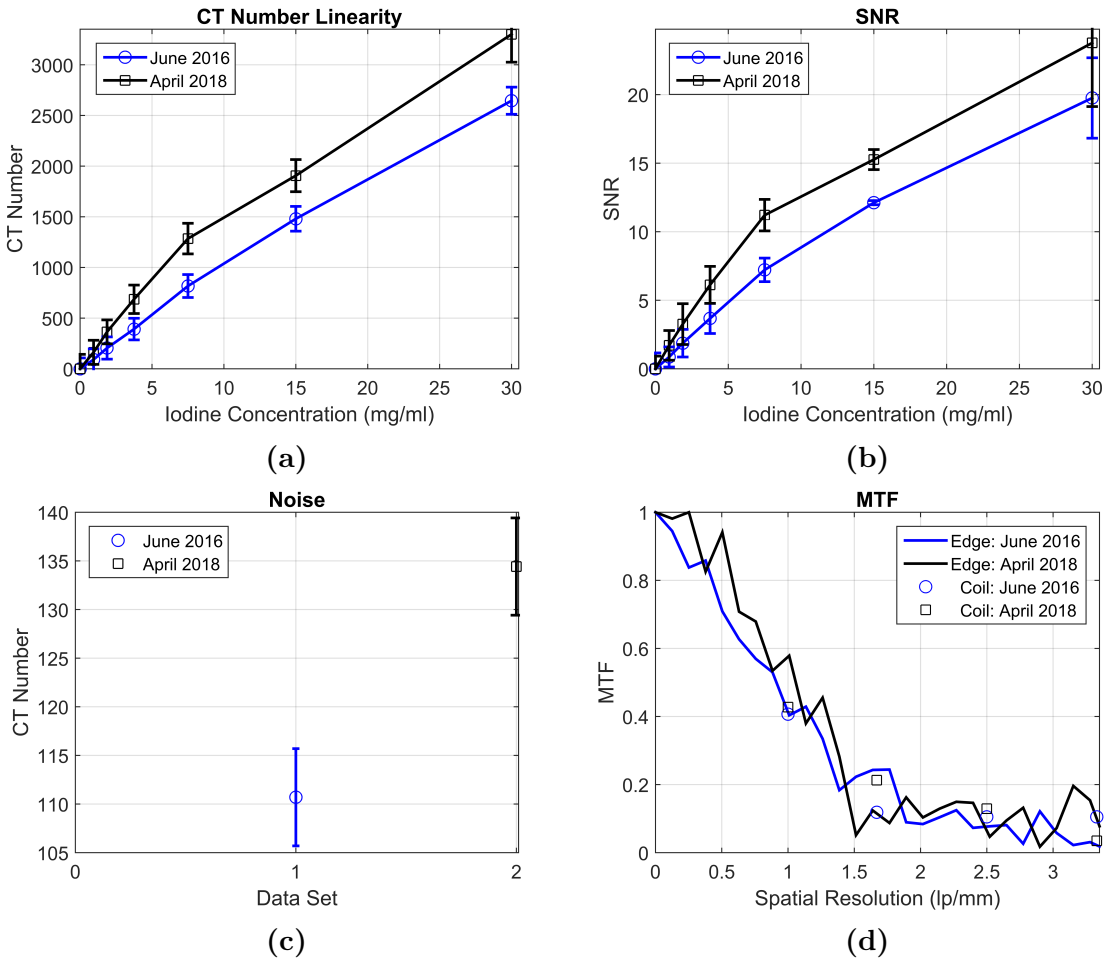

Figure 9.2: MicroCT image quality over time from June 13th 2016 (3 months after SARRP irradiator was acquired) compared to April 22nd 2018 under an imaging protocol of 60 kVp, 0.8 mA, 60 second scan time, 6 fps, 0.325 voxel size, and pancake geometry, comparing a) CT linearity, b) SNR, c) Noise, and d) slanted edge and coil MTF

mg/mL vials, where the change in concentration withing the vials of the 2018 scan produced higher SNR even with higher noise. These changing liquid vials over time caused difficulties in using SAPA for the newer scans, as the ROIs for CT linearity and SNR had to be reprogrammed in light of the evaporation. In terms of resolution, the coil MTFs between scans are within statistical differences, however, the slanted edge MTF for the 2018 scan was more volatile, likely due to the increased noise within the scan compared to the 2016 scan.

The SARRP manual recommends to perform a flood field calibration of the flat panel

detector after changing the tube voltage and tube current for microCT imaging. Since both the tube voltage and tube current did not need to be changed for imagining QA scanning in June 2018, the flood field calibration was not performed. However, even if the tube voltage and tube current do not need to be changed, it is best practice to perform a flood field calibration of the flat panel detector for all future monthly imaging QA scans. This will ensure that the detector gain for each pixel of the flat panel detector is properly calibrated on a monthly basis, as a safeguard in the event that calibration may be needed.

Beam hardening caused high noise due to the relatively large size of the Shelley phantom, and coupled with evaporation within the vials and the high cost of the Shelly phantom, a smaller, 100% solid material phantom should be used in the future. Our group has validated a heterogeneous 3D printed mouse-like phantom to be more representative of actual microCT scanning conditions carried out in the SARRP [31].

9.2 Annual QA

In addition to the above monthly QA tests, a number of QA tests should also be performed on an annual basis. The following tests evaluate the performance of the SARRP that are less likely to be in need of maintenance, as the characteristics are not expected to change as quickly as the ones for which are tested on a monthly basis, but are still important to evaluate to assure that the irradiator is operating as expected.

9.2.1 HVL

The HVL is determined based on the methods of section 6.2.2. Briefly, a PTW ionization chamber is placed in-air with a stand at a 50 cm SDD, with varying Cu (therapy beam) and Al (imaging beam) thicknesses placed in between the source and the ionization chamber to attenuate the beam to half its output. Experimental HVL measured within the SARRP at UVIC are displayed in **Table 9.1**. We measured first and second HVLs at time of commissioning on August 15th 2016 (September 9th, 2016 for imaging HVL) and again on April 22nd, 2018.

The 2016 and 2018 therapy beam HVL data were in relatively good agreement as the first and second HVLs were within 3% and 6%, respectively. Also, the most recent imaging beam HVLs were within a 7% difference for both first and second HVLs of the 2016 data. Percentage differences can be attributed to change in filter thickness between the years, as when our filter holder broke after our 2016 measurements, Xstrahl replaced both our filter holders and the filters. It has been shown that even small 0.05 mm Cu changes in filter thicknesses for ultra-thin filters ($\leq$ 0.30 mm) in kilovoltage dosimetry can change the properties of the beam [161].

9.2.2 Treatment Targeting Accuracy

Treatment targeting accuracy evaluates the spatial accuracy of the therapy beam to the isocenter of a planned image-guided irradiation. This is important as it validates if the treatment planning software is actually delivering the radiation dose to the prescribed location. The SARRP irradiator is quoted as being accurate up to 0.2 mm [140].

A pinhole approximately 1 mm in diameter was made by a thumbtack within EBT3 film. The film was then placed inside a solid water phantom specially machined to house film within its center. The phantom with film was then microCT scanned within the SARRP to obtain the location of the pinhole to use as the irradiation target in the treatment planning software of the SARRP. The center of the pinhole was placed at the isocenter in the treatment planning software, and dose was delivered using the 1 mm diameter collimated therapy beam. Three beams parallel to the film with gantry angles of -120°, 0°, and 120° were used to irradiated the target (**Figure 9.3**). This process is well known as a star-shot test. The distance from the center of each beam to the center of the pinhole was measured in mm using analysis software Fiji.

Gantry angles of -120°, 0°, and 120° resulted in deviated distances of 0.17, 0.18, and 0.23 mm, respectively, from the target. All results are within ±0.03 mm of the SARRP's target planning ability of 0.2 mm accuracy [140].

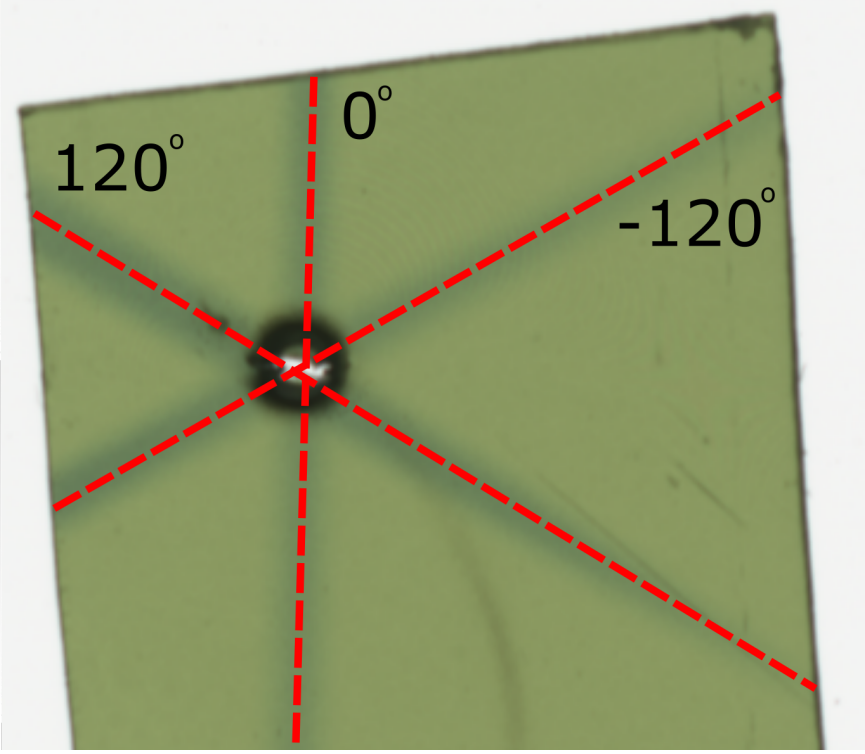

Figure 9.3: Film scan of our targeting phantom and pin-hole target, as the 1 mm diameter beam irradiated the target in the treatment plannng software at -120°, 0°, and 120° gantry angles.

9.2.3 Treatment Planning Dose Calculation Accuracy

Treatment planning dose calculation accuracy evaluates the accuracy of the dose calculations of the treatment planning software in terms of comparing the actual delivered dose to the intended prescribed dose. This is very important, as it validates if the treatment planning software is actually delivering the prescribed radiation dose that is expected.

The 6 x 6 x 4.2 cm^3 solid water phantom with similar setup (section 9.1.1) was used, with the phantom positioned at a 33 cm SSD with EBT3 film placed at a 1.5 cm depth within the phantom. After obtaining a microCT scan of the phantom within the SARRP (without the EBT3 film in place), the phantom was segmented as water (**Figure 9.4**) and a prescribed dose was set to deliver 5.0 Gy in a single fraction (gantry at 0°) at a 1.5 cm phantom depth in the treatment planning software.

The EBT3 film was scanned approximately 24 hours later and a dose of 4.52 Gy

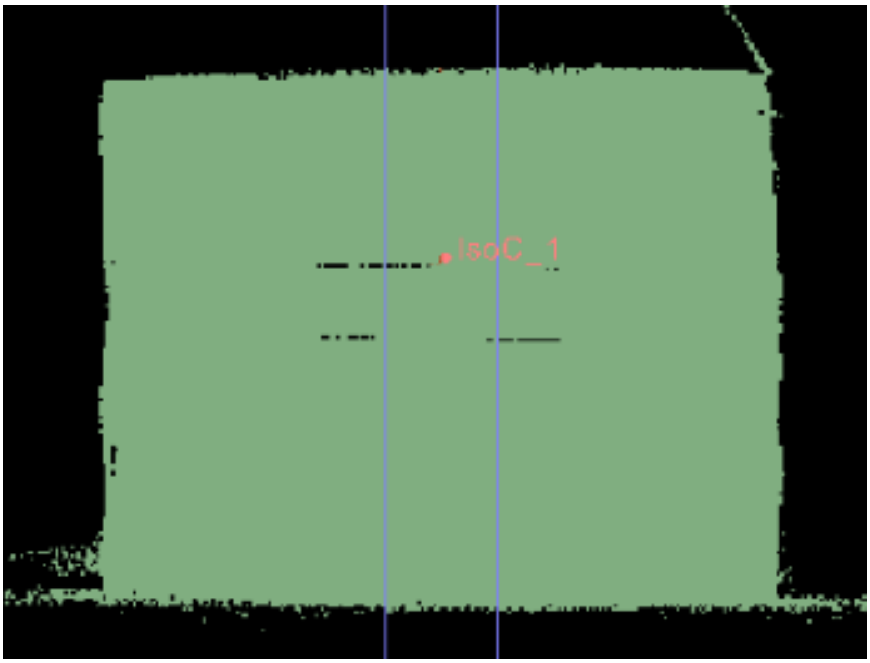

Figure 9.4: Pictured is a segmented 6 x 6 x 4.2 cm^3 solid water phantom in the Muriplan treatment software after microCT scanning. Dose calculations were taken and EBT3 film was placed at a 1.5 cm depth within the solid water phantom, with a 33 cm SSD and 1 x 1 cm^2 collimator, irradiating to a prescribed dose of 5.0 Gy.

was obtained from the film using our film calibration curve obtained for another study [63]. This resulted in 9.6% less dose than what was prescribed. The manual for the treatment planning software used by the Xstrahl SARRP, Muriplan, quotes a dose measurement vs dose calculation accuracy of 5%, including dose calculations overestimating beam penumbra by 1 mm for a 10 x 10 mm^2 field size. The current measurement-based dose calculation algorithm employed by the treatment planning software uses solid water PDD and profile measurements with various field sizes and SSDs to obtain beam fluence maps for dose calculations. Overall, this measurement-based fluence method lacks the degree of dose calculation accuracy that can be obtained through MC methods. Incorporating MC methods into the treatment planning system in the future will greatly improve dose calculation accuracy within the Xstrahl SARRP, as MC methods are the gold standard for dose calculations. Another source of error is in the EBT3 film measurement uncertainties, stated to be within 3.2% for similar dose measurements within a small animal irradiator [150].

Further dose calculation validation would benefit from a small solid water phantom specially machined for a pinpoint ionization chamber as an accurate means of treat-

ment planning dose output verification. Currently, our larger solid water slabs (30 x 30 x 2 cm^3) machined for our PTW farmer-type ionization chamber is too large to be microCT scanned within the SARRP.

The uniformity of the most commonly used 10 x 10 mm^2 collimator for the treatment beam was also assessed. Film was irradiated at a 2 cm depth in solid water at a 33 cm SSD in the 6 x 6 x 4.2 cm^3 solid water phantom and the film was scanned approximately 24 hours later. After window and leveling of the film, it can be seen that there was an oval-shape with a higher intensity than at the edges (**Figure 9.5**). This change in beam intensity was quantified in image analysis software Fiji, and it was found that the oval (displayed in **Figure 9.5**) had on average an 8.9% higher absolute dose than the dose near the edges of the field. This was also verified after looking at the commissioning film data, as this effect also existed at time of commissioning. This has also been documented as a problem for microbeam radiotherapy within the SARRP that used the 10 x 10 mm^2 square collimator [63].

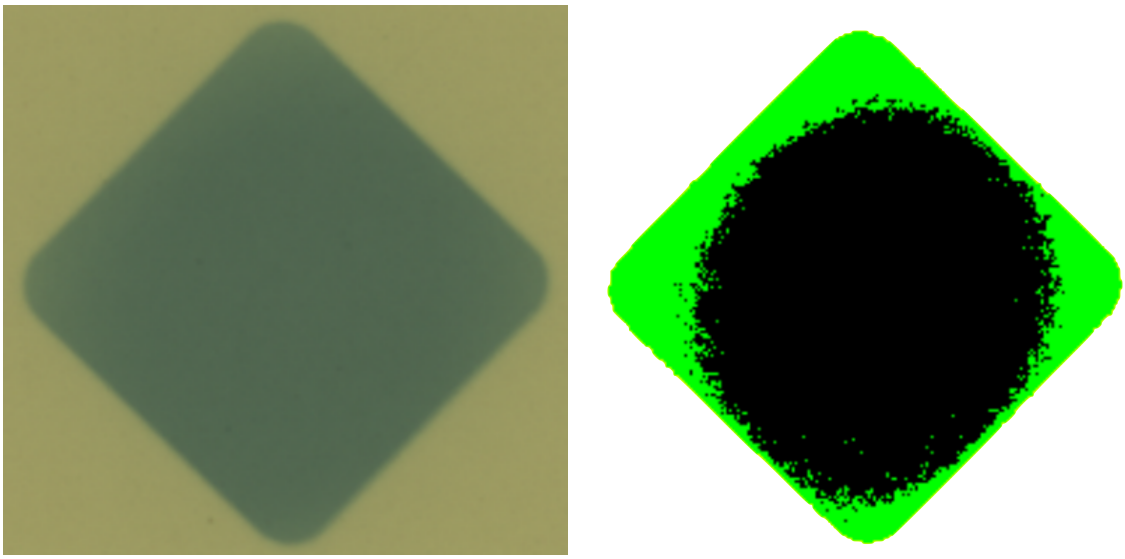

(a) **(b)**

Figure 9.5: Film scan of 10 x 10 mm^2 field size with at a 33 cm SSD in 2 cm of solid water with a) normal window and leveling, and b) after window and leveling to illustrate a non-uniform oval intensity (on average an 8.9% higher dose within the oval compared to the green region within the 10 x 10 mm^2 radiation field).

9.2.4 Laser Alignment

The alignment of the lasers to the isocenter was also examined. Lasers are important for visual placement of objects on the couch to align to isocenter, or to position an ionization chamber for in-air output measurements, but is not used for treatment purposes. If the positioning of the lasers changes over time, and the lasers are used for ionization chamber placement during output measurements, output measurements may change.

The location of the lasers relative to the radiation isocenter was examined. Film was first taped on top of the 6 x 6 x 4.2 cm^3 solid water phantom at a 35 cm SSD using an SSD pointer machined in-house, so that the EBT3 film was positioned at isocenter. Following the projection of the laser light onto the film, a pen and ruler were used to draw the center of the laser positions onto the film in the x- and y-axis directions as shown in **Figure 9.6a**. The phantom was irradiated for 2 minutes with the 1 mm diameter circular collimator, and then irradiated again for an additional 1 minute with the 3 x 3 mm^2 square collimator to help better visualize the radiation isocenter. A second EBT3 film was then taped along the side of the solid water phantom and the couch was moved so that the side surface of the phantom was at isocenter. The center of the laser li***g***ht was marked on with pen and ruler onto the film. With the gantry rotated to 90 degrees, the film was also irradiated with both the 1 mm circular diameter and 3 x 3 mm^2 square collimated beams as shown in **Figure 9.6b**.

After the films were scanned, distances from the center of the 1 mm diameter collimated beams were measured out to the center of the pen lines in the x, y, and z laser directions. For the x, y, and z directions, differences in the radiation isocenter and laser isocenter were 0.4, 1.1, and 0.1 mm, respectively. There was also a second y-value in the z-y plane, which also contained a 1.1 mm difference in laser isocenter compared to radiation isocenter. Since the lasers are not used for treatment purposes, and the active volume of our PTW farmer-type ionization chamber has a 6 mm diameter which is much larger than the maximum 1.1 mm deviation in radiation isocenter with the laser isocenter, adjustments do not need to be made to the lasers. However, the difference in laser isocenter must be taken into account if the small 1 mm^3 active volume scintillator dosimeter [112] is used within the SARRP. If adjustments are to be required, users must contact Xstrahl so that an Engineer can properly recalibrate the lasers.

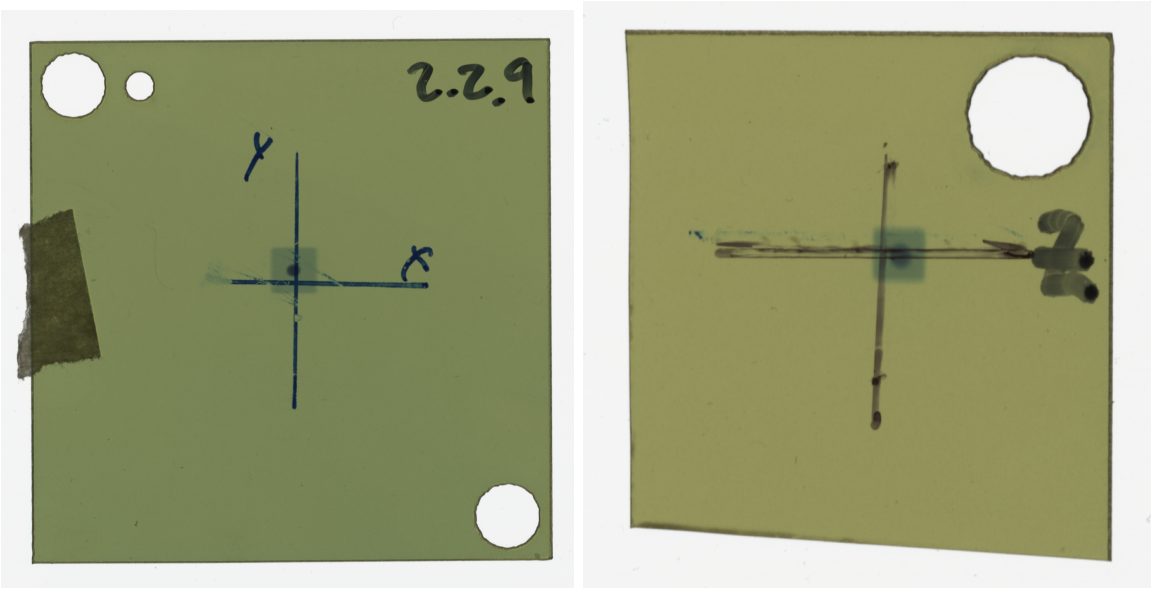

(a) **(b)**

Figure 9.6: Laser alignment to isocenter using the 3 x 3 mm^2 square and 1 mm circular diamter collimated beams for the a) x- and y-directions and the b) z-direction.

9.2.5 Couch Rotation

The rotational isocenter of the couch was also examined. Unlike standard imaging geometries where the x-ray source rotates around the stationary object, the couch rotates in the SARRP with a stationary x-ray source. These extra degrees of freedom of couch motion may lead to possible rotational errors.

A metal BB (2 mm diameter) was attached to the top of a small plastic cube and placed on the couch. The BB placement was chosen so that it was purposely positioned off-isocenter in the x-y plane (with the z-direction at isocenter). This was done so that during a couch rotation, if the rotation was perfect about the isocenter, the BB would follow a perfect circular path, and if not, it would follow an elliptical path. To follow the path of the BB, the on-board EPID was used to image the BB during a couch rotation with the gantry at 0° and EPID opposite to the source.

The couch was then rotated and EPID images were acquired with the on-board DCamViewer software at ±135°, ±90°, ±45°, and 0°. Due to a foreseen collision, the couch was stopped after ±135° was reached, as the couch would have had a collision with the EPID support column located below the gantry. After the seven

EPID images were acquired, all images were meshed together in Fiji so that the BB placement at each respective couch angle was visible in a single image.

The green circle in **Figure 9.7** represents a perfect circular rotation about the isocenter, and the red curve represents the actual rotation of the couch, with the red dots representing the BB locations during the couch rotation. After analyzing the distance from the center of the red BB positions to the green circle using analysis software Fiji, the deviation in distance compared to a perfect rotation (starting at the twelve o'clock position moving clockwise) was 0, 1.2, 0.5, 0.1, 0.2, 0.3, and 0.6 mm for the -90°, -135°, 135°, 90°, 45°, 0°, and -45° rotations, respectively. Through MC methods, microCT imaging dose with 1 cm positioning shifts results in a maximum of a 0%, 0.8%, and 1.5% change in imaging dose to a 20 g mouse body, organ, and flank tumor, respectively [109]. Thus, a 1.2 mm shift in couch rotation would produce negligible change in imaging dose. If the shits in couch rotation deviate greatly in the future, this may produce a distortion within the reconstructed microCT image, if not accounted for by the reconstruction software. A 1.2 mm shift in couch rotation is unlikely to effect treatment dose plans for targets much larger than 1 mm in diameter.

9.2.6 Additional QA

There are additional annual QA tests that were not completed before the writing of this dissertation, such as QA tests regarding accuracy/coincidence of the imaging and treatment isocenters. These important QA tests include determining the imaging isocenter of the flat panel imager, determination of the treatment isocenter of the EPID imager, and the overall coincidence of the imaging isocenter with the treatment isocenter. This is important, as if the imaging isocenter deviates drastically from the treatment isocenter, the delivered treatment plans will not be accurate. These tests can be accomplished with a cube phantom with a small metal bead (i.e., tungsten) located inside the cube. After a CBCT image is acquired with the metal bead placed off-center, the table is shifted so that the metal bead is shifted to the imaging isocenter, and then a collimated (i.e. 5 x 5 mm^2 square collimator) therapy beam is delivered with the EPID in place. The difference in distance between the center of the collimated beam with the center of the metal bead is then measured on the obtained EPID image to measure the coincidence between the imaging and therapy isocenters.

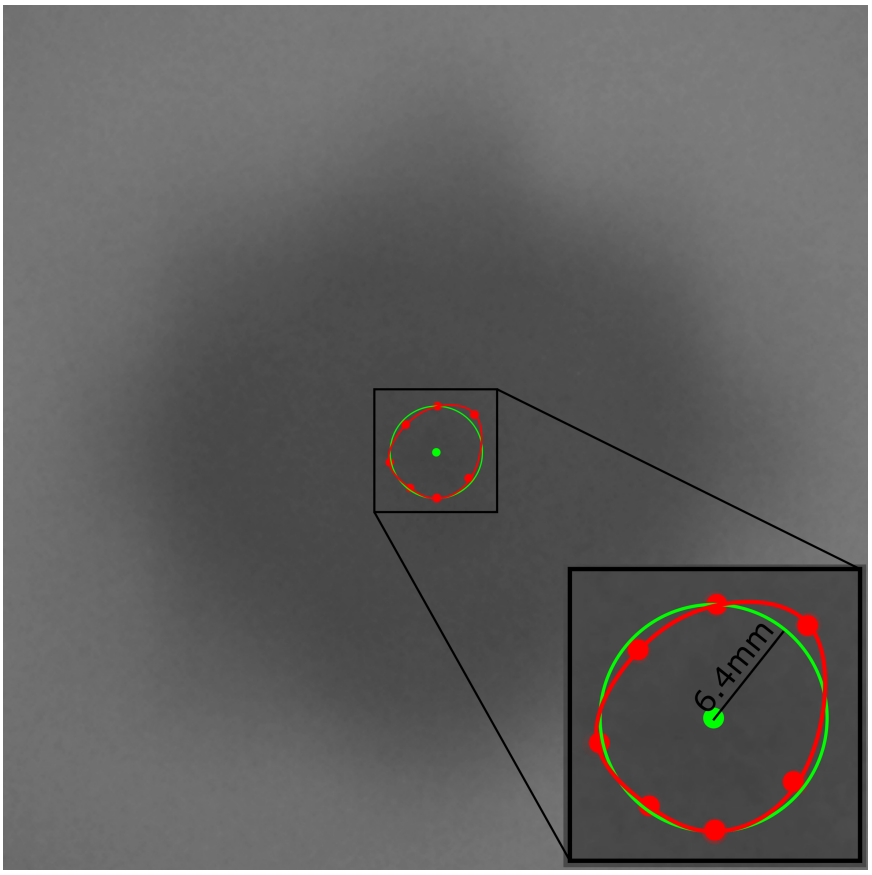

Figure 9.7: Metal bead on top of square phantom imaged using EPID imager with couch at 0°, 45°, 90°, 135°, -135°, -90°, and -45°. Images are overlaid together to map out movement of the metal bead with couch rotation, with green circle illustrating perfect couch rotation about the isocenter.

In addition, the alignment of the various collimators (i.e., 0.5 and 1 mm diameter circular, and 3 x 3, 5 x 5, and 10 x 10 mm^2 square collimators) to the imaging isocenter can be tested. The therapy beam can be delivered to the EPID imager (as described above) with the various collimators in place, and the distance from the imaging isocenter to the treatment isocenter for each respective collimator can be measured on the EPID to test the alignment of each collimator. This is important, as if the alignment of the collimators are different, the target will not be properly irradiated.

9.3 Miscellaneous, Non-Routine, and Future QA

During annual QA as maintenance checks, the following should be performed:

- Verify homing works properly with no errors when the SARRP powers on
- Test that the gantry can rotate from -135° all the way to 180°
- Test that the couch can move from -45 to 45 mm in the x and y directions, and -25 to 25 mm in the z direction, including the accuracy/consistency of the couch rotational speed, and accuracy of couch translation in the x-, y-, and z-directions
- Test of geometric accuracy in the x, y, and z directions
- Verify that the magnet that holds the CBCT detector in place works and that the protective shielding does not jam

In addition, a radiation safety survey should be conducted anytime service is done to the SARRP to check for any possible leakage from disassembled panels during service. This can be conducted with the Geiger counter that is housed within the SARRP room. For the radiation safety survey, direct uncollimated therapy beams at the four cardinal angles, and measure any possible radiation leakage along the edges of the SARRP for each respective cardinal angle. If needed, the principle investigator (PI) should be contacted to obtain previously recorded radiation safety surveys. During commissioning, the maximum radiation leakage was 0.5 μSv/h as read by a Geiger counter. Immediately notify the PI if leakage gets above the maximum commissioning leakage amount.

If anything changes within the SARRP that may change the primary radiation therapy beam, such as a change or servicing of the filter, internal collimation, or servicing of the x-ray tube, an output check following section 9.1.2 must be made. If the output has changed greatly (i.e., >5%) from previous outputs, an AAPM TG-61 must be performed to insure the beam quality has not drastically changed. If a change of >5% in output is still found, the treatment planning dose calculations files must be recommissioned to accommodate the new beam quality and dose rate.

Recently, novel QA procedures have been developed for the SARRP using the EPID to potentially supplement ionization chambers and film for monthly QA dosimetry [4].

Due to the ease of use and because no additional equipment is needed, EPID dosimetry could potentially be used for quick output checks before an irradiation is to take place, and used for possible daily QA. Possible QA tests with the EPID can allow for relative and absolute beam output measurements, dosimetry for HVL measurements, profile measurements, and beam targeting accuracy. Additionally, a promising advantage of using the EPID is the possibly for it to be used as a real-time dosimeter during irradiations [5], making the currently neglected EPID a potentially powerful tool. This would greatly reduce the time and resources needed in performing QA within the SARRP, and simplifying measurements in comparison to ionization chambers and film.

9.4 Summary

This chapter recommended QA tests to be perform for an image-guided small animal irradiator. Performing QA tests on a regular basis is imperative for verifying that the radiation output, mechanical operation, and overall performance of the irradiator is consistent to what is expected. This now marks the end of our journey through this dissertation (whew!!), and we will now concluded with an overall summary in the next and final chapter.

Chapter 10

Conclusions

"Remember me as you fall to sleep, fill your pockets with the dust and the memories, rises from the shoes on my feet. I won't be back here, though we may meet again."

–Slint

Microcomputed tomography (microCT) is a valuable tool in progressing preclinical imaging towards high resolution, highly accurate representations of the internal tissues of small animals. Obtaining such images assists researchers in understanding tumor development and tumor eradication for translation into improved treatments for human cancers. The image quality, absorbed imaging dose, and measurement of the imaging and therapy beams produced from image-guided small animal irradiators were investigated in great detail throughout this dissertation. More specifically, the reported findings aim to standardize microCT image quality across image-guided small animal irradiators, establish microCT imaging dose for the prevention of deterministic effects, and present a means to measure the imaging dose and treatment dose specifically for the small fields and energies used in preclinical IGRT.

10.1 Summary

Chapters 1–4 laid the foundations required to grasp the research topics presented throughout the main body of the dissertation that consists of three peer-reviewed publications. Presented was a detailed description and analysis of what microCT imaging is, the physics behind ionizing radiation propagation and how to measure it, and a detailed description of all the equipment and software used throughout this dissertation.

In **Chapter 5**, a multi-institutional study was performed to asses the microCT image quality of numerous image-guided small animal irradiators. It was found that microCT image quality varied greatly between institutions, thus tolerance levels were established to set a benchmark for acceptable microCT image quality standards for all image-guided small animal irradiators to achieve accurate dose delivery.

The image comparison was completed by first creating a fully automated quality assurance (QA) software SAPA (small animal phantom analyzer) for image analysis of the commercial Shelley micro-CT MCTP 610 phantom, in which quantitative analyses of CT number linearity, signal-to-noise ratio (SNR), uniformity and noise, geometric accuracy, spatial resolution by means of modulation transfer function (MTF), and CT contrast were performed. Phantom microCT scans from eleven institutions acquired with four different image-guided small animal irradiator units, including the commercial PXi X-RAD SmART and the small animal radiation research platform (Xstrahl SARRP), with varying parameters used for routine small animal imaging were analyzed. Multi-institutional data sets were compared using SAPA, tolerance levels for each QA test were established, and imaging protocols for QA were ultimately recommended.

By analyzing microCT data from 11 institutions, we established imaging QA tolerance levels for all image quality tests. CT number linearity of R^2>0.990 was acceptable in microCT data acquired at all but three institutions. Acceptable SNR (>36) and noise levels (<55HU) were obtained at five of the eleven institutions, where failing scans were acquired with current-exposure time of less than 120 mAs. Acceptable spatial resolution (>1.5 lp/mm for MTF=0.2) was obtained at all but four institutions due to their large image voxel size used (>0.275 mm). Ten of the eleven institutions passed the set QA tolerance for geometric accuracy (<1.5%) and nine of the

eleven institutions passed the QA tolerance for contrast (>2000 HU for 30 mgI/mL). We recommend performing imaging QA with 70 kVp, 1.5 mA, 120 second imaging time, 0.20 mm voxel size, and a frame rate of 5 fps for the PXi X-RAD SmART. For the Xstrahl SARRP, we recommend using 60 kVp, 1.0 mA, 240 second imaging time, 0.20 mm voxel size, and 6 fps. These imaging protocols should result in high quality images that pass the set tolerance levels on all systems. The average SAPA computation time for complete QA analysis for a 0.200 mm voxel, 400 slice Shelley phantom microCT data set was less than 20 s. Presented are image quality assurance recommendations for image-guided small animal radiotherapy systems that can aid researchers in maintaining high image quality, allowing for spatially precise conformal dose delivery to small animals.

Chapter 6 introduced the creation of an in-house Monte Carlo (MC) model of the Xstrahl SARRP, one of two commercial image-guided small animal irradiators currently available. The MC model of the Xstrahl SARRP was validated thoroughly with measurement and was applied to obtain absorbed microCT imaging dose to a mouse subject. MicroCT imaging dose to body, tumor, and organs were established for a comprehensive combination of imaging parameters.

The MC model was built in the BEAMnrc code and validated with a series of homogeneous and heterogeneous phantom measurements. A segmented microCT scan of a mouse was used in DOSXYZnrc to determine mouse organ microCT imaging doses to 15-35 g mice for the SARRP pancake (mouse lying on couch) and standard (mouse standing on couch) imaging geometries for 40-80 kVp tube voltages. Imaging dose for off-center positioning shifts and maintaining image noise across tube voltages were also calculated. Half-value layer (HVL) measurements for the 220 kVp therapy beam in the presence of the SARRP shielding cabinet were modeled in BEAMnrc and compared to the 100 cm source-to-detector distance (SDD) in the scatter free, narrow-beam geometry recommended by the American Association of Physicists in Medicine Task Group 61 (AAPM TG-61) protocol. For a 60 kVp, 0.8 mA, and 60 second scan protocol, maximum mean organ imaging doses to boney and non-boney structures were 10.5 cGy and 3.5 cGy, respectively, for an average size 20 g mouse. Current-exposure combinations above 323, 203, 147, 116, and 95 mAs for 40-80 kVp tube voltages, respectively, will increase body doses above 10 cGy. MicroCT mean body dose was 18% lower in pancake compared to standard imaging geometry. An 11% difference in measured HVL at a 50 cm SDD was found compared to MC sim-

ulated HVL for the AAPM TG-61 recommended scatter free geometry at a 100 cm SDD. This change in HVL resulted in a 0.5% change in absorbed dose to water calculations for the treatment beam. This establishment of absorbed imaging dose to a mouse model was then extended to varying microCT image quality scans.

Chapter 7 demonstrates the marriage between microCT image quality and the corresponding absorbed imaging dose. Varying image quality scans of mice were obtained within an Xstrahl SARRP with the resulting body, tumor, and organ doses calculated by MC methods. For a 32 g mouse, it was found that a scanning protocol of a 30 second scan time, 60 kVp tube voltage, 1.2 mA tube current, 12 fps, and a 0.275 mm^3 voxel size resulted in microCT image noise of 55 HU and a body dose of 2.49 cGy. This is in comparison to a common scanning protocol of a 60 second scan time, 60 kVp tube voltage, 0.8 mA tube current, 6 fps, and a 0.275 mm^2 resulting in microCT image noise of 93 HU and a body dose of 3.32 cGy. The microCT image noise was reduced by 40% and imaging time reduced by 50% while reducing imaging dose to the body by 25%. This reduction was due to doubling the frame rate from 6 to 12 fps per scan. This increase in frame rate did not produce artifacts within the microCT scan. MicroCT image noise and corresponding imaging dose was also analyzed for tube voltages and current-exposure times ranging from 40–80 kVp and 24–288 mAs, respectively. It was found that while holding all other imaging parameters constant, increasing the tube voltage from 40–50, 50–60, 60–70, and 70–80 kVp increased imaging dose to the body by 65%, 40%, 30%, and 25%, respectively, while reducing image noise by 30%, 23%, 22%, and 18%, respectively. Additionally, while holding all other imaging parameters constant, increasing the current-exposure time from 24 to 288 mAs linearly increases body dose while exponentially reducing image noise. Users of the Xstrahl SARRP may utilize these results as a reference to determine the amount of imaging dose delivered for a given amount of imaging noise produced in a microCT scan.

Chapter 8 presented a novel plastic scintillator dosimeter with applications in high resolution, real-time dosimetry of therapy and imaging x-ray beams delivered by a commercial image-guided small animal irradiator. A 1 mm diameter, 1 mm long polystyrene BCF-60 scintillating fiber dosimeter was characterized with 220 kVp therapy and 40, 50, 60, 70, and 80 kVp imaging beams on the Xstrahl SARRP. Scintillator output, sensitivity (charge per unit dose), linearity, and 0.2-mm resolution beam profile measurements were performed. A validated in-house MC model of the Xstrahl

SARRP was used to compute detailed energy spectra at locations of dosimetry, and validated scintillator measurement with MC simulations. Mass energy-absorption coefficients from the National Institute of Standards and Technology (NIST) tables convolved with MC-derived spectra were used in conjunction with Birks ionization quenching factors to correct scintillator output. An air-kerma calibration method was employed to correct scintillator output for in-air beam profile measurements with open, 5 x 5, and 3 x 3 mm^2 square field sizes, and compared to MC simulations.

Scintillator dose response showed excellent linearity ($R^2 \geq 0.999$) for all sensitivity measurements, including output as a function of tube current. Detector sensitivity was 2.41 μC Gy^{-1} for the 220 kVp therapy beam, and ranged from 1.21 to 1.32 μC Gy^{-1} for the 40–80 kVp imaging beams. Percentage differences in sensitivity between the therapy and imaging beams before sensitivity correction and after sensitivity correction using the Birks quenching factors were 52.3% and 10.2%, respectively. Percentage differences between the therapy and imaging beam sensitivities after using the air kerma calibration method for in-air measurements was excellent and below 0.3%. In-air beam profile measurements agreed to MC simulations within a mean difference of 2.4% for the 5 x 5 and 3 x 3 mm^2 square field sizes, however, the scintillator showed signs of volume averaging at the penumbra edges. The characterization of the scintillator detector system for small fields presents steps towards implementing real-time measurements for quality assurance and small animal treatment and imaging dose verification.

Chapter 9 presented a number of QA tests recommended to be performed within the Xstrahl SARRP. These QA tests assess any possible changes that may occur to the imaging and therapy beams, or mechanical properties of the irradiator over time. For monthly QA, it is recommended to perform in-air dose measurements to asses irradiator dose rate in contrast to in-phantom dose measurements. This is due to difficulties in setup reproducibility when only large solid water phantoms are available for in-phantom dosimetry with an ionization chamber. MicroCT image quality may be assessed by scanning an imaging QA phantom to establish a baseline in image quality to compare to future QA scans. It is recommended that a flood field correction for the flat panel detector be performed on a monthly basis to assure that the gain for each pixel of the detector is uniform.

For annual QA, it is strongly recommended that treatment planning dose calculation

accuracy be assessed, as the delivered dose for our QA test was 9.6% less than the prescribed dose. Additionally, treatment targeting accuracy, HVL, laser alignment, couch rotation isocenter, and a radiation safety survey should be performed on an annual basis. This chapter included a description of QA tests to be performed on a monthly and annual bases, as well as presenting their evaluated results. In the event that unwanted changes occur, recommendations on how to proceed are also described.

Finally, **Chapter 10** draws the entire dissertation to a formal and concise conclusion. It is hoped that the establishment of image quality standards, corresponding imaging dose, and methods to measure the imaging and therapy beams for preclinical models will be used by future researchers to get one small step closer to finding a cure for cancer. "It has not been 'fun,' in the conventional sense, but it has been, for the most part, a rewarding journey." [107]

10.2 Advances and Future Work

Development of two additional QA phantoms which are better representative of a murine model were tested within our research group. One phantom is also a cylinder-type phantom like the Shelley phantom used in this dissertation, but smaller in dimensions and consists of 3D printed tissue-specific materials to improve upon the Shelley phantom. The other phantom built within our research group is a 3D printed realistic murine phantom made based on the microCT scan and organ segmentation developed in this dissertation. Small holes for housing our small scintillator were included to obtain absorbed dose measurements at various points within the phantom for radiation therapy QA.

Future work could extend the absorbed dose to organ calculations in murine models to other types of small animals. The in-house MC model of the Xstrahl SARRP could be used in combination with a segmented microCT scan of any other small animal that can be scanned within the Xstrahl SARRP. Additionally, more organs could be segmented in future models to provide more detailed dose information. It is also recommended that actual elemental compositions of the specific animal to be scanned are used to improve dose calculation accuracy. This can be accomplished by using atomic absorption spectrometry methods. The in-house MC model of the Xstrahl SARRP is freely available to interested researchers to promote further research and

development.

To improve the spatial resolution of the dose measurements obtained by the 1 mm diameter plastic scintillator dosimeter used in this dissertation, a smaller 0.5 mm diameter plastic scintillator dosimeter is currently in development. This smaller model will look to mitigate the volume averaging effects found in the larger 1 mm diameter model, and possibly become a commercial dosimeter for other groups to use in preclinical research. Future studies can further validate the scintillator dosimeter in heterogeneous media and ultimately be used for real-time *in-vivo* dosimetry for image-guided small animal radiotherapy.

10.3 Technical Limitations

Technical limitations using the Xstrahl SARRP irradiator include issues regarding the imaging geometry which inherently creates relatively noisy images, tangled anesthesia cords with the rotating couch, and software glitches that delay procedures. The flat panel detector gets saturated when approximately a 1.5 mA tube current and higher is used, and standardized HUs are not assigned to images. Problems are also created by the unit not containing many necessary interlocks to prevent mistakes. It is not unlikely for the operator to forget to place the correct filter for imaging/therapy procedures, no interlocks are in place to verify if the correct collimator is used during therapy treatments, and there is no collision detection if a planned beam geometry and couch rotation combination will cause the treatment collimator to collide with the couch. In addition, the accuracy of how the beam fluence is determined by the user for treatment planning dose calibration may be questionable based on our treatment planning dose calculation accuracy QA test.

To address these limitations, imaging noise may be decreased if the mice were to be imaged either vertically (in a custom built holder) or at an angle, or if the detector saturation could be fixed in the future and a higher tube current could be used (although at the expense of higher imaging dose). Users of the Xstrahl SARRP must be very mindful of having long enough anesthesia and dosimetry cords, especially for imaging procedures, and double check to make sure the correct filters and collimators are in place before imaging and therapy procedures, including verifying that collisions will not happen before delivering a complex treatment plan. We are currently

performing a failure modes and effects analysis (FMEA) study to bring to light the impact of absent interlocks and to take actions to reduce potential failures in delivering a successful study objective. For future treatment planning accuracy, Xstrahl is currently working on upgrading it's treatment planning to incorporate Monte Carlo modeling to improve on the dose calculation accuracy.

Bibliography

[1] S. Agostinelli, J. Allison, K. a. Amako, J. Apostolakis, H. Araujo, P. Arce, M. Asai, D. Axen, S. Banerjee, G. . Barrand, et al. Geant4a simulation toolkit. *Nuclear Instruments and Methods in Physics Research Section A: Accelerators, Spectrometers, Detectors and Associated Equipment*, 506(3):250–303, 2003.

[2] E. Alhakeem and S. Zavgorodni. Output and ([formula:see text]) correction factors measured and calculated in very small circular fields for microdiamond and efd-3g detectors. *arXiv preprint arXiv:1802.00569*, 2018.

[3] K. Z. Alves, R. C. Soletti, M. A. de Britto, D. G. de Matos, M. Soldan, H. L. Borges, and J. C. Machado. In vivo endoluminal ultrasound biomicroscopic imaging in a mouse model of colorectal cancer. *Academic Radiology*, 20(1):90–98, 2013.

[4] A. Anvari, Y. Poirier, and A. Sawant. Development and implementation of epid-based quality assurance tests for the small animal radiation research platform (sarrp). *Medical Physics*, 2018.

[5] A. Anvari, Y. Poirier, and A. Sawant. Kilovoltage transit and exit dosimetry for a small animal image-guided radiotherapy system using built-in epid. *Medical Physics*, 2018.

[6] L. Archambault, A. S. Beddar, L. Gingras, F. Lacroix, R. Roy, and L. Beaulieu. Water-equivalent dosimeter array for small-field external beam radiotherapy. *Medical Physics*, 34(5):1583–1592, 2007.

[7] F. H. Attix. *Introduction to radiological physics and radiation dosimetry*. John Wiley & Sons, 2008.

[8] N. L. Ausborn, Q. T. Le, J. D. Bradley, H. Choy, A. P. Dicker, D. Saha, J. Simko, M. D. Story, A. Torossian, and B. Lu. Molecular profiling to optimize treatment in non-small cell lung cancer: a review of potential molecular targets for radiation therapy by the translational research program of the radiation therapy oncology group. *International Journal of Radiation Oncology, Biology, Physics*, 83(4):e453–e464, 2012.

[9] C. Badea, M. Drangova, D. W. Holdsworth, and G. Johnson. In vivo small-animal imaging using micro-ct and digital subtraction angiography. *Physics in Medicine & Biology*, 53(19):R319, 2008.

[10] H. Badri and K. Leder. Optimal treatment and stochastic modeling of heterogeneous tumors. *Biology Direct*, 11(1):40, 2016.

[11] J. Baines and L. Sim. The variation of hvl with focal spot to chamber distance as a function of beam quality for the pantak therapax 150 x-ray unit and the implications on dose to water determination using the ipemb code of practice. *Australasian Physical & Engineering Sciences in Medicine*, 37(3):559–566, 2014.

[12] C. Baltes, N. Radzwill, S. Bosshard, D. Marek, and M. Rudin. Micro mri of the mouse brain using a novel 400 mhz cryogenic quadrature rf probe. *NMR in Biomedicine*, 22(8):834–842, 2009.

[13] K. L. Barton, K. Misuraca, F. Cordero, E. Dobrikova, H. D. Min, M. Gromeier, D. G. Kirsch, and O. J. Becher. Pd-0332991, a cdk4/6 inhibitor, significantly prolongs survival in a genetically engineered mouse model of brainstem glioma. *PloS One*, 8(10):e77639, 2013.

[14] B. C. Baumann, J. L. Benci, P. P. Santoiemma, S. Chandrasekaran, A. B. Hollander, G. D. Kao, and J. F. Dorsey. An integrated method for reproducible and accurate image-guided stereotactic cranial irradiation of brain tumors using the small animal radiation research platform. *Translational Cncology*, 5(4):230–237, 2012.

[15] M. Bazalova, J.-F. Carrier, L. Beaulieu, and F. Verhaegen. Dual-energy ct-based material extraction for tissue segmentation in monte carlo dose calculations. *Physics in Medicine & Biology*, 53(9):2439, 2008.

[16] M. Bazalova and E. E. Graves. The importance of tissue segmentation for dose calculations for kilovoltage radiation therapy. *Medical Physics*, 38(6Part1):3039–3049, 2011.

[17] M. Bazalova and E. E. Graves. Engineering small animal conformal radiotherapy systems. In *Engineering in Translational Medicine*, pages 853–875. Springer, 2014.

[18] L. Beaulieu and S. 2015. Review of plastic and liquid scintillation dosimetry for photon, electron, and proton therapy. *Physics in Medicine & Biology*, 61(20):R305, 2016.

[19] A. Beddar, T. Mackie, and F. Attix. Water-equivalent plastic scintillation detectors for high-energy beam dosimetry: I. physical characteristics and theoretical considerations. *Physics in Medicine & Biology*, 37(10):1883, 1992.

[20] A. S. Beddar, T. Mackie, and F. Attix. Water-equivalent plastic scintillation detectors for high-energy beam dosimetry: Ii. properties and measurements. *Physics in Medicine & Biology*, 37(10):1901, 1992.

[21] S. Beddar. Real-time volumetric scintillation dosimetry. In *Journal of Physics: Conference Series*, volume 573, page 012005. IOP Publishing, 2015.

[22] H. Benmakhlouf and P. Andreo. Spectral distribution of particle fluence in small field detectors and its implication on small field dosimetry. *Medical Physics*, 44(2):713–724, 2017.

[23] M. J. Berger and J. Hubbell. Xcom: Photon cross sections on a personal computer. Technical report, National Bureau of Standards, 1987 (2018 version 1.5 Online).

[24] J. Birks and F. Brooks. Scintillation response of anthracene to 6-30 kev photoelectrons. *Proceedings of the Physical Society. Section B*, 69(7):721, 1956.

[25] J. B. Birks. The theory and practice of scintillation counting vol. 27, international series of monographs on electronics and instrumentation, 1964.

[26] J.-P. Bissonnette, P. A. Balter, L. Dong, K. M. Langen, D. M. Lovelock, M. Miften, D. J. Moseley, J. Pouliot, J.-J. Sonke, and S. Yoo. Quality as-

surance for image-guided radiation therapy utilizing ct-based technologies: A report of the aapm tg-179. *Medical Physics*, 39(4):1946–1963, 2012.

[27] B. J. Blyth, A. J. Cole, M. P. MacManus, and O. A. Martin. Radiation therapy-induced metastasis: radiobiology and clinical implications. *Clinical & Experimental Metastasis*, pages 1–14, 2017.

[28] A. E. Bogden, P. M. Haskell, D. J. LePage, D. E. Kelton, W. R. Cobb, and H. J. Esber. Growth of human tumor xenografts implanted under the renal capsule of normal immunocompetent mice. *Pathobiology*, 47(4):281–293, 1979.

[29] J. Boivin, S. Beddar, C. Bonde, D. Schmidt, W. Culberson, M. Guillemette, and L. Beaulieu. A systematic characterization of the low-energy photon response of plastic scintillation detectors. *Physics in Medicine & Biology*, 61(15):5569, 2016.

[30] J. M. Boone, O. Velazquez, and S. R. Cherry. Small-animal x-ray dose from micro-ct. *Molecular Imaging*, 3(3):15353500200404118, 2004.

[31] D. Y. Breitkreutz, S. Bialek, B. Vojnovic, A. Kavanagh, C. D. Johnstone, Z. Rovner, P. Tsouchlos, T. Kanesalingam, and M. Bazalova-Carter. A 3d-printed modular phantom for quality assurance of image-guided small animal irradiators: design, imaging experiments and monte carlo simulations. *Medical Physics*, 46(5), 2019.

[32] F. Bretin, M. A. Bahri, A. Luxen, C. Phillips, A. Plenevaux, and A. Seret. Monte carlo simulations of the dose from imaging with ge explore 120 micro-ct using gate. *Medical Physics*, 42(10):5711–5719, 2015.

[33] J. F. Briesmeister et al. Mcnptm-a general monte carlo n-particle transport code. *Version 4C, LA-13709-M, Los Alamos National Laboratory*, page 2, 2000.

[34] N. Brix, A. Tiefenthaller, H. Anders, C. Belka, and K. Lauber. Abscopal, immunological effects of radiotherapy: Narrowing the gap between clinical and preclinical experiences. *Immunological Reviews*, 280(1):249–279, 2017.

[35] T. A. Brown, K. R. Hogstrom, D. Alvarez, K. L. Matthews, K. Ham, and J. P. Dugas. Dose-response curve of ebt, ebt2, and ebt3 radiochromic

films to synchrotron-produced monochromatic x-ray beams. *Medical Physics*, 39(12):7412–7417, 2012.

[36] K. Burrell, S. Agnihotri, M. Leung, R. DaCosta, R. Hill, and G. Zadeh. A novel high-resolution in vivo imaging technique to study the dynamic response of intracranial structures to tumor growth and therapeutics. *Journal of Visualized Experiments: JoVE*, 76, 2013.

[37] J. T. Bushberg. *The essential physics of medical imaging*. Lippincott Williams & Wilkins, 2 edition, 2002.

[38] K. T. Butterworth, J. R. Nicol, M. Ghita, S. Rosa, P. Chaudhary, C. K. McGarry, H. O. McCarthy, G. Jimenez-Sanchez, R. Bazzi, S. Roux, et al. Preclinical evaluation of gold-dtdtpa nanoparticles as theranostic agents in prostate cancer radiotherapy. *Nanomedicine*, 11(16):2035–2047, 2016.

[39] C. S. G. Calcina, L. N. de Oliveira, C. E. de Almeida, and A. de Almeida. Dosimetric parameters for small field sizes using fricke xylenol gel, thermoluminescent and film dosimeters, and an ionization chamber. *Physics in Medicine & Biology*, 52(5):1431, 2007.

[40] S. K. Carlson, K. L. Classic, C. E. Bender, and S. J. Russell. Small animal absorbed radiation dose from serial micro-computed tomography imaging. *Molecular Imaging and Biology*, 9(2):78–82, 2007.

[41] D. Cavanaugh, E. Johnson, R. E. Price, J. Kurie, E. L. Travis, and D. D. Cody. In vivo respiratory-gated micro-ct imaging in small-animal oncology models. *Molecular Imaging*, 3(1):15353500200403184, 2004.

[42] N. Chattopadhyay, Z. Cai, Y. L. Kwon, E. Lechtman, J.-P. Pignol, and R. M. Reilly. Molecularly targeted gold nanoparticles enhance the radiation response of breast cancer cells and tumor xenografts to x-radiation. *Breast Cancer Research and Treatment*, 137(1):81–91, 2013.

[43] A. F. Chatziioannou. Instrumentation for molecular imaging in preclinical research: Micro-pet and micro-spect. *Proceedings of the American Thoracic Society*, 2(6):533–536, 2005.

[44] D. B. Chithrani, S. Jelveh, F. Jalali, M. van Prooijen, C. Allen, R. G. Bristow, R. P. Hill, and D. A. Jaffray. Gold nanoparticles as radiation sensitizers in cancer therapy. *Radiation Research*, 173(6):719–728, 2010.

[45] Y. Cho, D. J. Moseley, J. H. Siewerdsen, and D. A. Jaffray. Accurate technique for complete geometric calibration of cone-beam computed tomography systems. *Medical physics*, 32(4):968–983, 2005.

[46] R. Clarkson, P. Lindsay, S. Ansell, G. Wilson, S. Jelveh, R. Hill, and D. Jaffray. Characterization of image quality and image-guidance performance of a preclinical microirradiator. *Medical Physics*, 38(2):845–856, 2011.

[47] S. Cloude. *An introduction to electromagnetic wave propagation and antennas*. CRC Press, 1995.

[48] N. R. Council and Others. *Use of laboratory animals in biomedical and behavioral research*. National Academies Press, 1988.

[49] R. Craun and D. Smith. Analysis of response data for several organic scintillators. *Nuclear Instruments and Methods*, 80(2):239–244, 1970.

[50] J. Damodar, D. Odgers, D. Pope, and R. Hill. A study on the suitability of the ptw microdiamond detector for kilovoltage x-ray beam dosimetry. *Applied Radiation and Isotopes*, 135:104–109, 2018.

[51] V. De Coste, P. Francescon, M. Marinelli, L. Masi, L. Paganini, M. Pimpinella, G. Prestopino, S. Russo, A. Stravato, C. Verona, et al. Is the ptw 60019 microdiamond a suitable candidate for small field reference dosimetry? *Physics in Medicine & Biology*, 62(17):7036, 2017.

[52] S. Demaria, C. N. Coleman, and S. C. Formenti. Radiotherapy: changing the game in immunotherapy. *Trends in Cancer*, 2(6):286–294, 2016.

[53] S. A. Detombe, J. Dunmore-Buyze, I. E. Petrov, and M. Drangova. X-ray dose delivered during a longitudinal micro-ct study has no adverse effect on cardiac and pulmonary tissue in c57bl/6 mice. *Acta Radiologica*, 54(4):435–441, 2013.

[54] A. Dimitriadis, I. S. Patallo, I. Billas, S. Duane, A. Nisbet, and C. Clark. Characterisation of a plastic scintillation detector to be used in a multicentre

stereotactic radiosurgery dosimetry audit. *Radiation Physics and Chemistry*, 140:373–378, 2017.

[55] L.-H. Ding, M. Shingyoji, F. Chen, J.-J. Hwang, S. Burma, C. Lee, J.-F. Cheng, and D. J. Chen. Gene expression profiles of normal human fibroblasts after exposure to ionizing radiation: a comparative study of low and high doses. *Radiation Research*, 164(1):17–26, 2005.

[56] J. F. Dorsey, L. Sun, D. Y. Joh, A. Witztum, G. D. Kao, M. Alonso-Basanta, S. Avery, S. M. Hahn, A. Al Zaki, and A. Tsourkas. Gold nanoparticles in radiation research: potential applications for imaging and radiosensitization. *Translational Cancer Research*, 2(4):280, 2013.

[57] Y. Dou, Y. Guo, X. Li, X. Li, S. Wang, L. Wang, G. Lv, X. Zhang, H. Wang, X. Gong, et al. Size-tuning ionization to optimize gold nanoparticles for simultaneous enhanced ct imaging and radiotherapy. *ACS Nano*, 10(2):2536–2548, 2016.

[58] R. Dreindl, D. Georg, and M. Stock. Radiochromic film dosimetry: Considerations on precision and accuracy for ebt2 and ebt3 type films. *Zeitschrift für Medizinische Physik*, 24(2):153–163, 2014.

[59] R. T. Droege and R. L. Morin. A practical method to measure the mtf of ct scanners. *Medical Physics*, 9(5):758–760, 1982.

[60] L. Y. Du, J. Umoh, H. N. Nikolov, S. I. Pollmann, T.-Y. Lee, and D. W. Holdsworth. A quality assurance phantom for the performance evaluation of volumetric micro-ct systems. *Physics in Medicine & Biology*, 52(23):7087, 2007.

[61] S. Dufreneix, C. Di Bartolo, M. Bremaud, J. Mesgouez, C. Legrand, and D. Autret. P10. how to choose a detector for small fields measurements? *Physica Medica: European Journal of Medical Physics*, 32:371, 2016.

[62] D. J. Eaton and P. J. Doolan. Review of backscatter measurement in kilovoltage radiotherapy using novel detectors and reduction from lack of underlying scattering material. *Journal of Applied Clinical Medical Physics*, 14(6):5–17, 2013.

[63] N. M. Esplen, L. Chergui, C. D. Johnstone, and M. Bazalova-Carter. Monte carlo optimization of a microbeam collimator design for use on the small animal radiation research platform (sarrp). *Physics in Medicine & Biology*, 63(17):175004, 2018.

[64] L. Feldkamp, L. Davis, and J. Kress. Practical cone-beam algorithm. *JOSA A*, 1(6):612–619, 1984.

[65] L. Feldkamp, M. Kleerekoper, J. Kress, R. Freeling, C. Mathews, and A. Parfitt. Investigation of 3-dimensional structure of trabecular bone by computed-tomography of iliac biopsy samples. In *CALCIFIED TISSUE INTERNATIONAL*, volume 35, pages 669–669. SPRINGER VERLAG 175 FIFTH AVE, NEW YORK, NY 10010, 1983.

[66] L. A. Feldkamp, S. A. Goldstein, M. A. Parfitt, G. Jesion, and M. Kleerekoper. The direct examination of three-dimensional bone architecture in vitro by computed tomography. *Journal of Bone and Mineral Research*, 4(1):3–11, 1989.

[67] S. D. Figueroa, C. T. Winkelmann, W. H. Miller, W. A. Volkert, and T. J. Hoffman. Tld assessment of mouse dosimetry during microct imaging. *Medical Physics*, 35(9):3866–3874, 2008.

[68] F. S. Foster, J. Hossack, and S. L. Adamson. Micro-ultrasound for preclinical imaging. *Interface Focus*, page rsfs20110037, 2011.

[69] B. L. Franc, P. D. Acton, C. Mari, and B. H. Hasegawa. Small-animal spect and spect/ct: important tools for preclinical investigation. *Journal of Nuclear Medicine*, 49(10):1651–1663, 2008.

[70] P. Francescon, W. Kilby, and N. Satariano. Monte carlo simulated correction factors for output factor measurement with the cyberknife systemresults for new detectors and correction factor dependence on measurement distance and detector orientation. *Physics in Medicine & Biology*, 59(6):N11, 2014.

[71] A.-M. Frelin, J.-M. Fontbonne, G. Ban, J. Colin, and M. Labalme. Comparative study of plastic scintillators for dosimetric applications. *IEEE Transactions on Nuclear Science*, 55(5):2749–2756, 2008.

[72] E. C. Friedberg, G. C. Walker, W. Siede, and R. D. Wood. *DNA repair and mutagenesis*. American Society for Microbiology Press, 2005.

[73] O. Glasser. Wilhelm conrad röntgen and the early history of the roentgen rays, 1934.

[74] L. W. Goldman. Principles of ct and ct technology. *Journal of Nuclear Medicine Technology*, 35(3):115–128, 2007.

[75] L. W. Goldman. Principles of ct: radiation dose and image quality. *Journal of Nuclear Medicine Technology*, 35(4):213–225, 2007.

[76] K. Goldstone. Tissue substitutes in radiation dosimetry and measurement, in: Icru report 44. international commission on radiation units and measurements, usa (1989), 1989.

[77] E. J. Hall. *Radiobiology for the Radiologist*. Lippincott Williams and Wilkins, 5 edition, 2000.

[78] A. E. Hansen, F. P. Fliedner, J. R. Henriksen, J. T. Jørgensen, A. E. Clemmensen, B. Børresen, D. R. Elema, A. Kjær, and T. L. Andresen. Liposome accumulation in irradiated tumors display important tumor and dose dependent differences. *Nanomedicine: Nanotechnology, Biology and Medicine*, 14(1):27–34, 2018.

[79] S. J. Harder. Raman spectroscopy of tumour cells exposed to clinically relevant doses of ionizing radiation. Master's thesis, University of Victoria, 2013.

[80] S. J. Harder, M. Isabelle, L. DeVorkin, J. Smazynski, W. Beckham, A. G. Brolo, J. J. Lum, and A. Jirasek. Raman spectroscopy identifies radiation response in human non-small cell lung cancer xenografts. *Scientific Reports*, 6:21006, 2016.

[81] F. Hauth, M. Toulany, D. Zips, and A. Menegakis. Cell-line dependent effects of hypoxia prior to irradiation in squamous cell carcinoma lines. *Clinical and Translational Radiation Oncology*, 5:12–19, 2017.

[82] R. E. R. Hendee W R. *Medical imaging physics*. John Wiley & Sons, 2003.

[83] G. S. Herter-Sprie, H. Korideck, C. L. Christensen, J. M. Herter, K. Rhee, R. I. Berbeco, D. G. Bennett, E. A. Akbay, D. Kozono, R. H. Mak, et al. Image-

guided radiotherapy platform using single nodule conditional lung cancer mouse models. *Nature Communications*, 5:5870, 2014.

[84] M. Hirschberg, R. Beckmann, U. Brandenburg, H. Bruckmann, and K. Wick. Precise measurement of birks kb parameter in plastic scintillators. *IEEE Transactions on Nuclear Science*, 39(4):511–514, 1992.

[85] M. R. Hoerner, E. J. Stepusin, D. E. Hyer, and D. E. Hintenlang. Characterizing energy dependence and count rate performance of a dual scintillator fiber-optic detector for computed tomography. *Medical Physics*, 42(3):1268–1279, 2015.

[86] M. Holcik, C. Yeh, R. G. Korneluk, and T. Chow. Translational upregulation of x-linked inhibitor of apoptosis (xiap) increases resistance to radiation induced cell death. *Oncogene*, 19(36):4174, 2000.

[87] G. N. Hounsfield. Computerized transverse axial scanning (tomography): Part 1. description of system. *The British Journal of Radiology*, 46(552):1016–1022, 1973.

[88] J. D. HOWELL. Early clinical use of the x-ray. *Transactions of the American Clinical and Climatological Association*, 127:341, 2016.

[89] E. Hranitzky, P. R. Almond, H. D. Suit, and E. Moore. A cesium-137 irradiator for small laboratory animals. *Radiology*, 107(3):641–644, 1973.

[90] Y. Hseih, U. Begley, L. Endres, J. Keith, A. F. Hansen, L. Kaminsky, B. McCandless, and T. J. Begley. Activation of dna damage signaling components by diagnostic computed tomography (ct) scans detected in patient samples using an electrochemiluminescence-based assay platform. *Advances in Bioscience and Biotechnology*, 8(07):228, 2017.

[91] J. Hsieh and Others. *Computed tomography: principles, design, artifacts, and recent advances*. SPIE Bellingham, WA, 2009.

[92] Z. I. Hu, H. L. McArthur, and A. Y. Ho. The abscopal effect of radiation therapy: What is it and how can we use it in breast cancer? *Current Breast Cancer Reports*, 9(1):45–51, 2017.

[93] J. Hubbell. Photon mass attenuation and energy-absorption coefficients. *The International Journal of Applied Radiation and Isotopes*, 33(11):1269–1290, 1982.

[94] J. H. Hubbell and S. M. Seltzer. Tables of x-ray mass attenuation coefficients and mass energy-absorption coefficients 1 kev to 20 mev for elements z= 1 to 92 and 48 additional substances of dosimetric interest. Technical report, National Inst. of Standards and Technology-PL, Gaithersburg, MD (United States). Ionizing Radiation Div., 1995.

[95] F. H. Igney and P. H. Krammer. Immune escape of tumors: apoptosis resistance and tumor counterattack. *Journal of Leukocyte Biology*, 71(6):907–920, 2002.

[96] D. Ishihara, L. Pop, T. Takeshima, P. Iyengar, and R. Hannan. Rationale and evidence to combine radiation therapy and immunotherapy for cancer treatment. *Cancer Immunology, Immunotherapy*, 66(3):281–298, 2017.

[97] A. Ivashkevich, C. E. Redon, A. J. Nakamura, R. F. Martin, and O. A. Martin. Use of the γ-h2ax assay to monitor dna damage and repair in translational cancer research. *Cancer Letters*, 327(1):123–133, 2012.

[98] R. Jacques, R. Taylor, J. Wong, and T. McNutt. Towards real-time radiation therapy: Gpu accelerated superposition/convolution. *Computer methods and programs in biomedicine*, 98(3):285–292, 2010.

[99] D. Jaffray, D. Moseley, J. Chow, S. Kim, S. Ansell, G. Wilson, and C. Chiarot. We-d-330a-09: An image-guided irradiator for pre-clinical radiation therapy studies. *Medical Physics*, 33(6Part20):2241–2241, 2006.

[100] D. A. Jaffray, J. H. Siewerdsen, J. W. Wong, and A. A. Martinez. Flat-panel cone-beam computed tomography for image-guided radiation therapy. *International Journal of Radiation Oncology, Biology, Physics*, 53(5):1337–1349, 2002.

[101] V. Jain, P. V. Kumar, P. Koya, G. Jaikrishan, and B. Das. Lack of increased dna double-strand breaks in peripheral blood mononuclear cells of individuals from high level natural radiation areas of kerala coast in india. *Mutation Research/Fundamental and Molecular Mechanisms of Mutagenesis*, 788:50–57, 2016.

[102] V. Jain, D. Saini, P. V. Kumar, G. Jaikrishan, and B. Das. Efficient repair of dna double strand breaks in individuals from high level natural radiation areas of kerala coast, south-west india. *Mutation Research/Fundamental and Molecular Mechanisms of Mutagenesis*, 806:39–50, 2017.

[103] P. Jakob. Small animal magnetic resonance imaging: basic principles, instrumentation and practical issue. In *Small Animal Imaging*, pages 151–164. Springer, 2011.

[104] K. Jang, W. Yoo, J. Seo, J. Heo, J. Moon, J.-Y. Park, E. Hwang, D. Shin, S.-Y. Park, H.-S. Cho, et al. Fabrication and optimization of a fiber-optic radiation sensor for proton beam dosimetry. *Nuclear Instruments and Methods in Physics Research Section A: Accelerators, Spectrometers, Detectors and Associated Equipment*, 652(1):841–845, 2011.

[105] J. Jiang, K. Gao, Y. Zhou, A. Xu, S. Shi, G. Liu, and Z. Li. Electroacupuncture treatment improves learning-memory ability and brain glucose metabolism in a mouse model of alzheimers disease: using morris water maze and micro-pet. *Evidence-Based Complementary and Alternative Medicine*, 2015, 2015.

[106] H. E. Johns and J. R. Cunningham. *The physics of radiology*. Thomas, Springfield, Illinois, 4th Edition, 1983.

[107] B. Johnstone. *Critical Travel Pedagogy: Promoting a Critical Consciousness through International Travel Experiences*. PhD thesis, UCLA, 2014.

[108] C. D. Johnstone. Validation of in-house dose calculation software for superficial x-ray therapy. Master's thesis, San Diego State University, Montezuma Publishing, 2013.

[109] C. D. Johnstone and M. Bazalova-Carter. Microct imaging dose to mouse organs using a validated monte carlo model of the small animal radiation research platform (sarrp). *Physics in Medicine & Biology*, 63(11), 2018.

[110] C. D. Johnstone, R. LaFontaine, Y. Poirier, and M. Tambasco. Modeling a superficial radiotherapy x-ray source for relative dose calculations. *Journal of Applied Clinical Medical Physics*, 16(3):118–130, 2015.

[111] C. D. Johnstone, P. Lindsay, E. E. Graves, E. Wong, J. R. Perez, Y. Poirier, Y. Ben-Bouchta, T. Kanesalingam, H. Chen, A. E. Rubinstein, et al. Multi-institutional microct image comparison of image-guided small animal irradiators. *Physics in Medicine & Biology*, 62(14):5760, 2017.

[112] C. D. Johnstone, F. Therriault-Proulx, L. Beaulieu, and M. Bazalova-Carter. Characterization of a plastic scintillating detector for the small animal radiation research platform (sarrp). *Medical Physics*, 46:1, 2019.

[113] M. C. Joiner and A. Van der Kogel. *Basic clinical radiobiology*, volume 2. CRC press, 2016.

[114] P. Judy. The line spread function and modulation transfer function of a computed tomographic scanner. *Medical Physics*, 3(4):233–236, 1976.

[115] Y. Kamio and H. Bouchard. Correction-less dosimetry of nonstandard photon fields: a new criterion to determine the usability of radiation detectors. *Physics in Medicine & Biology*, 59(17):4973, 2014.

[116] K. Kanagaraj, S. A. S. Basheerudeen, M. Jose, A. Ozhimuthu, P. Selvam, S. Pattan, V. Perumal, et al. Assessment of dose and dna damages in individuals exposed to low dose and low dose rate ionizing radiations during computed tomography imaging. *Mutation Research/Genetic Toxicology and Environmental Mutagenesis*, 789:1–6, 2015.

[117] I. Kawrakow. Accurate condensed history monte carlo simulation of electron transport. i. egsnrc, the new egs4 version. *Medical Physics*, 27(3):485–498, 2000.

[118] I. Kawrakow and D. Rogers. The egsnrc code system: Monte carlo simulation of electron and photon transport. *NRCC Report PIRS-701*, 2000.

[119] F. M. Khan et al. *The physics of radiation therapy*. published LIPPINCOTT WILLIAMS & WILKINS, 3 edition, 2003.

[120] E. L. Kiehl, S. Stojadinovic, K. T. Malinowski, D. Limbrick, S. C. Jost, J. R. Garbow, J. B. Rubin, J. O. Deasy, D. Khullar, E. W. Izaguirre, et al. Feasibility of small animal cranial irradiation with the micrort system. *Medical Physics*, 35(10):4735–4743, 2008.

[121] T. K. Kumar and K. V. Reddy. Effective atomic numbers for materials of dosimetric interest. *Radiation Physics and Chemistry*, 50(6):545–553, 1997.

[122] S. Kunjachan, A. Detappe, R. Kumar, T. Ireland, L. Cameron, D. E. Biancur, V. Motto-Ros, L. Sancey, S. Sridhar, G. M. Makrigiorgos, et al. Nanoparticle mediated tumor vascular disruption: a novel strategy in radiation therapy. *Nano Letters*, 15(11):7488–7496, 2015.

[123] J. Lambert, D. McKenzie, S. Law, J. Elsey, and N. Suchowerska. A plastic scintillation dosimeter for high dose rate brachytherapy. *Physics in Medicine & Biology*, 51(21):5505, 2006.

[124] J. Lambert, Y. Yin, D. R. McKenzie, S. H. Law, A. Ralston, and N. Suchowerska. A prototype scintillation dosimeter customized for small and dynamic megavoltage radiation fields. *Physics in Medicine & Biology*, 55(4):1115, 2010.

[125] C. Le Deroff, A.-M. Frelin-Labalme, and X. Ledoux. Characterization of a scintillating fibre detector for small animal imaging and irradiation dosimetry. *The British Journal of Radiology*, 90(1069):20160454, 2016.

[126] D. A. Lee, J. Salvatierra, E. Velarde, J. Wong, E. C. Ford, and S. Blackshaw. Functional interrogation of adult hypothalamic neurogenesis with focal radiological inhibition. *Journal of Visualized Experiments: JoVE*, 81, 2013.

[127] W. Leo. Techniques for nuclear and particle physics experiments. *Nuclear Instrumentation Methods in Physics Research*, 834:290, 1988.

[128] F. Lessard, L. Archambault, M. Plamondon, P. Després, F. Therriault-Proulx, S. Beddar, and L. Beaulieu. Validating plastic scintillation detectors for photon dosimetry in the radiologic energy range. *Medical Physics*, 39(9):5308–5316, 2012.

[129] D. Létourneau, J. Pouliot, and R. Roy. Miniature scintillating detector for small field radiation therapy. *Medical Physics*, 26(12):2555–2561, 1999.

[130] C. S. Levin and H. Zaidi. Current trends in preclinical pet system design. *PET Clinics*, 2(2):125–160, 2007.

[131] S. A. Lloyd, I. M. Gagne, M. Bazalova-Carter, and S. Zavgorodni. Validation of varian truebeam electron phase–spaces for monte carlo simulation of mlc-shaped fields. *Medical Physics*, 43(6Part1):2894–2903, 2016.

[132] V. C. Lo, M. K. Akens, S. Moore, A. J. Yee, B. C. Wilson, and C. M. Whyne. Beyond radiation therapy: photodynamic therapy maintains structural integrity of irradiated healthy and metastatically involved vertebrae in a pre-clinical in vivo model. *Breast Cancer Research and Treatment*, 135(2):391–401, 2012.

[133] M. Löbrich, A. Shibata, A. Beucher, A. Fisher, M. Ensminger, A. A. Goodarzi, O. Barton, and P. A. Jeggo. γh2ax foci analysis for monitoring dna double-strand break repair: strengths, limitations and optimization. *Cell Cycle*, 9(4):662–669, 2010.

[134] D. A. Low, P. Parikh, J. F. Dempsey, S. Wahab, and S. Huq. Ionization chamber volume averaging effects in dynamic intensity modulated radiation therapy beams. *Medical Physics*, 30(7):1706–1711, 2003.

[135] C. Ma and D. Rogers. Beamdp as a general-purpose utility. *NRC Report PIRS 509e (Rev A)*, 2004.

[136] C.-M. Ma, C. Coffey, L. DeWerd, C. Liu, R. Nath, S. Seltzer, and J. Seuntjens. Aapm protocol for 40–300 kv x-ray beam dosimetry in radiotherapy and radiobiology. *Medical Physics*, 28(6):868–893, 2001.

[137] J. Mahmood, S. Jelveh, A. Zaidi, S. R. Doctrow, M. Medhora, and R. P. Hill. Targeting the renin–angiotensin system combined with an antioxidant is highly effective in mitigating radiation-induced lung damage. *International Journal of Radiation Oncology Biology Physics*, 89(4):722–728, 2014.

[138] R. Marconi, S. Strolin, G. Bossi, and L. Strigari. A meta-analysis of the abscopal effect in preclinical models: Is the biologically effective dose a relevant physical trigger? *PloS One*, 12(2):e0171559, 2017.

[139] O. A. Martin, R. L. Anderson, K. Narayan, and M. P. MacManus. Does the mobilization of circulating tumour cells during cancer therapy cause metastasis? *Nature Reviews Clinical Oncology*, 14(1):32, 2017.

[140] M. Matinfar, E. Ford, I. Iordachita, J. Wong, and P. Kazanzides. Image-guided small animal radiation research platform: calibration of treatment beam alignment. *Physics in Medicine & Biology*, 54(4):891, 2009.

[141] K. Mcconnell, X. Li, M. Obeidat, N. Kirby, and E. Shim. direct measurement of a change in biological damage between low and high energy x-ray beams using a novel dna dosimeter: mo-ab-fs4-03. *Medical Physics*, 44(6):3032, 2017.

[142] J. A. Meganck, K. M. Kozloff, M. M. Thornton, S. M. Broski, and S. A. Goldstein. Beam hardening artifacts in micro-computed tomography scanning can be reduced by x-ray beam filtration and the resulting images can be used to accurately measure bmd. *Bone*, 45(6):1104–1116, 2009.

[143] N. Miyahara, T. Kokubo, Y. Hara, A. Yamada, T. Koike, and Y. Arai. Evaluation of x-ray doses and their corresponding biological effects on experimental animals in cone-beam micro-ct scans (r-mct2). *Radiological Physics and Technology*, 9(1):60–68, 2016.

[144] C. Moore, T. Wood, C. Cawthorne, K. Hilton, S. Maher, J. Saunderson, S. Archibald, and A. Beavis. A method to calibrate the rs 2000 x-ray biological irradiator for radiobiological flank irradiation of mice. *Biomedical Physics & Engineering Express*, 2(3):037001, 2016.

[145] C. M. Moran, S. D. Pye, W. Ellis, A. Janeczko, K. D. Morris, A. S. McNeilly, and H. M. Fraser. A comparison of the imaging performance of high resolution ultrasound scanners for preclinical imaging. *Ultrasound In Medicine And Biology*, 37(3):493–501, 2011.

[146] J. Morin, D. Béliveau-Nadeau, E. Chung, J. Seuntjens, D. Thériault, L. Archambault, S. Beddar, and L. Beaulieu. A comparative study of small field total scatter factors and dose profiles using plastic scintillation detectors and other stereotactic dosimeters: the case of the cyberknife. *Medical Physics*, 40(1), 2013.

[147] R. Müller and P. Rüegsegger. Morphological validation of the 3d structure of non-invasive bone biopsies. *Abstracts 10th Int. Workshop on Bone Densitometry. Bone Miner,*, 25:8, 1994.

[148] W. Ngwa and Z. Ouyang. Following the preclinical data: Leveraging the abscopal effect more efficaciously. *Frontiers in Oncology*, 7:66, 2017.

[149] H. Nikjoo and L. Lindborg. Rbe of low energy electrons and photons. *Physics in Medicine & Biology*, 55(10):R65, 2010.

[150] C. Noblet, S. Chiavassa, F. Smekens, D. Sarrut, V. Passal, J. Suhard, A. Lisbona, F. Paris, and G. Delpon. Validation of fast monte carlo dose calculation in small animal radiotherapy with ebt3 radiochromic films. *Physics in Medicine & Biology*, 61(9):3521, 2016.

[151] M. Obeidat, K. A. McConnell, X. Li, B. Bui, S. Stathakis, N. Papanikolaou, K. Rasmussen, C. S. Ha, S. E. Lee, E. Y. Shim, et al. Dna double-strand breaks as a method of radiation measurements for therapeutic beams. *Medical Physics*, 2018.

[152] P. Papaconstadopoulos, L. Archambault, and J. Seuntjens. Experimental investigation on the accuracy of plastic scintillators and of the spectrum discrimination method in small photon fields. *Medical Physics*, 44(2):654–664, 2017.

[153] A. P. Patel, I. Tirosh, J. J. Trombetta, A. K. Shalek, S. M. Gillespie, H. Wakimoto, D. P. Cahill, B. V. Nahed, W. T. Curry, R. L. Martuza, et al. Single-cell rna-seq highlights intratumoral heterogeneity in primary glioblastoma. *Science*, 344(6190):1396–1401, 2014.

[154] L. Peralta. Temperature dependence of plastic scintillators. *Nuclear Instruments and Methods in Physics Research Section A: Accelerators, Spectrometers, Detectors and Associated Equipment*, 883:20–23, 2018.

[155] L. Peralta and F. R^{e}go. Response of plastic scintillators to low-energy photons. *Physics in Medicine & Biology*, 59(16):4621, 2014.

[156] M. Peron and P. Cassette. A compton coincidence study of liquid scintillator response to low-energy electrons. *Nuclear Instruments and Methods in Physics Research Section A: Accelerators, Spectrometers, Detectors and Associated Equipment*, 369(2-3):344–347, 1996.

[157] T. E. Peterson and S. Shokouhi. Advances in preclinical spect instrumentation. *Journal of Nuclear Medicine*, 53(6):841–844, 2012.

[158] M. Petric, J. Robar, and B. Clark. Development and characterization of a tissue equivalent plastic scintillator based dosimetry system. *Medical Physics*, 33(1):96–105, 2006.

[159] R. Pidikiti. *Development of Monte Carlo Treatment Planning and Dosimetry System for Small Animal Irradiator*. PhD thesis, UT Southwestern, 2012.

[160] E. I. Piechowiak, J.-F. W. Peter, B. Kleb, K. J. Klose, and J. T. Heverhagen. Intravenous iodinated contrast agents amplify dna radiation damage at ct. *Radiology*, 275(3):692–697, 2015.

[161] Y. Poirier, C. D. Johnstone, and C. Kirkby. The impact of ultrathin filter design on dosimetry and radiation biological effectiveness in modern image-guided small animal irradiators. *British Journal of Radiology*, 91(1095), 2019.

[162] G. Poludniowski, G. Landry, F. DeBlois, P. Evans, and F. Verhaegen. Spekcalc: a program to calculate photon spectra from tungsten anode x-ray tubes. *Physics in Medicine & Biology*, 54(19):N433, 2009.

[163] A. Popovtzer, A. Mizrachi, M. Motiei, D. Bragilovski, L. Lubimov, M. Levi, O. Hilly, I. Ben-Aharon, and R. Popovtzer. Actively targeted gold nanoparticles as novel radiosensitizer agents: an in vivo head and neck cancer model. *Nanoscale*, 8(5):2678–2685, 2016.

[164] I. Popp, A. L. Grosu, G. Niedermann, and D. G. Duda. Immune modulation by hypofractionated stereotactic radiation therapy: therapeutic implications. *Radiotherapy and Oncology*, 120(2):185–194, 2016.

[165] A. Ralston, P. Liu, K. Warrener, D. McKenzie, and N. Suchowerska. Small field diode correction factors derived using an air core fibre optic scintillation dosimeter and ebt2 film. *Physics in Medicine & Biology*, 57(9):2587, 2012.

[166] K. J. Redmond, P. Achanta, S. A. Grossman, M. Armour, J. Reyes, L. Kleinberg, E. Tryggestad, A. Quinones-Hinojosa, and E. C. Ford. A radiotherapy technique to limit dose to neural progenitor cell niches without compromising tumor coverage. *Journal of Neuro-Oncology*, 104(2):579–587, 2011.

[167] G. Reggiori, A. Stravato, P. Mancosu, F. Lobefalo, L. Paganini, F. Zucconi, V. Palumbo, A. Gaudino, M. Scorsetti, and S. Tomatis. Small field character-

ization of a nanochamber prototype under flattening filter free photon beams. *Physica Medica*, 2017.

[168] E. L. Ritman. Current status of developments and applications of micro-ct. *Annual Review of Biomedical Engineering*, 13:531–552, 2011.

[169] M. Rodriguez, H. Zhou, P. Keall, and E. Graves. Commissioning of a novel microct/rt system for small animal conformal radiotherapy. *Physics in Medicine & Biology*, 54(12):3727, 2009.

[170] D. Rogers, B. Faddegon, G. Ding, C.-M. Ma, J. We, and T. Mackie. Beam: a monte carlo code to simulate radiotherapy treatment units. *Medical Physics*, 22(5):503–524, 1995.

[171] D. Rogers, B. Walters, I. Kawrakow, et al. Beamnrc users manual. *NRC Report Pirs*, 509:12, 2009.

[172] C. T. Rueden, J. Schindelin, M. C. Hiner, B. E. DeZonia, A. E. Walter, E. T. Arena, and K. W. Eliceiri. Imagej2: Imagej for the next generation of scientific image data. *BMC Bioinformatics*, 18(1):529, 2017.

[173] P. Rüegsegger, B. Koller, and R. Müller. A microtomographic system for the nondestructive evaluation of bone architecture. *Calcified Tissue International*, 58(1):24–29, 1996.

[174] F. Salvat, J. M. Fernández-Varea, and J. Sempau. Penelope-2006: A code system for monte carlo simulation of electron and photon transport. In *Workshop Proceedings*, volume 4. Nuclear Energy Agency, Organization for Economic Co-operation and Development Barcelona, Spain, 2006.

[175] R. Sanchez and M. Smith. Photopolymer utb in c-137. *Wubb Dubb*, 2(4):8–15, 2015.

[176] J. Schindelin, I. Arganda-Carreras, E. Frise, V. Kaynig, M. Longair, T. Pietzsch, S. Preibisch, C. Rueden, S. Saalfeld, B. Schmid, et al. Fiji: an open-source platform for biological-image analysis. *Nature Methods*, 9(7):676, 2012.

[177] C. A. Schneider, W. S. Rasband, and K. W. Eliceiri. Nih image to imagej: 25 years of image analysis. *Nature Methods*, 9(7):671, 2012.

[178] J. Seco and F. Verhaegen. *Monte Carlo techniques in radiation therapy*. CRC Press, 2013.

[179] M. J. Selby, J. J. Engelhardt, R. J. Johnston, L.-S. Lu, M. Han, K. Thudium, D. Yao, M. Quigley, J. Valle, C. Wang, et al. Preclinical development of ipilimumab and nivolumab combination immunotherapy: mouse tumor models, in vitro functional studies, and cynomolgus macaque toxicology. *PLoS One*, 11(9):e0161779, 2016.

[180] C. A. Smith and M. L. Freeman. Preclinical advances in combined-modality cancer immunotherapy with radiation therapy. *International Journal of Radiation Oncology, Biology, Physics*, 94(1):11–14, 2016.

[181] K. Song, R. Pidikiti, S. Stojadinovic, M. Speiser, S. Seliounine, D. Saha, and T. Solberg. An x-ray image guidance system for small animal stereotactic irradiation. *Physics in Medicine & Biology*, 55(23):7345, 2010.

[182] S. Stojadinovic, D. Low, A. Hope, M. Vicic, J. Deasy, J. Cui, D. Khullar, P. Parikh, K. Malinowski, E. Izaguirre, et al. Micro-rt small animal conformal irradiator. *Medical physics*, 34(12):4706–4716, 2007.

[183] R. Taschereau and A. F. Chatziioannou. Fdg-pet image-based dose distribution in a realistic mouse phantom from monte carlo simulations. In *Nuclear Science Symposium Conference Record, 2005 IEEE*, volume 3, pages 4–pp. IEEE, 2005.

[184] F. Therriault-Proulx, L. Beaulieu, L. Archambault, and S. Beddar. On the nature of the light produced within pmma optical light guides in scintillation fiber-optic dosimetry. *Physics in Medicine & Biology*, 58(7):2073, 2013.

[185] V. Tretyak. Semi-empirical calculation of quenching factors for ions in scintillators. *Astroparticle Physics*, 33(1):40–53, 2010.

[186] E. Tryggestad, M. Armour, I. Iordachita, F. Verhaegen, and J. Wong. A comprehensive system for dosimetric commissioning and monte carlo validation for the small animal radiation research platform. *Physics in Medicine & Biology*, 54(17):5341, 2009.

[187] J. E. Turner. *Atoms, radiation, and radiation protection*. John Wiley & Sons, 3 edition, 2008.

[188] I. S. Vala, L. R. Martins, N. Imaizumi, R. J. Nunes, J. Rino, F. Kuonen, L. M. Carvalho, C. Rüegg, I. M. Grillo, J. T. Barata, et al. Low doses of ionizing radiation promote tumor growth and metastasis by enhancing angiogenesis. *PloS One*, 5(6):e11222, 2010.

[189] E. Van de Casteele, D. Van Dyck, J. Sijbers, and E. Raman. A model-based correction method for beam hardening artefacts in x-ray microtomography. *Journal of X-ray Science and Technology*, 12(1):43–57, 2004.

[190] G. van der Horst, J. J. van Asten, A. Figdor, C. van den Hoogen, H. Cheung, R. F. Bevers, R. C. Pelger, and G. van der Pluijm. Real-time cancer cell tracking by bioluminescence in a preclinical model of human bladder cancer growth and metastasis. *European Urology*, 60(2):337–343, 2011.

[191] G. Van Gompel, K. Van Slambrouck, M. Defrise, K. J. Batenburg, J. de Mey, J. Sijbers, and J. Nuyts. Iterative correction of beam hardening artifacts in ct. *Medical physics*, 38(S1):S36–S49, 2011.

[192] S. J. van Hoof, P. V. Granton, and F. Verhaegen. Development and validation of a treatment planning system for small animal radiotherapy: Smart-plan. *Radiotherapy and Oncology*, 109(3):361–366, 2013.

[193] F. Verhaegen, P. Granton, and E. Tryggestad. Small animal radiotherapy research platforms. *Physics in Medicine & Biology*, 56(12):R55, 2011.

[194] B. Walters, I. Kawrakow, D. Rogers, et al. Dosxyznrc users manual. *NRC Report Pirs*, 794, 2005.

[195] L. Wang, L. Perles, L. Archambault, N. Sahoo, D. Mirkovic, and S. Beddar. Determination of the quenching correction factors for plastic scintillation detectors in therapeutic high-energy proton beams. *Physics in Medicine & Biology*, 57(23):7767, 2012.

[196] Y.-F. Wang, S.-C. Lin, Y. H. Na, P. J. Black, and C.-S. Wuu. Dosimetric verification and commissioning for a small animal image-guided irradiator. *Physics in Medicine & Biology*, 2018.

[197] R. Ward, W. D. Carroll, P. Cunningham, S.-A. Ho, M. Jones, W. Lenney, D. Thompson, and F. J. Gilchrist. Radiation dose from common radiologi-

cal investigations and cumulative exposure in children with cystic fibrosis: an observational study from a single uk centre. *BMJ Open*, 7(8):e017548, 2017.

[198] I. Willekens, N. Buls, T. Lahoutte, L. Baeyens, C. Vanhove, V. Caveliers, R. Deklerck, A. Bossuyt, and J. de Mey. Evaluation of the radiation dose in micro-ct with optimization of the scan protocol. *Contrast Media & Molecular Imaging*, 5(4):201–207, 2010.

[199] J. F. Williamson, J. Dempsey, A. Kirov, J. Monroe, W. Binns, and H. Hedtjärn. Plastic scintillator response to low-energy photons. *Physics in Medicine & Biology*, 44(4):857, 1999.

[200] T. Wilson and J. W. Hastings. Bioluminescence. *Annual Review of Cell and Developmental Biology*, 14(1):197–230, 1998.

[201] J. Wong, E. Armour, P. Kazanzides, I. Iordachita, E. Tryggestad, H. Deng, M. Matinfar, C. Kennedy, Z. Liu, T. Chan, et al. High-resolution, small animal radiation research platform with x-ray tomographic guidance capabilities. *International Journal of Radiation Oncology, Biology, Physics*, 71(5):1591–1599, 2008.

[202] G. M. Woods, K. Bondra, C. Chronowski, J. Leasure, M. Singh, L. Hensley, T. P. Cripe, A. Chakravarti, and P. J. Houghton. Radiation therapy may increase metastatic potential in alveolar rhabdomyosarcoma. *Pediatric Blood & Cancer*, 62(9):1550–1554, 2015.

[203] L. Wootton, R. Kudchadker, A. Lee, and S. Beddar. Real-time in vivo rectal wall dosimetry using plastic scintillation detectors for patients with prostate cancer. *Physics in Medicine & Biology*, 59(3):647, 2014.

[204] D. Wu, L. Li, L. Zhang, Y. Xing, Z. Chen, and Y. Xiao. Geometric calibration of cone-beam ct with a flat-panel detector. In *2011 IEEE Nuclear Science Symposium Conference Record*, pages 2952–2955. IEEE, 2011.

[205] J. Wuerfel. Dose measurements in small fields. *Medical Physics*, 1(1):81–90, 2013.

[206] K. Yang, A. L. Kwan, D. F. Miller, and J. M. Boone. A geometric calibration method for cone beam ct systems. *Medical physics*, 33(6Part1):1695–1706, 2006.

[207] R. Yao, R. Lecomte, and E. S. Crawford. Small-animal pet: what is it, and why do we need it? *Journal of Nuclear Medicine Technology*, 40(3):157–165, 2012.

[208] W. J. Yoo, S. H. Shin, D. Jeon, S. Hong, H. I. Sim, S. G. Kim, K. W. Jang, S. Cho, W. S. Youn, and B. Lee. Measurement of entrance surface dose on an anthropomorphic thorax phantom using a miniature fiber-optic dosimeter. *Sensors*, 14(4):6305–6316, 2014.

[209] J. Zeng, A. P. See, J. Phallen, C. M. Jackson, Z. Belcaid, J. Ruzevick, N. Durham, C. Meyer, T. J. Harris, E. Albesiano, et al. Anti-pd-1 blockade and stereotactic radiation produce long-term survival in mice with intracranial gliomas. *International Journal of Radiation Oncology, Biology, Physics*, 86(2):343–349, 2013.

[210] B. Zhang, K. K.-H. Wang, J. Yu, S. Eslami, I. Iordachita, J. Reyes, R. Malek, P. T. Tran, M. S. Patterson, and J. W. Wong. Bioluminescence tomography–guided radiation therapy for preclinical research. *International Journal of Radiation Oncology Biology Physics*, 94(5):1144–1153, 2016.

[211] P. Zhang, B. Wang, X. Chen, D. Cvetkovic, L. Chen, J. Lang, and C.-M. Ma. Local tumor control and normal tissue toxicity of pulsed low-dose rate radiotherapy for recurrent lung cancer: an in vivo animal study. *Dose-Response*, 13(2):1559325815588507, 2015.

[212] Q. Zheng, Y. Liu, H. Zhou, Y. Du, B. Zhang, J. Zhang, G. Miao, B. Liu, and H. Zhang. X-ray radiation promotes the metastatic potential of tongue squamous cell carcinoma cells via modulation of biomechanical and cytoskeletal properties. *Human & Experimental Toxicology*, 34(9):894–903, 2015.

[213] H. Zhou, M. Rodriguez, F. Van den Haak, G. Nelson, R. Jogani, J. Xu, X. Zhu, Y. Xian, P. T. Tran, D. W. Felsher, et al. Development of a micro-computed tomography–based image-guided conformal radiotherapy system for small animals. *International Journal of Radiation Oncology, Biology, Physics*, 78(1):297–305, 2010.

Appendix A

Biological Considerations in Medical Physics

Within this dissertation we have described absorbed dose to matter by way of energy absorbed per unit mass using Gy. Biological considerations suggest that there may not necessarily be a 1-to-1 correspondence between the amount of energy absorbed in tissue and the amount of cellular damage. In fact, the biological damage imparted on a cell will be dependent on key characteristics of the radiation including energy, dose rate, and radiation type.

A.1 Biological Considerations

The Irradiation of tissues can be described by determining the amount of absorbed dose needed to achieve a biological damage of 50% cell death from different kinds of radiation [77]. The level of cell death will vary for identical amounts of doses delivered from different types of radiation, i.e., electrons, photons, protons, neutrons, γ-rays, etc. Equivalent dose (H) is a quantity representing the stochastic effects of ionizing radiation in the body, where the SI unit is the sievert (Sv), where

$$1\,\mathrm{Sv} = 100\,\mathrm{rem}, \tag{A.1}$$

with conventional units of rem. The units of Sv and rem were established to describe the amount of ionizing radiation humans receive based on the biological impact. This is in comparison to using exposure and absorbed dose, which relates the amount of energy absorbed in matter without consideration of the biological effectiveness from different types of ionizing radiation sources.

RBE is a metric established to account for variations in biological effect arising from different types of radiation. RBE is defined as the ratio of the doses required by two different types of ionizing radiation to cause the same level of cell death within the same living tissue, defined as

$$RBE = \frac{D_{\mathrm{R}}}{D_{\mathrm{X}}}. \tag{A.2}$$

D_{R} is a reference dose of ionizing radiation of a given type, and D_{X} is the dose of another ionization radiation type that produces the same amount of biological cell death in the same tissue. This is important in preclinical research, as an RBE for the 220 kVp x-rays found in preclinical irradiators have not been agreed upon, with RBE values ranging from 1.00 to 1.11 as reported by a review paper [149]. This suggests that we do not fully understand the processes of radiation damage when comparing preclinical kV x-rays studies to MV x-ray irradiations.

Levels of radiation induced cell damage are directly quantified by measuring the double strand breaks in irradiated tissues using γH2AX through immunofluorescence [133]. Radiation induced deoxyribonucleic acid (DNA) damage is formed through the production of free radicals both directly on the DNA and indirectly through the ionization of cytosolic constituents which can then cause chemical changes on the DNA. DNA strand breaks are recognized and addressed through the prompt initiation of the DNA damage response (DDR) pathway which includes the initial phosphorylation of H2AX (γH2AX) [79, 113]. The DDR ultimately leads to either repair of the DNA damage and cell survival, cell death, or DNA mutations. Ionization chambers cannot measure DDR, however, research is progressing towards directly measuring this using DNA dosimeters [141, 151]. In addition, it has been found that DNA damage is dependent on the heterogeneity of a tumor, where common radiotherapy treatments treat tumors as homogeneous targets [10, 153].

These biological considerations may also be extended to dose rate imparted by ioniz-

ing radiation, which is commonly disregarded as an important factor in overall impact on cell death (including changing of the molecular chemistry within tissues). For example, it is commonplace to relate the amount of dose obtained in diagnostic x-rays and other types of ionizing radiation exposures with the amount of annual radiation received from natural background radiation [37, 82, 119, 187] (i.e., exposure to naturally occurring radioisotopes in nature, cosmic background radiation, terrestrial radiation, and internal inhalation/ingestion, and is directly compared to man-made ionizing radiation). However, even though the amount of absorbed dose from natural background radiation in one year (˜2-3mSv [119]) can be on the order of a single chest CT x-ray (0.57-1.69 mSv [197]) and abdominal CT x-ray (2.9-3.9 mSv [197]), the fact is that the exposure from natural background radiation is over the course of 365 days, where in medical imaging, the typical exposure is on the order of 10 seconds. In comparison, that's approximately a 3,000,000 times higher dose rate difference!

Dose rate is a relevant factor in radiobiology and assessing the biological effect of radiation dose because, biologically, the amount of cell damage induced in a cell, and the quality of cellular repair, is directly dependent on the amount of ionizing radiation imparted into a cell for a given amount of time. This includes the amount of time a cell has to repair itself before it is exposed to ionizing radiation again [72, 77]. In terms of natural background radiation acquired in a single year, the dose rate to human tissues is likely low enough to allow for adequate DNA repair, and not cause an abundance of double strand DNA breaks [101, 102]. On the other hand, even though the total amount of absorbed dose from the average CT scan can be on the order of the annual background radiation absorbed, the relatively much higher dose rate may be more probable to cause single and double strand breaks in DNA that lead to cell death and mutation [90, 116, 160].

The biological impact of radiation extends beyond cell death, mutation, and repair, as irradiation can lead to significant biological responses in living systems. An example of the importance of the biological response to radiation is the abscopal effect, whereby distant metastatic disease has been found to respond to a single localized radiation treatment with specific dose rates [34, 92, 96, 138, 148]. Radiation has also been found to exert migratory effects on cancer. Certain fractionation schemes have been observed to cause radiated-induced release of actively proliferating tumor cell fragments and changes in gene expression. These tumor fragments have been found in both the bloodstream and lymph nodes, suggesting the possibility of radiation-

induced metastases [27, 139, 202, 212]. This illustrates that fractionation and dose rate may influence metastatic formation in some tumor sites. These are potentially significant findings that may change how we properly irradiate tumors in the future, and illustrates that we still do not fully understand how radiation interacts with human tissues. These observations imply that biological considerations are very important in Medical Physics and in preclinical studies, and should be taken into consideration.

Appendix B

Validation of SARRP Monte Carlo Model

Our MC model of the SARRP has been validated with depth dose and profile measurements in homogeneous and heterogeneous phantoms. Validation was performed to illustrate our SARRP Monte Carlo model accuracy for the distribution of phase space files to interested users: included are all imaging beams (40–80 kVp) and therapy beams (open, 10x10, 5x5, and 3x3 mm2 square and 1 mm diameter circular collimated fields).

B.1 Homogeneous Phantom Film Measurements

Depth dose and beam profiles were measured using GAFCHROMIC EBT3 radiochromic film (International Specialty Products, Wayne, NJ) for the 10 x 10, 5 x 5, and 3 x 3 mm^2 square and 1 mm diameter circular fields. EBT3 film was used as the most suitable film for dosimetry of small kilovoltage x-ray beams, offering high spatial resolution. EBT3 has also shown to have weak energy dependence at kV energies, making it advantageous for kV x-ray beams where beam hardening effects can occur [35]. The EBT3 film was calibrated and analyzed by Xstrahl Inc. during our commissioning process. Films were scanned with a uniform 0.0635 mm resolution.

The jig used for homogeneous phantom measurements was specially made and dis-

tributed by Xstrahl Inc. for SARRP commissioning (**Figure B.1a**). It consisted of fourteen 6 x 6 x 0.5 cm^3 solid water slabs (CIRS, Norfolk, VA) where EBT3 films were sandwiched between slabs at nominal 0, 5, 10, 15, 20, 30, 40, 50, and 70 mm depths at 31.2, 34.2, and 37.2 cm SSDs. Irradiations were performed with 220 kVp tube voltage, 13 mA tube current, and a 1.5-minute exposure time for all data sets.

In addition, the dose delivered by the 60 kVp imaging beam was measured in a larger 30 x 30 x 4.5 cm^3 solid water phantom. Films at 0, 0.5, 1.5, 2.5, and 3.5 cm depths were irradiated for 1 minute with an open 60 kVp beam and 10 mA tube current at a 33 cm SSD.

B.2 Heterogeneous Phantom Film Measurements

A heterogeneous phantom was built and consisted of Gammex (Gammex, Inc., Middleton, WI) solid water (30 x 30 x 0.5 cm^3), lung (30 x 30 x 2 cm^3), and solid cortical bone (30 x 30 x 0.5 cm^3) slabs. GAFCHROMIC EBT3 film was placed above and below each solid water slab (**Figure B.1a**), located at 0, 0.5, 2.5, 3.0, and 3.6 cm depths. The phantom was irradiated with a 220 kVp and 13 mA therapy beam for 1 minute with a 10 x 10 mm^2 collimation, and an open 60 kVp and 10 mA imaging beam for 2 minutes at a 33 cm SSD.

B.3 Homogeneous Phantom Dose Calculations

Homogeneous measurements of Section B.1 were compared to MC simulations in DOSXYZnrc for validation. A virtual water phantom was created in DOSXYZnrc to replicate the same 6 x 6 x 7.24 cm^3 solid water phantom that was used for film depth dose and beam profile measurements. Phase space files for each corresponding beam were inserted into DOSXYZnrc at the experimentally used SSDs of 31.2, 34.2, and 37.2 cm. Dose calculation resolution in the z-direction (along beam direction) for depth dose calculations was 1 mm. Resolution in the x- and y-directions was 0.5 mm, and 0.1 mm for all square fields and small circular fields, respectively. Each particle from the phase space was recycled 10 times for square fields and 99 times for circular

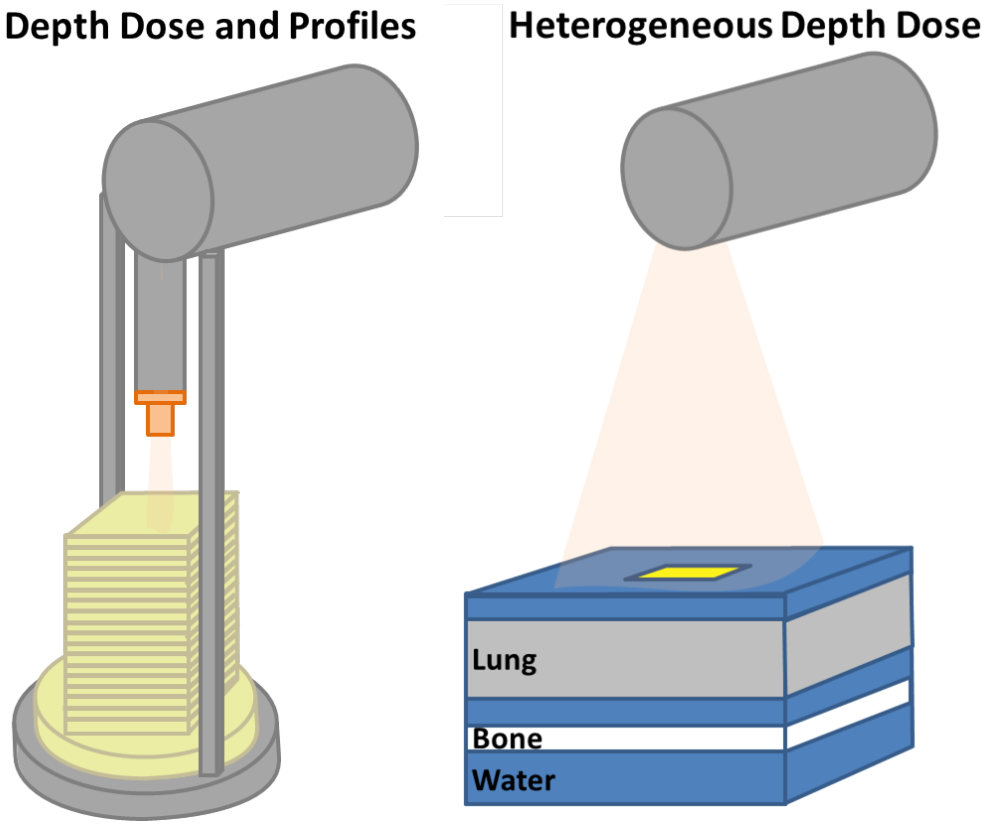

Figure B.1: Experimental setup for a) homogeneous and b) heterogeneous phantom film measurements.

fields to improve dose-computation statistics [186], with a photon splitting number of 10 for all fields.

B.4 Heterogeneous Phantom Dose Calculations

Heterogeneous measurements of Section B.2 were compared to MC simulations in DOSXYZnrc for further validation. To better illustrate microCT imaging output, film output of the 60 kVp imaging beam was scaled down to a 0.8 mA tube current (typical microCT imaging tube current) and 1 minute irradiation time (typical microCT imaging time). Elemental compositions and mass densities of the heterogeneous slabs were obtained from the manufacturer. Dose calculation resolution in the z-direction for depth dose calculations was 1 mm.

B.5 Homogeneous Phantom Results

For all field sizes, beam energies, and SSDs, depth dose data from MC agreed with our measurements within a mean difference of 2.6%, with a maximum difference of 9.1% (**Figure B.2**). These results show good agreement between measurement and our MC simulations, with absolute dose output in cGy/min determined by **Equation 8.5**. For the small 1 mm circular field size, MC-calculated dose was higher than measured, thus a scale factor needed to be applied. For such small field sizes, this may be due to a small tilt in the nozzle that reduces output.

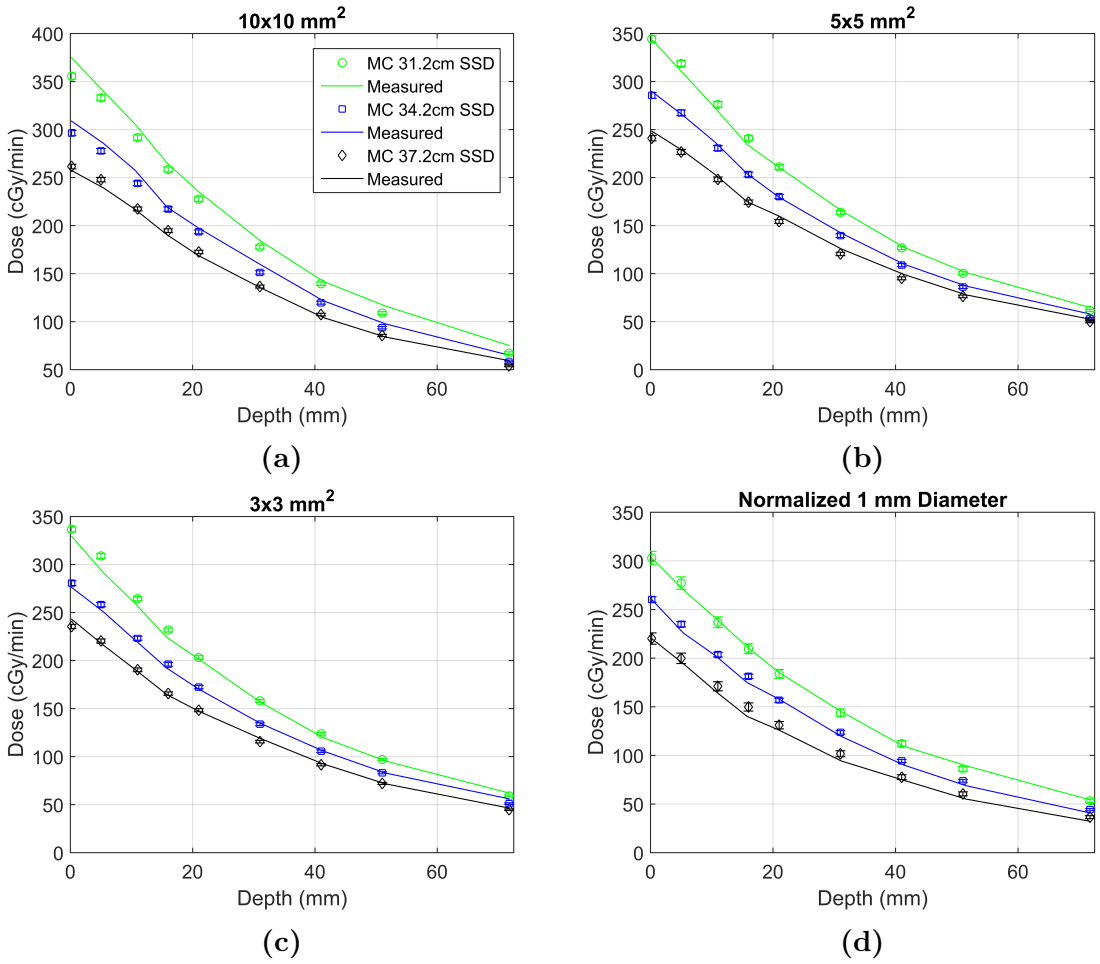

Figure B.2: Depth doses at 31.2, 34.2, and 37.2 cm SSDs, respectively, for the a) 10 x 10 mm^2, b) 5 x 5 mm^2, c) 3 x 3 mm^2 square field sizes, and d) 1 diameter circular field size. Note that the square field sizes directly output dose rate in cGy/min, while the circular field sizes are normalized to the first measurement depth.

Beam profiles for 31.2, 34.2, and 37.2 cm SSDs are illustrated in **Figures B.3**, **B.4**,

and **B.5**, respectively. For all square fields, beam energies, and SSDs, profile data from MC agreed with our measurement within a mean difference of 2.1%, with a maximum difference of 7.2%. For circular fields, a mean difference of 4.6% with a maximum difference of 11.3% was obtained. This shows reasonable agreement, as the larger percent differences with the smaller circular fields are to be expected, as slight imperfections in the setup, such as nozzle tilt, can greatly influence beam output.

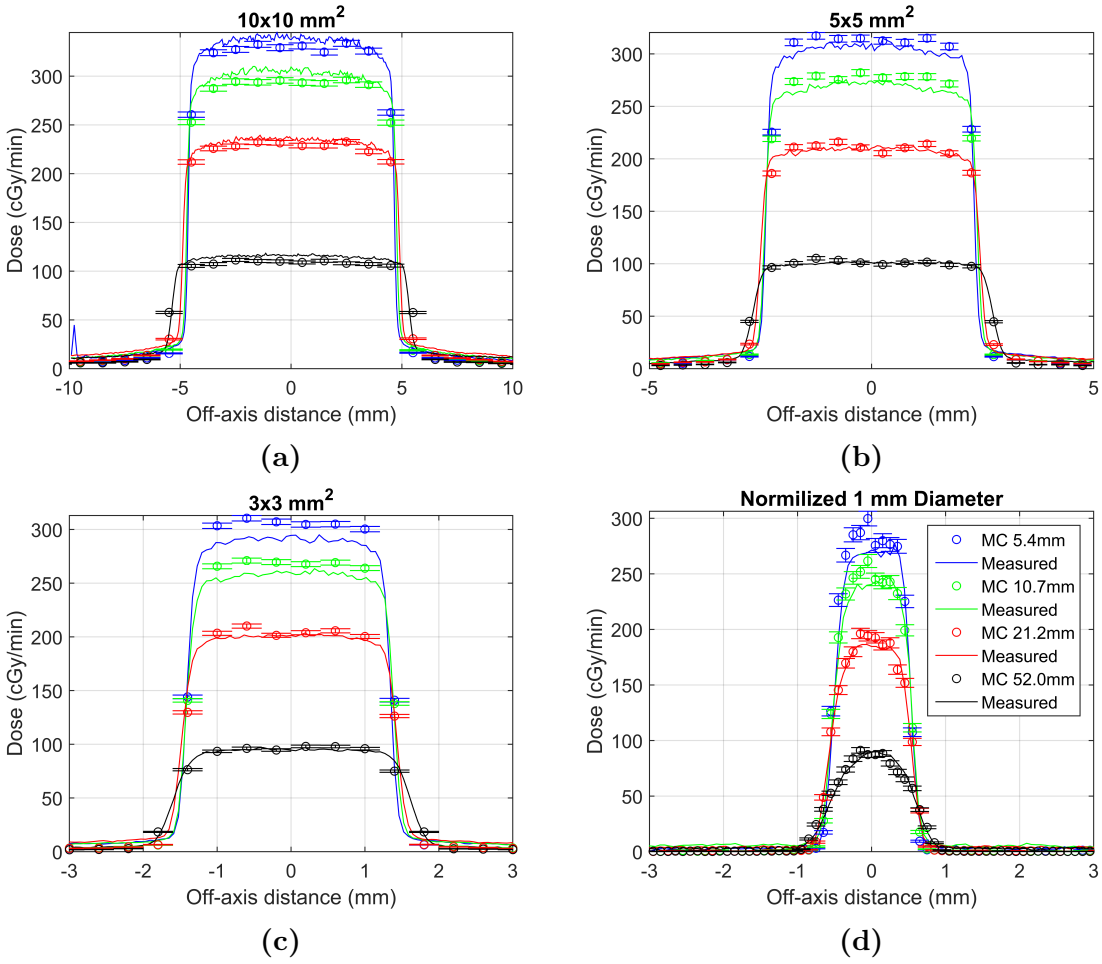

Figure B.3: Beam profiles at a 31.2 cm SSD at 5.41, 10.68, 21.21, and 52.02 mm depths for the a) 10 x 10 mm^2, b) 5 x 5 mm^2, c) 3 x 3 mm^2 square field sizes, and d) 1 mm diameter circular fields. Note that the square fields directly output in cGy/min, while the circular field is normalized to the central axis surface doses.

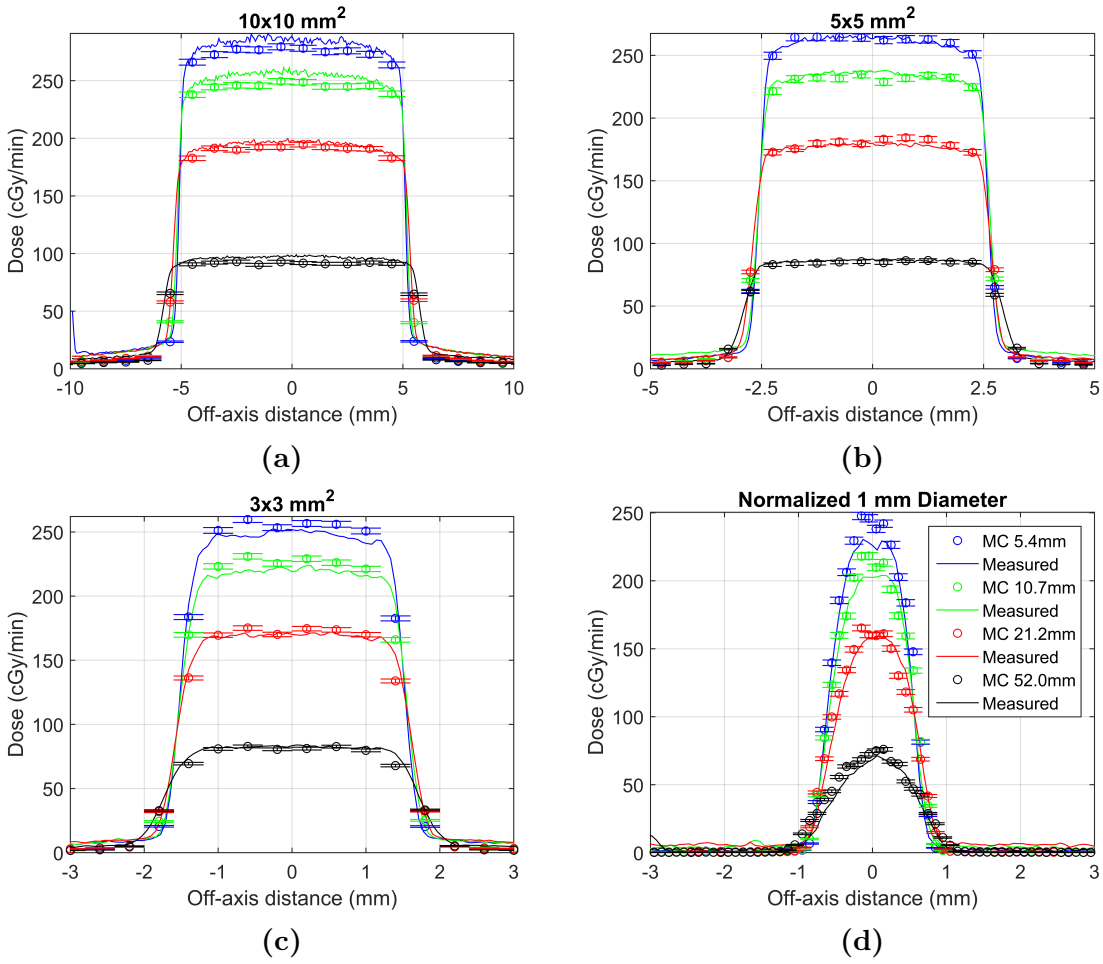

Figure B.4: Beam profiles at a 34.2 cm SSD at 5.41, 10.68, 21.21, and 52.02 mm depths for the a) 10 x 10 mm^2, b) 5 x 5 mm^2, c) 3 x 3 mm^2 square field sizes, and d) 1 mm diameter circular fields. Note that the square fields directly output in cGy/min, while the circular field is normalized to the central axis surface doses.

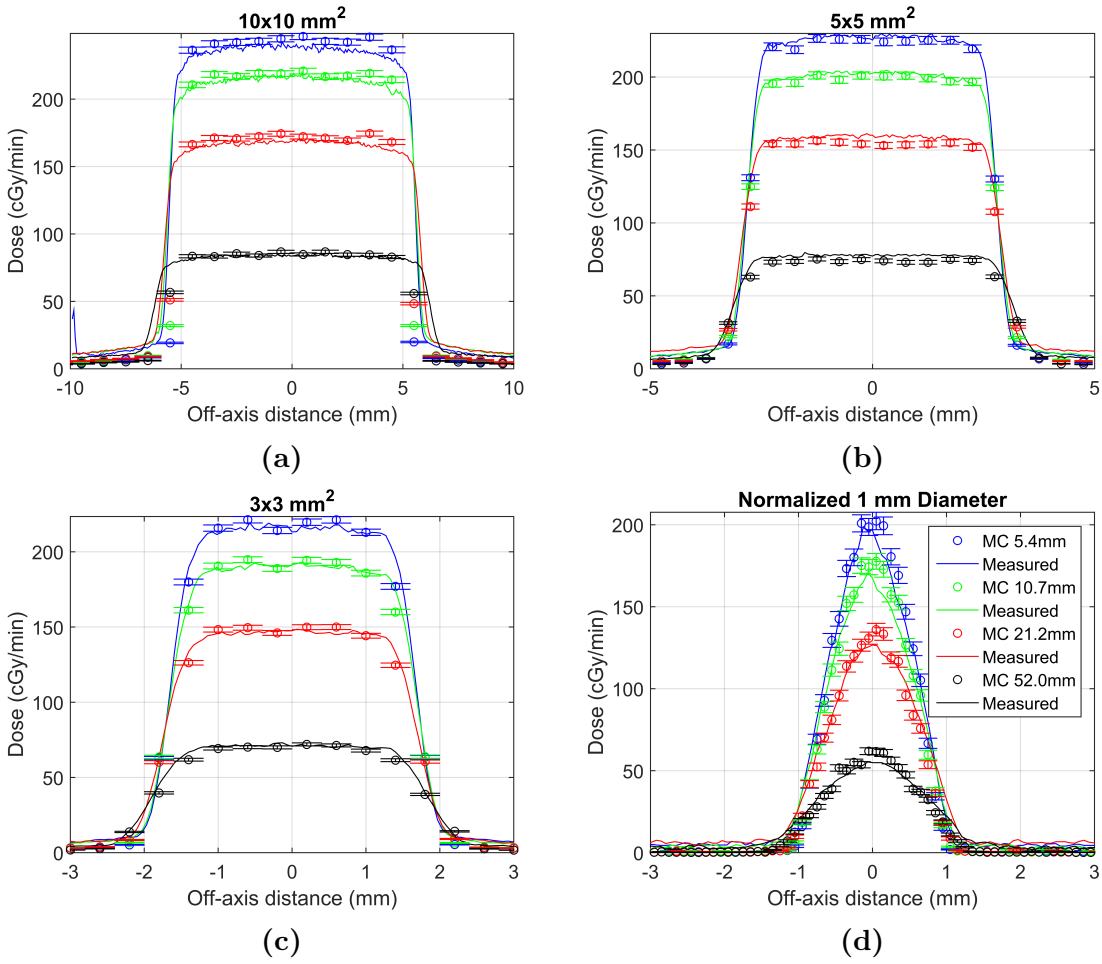

Figure B.5: Beam profiles at a 37.2 cm SSD at 5.41, 10.68, 21.21, and 52.02 mm depths for the a) 10 x 10 mm^2, b) 5 x 5 mm^2, c) 3 x 3 mm^2 square field sizes, and d) 1 mm diameter circular fields. Note that the square fields directly output in cGy/min, while the circular field is normalized to the central axis surface doses.

B.6 Heterogeneous Phantom Results

Results for the heterogeneous phantom measurements and MC simulations are illustrated in **Figure B.6**. For the 220 kVp therapy beam, MC simulations agreed with heterogeneous film measurement within a mean difference of 2.1% and a maximum difference of 2.7%. For the 60 kVp imaging beam, MC simulations agreed with the heterogeneous film measurements within a mean difference of 2.8%, excluding the lowest dose point. The maximum dose difference of 30% was found for the lowest

dose point, which might have been due to the low dose delivered to the film (17 cGy). For comparison, homogeneous solid water depth dose curves are included with heterogeneous depth dose curves in **Figure B.6**. For the 60 kVp imaging beam, MC simulations agreed with our homogeneous film measurements within a mean difference of 1.7% and maximum difference of 2.5%.

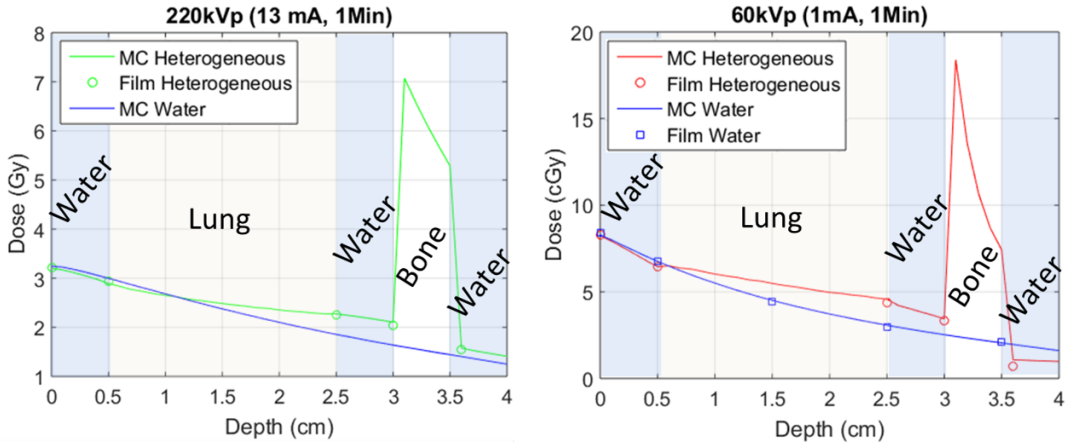

(a) **(b)**

Figure B.6: Heterogeneous and solid water phantom depth doses for a) 220 kVp therapy beam and b) 60 kVp imaging beam, acquired at a 33 cm SSD.

Appendix C

NOTES